In Situ and Satellite Observations of the Visible and Infrared Albedo of Sea Ice During Spring Melt

By

Roger A. De Abreu

A thesis
presented to the University of Waterloo
in fulfillment of the
thesis requirement for the degree of Doctor of Philosophy
in
Geography

Waterloo, Ontario, Canada, 1996

© Roger De Abreu 1996

National Library of Canada
Acquisitions and Bibliographic Services
395 Wellington Street
Ottawa ON K1A 0N4
Canada

Bibliothèque nationale du Canada
Acquisitions et services bibliographiques
395, rue Wellington
Ottawa ON K1A 0N4
Canada

Your file Votre référence

Our file Notre référence

The author has granted a non-exclusive licence allowing the National Library of Canada to reproduce, loan, distribute or sell copies of his/her thesis by any means and in any form or format, making this thesis available to interested persons.

The author retains ownership of the copyright in his/her thesis. Neither the thesis nor substantial extracts from it may be printed or otherwise reproduced with the author's permission.

L'auteur a accordé une licence non exclusive permettant à la Bibliothèque nationale du Canada de reproduire, prêter, distribuer ou vendre des copies de sa thèse de quelque manière et sous quelque forme que ce soit pour mettre des exemplaires de cette thèse à la disposition des personnes intéressées.

L'auteur conserve la propriété du droit d'auteur qui protège sa thèse. Ni la thèse ni des extraits substantiels de celle-ci ne doivent être imprimés ou autrement reproduits sans son autorisation.

0-612-21339-0

Canada

The University of Waterloo requires the signature of all persons using or photocopying this thesis. Please sign below, and give address and date.

ABSTRACT

Using *in situ* and satellite data, this thesis identifies and explains the spatial and temporal characteristics of sea ice visible (0.15-0.70 μm) and infrared albedo (0.7-4.0 μm) during the annual spring melt. Specifically, spectral albedo and complementary physical measurements were collected over first-year and multiyear ice located in the Barrow St./Lancaster Sound area of the Canadian Archipelago in the spring of 1993. Concurrently, clear-sky Advanced Very High Resolution Radiometer (AVHRR) satellite data from NOAA 12 were recorded for analysis. Of specific interest was the utility of the satellite's visible (0.58-0.68 μm) and near-infrared (0.73-1.1 μm) channels for estimating visible and infrared sea ice surface albedo during the dynamic spring transition period. Surface albedos were inverted from satellite top-of-atmosphere radiances after correcting for sensor calibration drift, scene anisotropy and atmospheric attenuation. In order to determine the uncertainty in the inversion method, a complete error budget for the satellite-derived surface albedos was performed. The sensitivity of the method to uncertainties in input parameters was also examined.

A significant drift (8-25%) was detected in the calibrations of the visible and near-infrared satellite channels. Updated calibration coefficients were derived and are presented herein. Scene anisotropy was corrected using scene models derived from Nimbus-7 ERBE data. The high variability in the anisotropic reflectance factors for individual view configurations limits the precision of the albedo inversion method presented here. A statistical approach was used to remove atmospheric attenuation effects by incorporating linear coefficients derived from radiative transfer simulations. During winter and early spring in the arctic, increased atmospheric turbidity warrants careful specification of aerosol optical depth within the atmospheric correction procedure. Simulated albedo surfaces were used to derive linear coefficients used to convert narrowband albedos to broadband visible and infrared albedos. The satellite-derived surface albedos compared well to *in situ* albedo measurements (0.05-0.1). However the inversion method suffers from uncertainty

regarding the employed anisotropic reflectance factors. The *in situ* albedo observations were used along with the satellite-derived albedo data to identify and characterize the spatial and temporal variability of sea ice albedo over the experiment region. Pairwise image comparison techniques were used to examine change between image dates and differences between visible and infrared albedo. Principal component analysis was used to identify the major and minor scale variance structures in the multitemporal satellite albedo dataset.

The satellite and *in situ* albedo measurements indicated that sea ice albedo is high and relatively homogeneous over the study scene for winter and early spring conditions. Variability in visible albedo for this part of the season was found to be linked to the visibility of the darker underlying ice surface. Due to their thick snow volumes, visible albedo of multiyear ice melt pond areas stayed constant for the winter and the onset of melt periods. Alternatively, thinner volumes on first year ice resulted in visible albedo decreasing with the onset of melt conditions. The consistently lower infrared albedo decreased in response to the seasonal enlargement of snow grains in the top layer of the snow volumes. The saturation of the snow volumes resulted in decreases in both the visible and infrared albedo. The subsequent development of surface melt ponds resulted in significant decreases in both visible and infrared albedo, as well as an increase in the scene variability. The higher ponding on ice that consolidated in late 1992 compared to that ice which consolidated in late winter 1993 illuminated the importance of snow depth and ice macromorphological characteristics in determining late season patterns of albedo. Breakup and dispersal of ice in the study scene resulted in a significant lowering of the magnitude and variability of both visible and infrared albedo. High frequency fluctuations in albedo were found due to melt water drainage and ice convergence and divergence. Feedback diagrams describing the relationships between both seasonal visible and infrared albedo and relevant environmental factors are presented herein.

ACKNOWLEDGMENTS

Over the life of this work, I often looked forward to the time when all that remained was to formally thank those that assisted me in its completion. Now that it has arrived, I take up the task with much enthusiasm.

First, I would like to thank my parents Eugene and Joan Ann De Abreu. Their support and love throughout my education knew no bounds. To my Dad, who went to work each morning for the past 35 years to give me the chance to learn, a simple thank-you feels inadequate. It was his example that helped me get behind my desk each morning to face this work. As for my mom, I will always remember her saying to me "while money and gold withers away, a good education is here to stay". I took her advice to heart. With much love and respect, I thank-you both.

I would like to express my appreciation to my most patient supervisor, Dr. Ellsworth LeDrew. I met Dr. LeDrew as an undergraduate and his genuine enthusiasm for climatology and remote sensing was apparently contagious. There is little doubt that the completion of this thesis is also the fruit of many late nights on his part. Throughout the years I have watched him relentlessly work to provide an environment where I and others were able to visit places and use instruments that other students can only dream about. During my studies, I could always count on him to bring me back to Earth and put me back on track. Ells, thank-you for your ideas, your hard work and your confidence in me and this thesis.

I was fortunate to travel this road with many other graduate students, and needless to say, it is a road best shared. I wish to acknowledge the important role their encouragement and their laughter played in the completion of this thesis. A special thanks to Tim Papakyrikou, whose penchant for "good science" encouraged me to take a harder look at my work. Thank you to Faye Shultz, Kathleen Lamonthe and Lynn Finch for looking out for me all these years at the lab and within the department. I would also like to thank my

thesis committee: Dr. Doug Dudycha, Dr. James Kay and Dr.Phillip Howarth. Your thesis comments were welcome and always constructive.

A special thank-you to the SIMMS crew, especially Kevin Misurak for processing the geophysical data presented within. I would like to thank the Atmospheric Environment Service and Mohammed Shokr for providing the AVHRR data. Thank-you to Don Perovich of CRREL for providing the surface ARF data. Also thanks to the Canada Centre for Remote Sensing for permitting the reproduction of their quicklook TM imagery. Also thanks to the Polar Continental Shelf Project Resolute for providing the invaluable logistical support for this study. Grants from the Northern Studies Scientific Training Program assisted with my travel to and from the Arctic. Finally, I would like to thank the Natural Sciences and Engineering Resource Council of Canada for their invaluable support throughout this study.

The following were also instrumental in the completion of this work:
Granny...Rich and Wayne...Andrey, Kat and Mom Spiwak... ...Tom and Bernie Shuttleworth for providing my thesis oasis in Port Dover...Steve Krasnozan for the late morning distractions...my Gateway 386-33 Pentium-Killer...radio, radio...Town of Milton...tea...the Net...undo...Aruba...our '83 red Honda Civic...Mike Campbell for the early afternoon distractions...PPP...no-work Saturday morning policy...Saturday mornings...June 27, 1992...TNP's WWII comment...Mirka.

DEDICATION

I dedicate this thesis to the most patient person I know, my wife Alex.

Alex, to list your contributions to this thesis would easily double its size. Please accept the following words as meagre payment to the large debt of gratitude I owe to you. To begin, the completion of this thesis is testament to your hard work and diligence. It was only through your many successes that I was able to selfishly escape from the real world and concentrate on things like sea ice and albedo. Your unswaying confidence in the completion of this work was an anchor that I clung to when I was adrift in one of the many low points along the way. I will never forget your encouragement to take up and complete this challenge. With its completion, I look back on it as a quest we embarked on as one and finished together.

Thank-you Alex, for seeing good when all I could see was bad, for seeing the end when all I could see was the middle, and most of all, for your patience, strength and your love. With the completion of the chapters within, we start our own new chapter...we will write these ones together this time...

Shine! shine! shine!
Pour down your warmth, great sun!
While we bask, we too together.

Two together!
Winds blow south, winds blow north,
Day come white, or night come black,
Home, or rivers and mountains from home,
Singing all time, minding no time,
While we too keep together.

Walt Whitman, 1859

TABLE OF CONTENTS

1 INTRODUCTION 1

1.1 Statement of Objectives 2

1.2 Thesis Organization 4

2 THE CLIMATIC SIGNIFICANCE OF SEA ICE ALBEDO 5

2.1 The Arctic Sea Ice Volume 5
2.1.1 Seasonal Evolution of the Sea Ice Volume 6
2.1.2 Climatic Importance of Sea Ice 9

2.2 The Role of Sea Ice Albedo in the Climate System 10
2.2.1 Albedo and Related Nomenclature 11
2.2.2 The Role of Surface Sea Ice Albedo in Surface Energy Balance 13

2.3 Conclusions 23

3 IN SITU MEASUREMENT OF SEA ICE SPECTRAL ALBEDO 24

3.1 The Albedo of Sea Ice -- A Theoretical Perspective 25
3.1.1 Snow-Covered Sea Ice 25
3.1.2 Bare Sea Ice 34
3.1.3 Melt Ponds 38

3.2 Field Observations of Sea Ice Albedo 39
3.2.1 Allwave Albedo Measurements 40
3.2.2 Spectral Albedo Measurements 40

3.3 Sea Ice Albedo Measurements During SIMMS 43
3.3.1 An Overview of the 1993 SIMMS Experiment 43
3.3.2 Albedo Measurement Objectives 53
3.3.3 Instrumentation 54
3.3.4 Spectral Albedo Measurements 55
3.3.5 Potential Error Sources 56
3.3.6 Ancillary Measurements 64

3.4 Seasonal Variation in the Visible and Near-infrared Albedo of Sea Ice. 65
3.4.1 Assessment of Albedo Evolution With Time 66
3.4.2 Spring Transformation of Visible and Near-Infrared Sea Ice Albedo 75

3.5 Conclusions 98

4 ESTIMATING SURFACE ALBEDO FROM AVHRR 1 AND 2 101

4.1 Introduction 101

4.2 Sensor and Platform Description 102

4.3 Previous Investigations 103

4.4 Data Extraction and Cloud Detection 110

4.5 Calibration and Conversion to TOA Reflectances 112
4.5.1 Calibration 112
4.5.2 TOA Reflectance Conversion 118

4.6 Anisotropic Correction 119
4.6.1 Taylor and Stowe Anisotropic Reflection Factors 122

4.7 Atmospheric Correction 128
4.7.1 Atmospheric Attenuation 129
4.7.2 Theory of Atmospheric Correction 132
4.7.3 In Situ Atmospheric Measurements 138
4.7.4 Implementation of Atmospheric Correction 151
4.7.5 Results 161

4.8 Narrow-to-Broadband Conversion 163
4.8.1 Data 165
4.8.2 Method 173
4.8.3 Results 174

4.9 Solar Zenith Angle Normalization 184

4.10 Sources of Uncertainty 185
4.10.1 Calculation of TOA Reflectance 188
4.10.2 Anisotropic Correction 189
4.10.3 Atmospheric Correction 200
4.10.4 Narrow to Broadband Conversion 206

4.11 Accuracy of Satellite Albedo Measurements 209

4.12 Summary of Findings 211

4.13 Conclusions 216

5 LARGE-SCALE VARIABILITY IN SEA ICE ALBEDO 218

5.1 Introduction 218

5.2 Image Preparation 219
5.2.1 Registration of AVHRR Data 219
5.2.2 Sub-Area Extraction and Masking of Land/Ice 219
5.2.3 Generation of Difference Images 220

5.3 Scene Description 221
5.3.1 Ice Conditions 223
5.3.2 Snow Conditions 225

5.4 Scene Variability of Visible and Infrared Sea Ice Albedo 226
5.4.1 April, May - Snow-Covered Sea Ice 241
5.4.2 June - Surface Melt 244
5.4.3 July - Drainage and Breakup 252
5.4.4 Summary 257

5.5 Multitemporal Principal Component Analysis of AVHRR Albedo Data 259
5.5.1 Overview of Technique 260
5.5.2 Results 263
5.5.3 Summary 272

5.6 Spectral Variability of Sea Ice Albedo 273
5.6.1 Normalized Difference Snow-Ice Index (NDSII) 274
5.6.2 Summary 279

5.7 Summary of Findings 279
5.7.1 Winter/Onset of Melt 279
5.7.2 Advanced Melt 283
5.7.3 Breakup / Dispersal 286

5.8 Conclusions 289

6 CONCLUSIONS 290

6.1 Winter/Onset of Melt 293
6.1.1 Visible Albedo 293
6.1.2 Infrared Albedo 296

6.2 Advanced Melt/Breakup 297

APPENDIX 1. WISCOMBE AND WARREN SNOW MODEL 305

APPENDIX 2. ASD SPECTROMETER SETUP 308

APPENDIX 3. CORRECTING CLEAR-SKY SPECTRAL ALBEDO 309

APPENDIX 4. DETERMINING CLEAR-SKY SURFACE GLOBAL IRRADIANCE 312

LITERATURE CITED 315

LIST OF FIGURES

Figure 2.1 WMO classification for the evolution of thin, new ice. 7
Figure 2.2 Viewing geometry of (a) albedo vs. (b) reflectance 12
Figure 2.3 Simple feedback diagram 16
Figure 2.4 Positive sea ice albedo feedback. 16
Figure 3.1 Absorption coefficient of pure ice 27
Figure 3.2 Modelled spectral albedo of snow 27
Figure 3.3 Modelled effect of grain size (mean radius) on the spectral albedo of snow 31
Figure 3.4 Modelled effect of internally mixed carbonic soot on snow albedo. 31
Figure 3.5 Modelled effect of snow depth on snow albedo on sea ice 33
Figure 3.6 Modelled bare ice albedo vs. ice depth from Grenfell (1983) 36
Figure 3.7 Modelled bare ice albedo during cooling and warming phase from Grenfell (1983). 36
Figure 3.8 Location of SIMMS experiment region 45
Figure 3.9 Seasonal change in solar irradiance measured at AES Resolute 45
Figure 3.10 Daily mean air temperature during SIMMS '93. 46
Figure 3.11 Early spring (a) and late spring (b) icescapes during SIMMS '93. 49
Figure 3.12 Thematic Mapper Image of SIMMS '93 sampling sites 50
Figure 3.13 Raw vs. processed albedo spectra. 58
Figure 3.14 Fractional deviation in RCR cosine response 58
Figure 3.15 Effects of RCR calibration on field albedo spectra 60
Figure 3.16 Sampling dates of (a) first year ice site and (b) multi-year ice site albedo data. 63
Figure 3.17 Spectral albedo of (a) first year ice site and (b) multi-year ice site 67
Figure 3.18 Seasonal change in allwave albedo 68
Figure 3.19 Seasonal change in visible and near-infrared broadband albedo 69
Figure 3.20 Dendrograms for (a) visible albedo and (b) near-infrared albedo. 72
Figure 3.21 Visble and near infrared albedo groupings 74
Figure 3.22 The seasonal tranformation of the sea ice snow volume and broadband albedo 76
Figure 3.23 Snow density of FYI snow volumes during Dry Snow period. 78
Figure 3.24 Variation of first year ice snow grain radi with depth 79
Figure 3.25 Average first year ice albedo spectra for Dry Snow stage 81
Figure 3.26 Comparison of May 15 albedo to modelled albedo 83
Figure 3.27 Snow density of MYI snow volumes during Dry Snow stage 85
Figure 3.28 Variation of multi-year ice snow grain radi with depth 85
Figure 3.29 Comparison of May 8 albedo to modelled albedo 87
Figure 3.30 Snow density of FYI snow volumes during Wet Snow stage. 90
Figure 3.31 First year ice melt pond albedo. 94
Figure 3.32 Contrast in FYI and MYI late season ponding measured via balloon photography 96
Figure 3.33 Multi-year ice melt pond albedo. 97
Figure 3.34 Spectral albedo of debris-laden multi-year ice melt pond and snow cover. 99
Figure 4.1 AVHRR Channel 1,2 Normalized Spectral Response 105
Figure 4.2 Surface albedo inversion methodology 109
Figure 4.3 Change in calibration gain for NOAA 7, 9, and 11 AVHRR 114
Figure 4.4. Typical geometry of sun-target-sensor 116
Figure 4.5 Satellite-sun geometry of study dataset 121
Figure 4.6. Taylor and Stowe (1984) Sea Ice Anisotropic Reflection Factor Models 124
Figure 4.7 Effects of ARF application to TOA AVHRR 1 and 2 reflectances 127
Figure 4.8. Scattering processes in the atmosphere 130

Figure 4.9. Atmospheric Transmission within AVHRR Channels 1 and 2 137
Figure 4.10 SAM II weekly average aerosol optical depths @1.0 μm at high latitudes. 146
Figure 4.11 *In situ*-measured daily average aerosol optical depths at 0.5 μm 148
Figure 4.12 Spectral Adjustment of Aerosol Optical Depth 151
Figure 4.13 Koepke Coefficients for (a) AVHRR 1 and (b) AVHRR 2 155
Figure 4.14 AVHRR surface albedos determined via Koepke coefficients and 6S code. 159
Figure 4.15 Visible and infrared broadband regions of the surface global irradiance. 165
Figure 4.16 Modelled surface irradiances 168
Figure 4.17 Visible spectrum: (a) spectral irradiance in AVHRR 1 171
Figure 4.18 Infrared spectrum: (a) spectral irradiance in AVHRR 2 172
Figure 4.19 Comparison of AVHRR 1 albedo with corresponding visible albedo 175
Figure 4.20 Proportion of visible flux within AVHRR 1 176
Figure 4.21. Comparison of AVHRR 2 albedo with corresponding infrared albedo 178
Figure 4.22 Proportion of infrared flux within AVHRR 2 179
Figure 4.23 Same data as figure 4.21 except infrared albedo transformed ($\sqrt{\alpha_{ir}}$). 182
Figure 4.24 Visible and infrared surface albedo 183
Figure.4.25 Dependence of allwave albedo on solar zenith angle 185
Figure 4.26 Error in calculated visible albedo due to 0.05 error in the derivation of TOA 190
Figure 4.27 Error in calculated visible albedo to due to 0.1 error in ARF 197
Figure 4.28 Error in calculated infrared albedo to due to 0.1 error in ARF 198
Figure 4.29 Error in calculated surface albedo due to 201
Figure 4.30 Error in calculated surface albedo due to total error in atmospheric correction 207
Figure 4.31 Error in calculated surface albedo due to total error in atmospheric correction 208
Figure 4.32 Emulated surface measurements of AVHRR albedo data 212
Figure 5.1 Relative location of AVHRR study scene (dashed lines) 221
Figure 5.2 April 21, 1993 ERS-1 SAR image of SIMMS experiment region. 222
Figure 5.3 Ice regimes in AVHRR study scene. Dotted lines indicate ice regime boundaries. 223
Figure 5.4(a) April 30 visible albedo 228
Figure 5.4(b) May 3 visible albedo 228
Figure 5.5(a) April 30 infrared albedo 229
Figure 5.5(b) May 3 infrared albedo 229
Figure 5.4(c) June 4 visible albedo 230
Figure 5.4(d) June 9 visible albedo 230
Figure 5.5(c) June 4 infrared albedo 231
Figure 5.5(d) June 9 infrared albedo 231
Figure 5.4(e) June 16 visible albedo 232
Figure 5.4(f) June 20 visible albedo 232
Figure 5.5(e) June 16 infrared albedo 233
Figure 5.5(f) June 20 infrared albedo 233
Figure 5.4(g) July 7 visible albedo 234
Figure 5.4(h) July 29 visible albedo 234
Figure 5.5(g) July 7 infrared albedo 235
Figure 5.5(h) July 29 infrared albedo 235
Figure 5.6 Thematic visible albedo maps 236
Figure 5.7 Thematic infrared albedo maps 237
Figure 5.8 Daily mean air temperature during SIMMS '93. 238
Figure 5.9 Absolute change in surface albedo between acquisition dates 239
Figure 5.10 Change in sea ice albedo with distance from shore 248

Figure 5.11 Clear sky broadband visible and infrared albedo vs. the proportion of melt ponds. 251
Figure 5.12 Thematic Mapper Quicklook imagery of 1993 ice breakup 254
Figure 5.13 Seasonal change in satellite-derived visible and infrared albedo 258
Figure 5.14 Seasonal variability in visible and infrared albedo over AVHRR scene 258
Figure 5.15(a) Visible Albedo -- Principal component 1 266
Figure 5.15(b) Infrared Albedo -- Principal component 1 266
Figure 5.15(c) Visible Albedo -- Principal component 2 269
Figure 5.15(d) Infrared Albedo -- Principal component 3 269
Figure 5.15(e) Visible Albedo -- Principal component 3 271
Figure 5.15(f) Infrared Albedo -- Principal component 2 271
Figure 5.16 Seasonal change in Normalized Difference Sea Ice Index (NDSII) 276
Figure 6.1 Winter/Onset of Melt visible albedo feedback. 294
Figure 6.2 Winter/Onset of Melt infrared albedo feedback 294
Figure 6.3 Advanced Melt/Breakup visible albedo feedback 299
Figure 6.4 Advanced Melt/Breakup infrared albedo feedback 299
Figure A3.1 Ratio of diffuse/total irradiance on clear days. 311

LIST OF TABLES

Table 2.1 Parameterization of sea ice albedo in GCMs. 19
Table 2.2 Sea ice albedo parameterization of Ebert and Curry's (1993) 1-D sea ice model 22
Table 3.1 Surface dataset collected during SIMMS '93 52
Table 3.2 Remote sensing datasets collected during SIMMS '93 53
Table 3.3 Spectral albedo sampling dates 63
Table 3.4 Calculated broadband visible and near infrared albedo. 70
Table 3.5 Input parameters for snow albedo model 82
Table 4.1 Characteristics of AVHRR on NOAA 12 104
Table 4.2 Monthly mean parameterized regional sea ice (>10% ice cover) surface albedos 107
Table 4.3 Sun-target-sensor geometry of AVHRR dataset 112
Table 4.4 Determination of TOA radiance as viewed by NOAA 12 on April 30 overpass. 116
Table 4.5 Adjustment of NOAA 12's AVHRR 1 and 2 calibration gain. 118
Table 4.6. Comparison of TOA reflectances determined by pre-launch and updated calibration 119
Table 4.7 Distribution of T&S ARF models 123
Table 4.8 Conversion of AVHRR 1 and 2 TOA reflectance to TOA albedo 127
Table 4.9 Aerosol Models used in Transmissivity Modelling 136
Table 4.10 Atmospheric transmittances integrated over AVHRR Chn. 1 and 2 136
Table 4.11 Inputs to Atmospheric Correction 140
Table 4.12 Monthly average aerosol optical depths (0.55 μm) at Resolute, N.W.T. 149
Table 4.13 Atmospheric parameters for Koepke model 155
Table 4.14 Conversion of AVHRR 1 and 2 TOA albedo to surface albedos via 159
Table 4.15 Comparison of AVHRR 1 and AVHRR 2 surface albedos derived via 6S code 161
Table 4.16 Modelled atmosphere for narrow to broadband conversion 167
Table 4.17 Spring sea ice surfaces observed in SIMMS '93 173
Table 4.18 Comparison of AVHRR 1 albedo with corresponding visible albedo 175
Table 4.19 Comparison of AVHRR 2 albedo with corresponding infrared albedo 178
Table 4.20 Derived regression parameters for infrared NTB model. 182
Table 4.20 Conversion of narrowband channel albedos to broadband albedos 183
Table 4.22 Variability of sea ice ARFs over various view configurations 191
Table 4.23 Comparison between *in situ* and satellite measured visible and infrared albedo. 213
Table 5.1 Eigenvalues and eigenvectors of covariance matrix for the visible albedo dataset. 264
Table 5.2 Eigenvalues and eigenvectors of covariance matrix for the infrared albedo dataset. 264
Table 5.3 Dependence of NDSII on snow depth. 277

LIST OF ACRONYMS

AES	Atmospheric Environment Service (Canada)
AIO	Atmosphere-ice-ocean
ARF	Anisotropic reflectance factor
AVHRR	Advanced Very High Resolution Radiometer (TIROS-N)
AVHRR 1	AVHRR channel 1 (NOAA 12)
AVHRR 2	AVHRR channel 2 (NOAA 12)
BRDF	Bidirectional reflectance distribution function
C-ICE	Collaborative Interdisciplinary Cryosphere Experiment
CCC	Canadian Climate Centre
CEAREX	Coordinated Eastern Arctic Experiment
DMSP	Defense Meteorological Satellite Program (US)
DNs	Digital numbers
E-A	Earth-atmosphere
EBM	Energy balance modelling
EOS	Earth Observation Satellite
ERBE	Earth Radiation Budget Experiment (US)
FYI	First year ice
GAC	Global area coverage
GCM	General circulation model
HIRS	High-Resolution Infrared Radiation Sounder
ICP	Ice crystal precipitation
IFOV	Instantaneous field of view
ISCCP	International Satellite Cloud Climatology Program
LAC	Local area coverage
LEADEX	Lead Experiment
MISR	Multi-angle Imaging Spectro-Radiometer (EOS-AM1)
MODIS	Moderate Resolution Imaging Spectrometer (EOS-AM1)
MSU	Microwave Sounding Unit (TIROS-N)
MYI	Multi-year ice
NDSI	Normalized Difference Snow Index
NDSII	Normalized Difference Snow-Ice Index
NDVI	Normalized-Difference Vegetation Index
NOAA	National Oceanic Atmospheric Administration (US)
NTP	Normal temperature and pressure
OLS	Operational Line Scanner (DMSP)
PCA	Principal component analysis
ppmw	parts per million by weight
RCR	Remote cosine receptor
SAM II	Stratospheric Aerosol Measurement II
SAR	Synthetic aperture radar
SHEBA	Surface Heat Budget of the Arctic Ocean
SIMMS	Sea Ice Monitoring and Modelling Site

SMMR	Scanning Multichannel Microwave Radiometer (Nimbus-7, Seasat-A)
SSA	Single scattering albedo
T&S	Taylor and Stowe (184)
TIROS	Television and Infrared Observation Satellite
TM	Thematic Mapper (Landsat 5)
TOA	Top of the atmosphere
TOMS	Total Ozone Mapping Spectrometer (NIMBUS-7)
TOVS	TIROS-N Operational Vertical Sounder
WMO	World Meteorological Organization
6S	Second Simulation of the Satellite Signal in the Solar Spectrum

NOMENCLATURE

$\tilde{\alpha}_{ir}$	estimated broadband infrared (0.70-4.0 μm) albedo
$\tilde{\alpha}_{ir}^{\cdot}$	transformed estimated broadband infrared (0.70-4.0 μm) albedo
χ	eigenvalue
ν	ratio of diffuse irradiance to total irradiance
$\Psi\alpha$	difference albedo image
ϖ_n	filtered response of satellite channel n
ϑ_v	absolute humidity
f	anisotropic reflectance factor (ARF)
α	albedo
α_∞	semi-infinite albedo
$\alpha_{1,2}$	surface AVHRR 1 and AVHRR 2 channel albedo
α_A	broadband allwave (0.15-4.0 μm) albedo
α_f	finite albedo
α_I	ice albedo
α_{ir}	broadband infrared (0.70-4.0 μm) albedo
$\alpha_{ir}^{\cdot}$	transformed broadband infrared (0.70-4.0 μm) albedo
α_λ	spectral albedo
α_m	mixed surface albedo
α_{mp}	melt pond albedo
α_S	snow albedo
α_s	surface albedo
α_{TOA}	TOA albedo
α_{vis}	broadband visible (0.15-0.70 μm) albedo
δ	fractional uncertainty in measurement
Δ	measurement error
Δ_λ^{rcr}	deviation from cosine response
$\varepsilon_{s,i}$	emissivity of snow/ice (0.99)
ϕ	relative azimuth angle
$\phi^{\cdot}$	viewing azimuth angle
η	narrow to broadband conversion factor
η_{ice}	density of ice
λ	wavelength
λ_v	wavelength of incident light in a vacuum
θ	solar or illumination angle
$\theta^{\cdot}$	viewing incident or satellite angle
ρ	reflectance
ρ_a	atmospheric reflectance at TOA
ρ_λ	spectral reflectance
ρ_s	surface reflectance
ρ_{TOA}	TOA reflectance

σ	standard deviation
σ^2	variance
σ_B	Stefan-Boltzman constant (5.67×10^{-8} W/m^2/K^4)
τ	layer optical depth
τ_a	aerosol optical depth
τ_A	atmosphere optical depth
τ_g	gaseous absorption optical depth
τ_r	Rayleigh optical depth
τ_S	snow optical depth
ω	single scattering albedo
Ω_S	snow age factor

a	eigenvector
$b_{1,2}$	spectral range of radiometer channel
d	sun-Earth distance (AU)
g	asymetry factor
i	channel or band number
j	pixel location
k	line location
k_{abs}	volume absorption coefficient
k_{ext}	volume extinction coefficient
k_{sca}	volume scattering coefficient
m_{im}	imaginary part of refractive index of pure ice
r	grain radius
s	atmospheric spherical reflectance
u	cos (θ^*)
w	precipitable water amount
z	depth of layer
z_S	depth of snow layer

C	channel calibration offset
CC	covariance matrix
CF	correction factor
D_1	length of snow grain major axis
D_2	length of snow grain minor axis
E^d	diffuse irradiance
E^D	direct irradiance
E_i	incident irradiance within channel i
E_λ	incident spectral irradiance
E_s	irradiance at surface
E_{TOA}	exoatmospheric irradiance
F_l	upward turbulent latent heat flux
F_{LW}	incident longwave flux

F_{net}	net radiative surface flux
F_s	upward turbulent sensible heat flux
F_{SW}	incident shortwave flux
G	channel calibration gain
I_O	absorbed fraction of incident shortwave flux
K	Degrees Kelvin
L	radiance
L_a	path radiance
LEW	liquid equivalent water depth
L_s	target radiance
L_{TOA}	TOA radiance
M_λ	reflected spectral irradiance
P_{mp}	melt pond fraction
Q_{ext}	extinction efficiency
S	instrument signal response
T	total atmospheric transmittance
T_0	surface temperature
T_d	diffuse atmospheric transmittance
T_D	direct atmospheric transmittance
T_g	two-way transmittance due to gaseous absorption
T_i	freezing temperature for sea water (-2 °C)
T_t	two-way transmittance due to scattering
W	Watts

1 INTRODUCTION

As society begins to accept the premise that human activity has the potential to influence the Earth's climate, physical scientists are increasingly being called upon to identify these anthropogenic perturbations and to predict the direction and magnitude of any change in the Earth's climate system. Current large-scale modelling efforts suggest that, compared to the rest of the globe, the arctic will experience an amplified warming under current climate change scenarios (e.g. $2xCO_2$). Climatologists acknowledge that these simulations only crudely represent the climate system and these results should be accepted in that context. In fact, the simplistic treatment of sea ice in large-scale climate models belies its significance in controlling climate in both the arctic and the rest of the world. The arctic's heightened sensitivity to global warming is acknowledged to be mainly caused by the sensitivity of sea ice *albedo* to surface temperature and vice versa.

Albedo is a deceptively simple variable that refers to the fraction of incident solar radiation (0.15-4.0 μm) reflected from a surface. It thus controls the amount of energy entering the sea ice volume. Long recognized as a critical climate variable, the improvement of the parameterization of sea ice albedo has been given high priority in climate studies. Unfortunately, these efforts are hindered by a dearth of observational data. Sea ice albedo data that have been collected are often stationary, limited in time, and collected with different instruments over different surfaces and under different atmospheric conditions. As a result, little is known regarding the spatial and seasonal variability of sea ice albedo over large areas. However, this type of information is required for the proper incorporation of sea ice in climate models. There is the potential to use sea ice albedo as

an indicator of climate change in the arctic. Yet, in order to differentiate real climate change from the system's natural variability, the elemental variability of sea ice albedo must be known; it is not. Also required for an accurate parameterization of surface albedo is the identification of the environmental variables and processes that influence both the temporal and spatial variability of sea ice albedo.

Scientists agree that increased observation of the Earth system is needed to properly investigate climate change. These observations must be systematic, accurate and capable of resolving the important spatial and temporal characteristics of the many processes that define the climate system. In terms of the polar regions, satellite remote sensing is the only viable method of performing this task. Sensors operating at microwave wavelengths have proven their ability to provide valuable scientific and operational sea ice information in the arctic (LeDrew, 1992). While these instruments have the enviable ability to penetrate cloud cover, they cannot directly measure reflected solar radiation. On the other hand, mapping surface albedo is the most natural application for sensors operating within the solar spectrum. These *optical* sensors are capable of directly measuring portions of the visible (0.15-0.70 μm) and infrared (0.70-4.0 μm) radiation reflected from sea ice surfaces. While considerable attention has been given to extracting surface albedo from optical satellite data collected over lower latitude terrestrial surfaces, relatively little effort has been devoted to examining the utility of these data over polar surfaces.

1.1 Statement of Objectives

This thesis has three major objectives.

1. *Examine the interaction of incident solar radiation with a seasonally varying snow-covered sea ice volume and to relate the fraction and spectral characteristics of the incident radiation returned to the atmosphere (spectral albedo) to the geophysical characteristics of the volume.*

A combined approach utilizing both empirical measurement and theoretical modelling is used to examine sea ice albedo. Spectral albedo data collected primarily during the Seasonal Sea Ice Monitoring and Modelling Site (SIMMS) 1993 experiments in the Canadian Arctic Archipelago are used to identify the seasonal characteristics of springtime sea ice albedo. Coincident geophysical measurements and a theoretical snow albedo model are used to relate surface albedo to the physical state of the volume. Of specific interest is the identification of the major stages in the evolution of both new and old sea ice spectral albedo throughout the observed spring transition in 1993.

2. *Assess the ability of narrowband visible and near-infrared satellite data to measure the seasonal variability of sea ice albedo.*

Narrowband Channel 1 (0.58-0.68 μm) and Channel 2 (0.72-1.1 μm) Advanced Very High Resolution Radiometer (AVHRR) satellite data have been identified as a potential source of surface albedo information in the arctic. However, little is known regarding the feasibility of using top-of-the-atmosphere (TOA) data collected by these two channels to measure clear-sky surface albedo in polar regions. This investigation examines a multistep method capable of converting TOA raw digital numbers (DNs) of AVHRR 1 and AVHRR 2 into climatological broadband visible (0.28-0.7 μm) and infrared (0.7-4.0 μm) albedo respectively. The sensitivity of the final satellite derived albedo is examined in the context of the uncertainty involved in each step of the inversion process.

3. Describe and interpret small and large-scale patterns in surface visible and infrared albedo during the spring transition season.

The satellite-derived surface albedo data are used to map the spatial and temporal variability of the visible and near-infrared albedo of sea ice throughout the spring transition period. Of specific interest is the identification of the dominant patterns of sea ice albedo

variability for the entire spring season. Using *in situ* data, the environmental factors responsible for the ensuing patterns are identified.

1.2 Thesis Organization

The thesis begins with this chapter, a brief introduction to sea ice albedo and remote sensing and, as well, a statement of thesis objectives. The purpose of the following chapter, Chapter 2, is to explain the motivation behind this work by placing it in the appropriate scientific context. Specifically, the chapter examines the role of sea ice albedo in the climate system and describes previous attempts to measure, model and parameterize this variable. The first objective of this thesis is addressed in Chapter 3. The SIMMS experiment and the measurement methodology are described. The spring transformation of spectral albedo over both new and old ice covers is examined in conjunction with the seasonal metamorphism of the snow and ice cover. In Chapter 4, a methodology for measuring surface visible and near-infrared albedo using satellite, narrowband AVHRR data is presented. Uncertainties in the extraction methodology and sensitivities to input parameters are examined. Using the satellite-derived albedo data, the spatial and temporal variability of sea ice surface albedo in the SIMMS region is examined in Chapter 5. In Chapter 6, the concluding chapter, the findings of this investigation are summarized in the context of climate studies in the arctic.

2 THE CLIMATIC SIGNIFICANCE OF SEA ICE ALBEDO

The objective of this chapter is to explain the motivation behind this research by examining the role of sea ice albedo in both the arctic and global energy balance. The chapter begins with a rudimentary description of the physical sea ice volume and its known seasonal characteristics. The term *albedo* is defined and expanded upon. The role of sea ice in the local and global energy balance is discussed. Current treatments of sea ice albedo in climate models are discussed.

2.1 The Arctic Sea Ice Volume

To those unfamiliar with the term, sea ice may conjure up images of cold, dry, flat and bare slabs of white ice forever covering the polar oceans. In fact, more than a century of observations have proved otherwise. The sea ice volume is a very complex, dynamic medium that displays a wide range of spatial and temporal variability. This variability is intrinsically linked to both the dynamic and thermodynamic variations in the atmosphere and ocean (Hibler, 1980). A seasonal snowcover often covers arctic sea ice from consolidation to melt. Its presence is of considerable significance to the evolution of sea ice and is thus, in this work, considered a part of the sea ice volume. The following section describes the fundamental physical characteristics of the formation, growth and annual decay of arctic sea ice. It concludes with a description of the climatic significance of sea ice.

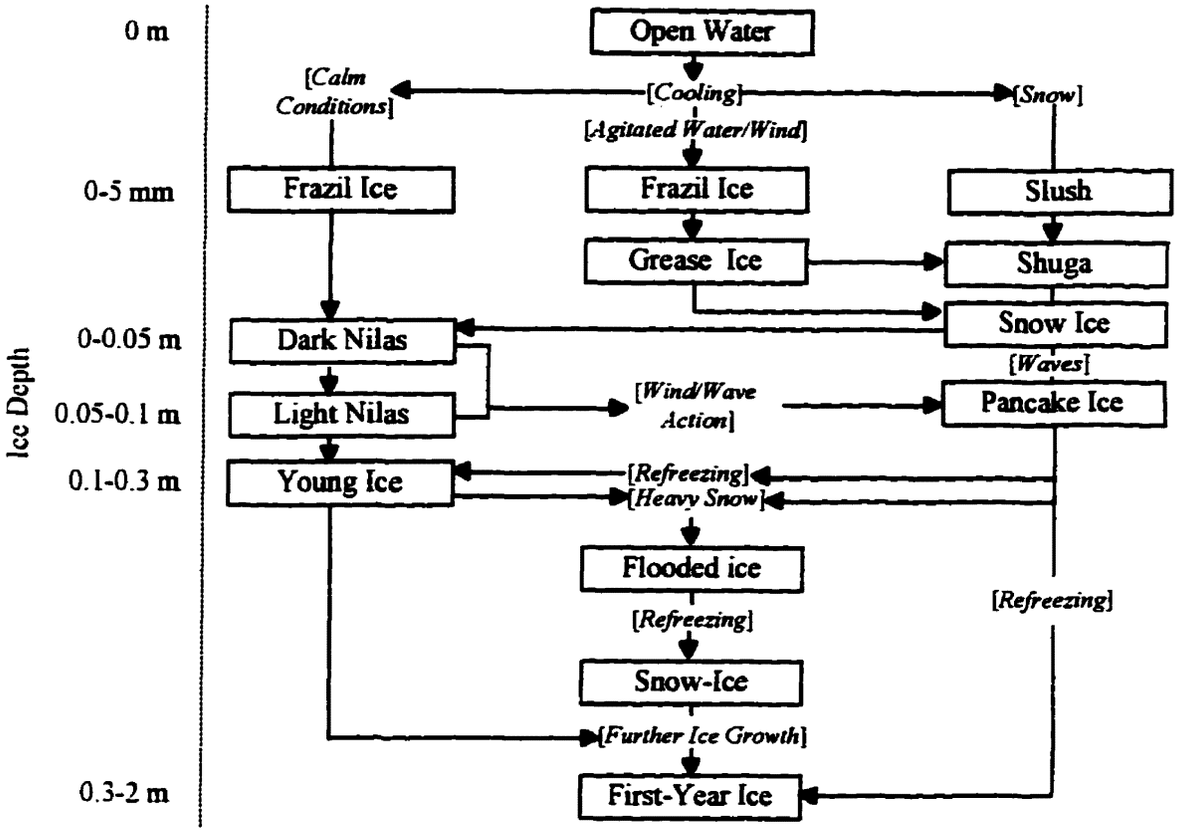
2.1.1 Seasonal Evolution of the Sea Ice Volume

2.1.1.1 Formation

The formation, growth and decay of sea ice is characterized by a wide variety of changes in the physical properties of the volume. Figure 2.1 contains a schematic that describes the evolution of new ice based on the World Meteorological Organizations (WMO) classification system. Sea ice is formed by the freezing of sea water. Unlike fresh water, sea water contains salt (30-35 parts per thousand ($^0/_{00}$)) which proves to be significant in the evolution of sea ice. Sea ice begins to form by cooling at the ocean surface which results in the formation of small ice platelets and needles termed *frazil*. The unconsolidated frazil ice crystals and sea water together form a soupy mixture known as *grease ice*. Under calm conditions, grease ice begins to congeal to form an elastic, translucent layer up to 10 cm thick known as *nilas*. Wind and wave action often break up the nilas sheets to form separate floes. These floes, known as pancake ice, have raised edges due to their constant bumping into one another and by grease ice mixtures lapping up onto the floe. Eventually, these pancake fields are allowed to consolidate into ice sheets. If the ice has consolidated against land it is commonly termed *landfast* or *fast ice*. Ice formation primarily begins in the fall with the lowering of suffice temperatures brought on by the annual decrease in solar insolation.

For much of the year, sea ice is covered by a seasonal snow volume. The extent and duration of this snowcover are crucial to the evolution of the underlying sea ice volume. After initial deposition, predominantly in the fall months, the snowpack is modified by wind erosion, diurnal melting and freezing rain (Male, 1980). Due to persistent surface winds, the arctic snowcover is transient in nature. This constant eolian redistribution of snow in the fall and polar winter results in the transformation of snow crystals to minute, rounded snow grains. Snow depths are highly variable and are largely a function of surface features which serve to cause local non-uniformities in the near-surface wind flow. The resultant changes in wind velocities affect the snow accumulation pattern (Kind, 1981) and give rise to the high spatial variability of snow depth found on sea ice.

Figure 2.1 WMO classification for the evolution of thin, new ice. Ice types are shown in boxes and environmental processes are in italics within square brackets



Source: Adapted from Grenfell *et.al.* (1992) and Weeks (1976)

2.1.1.2 Growth

Both thermodynamic and mechanical forces are responsible for growth of the ice volume. Thermodynamically, the formation of a consolidated frazil layer serves to insulate the warm ocean from the cold atmosphere. This ensuing thermal gradient results in heat being conducted upward through the overlying ice which in turn freezes sea water in contact with the bottom of the ice sheet. Sea ice predominantly consists of columnar ice crystals which are orientated parallel to the direction of heat flow. These columnar crystals consist of dendritic plates of pure ice separated by small brine inclusions. Rapid cooling of sea

water results in brine entrapment in the crystal matrix. The amount of entrapped brine is dependent on the salinity of the water and the growth rate. The more rapid the growth, the more salt that is entrapped in the ice. Young ice can have a salinity as high as 10-15$^{0}/_{00}$ (Weeks, 1981). In growing ice sheets, brine loss is mainly due to gravity drainage and brine expulsion due to pressure increases within the brine pockets due to freezing. Brine drainage results in air filling brine cavities and thus increasing the porosity and decreasing the density of the ice volume. Arctic sea ice in its first-year of thermodynamic growth, commonly termed *first-year ice*, often reach thicknesses of 1-2 m. First-year ice that survives a summer's melt and encounters another winter growth season is termed *multiyear ice*. Multiyear ice can be as old as 3-7 years with thicknesses ranging from a few metres to tens of metres.

Apart from landfast ice, sea ice is constantly moving, driven primarily by surface winds. Compressive and shearing forces act to increase sea ice thicknesses through the creation of pressure ridges and through ice floes riding up on each other, or rafting. These same forces can create areas of open water where rapid new ice growth and intense heat loss may occur (Maykut, 1982). These new ice lead areas can quickly close due to convergent winds and as a result, the thin ice is crushed against the adjacent thicker ice leaving behind ridges of deformed ice often several metres thick above and below the water line. This type of ridged ice is a major component of the distribution of ice thickness and may be responsible for up to 50% of the ice volume in the arctic (Wadhams, 1994).

Over a typical year, sea ice cover in the northern hemisphere fluctuates from a minimum of 8×10^{6} km^{2} (August) to a maximum of 15×10^{6} km^{2} (February) (Maykut, 1982). This dynamic cover is made up of seasonal first-year ice and multiyear ice which has survived the summer melt period. The Central Arctic is predominantly multiyear ice up to 3 m thick (Barry et al., 1984). First-year ice accounts for 40-50% of the ice concentration when the ice is at maximum extent (Carsey, 1982)

2.1.1.3 Decay

While a more complete examination of the spring decay of sea ice is offered later with the benefit of *in situ* observations, a cursory description is offered here. In general, the factors responsible for the annual decay of sea ice are agreed upon. A number of studies have modelled the decay and examined it *in situ* (Langleben, 1972; Maykut and Perovich, 1987). Increased insolation and minimal cloudcover in the early spring begins the decay of the sea ice volume. The excellent insulating properties of the snowcover causes a temperature gradient to quickly develop across the snow volume in the early spring as temperatures rise. The daily increases in incident radiation are closely followed by the decomposition of the snowcover. The onset of melt conditions increases the amount of free water in the snowpack and causes rapid metamorphism within the volume. As the snowcover deteriorates, the accompanying decrease in surface albedo causes more and more energy to be absorbed within the sea ice cover. The once homogeneous snowcover is usually replaced by a heterogeneous system of drainage channels eventually exposing bare ice surfaces and, depending on the amount of meltwater and morphology of the surface, producing melt ponds of various sizes. Surface melt on multiyear ice drains preferably into inter-hummock melt ponds. The springtime development of this drainage system and the subsequent refreezing of the floe encourages the development of the hummock-like surfaces characteristic of multiyear ice floes. The surface water of first-year ice accumulates in drift depressions and subsequently drains through cracks, leads and holes leaving behind a fragile, porous white ice layer. Reduced in strength, the ice cover eventually breaks up allowing radiation absorbed by the open water to further weaken the ice cover by melting the sides and bottoms of individual floes.

2.1.2 Climatic Importance of Sea Ice

On a global scale, polar regions represent an energy sink whose intensity controls the strength of the equator-pole energy gradient. The present pattern of the Earth's atmospheric circulation is largely driven by the poleward transport of energy across this

gradient via the atmosphere and ocean. Throughout its formation, growth and decay, sea ice plays a significant role in key large-scale processes of the Earth's climate system. Some of the major roles are:

- The high albedo of sea ice relative to that of open ocean reduces the amount of shortwave radiation absorbed at the surface. The radiation balance of the Arctic Basin is thus very sensitive to the any changes to the surface albedo and sea ice extent.
- Sea ice controls ocean salinity through brine[1] injection during ice growth and fresh water injection during melt. Increased salinity increases water density thus encouraging convection, while the lowering of salinity causes a stabilization of the water column.
- In marginal ice zones, the transition to open water encourages eddy formation, oceanic upwelling and cyclogenesis.
- The sea ice cover decouples the warm ocean from the cold atmosphere thus preventing the direct transfer of energy between the two systems.

These processes intimately link sea ice cover to the atmosphere and ocean over a wide range of spatial (metres to kilometres) and temporal (diurnal to decadal) scales (Carsey *et al.*, 1993). Of specific interest here is the spatial and temporal variability of sea ice albedo and its influence on the evolution of the sea ice volume.

2.2 The Role of Sea Ice Albedo in the Climate System

Among the natural surfaces of the Earth, the polar basins with varying sea ice cover likely exhibit the largest range in surface albedo. As mentioned, this variability is a significant control on both the local and global energy balance. Although its importance has been acknowledged, attempts at measuring and modelling sea ice albedo have been sparse in relation to other global climate variables. The following section begins by defining the various expressions of the term *albedo* utilized in this work. Subsequently, the role of sea

[1] Brine refers to the mixture of salt and water

ice albedo in the local and global energy balance is then described and current methods of parameterizing sea ice albedo in climate models are examined.

2.2.1 Albedo and Related Nomenclature

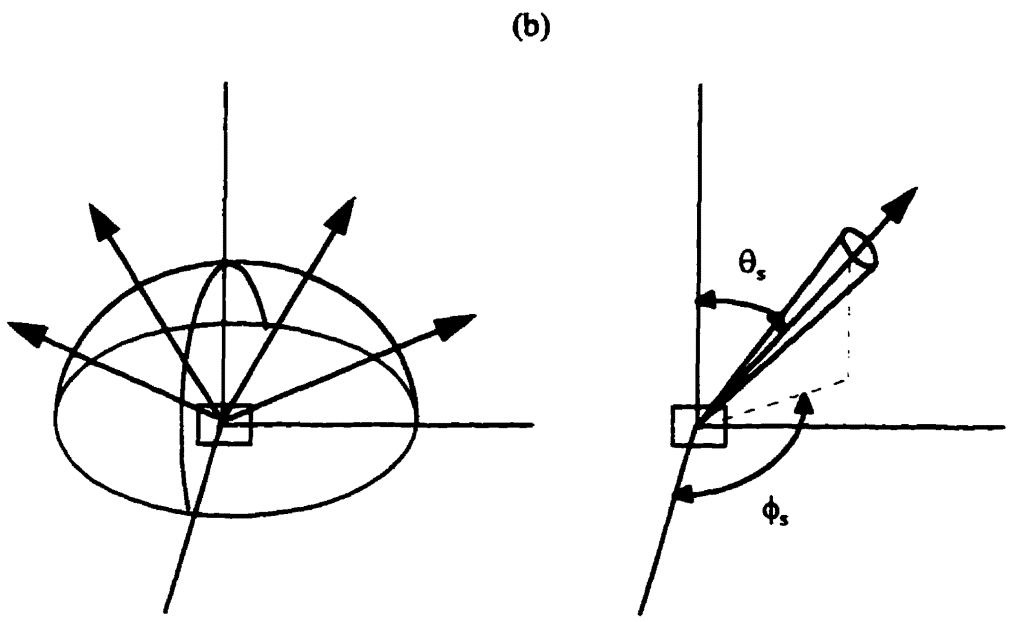
The term albedo originates directly from the Latin word (*albus*) meaning white. In simple terms, albedo was considered to be a measure of an object's brightness or whiteness (Henderson-Sellers and Hughes, 1982). This measure is usually expressed as the ratio of the energy reflected from the object to the energy incident on the object. Nicodemus et al. (pg. 2;1977) define reflection as the "process by which electromagnetic flux, incident on a stationary surface or medium, leaves that surface or medium from the incident side without change in frequency". Today there exists much confusion and little standardization in the literature over the usage of the terms *albedo* and *reflectance*. In the context of this work, the following five terms are defined and distinguished: *spectral reflectance, spectral albedo, visible albedo, infrared albedo and allwave albedo*. It should be noted that the usage of these terms may differ from other investigations.

The terms *albedo* and *reflectance* are distinguished by the measurement of the radiation reflected from the surface. Figure 2.2 illustrates the difference between the two terms. The term *albedo* (α) refers here to the fraction of incident flux that is reflected from a surface in all upward directions, in other words, integrated over the celestial hemisphere (Figure 2.2(a)). The reflected flux is usually measured by instruments employing hemispherical collectors, such as pyranometers.

The term *reflectance* (ρ) will refer to the fraction of incident flux that is reflected into a certain direction. The term is a function of the viewing incident ($\theta^{\cdot}$) and azimuth ($\phi^{\cdot}$) angle, i.e. $\rho(\theta^{\cdot},\phi^{\cdot})$. These directional measurements are typically made by surface or orbital radiometers employing a narrow aperture. Since these measurements are

often made on clear-sky days when the incident solar beam is considered to be restricted to a small solid angle[2], the term *bidirectional reflectance* is often used to describe these types of measurements.

Figure 2.2 Viewing geometry of (a) albedo vs. (b) reflectance



When the word *spectral* is used in conjunction with reflectance and albedo (i.e. *spectral reflectance* (ρ_λ) and *spectral albedo* (α_λ)) the measurement is defined at discrete spectral wavelengths. Albedo measurements refer to those integrated over various spectral ranges or broadbands of the solar spectrum. *Visible albedo* (α_{vis}) refers to the albedo integrated over the visible part of the solar spectrum from 0.15-0.70 μm. *Infrared albedo* (α_{ir}) refers to the albedo integrated over the infrared part of the solar spectrum from 0.70-4.0 μm. *Allwave* albedo (α_s), or what is sometimes called broadband or climatological albedo, implies a measure integrated over the entire

[2] A solid angle refers to a geometrical surface consisting of lines originating from a common point and passing through a closed curve or polygon (Borowski and Borwein. 1991).

range of the solar spectrum (0.15-4.0 μm). This range is also referred to as the *shortwave* range of the electromagnetic spectrum.

Both albedo and reflectance are expressed as unitless ratios represented by a value between 0 and 1, with a total reflector having a value of unity and a total absorber (e.g. black body) having a value of zero. Most natural surfaces fall somewhere in between. In climatology, two types of albedo are distinguished, the surface albedo and the planetary (system) albedo. The surface albedo refers to the reflectivity of the Earth's surface as measured below the overlying atmosphere. The planetary or TOA albedo pertains to the reflectivity of the Earth-atmosphere system as measured above the Earth's atmosphere from space. This measure represents the reflectivity of both the surface and the atmosphere, as well as its constituents. While there exists a close link between the two variables, this thesis focuses on the former use of the term, that is surface albedo.

2.2.2 The Role of Surface Sea Ice Albedo in Surface Energy Balance

In climate studies, the albedo of sea ice is most commonly expressed as an allwave albedo (α_A), i.e. integrated across the solar spectrum. It is calculated as the ratio of the reflected spectral irradiance (M_λ) to the incident irradiance (E_λ). Irradiance refers to an energy flux incident on a plane expressed as a density, e.g. W/m^2. Numerically, the allwave albedo is expressed as:

$$\alpha_A = \frac{\int_{.4.0}^{0.15} M_\lambda d\lambda}{\int_{.4.0} E_\lambda d\lambda} \qquad [2\text{-}1]$$

where the limit of the integration is defined by the spectral range (0.15-4.0 μm). This limit can be subdivided into a visible (0.15-0.70 μm) and infrared (0.70-4.0 μm) albedo to take into consideration the strong spectral dependence of snow and ice albedo.

2.2.2.1 Albedo and the Surface Energy Balance

The shortwave radiation regime in the polar regions can be best described as extremes separated by the Earth's vernal and autumnal equinoxes (March 20/21 and September 22/23 respectively). Spring is characterized by incident solar radiation at the top of the atmosphere increasing daily until June 21/22 (summer solstice). As an example, at Resolute Bay, N.W.T. (74°43'N,95°00'W), there is no sun rise between November 9 and February 3 and the sun doesn't set from April 27 to August 17 (Cogley and Henderson-Sellers, 1984). This large amount of daily insolation is countered in the atmosphere from highly reflective cloud tops and at the surface by high-albedo sea ice that is present over much of the Arctic Basin for a considerable part of the year.

Sea ice albedo is a strict control on the net shortwave flux at the surface of the sea ice volume. The net radiative flux available at the sea ice surface can be expressed using both radiative and energy balance terms after Ebert and Curry (1993) as:

$$(F_{net})_0 \equiv (1-\alpha_A)(1-I_0)F_{sw} - F_s - F_l + \varepsilon_{s/i}(F_{lw} - \sigma_B t_0^{\ 4}) \qquad [2\text{-}2]$$

where F_{net} is the net radiative flux at the surface (positive downward), α_A is the allwave surface albedo, I_0 is the absorbed fraction of shortwave flux that penetrates the ice interior and forms brine pockets, F_{sw} and F_{lw} are the incident shortwave and longwave fluxes, F_s is the upward turbulent sensible heat flux, F_l is the upward turbulent latent heat flux, $\varepsilon_{s/i}$ is the longwave emmissivity of snow and/or ice (0.99), σ_B is the Stefan-Boltzman constant (5.67×10^{-8} W/m^2/K^4) and t_0 is the surface temperature. The onset of freeze-up or melt conditions is dependent on the energy balance at the snow/ice surface. The physical state of the volume feeds back on this balance through the surface albedo (Shine, 1984). Snow-covered sea ice can have an allwave albedo as high as 0.90. As the snowcover melts and reveals more of the underlying ice, surface albedo can decrease 45-50% from this high value. Total

ablation of the sea ice cover reveals the darker, very low-albedo surface of open water. The lower the surface albedo, the more energy available at the sea ice surface for melt processes. The higher the surface albedo, the less shortwave energy available in the sea ice volume. This intimacy is best explained through the concept of the *sea ice-albedo feedback*.

2.2.2.2 Sea Ice-Surface Albedo Feedback

The concept of a sea ice albedo feedback was introduced formally by the energy balance modelling (EBM) efforts of Budyko (1969) and Sellers (1969). The concept can be illustrated with the use of a feedback diagram. These diagrams have been used by others to describe various processes within the climate system (Kellog, 1983; LeDrew, 1986; Curry *et al.*, 1995). Figure 2.3 contains a simple feedback diagram. Components A, B and C of the diagram are linked by positive or negative loops. A link with a positive sign indicates that the original perturbation in the original component results in a change in the linked component of the same direction. A negative link indicates that a change in original component results in an opposite change in the linked component. For example, an increase in A results in a decrease in B. The decrease in B results in a decrease in C. A decrease in C results in an increase in A. Since the ultimate result of the initial increase in A is a further increase in A, the feedback loop is self-amplifying and termed positive.

Figure 2.4 illustrates the positive sea ice - albedo feedback mechanism in the arctic. Briefly, the initial air temperature is perturbed by a lower latitude advection of heat. In fact, the onset of melt conditions in the arctic is believed to be triggered synoptically. The increased air temperature causes an increase in the air to surface heat flux.

Figure 2.3 Simple feedback diagram

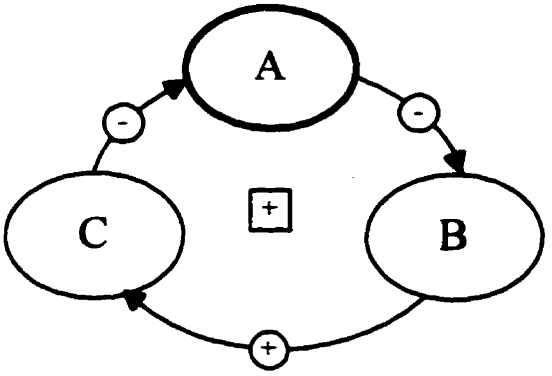
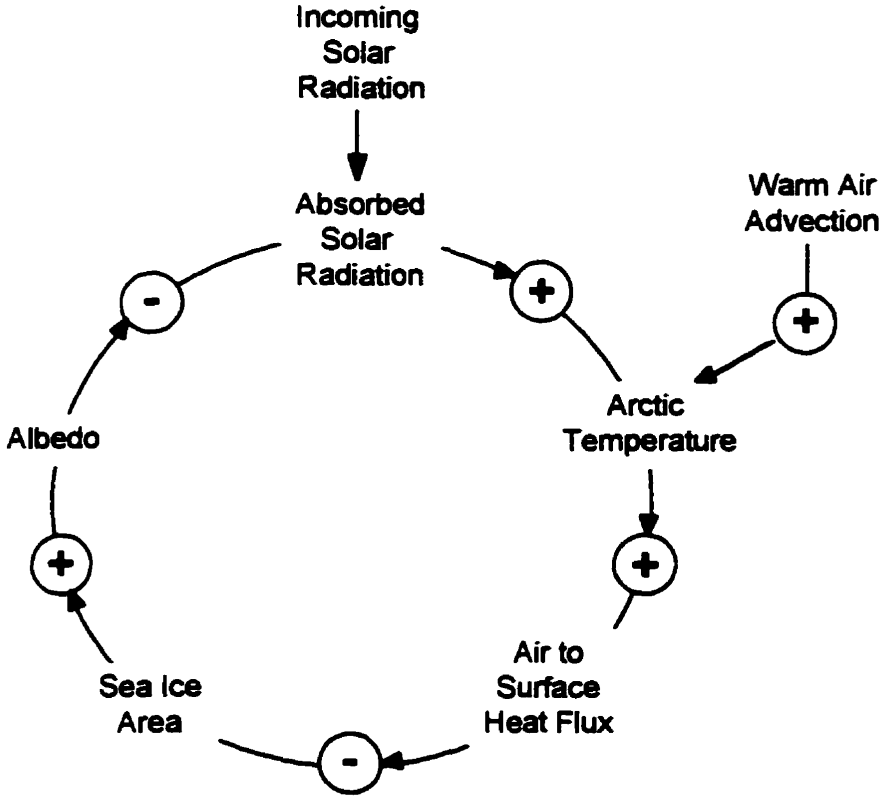


Figure 2.4 Positive sea ice albedo feedback.



Source: Adapted from Kellog, 1983

This results in the replacement of the highly reflective sea ice cover with a lower albedo water surface. This lowering of surface albedo increases the amount of absorbed solar radiation which further increases the arctic air temperature. Since the high stability of the arctic's lower atmosphere discourages mixing, much of this heat is redirected to the surface. In this positive feedback scenario, the result is an amplification of the original perturbation and an overall increased sensitivity (LeDrew, 1986). This is the main reason given for the amplification of global warming in the polar regions predicted by global circulation models. Ross et al. (pg. 13115, 1987) state that since Fletcher's (1965) early heat budget studies to more recent general circulation model (GCM) simulations (Meehl and Washington, 1990), surface albedo has been identified as a "high leverage parameter capable of enhancing thermal changes in high latitudes." Studies have shown that small changes in sea ice albedo lead to large changes in sea ice thickness, areal extent and timing of melt (Shine and Sellers, 1985). It is important to note that the positive sea ice albedo feedback is likely only one of many positive and negative feedback mechanisms ongoing in the arctic. For example, the high sensitivity of GCM results to sea ice albedo may be offset by the effects of cloudcover. Since large-scale climate models do not properly incorporate all components of the climate system, the net effects of these feedback mechanisms are not understood (LeDrew, 1986).

2.2.2.3 Parameterization of Sea Ice Albedo

Given its importance in regulating the amount of energy entering the snow/ice volume and its central role in the ice-albedo feedback, sea ice albedo is explicitly represented in both sea ice and climate models. However, the degree of sophistication of this representation varies greatly between and within model types as shown in the reviews by Morassutti (1989) and more recently by Barry (1996). These reviews reveal the diversity in both the parameterization and prescription of sea ice albedo within large-scale climate models. This diversity and the often simplistic albedo parameterization is

partly a result of the dearth of accurate, systematic measurements of sea ice albedo that include the quantity's inherent spectral, spatial and temporal variability.

Climate Models

The apparent sensitivity of climate model results to sea ice albedo warrants the incorporation of accurate parameterizations. However, given the size and complexity of general circulation models (GCMs), simple parameterizations of sea ice and other components of the climate system are desired whenever possible. Current parameterizations of sea ice albedo are limited by the rudimentary incorporation of the sea ice component in GCMs. This limits the availability of prognostic variables upon which to base a realistic parameterization. Often these variables are restricted to such quantities as ice thickness, snow depth and surface temperature. As a result the parameterizations are simplistic, often consisting of prescribed albedo values for certain broad classes of ice, e.g. snow-covered ice, bare ice and open water. Table 2.1 describes the parameterization of sea ice albedo in current general circulation models. The parameterization of sea ice albedo has improved in the last decade through the incorporation of more physical processes such as snow depth and age (Barry, 1996). Previously, sea ice albedo was often based simply on latitude and/or surface temperature. The Canadian Climate Centre (CCC) GCM's parameterization of sea ice albedo is characteristic of sea ice albedo parameterizations in large-scale climate models and is described below in more detail.

The CCC second generation GCM or CCC2 parameterizes sea ice albedo (α_I) for the following two spectral intervals: 1 -- 0.3-0.68 μm and 2 --0.68-4.0 μm. After McFarlane *et al.*, (1992), the model's parameterizations for bare sea ice albedo (α_I) for intervals 1 and 2 are:

$$\left[(\alpha_I)_1,(\alpha_I)_2\right] = (0.75,0.55) - 0.1\min\left[(t_0 - t_I)/(0.5,4)\right] \qquad [2\text{-}3]$$

where t_0 is the daily mean surface temperature and t_f is the freezing temperature for sea water (-2 °C). The last term accounts for the appearance of melt ponds on the surface after temperatures reach above freezing. It is constrained to be non-negative. As Table 2.1 shows, albeit crudely, the CCC model is the only model to incorporate the influence of melt ponds on surface albedo. For snow-covered sea ice, the albedo of snow (α_S) is used and is parameterized as follows:

$$\left[(\alpha_S)_1,(\alpha_S)_2\right] = (0.9,0.7) - 0.15\Omega_S \qquad [2\text{-}4]$$

where Ω_S is a snow age factor described in detail in McFarlane *et al.* (1992). If the mass of snow within the horizontal grid is greater than 10 kg/m^2 (about 3 cm of accumulated snow), the surface is considered completely snow-covered and the albedo of snow is used.

Table 2.1 Parameterization of sea ice albedo in GCMs.

	Model				
Albedo dependent on	CCC	GFDL	GISS	NCAR	UKMO
Fractional snow cover	•		•		•
Ice surface temperature	•	•		•	•
Ice thickness			•	•	
Snow accumulates on ice	•	•	•	•	
Melt ponds	•				
Lead fraction	•				•
Spectral range	vis/nir	vis/nir	vis/nir	vis/nir	

Source: Adapted from Barry (1996).

Notes:
CCC = Canadian Climate Centre
GFDL = Geophysical Fluid Dynamics Laboratory
GISS = Goddard Institute for Space Sciences
NCAR=National Center for Atmospheric Research
UKMO=United Kingdom Meteorological Office

As large-scale climate models incorporate more detailed, physically-based sea ice components, improved parameterizations of sea ice albedo can be accommodated. These models will ask more of the observational dataset, i.e., accurate, detailed information of sea ice albedo will be required. The following section briefly describes a physical sea ice model that incorporates a more detailed albedo parameterization scheme.

Physical Sea Ice Models

In order to assess the current results of general circulation models and to identify those sea ice components that require improvement, scientists are developing more realistic and complex dynamic (Flato and Hibler, 1992) and thermodynamic (Semtner, 1984; Ebert and Curry, 1993) sea ice models . Models such as these allow the incorporation of sophisticated treatments of ice, oceanic and atmospheric components that are beyond the reach of today's large-scale climate models. These models are often a precursor to the improvement of the physical surface components of large-scale, multi-dimensional climate models.

Ebert and Curry (1993) employed a detailed one-dimensional thermodynamic sea ice model to examine the sensitivity of sea ice thermodynamics to the physical processes of the climate system in order to identify those feedbacks that require accurate representation in larger scale climate models. The study identified a number of important positive and negative feedbacks operating in the sea ice system. Among them was the previously described positive surface albedo feedback. Heeding the call for accurate albedo representation in sea ice models (Shine and Henderson-Sellers (1985), Ebert and Curry (1993) employ a detailed albedo parameterization (Table 2.2) that is sensitive to the physical state of the ice surface. The albedo parameterizations are based on theoretical albedo models (Wiscombe and Warren, 1980) and unfortunately, on a very small number of field observations (Grenfell and Perovich, 1984; Grenfell and Maykut, 1977). Still, the parameterization is one of the most

sophisticated to date. Most of the scheme's uncertainty lies in the albedo of the ice surface during the spring transition period.

Table 2.2 Sea ice albedo parameterization of Ebert and Curry's (1993) 1-D sea ice model

Surface Type	Band 1 0.25-0.69 μm	Band 2 0.69-1.19 μm	Band 3 1.19-2.38 μm	Band 4 2.38-4.00 μm
Dry snow				
Direct	0.98-.008 m_0	0.902-0.116 m_0	0.384-0.222 m_0	0.053-0.047 m_0
Diffuse	0.975	0.832	0.250	0.025
Melting snow				
$h_s \geq 0.1$ m	0.871	0.702	0.079	0.010
h_s 0.1 m	linearly reduced to bare ice value	linearly reduced to bare ice value	linearly reduced to bare ice value	linearly reduced to bare ice value
Bare sea ice				
h_i 1 m	0.760+0.14 ln h_i	0.247+0.029 ln h_i	0.055	0.036
$1 \leq h_i < 2$ m	0.770+0.018 (h_i-1)	0.247+0.196 (h_i-1)	0.055	0.036
$h_i \geq 2$ m	0.778	0.443	0.055	0.036
Melt pond	0.150+exp(-8.1h_p-0.47	0.054+exp(-31.8 h_p-0.94	0.033+exp(-2.6 h_p-3.82)	0.030
Open water				
Direct	α_w+0.008	α_w-0.007	α_w-0.007	α_w-0.007
Diffuse	0.060	0.060	0.060	0.060

Note: μ_0 = cosine of solar zenith angle; h_s= snow depth; h_i= ice depth; h_p= pond depth; α_w=0.026/(μ_0 $^{1.7}$+0.065)+0.015(μ_0 -0.1)(μ_0 -0.5)(μ_0 -1.0)

Unlike lower-latitude terrestrial surfaces, the albedo of sea ice has received relative little attention. The reasons for this have been discussed. Henderson and Wilson (1983) state that it is unlikely that GCMs will reparameterize cryospheric surface processes until better observational data are made available. In response, there have been attempts to improve the observational record of sea ice albedo in the arctic, as

well as in Antarctica. As a result, sea ice parameterizations have become more realistic. However, without proper means to validate these model simulations, their accuracy is unknown. Field observation, the traditional source of albedo information, continues albeit with more advanced measurement technology. The value of these measurements continue to be hindered by their inherent lack of spatial and temporal coverage. Satellite remote sensing has been heralded as the most practical means to measure sea ice albedo at spatial and temporal scales appropriate for climate studies. However, thus far, attempts at measuring arctic sea ice albedo have been lacking any type of field validation. As a result, the utility of using satellite data to measure surface albedo is still unknown.

2.3 Conclusions

The physical state of the sea ice volume plays a significant role in the Earth's climate system. The sea ice volume is linked to the larger climate system through its seasonally dynamic surface albedo. Given this important role, sea ice albedo is explicitly included in most sea ice and large-scale climate models. However, the simple parameterization of sea ice albedo belies its leverage in the local and global climate system. Since many observational datasets are limited in spatial, temporal and spectral dimensions, improvements in current parameterizations are delayed by the dearth of appropriate sea ice albedo data. Climatologists are interested in how sea ice albedo changes seasonally and annually over large geographic areas. To this point, sea ice albedo observations have been collected over short periods and over small spatial scales. While these efforts have been instrumental in the development of our current understanding of the climate system, many acknowledge the need for more systematic observations of sea ice albedo that are capable of identifying the spectral, spatial and temporal characteristics of the quantity at climatological scales. With this in mind, the objectives presented in Chapter 1 were formulated and subsequently addressed in the work presented in the remainder of this thesis. The following chapter examines the spring evolution of the visible and infrared

albedo of sea ice through the analysis of spectral albedo and snow/ice geophysical data collected *in situ*.

3 IN SITU MEASUREMENTS OF SEA ICE SPECTRAL ALBEDO

In recent years, increased attention on the climate of polar regions has highlighted a need for improved observational datasets of sea ice albedo. Specifically, improved climate models and remote sensing technologies require information regarding the spectral characteristics of sea ice albedo throughout the year. Since measuring sea ice albedo has been a traditional exercise in most arctic expeditions and experiments, it is discouraging to see disparate surface albedo values among datasets. Henderson-Sellers and Wilson (pg. 1745, 1983) blame discrepancies between surface albedo datasets on the inherent variability of albedo as a "function of surface type, state and incoming radiation, etc. and the lack of a coherent and rigorous measurement program."

This chapter examines the *in situ* measurement of the spectral albedo of sea ice. First, the optical properties of sea ice responsible for sea ice albedo are described and the use of radiative transfer models to predict snow and sea ice albedo is reviewed. Previous investigations of sea ice albedo that hold particular significance to this investigation are described. Using sea ice spectral albedo measurements collected during SIMMS '93 and SIMMS '95, the spring transition of the visible and near-infrared albedo of sea ice is examined. Of specific interest here is a description of the seasonal transition in spectral sea ice albedo with the onset of melt conditions and the identification of the physical factors of the sea ice volume that drive this change.

3.1 The Albedo of Sea Ice -- A Theoretical Perspective

Sea ice albedo is intimately linked to the physical properties of the ice volume and vice versa. This relationship was characterized in the previous chapter as a positive feedback mechanism (Figure 2.3). With the onset of melt conditions, the physical characteristics of the sea ice volume begin to change. This seasonal metamorphosis of the sea ice volume exerts significant control over the optical properties of the entire ice volume. The sea ice volume is considered an optically complex medium whose albedo is primarily controlled by the optical properties of its near-surface layers. Volume scattering within these layers is largely responsible for the albedo of sea ice. At any given time, the characteristics of these surface layers may vary widely over horizontal distances of metres and vertical distances of millimetres. This variability defines the spectral, spatial and temporal characteristics of sea ice albedo.

The interaction of solar radiation with a sea ice volume has been theoretically investigated through the use of radiative transfer models. These models are useful for directing and interpreting field observations of sea ice albedo. Before examining the field observations of sea ice albedo collected in this investigation, it is useful to review the theoretical modelling of the albedo of sea ice. For this discussion, the icescape (LeDrew and Barber, 1994) is separated into three general categories: snow-covered sea ice, bare sea ice and melt pond covered ice. Based on observations, this simplification adequately represents the sea ice volume for the purposes of this discussion.

3.1.1 Snow-Covered Sea Ice

For much of its existence, sea ice is covered by a seasonal snowcover whose depth can range from millimetres to well over a metre. The albedo of the snow-covered sea ice volume is dependent on the transparency of this overlying snow layer, which in turn is a function of its internal structure. Due to its continual internal metamorphism, snowcover exhibits a much wider range of optical properties than does sea ice (Grenfell and Maykut,

1977). Essentially the transparency or *optical depth* (τ) of a snowpack is dependent on the bulk optical properties of the constituents of the volume: ice grains, air, water (at 0° C) and particulate impurities (dust, soot). Snow optical depth (τ_S) is a dimensionless measure of the thickness of a snow layer and is defined as:

$$\tau_S = k_{ext} z_S \qquad [3\text{-}1]$$

where k_{ext} is the volume's extinction coefficient and z_S is the depth of the snow layer. Since snow and ice are optically complex, i.e. incident radiation is lost through both absorption and scattering, the extinction coefficient is equivalent to:

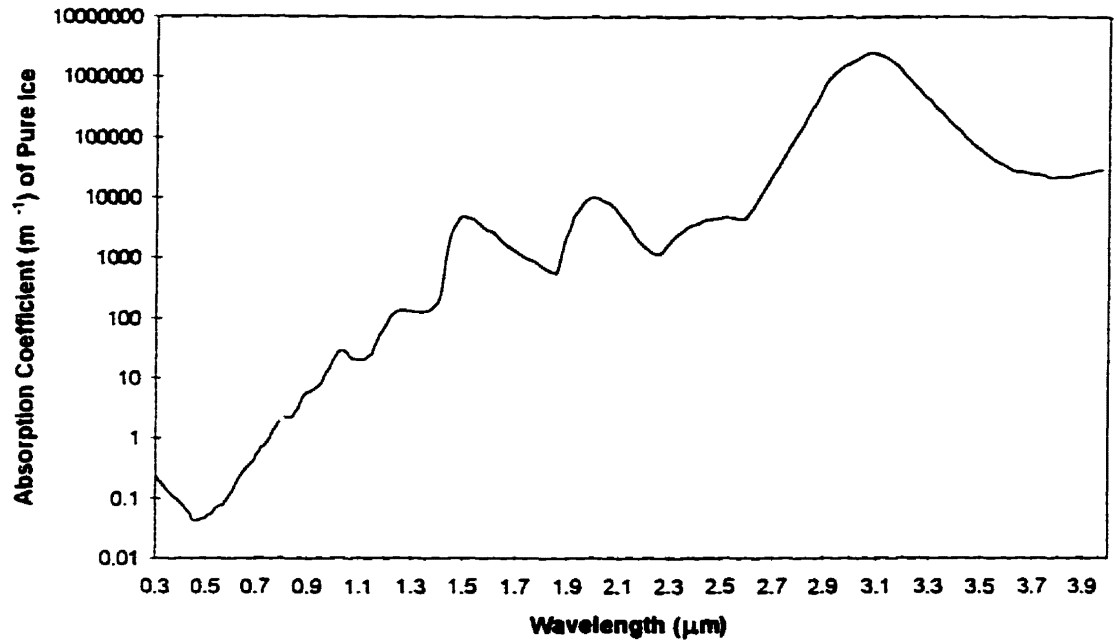
$$k_{ext} = k_{sca} + k_{abs} \qquad [3\text{-}2]$$

where k_{sca} and k_{abs} are the scattering and absorption coefficients respectively. The scattering coefficient is the reciprocal of the average distance a photon travels through the volume before it is scattered. Similarly, the reciprocal of the absorption coefficient is the average distance a photon travels in pure bubble free ice before being absorbed (Mullen and Warren, 1988). In terms of a pure snowpack, i.e. no impurities present, the volume's absorption coefficient is related only to the imaginary part of the refractive index of pure ice (m_{im}) through the following:

$$k_{abs} = \frac{4\pi m_{im}}{\lambda_v} \qquad [3\text{-}3]$$

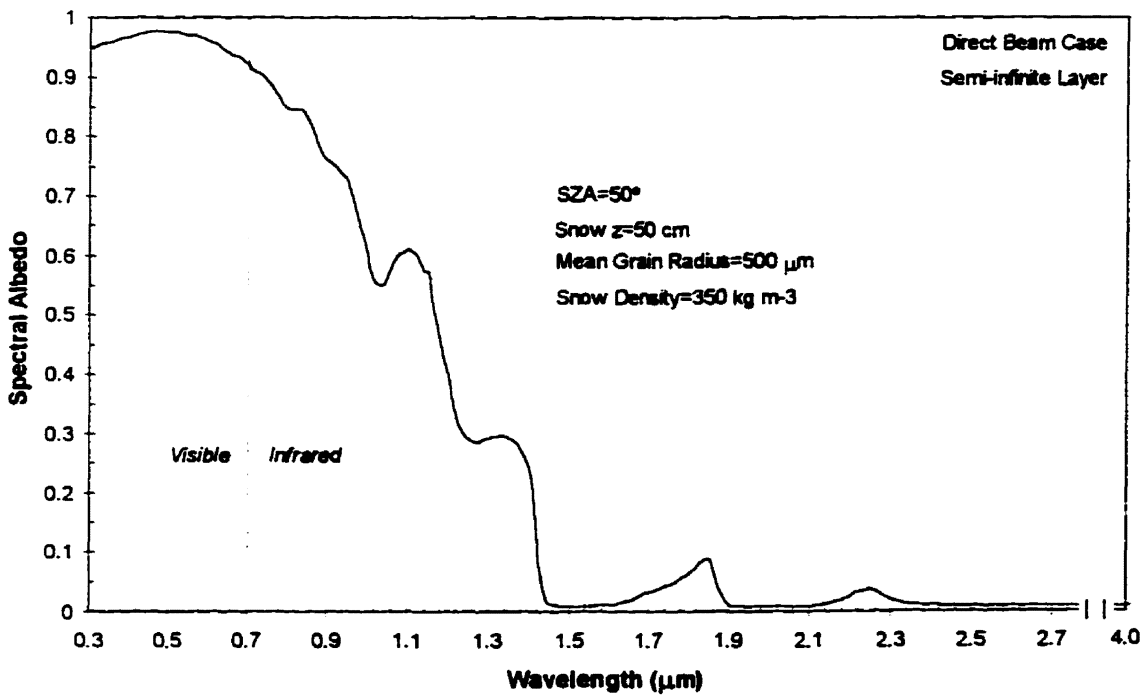
where λ_v is the wavelength of incident light in a vacuum. The absorption coefficient for pure ice within the solar spectrum is shown in Figure 3.1. Unlike other optical properties, the absorption coefficient of ice is a strong function of wavelength and is thus responsible for the characteristic shape of the spectral albedo of ice. Over the visible part of the spectrum, the absorption coefficient for ice is low, implying that radiation incident at these wavelengths would likely be scattered by ice grains instead of being absorbed.

Figure 3.1 Absorption coefficient of pure ice



(Source: Warren. 1984)

Figure 3.2 Modelled spectral albedo of snow



The result is a higher probability of light leaving the snowpack and thus a higher albedo. However, absorption of ice increases rapidly with wavelength in the red and infrared portions of the spectrum. This results in a steadily decreasing albedo as wavelength increases. The presence of impurities can affect spectral albedo by their substantially different absorption coefficients. As will be shown, these differences usually manifests themselves as a change in the magnitude and/or shape of the albedo spectra.

The spectral albedo of snow is characterized by a spectral curve high in the visible portion of the electromagnetic spectrum and consistently lower in the infrared. Figure 3.2 shows a typical snow albedo spectra for a pure semi-infinite snowpack. The general shape of snow spectra is due the absorption coefficients of the two main constituents of the pack, ice and water. Although, the amount of ice and liquid water in the snow volume will change with season, their similar absorption coefficients result in the shape of the albedo spectra shape being relatively invariable over time. The peaks and valleys in the infrared snow albedo are due to the valleys and peaks in the absorption coefficient of ice respectively.

Fortunately, the albedo of snow has received considerable attention from both the empirical and modelling communities. A comprehensive review of the optical properties of snow and snow albedo is provided in Warren (1982). Considerable effort has been invested in modelling the albedo of snow (Bohren and Barkstrom, 1974; Choudhury and Chang, 1981). Wiscombe and Warren (1980) developed a snow model that predicts spectral albedo over the solar spectrum for various snow grain sizes and illumination conditions. The model is described in detail in Appendix 1. The model, hereafter referred to as the WW model, appears to adequately reproduce observational measurements and is used here to describe the spectral albedo of snow.

The intensity of a beam passing through a layer is reduced by extinction to $e^{-\tau}$ of its original value. The optical depth of unity corresponds roughly to the depth where one can distinguish objects through a layer (Barkstrom *et al.*, 1975). If the snowcover is deep enough where the underlying ice surface does not contribute to the surface albedo, it is

considered optically thick or *semi-infinite*. Wiscombe and Warren's (1980) definition of a semi-infinite volume is used here, i.e., a volume where the albedo at all wavelengths is within 1% of that of an infinitely thick snowpack. The sea ice albedo is then essentially a snow albedo. Conversely, in the case of a *finite* snowcover, the underlying ice volume significantly effects the albedo. Both of these cases are now considered further.

3.1.1.1 Semi-Infinite Snow Volume Over Sea Ice

In a semi-infinite snow layer, the scattering and absorption of incident radiation is considered to occur entirely within the snowpack. Observational and modelling efforts have identified grain size and the presence of the impurities as the two limiting factors in the albedo of an optically thick snowcover. Figure 3.3 shows the theoretical spectral albedo of snow for various grain sizes in a semi-infinite snow layer. Grain size is specified in the model by the radius of an optically equivalent sphere (Wiscombe and Warren, 1980). Increasing grain size, simulated here by various sizes of grain radii[3], results in a slight decrease in albedo in the visible spectrum and large decreases in albedo in the infrared spectrum. A photon has a chance to scatter when it is at an air-ice interface and it has a chance for absorption when it is passing through an ice grain. Larger ice grains result in a longer path length through the grain, thus there is a greater chance for absorption and less volume scattering within the volume over all wavelengths (Grenfell and Maykut, 1977; Warren, 1982). Dozier (1989) qualifies this by pointing out that increasing grain size does not significantly affect snow albedo in the visible spectrum because of the low absorption coefficient of ice in that region, i.e. there is a low probability that a light photon will be absorbed when it enters an ice grain. Increasing the size of the ice grain will not likely increase this probability significantly. However, in the near infrared region, ice is moderately absorptive and thus albedo is more sensitive to grain size, especially at 1.0 - 1.3 μm.

Since one of the more noticeable changes in the snow volume during spring is the melting of snow grains and the increase in liquid water in the pack, the effect of increased liquid

[3] A mean grain radius of 100 μm is considered representative of a new snow layer

water on albedo deserves attention. Under laboratory conditions, O'Brien and Munis (1975) blew warm air over a snow sample to increase the volume's liquid water content. A decrease in reflectance was observed. However when the sample was refrozen, thus reducing the liquid water in the snow, the reflectance did not increase significantly. Since water and ice have similar refractive indexes in the solar spectrum, liquid water present within a snowcover does not affect reflectance by itself. Instead, liquid water within the pack fills pores spaces between individual snow grains encouraging the development of grain clusters (Colbeck, 1979). These grain clusters effectively mimic larger grains thus causing decreased reflectance, particularly in the near-infrared regions. The presence of liquid water can speed up the rate of grain metamorphosis, thus a short exposure to melting conditions can reduce albedo considerably (Wiscombe and Warren, 1980).

The other important factor affecting the albedo of a semi-infinite layer is the presence of impurities. The inability of the WW model of pure snow to reproduce the arctic ice island spectral albedo measurements of Grenfell and Maykut (1977) highlighted the need to address the absorptive effects of snowpack impurities such as soot and dust. This was first theoretically addressed in Warren and Wiscombe (1980) with their modelling of an impure snowpack. Assuming that the impurities were externally mixed in the volume, i.e. the soot or dust particles are outside of the snow grain, Warren and Wiscombe showed that small amounts of dust (~10 parts per million by weight (ppmw)) and carbon soot (~0.1 ppmw) can reduce visible albedo by a few percent (Warren, 1982). Chylek et al.,(1983) showed that approximately half as much soot is needed for the same reduction if the soot particles are present within the snow grains, i.e. internally mixed.

The effect of soot on the albedo of a new snowpack (grain radius(r)=100 mm) is modelled in Figure 3.4. Its influence on albedo is determined by the refractive index of the impurity, its volume fraction and distribution within the volume. In this example, the absorption coefficient of the ice grains is based on Chylek et al's (1983) refractive index (imaginary part) of two internally mixed soot-ice mixtures with volume fractions of 1x10-8 (typical of very pure snowpack) and 5x10-8 (typical of snow in rural areas).

Figure 3.3 Modelled effect of grain size (mean radius) on the spectral albedo of snow

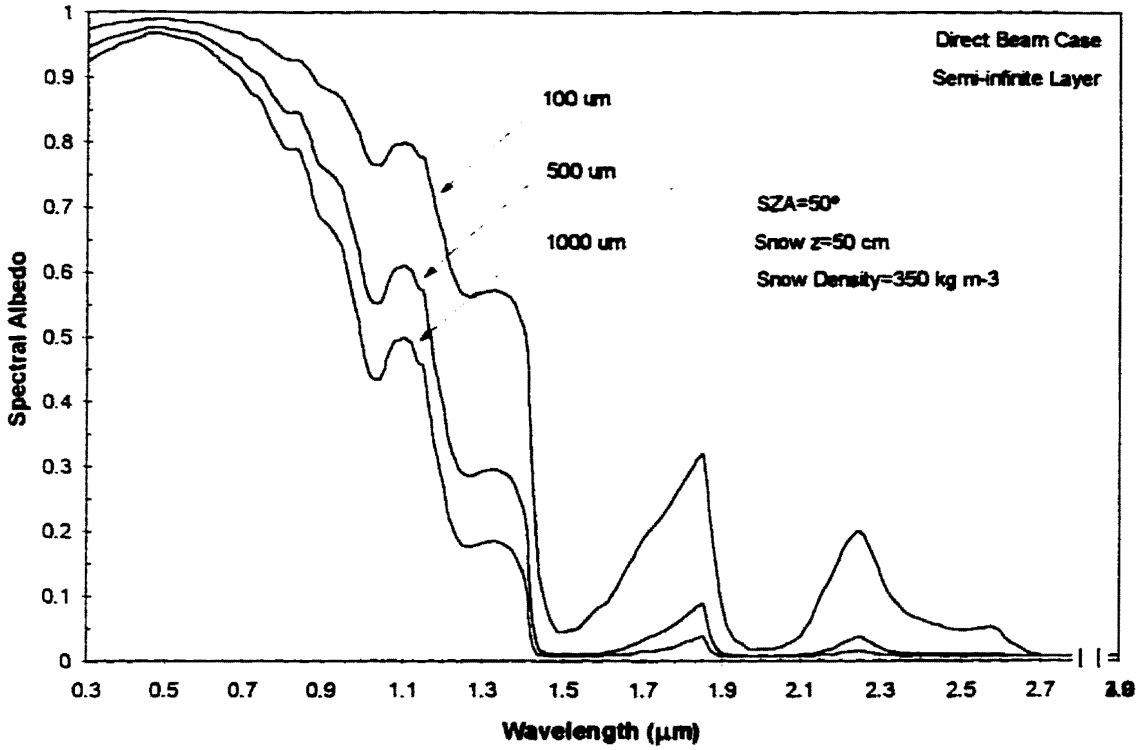
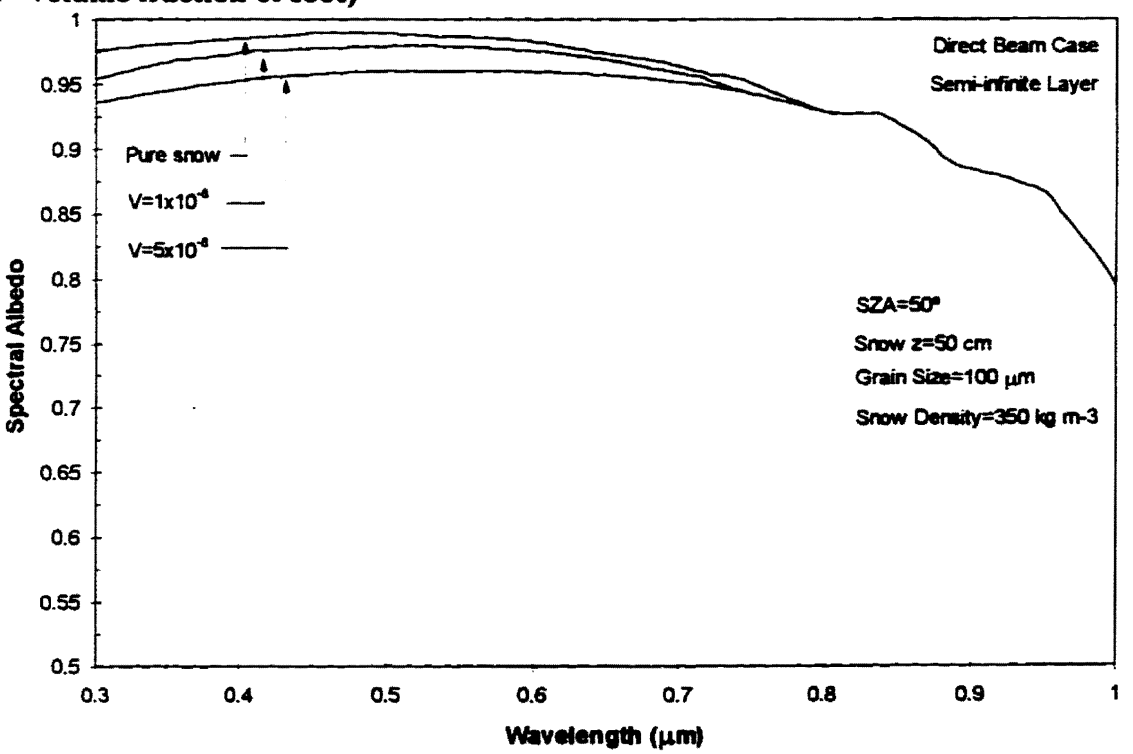


Figure 3.4 Modelled effect of internally mixed carbonic soot on snow albedo. (V=volume fraction of soot)



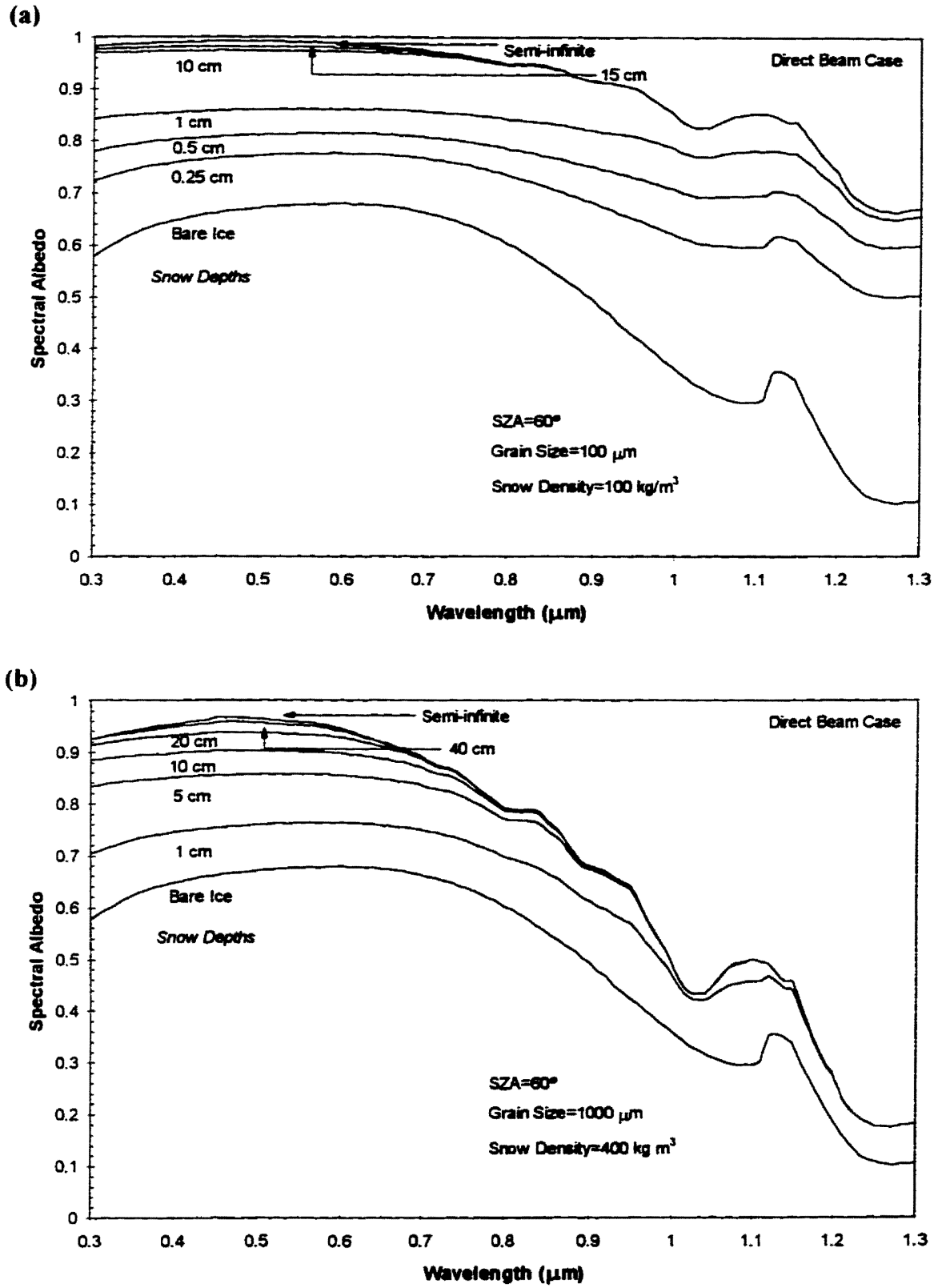
The presence of soot increases the absorption coefficient of an ice grain and thus reduces albedo. In the case of soot and dust, this reduction is limited to wavelengths <1.0 μm. The absorptive effects of ice grains beyond 1 μm dominate such that any effects due to impurities are insignificant. Since the absorption coefficient of soot is also independent of wavelength from 0.3-0.9 μm (Dalzell and Sarofim, 1969), its presence causes a flattening of the albedo spectra in the visible spectrum (Wiscombe and Warren, 1980) (Figure 3.4).

In the arctic, there are two major sources of impurities for sea ice snow volumes. The natural source is crustal material blown onto the ice from adjacent land areas. This is especially prevalent in coastal areas when the snow has disappeared from the land with the spring thaw. The other major source is anthropogenic in origin. Airborne carbon particulates originating from lower latitude industrial areas are transported to the arctic regions and cause increased atmospheric turbidity or arctic haze. Spring precipitation eventually removes these particulates from the air and incorporates them into the arctic snowpack thus reducing its albedo (Hall, 1988). Arctic haze will be discussed further in the next chapter.

3.1.1.2 Finite Snow Volume Over Sea Ice

The albedo of the underlying ice surface contributes to the overall surface albedo of an optically finite snow volume. The factors that affect the albedo of a semi-infinite snowpack effect the finite volume albedo as well. In the case of finite volume, two additional factors are important to surface albedo: the albedo of the underlying surface and the snow depth. Figure 3.5 compares the transparency of a snow volume consisting of new snow (r=100 μm, density = 100 kg/m^3) and old snow (r=1000 μm, density = 400 kg/m^3) overlying bare ice. The top spectra in each case represents an optically semi-infinite snowpack. At the short visible wavelengths, the decrease in snow depth results in a lowering of surface albedo as the darker underlying ice surface interacts increasingly with incident radiation. In the near-infrared, the decrease in albedo with snow depth is much less noticeable. In terms of incident radiation greater than 1.3 μm, most snow surfaces can be considered optically semi-infinite. The transparency of a pure snow

Figure 3.5 Modelled effect of snow depth on snow albedo on sea ice for grain radius of (a) 100 μm and (b) 1000 μm.



volume is dependent on its grain size and density. The model indicates that just over 15 cm of snow is required to make the new snow volume optically thick and thus negate the influence of the underlying ice (Figure 3.5(a)). In the case of the old snow volume (Figure 3.5(b)), almost twice as much snow is needed to do the same. Snow volumes with smaller grains scatter light more efficiently thus decreasing the penetration depth of incident radiation. Also significant is the influence of very thin snowcovers on sea ice albedo for both cases. A 0.25 cm dusting of new snow increases bare ice visible albedo by 15% and triples infrared albedo at some wavelengths. A 1 cm old snowcover increases bare ice visible and infrared albedo by 14% and 6% respectively. As snow grain size increases, absorption of incident radiation increases at the snow surface. As a result, the sensitivity of infrared albedo on snow depth decreases with snow grain size.

3.1.2 Bare Sea Ice

Compared to the modelling and observational efforts committed to understanding the albedo of snow, limited time has been invested in understanding the albedo of bare sea ice. Part of this inequity can be blamed on the difficulty (and danger) in sampling an often thin sea ice cover after snow melt or just after freeze-up. Sea ice albedo measurements have been carried out via polar experiments, but compared to snow surfaces, very little spectral data over bare and/or melting sea ice have been collected. Theoretically, the assumptions of radiative transfer theory in snow are somewhat applicable to sea ice given their shared granular characteristics. Similar to snow, the modelling of the radiative transfer in sea ice is often based on the assumption that the media can be represented by a plane parallel system with layers consisting of air, saline ice and water. Also, like snow, the distance between scatterers are assumed to be larger than the size of incident radiation and thus Mie scattering theory is applicable (Grenfell and Perovich, 1986).

A detailed review of the evolution of sea ice radiative transfer models is provided in Grenfell and Perovich (1986). Early attempts at modelling radiative transfer within sea ice were made with one-dimensional thermodynamic models which did not predict, but

employed prescribed surface albedos (Maykut and Untersteiner, 1971). These early attempts ignored the spectral dependence of the absorption coefficients of ice and brine and the incident irradiance by employing a bulk extinction coefficient and incorrectly assumed that the absorption of radiation within the ice volume strictly followed Bouguer's Law[4], i.e. an exponential decay dependent on layer thickness and bulk extinction coefficient. Improvements were made with the incorporation of a two-stream (upwelling and downwelling irradiance) spectral model that more realistically parameterized radiative transfer within the ice (Grenfell, 1979; Perovich, 1990). Perovich (1990) developed a simple, multi-layer radiative transfer model to investigate the attenuation of visible and near-infrared radiation in a spatially and temporally varying sea ice cover. While the model is useful for providing regional estimates of albedo and transmission where measurements are available, the physical properties of the ice are not directly related to the optical properties of the volume (Grenfell, 1991).

The current genre of sea ice radiative transfer models more realistically emulate both the extinction of light and the intimate relationship between the optics and the physical properties of the ice volume. Although these physically based models represent an significant increase in complexity, they are considered more accurate than previous formulations. Using a multi-stream, single layer model, Grenfell (1983) and Grenfell and Perovich (1986), examined how the evolution of first-year ice affects the optical properties of sea ice. Figure 3.6 shows their modelled spectral albedo for ice thickness of 1 cm to 3 m representing a move from a gray-black surface to an intermediate gray-white surface (Grenfell, 1983). Since the volume is dominated by the optical properties of the ice constituent, the shape of the ice spectra is generally similar to that of snow. Bare ice visible albedo is dominated by volume scattering and thus found to be dependent on ice depth. At infrared wavelengths, absorption at the very top layers dominates resulting in a lower albedo independent of ice depth.

[4] According to Bouger's law, the attenuation of light through a medium is proportional to the distance traversed in the medium and to the local flux of radiation. It is also referred to as Beer's Law or Lambert's Law.

Figure 3.6 Modelled bare ice albedo vs. ice depth from Grenfell (1983)

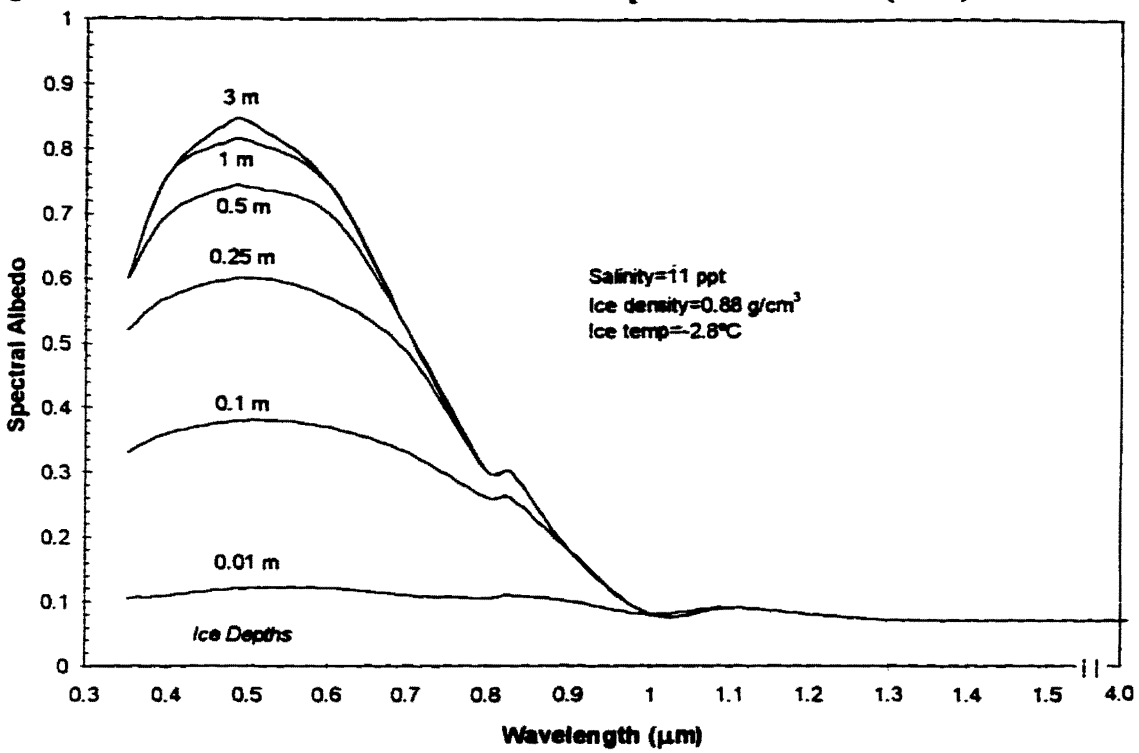


Figure 3.7 Modelled bare ice albedo during cooling and warming phase from Grenfell (1983).

(Single ice layer. salinity=11 ppt. growth rate=$8x10^{-5}$ cm/s).

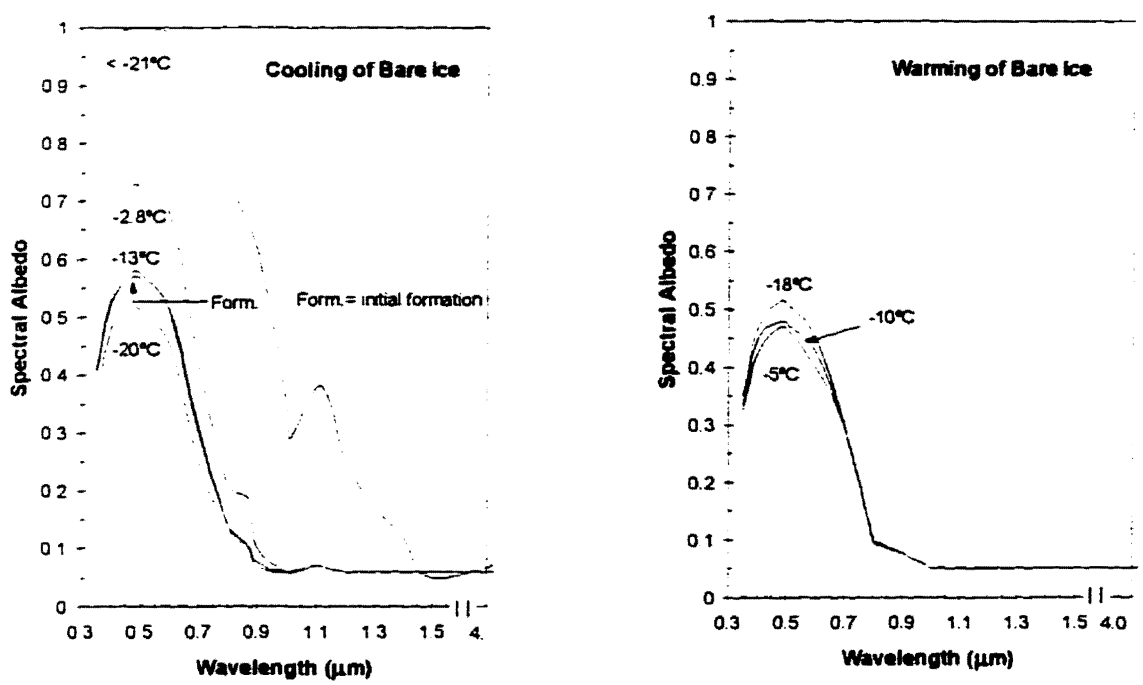


Figure 3.7 shows modelled spectral albedo from Grenfell (1983) for bare ice for two growth phases: cooling after formation and the warming of cold ice. The modelled albedo increases quickly after formation due to the transformation of the modelled brine structure from cylinders to more efficiently scattering spheres. The albedo quickly decreases as these spheres shrink in size and it is doubtful whether this rapid increase at 2.8°C would be observable. Throughout this phase there are minimal changes in the visible albedo and much less in the infrared. The albedo of ice below the eutectic point (< 21-23°C) is included in Figure 3.7. This ice temperature is common in the upper layers of sea ice during winter and early spring. Below the eutectic point, all liquid in the ice volume freezes and the salt is precipitated out as solid cubes. The number density of these crystals would be much greater than the brine inclusions resulting in more efficient scattering and the much higher albedo shown in Figure 3.7. Thus in early spring, bare ice surfaces can be expected to yield albedos similar to adjacent snow-covered surfaces.

In the warming phase, the enlargement and interconnection of brine pockets and the growth of air bubbles within these inclusions reduce scattering in the volume and consequentially reduce albedo. Again changes in albedo appear to be minimal and restricted to visible wavelengths in this phase. However, the widespread applicability of these results are questionable given the sensitivity of the model to the growth rate of the ice and the distribution of brine and air bubbles within the volume. Also the model ignores the effects of brine expulsion from the ice and also cannot accommodate a surface granular layer that is commonly found overlying bare ice covers after the removal of the snow layer. This layer has been observed to scatter more efficiently and cause an increase in surface albedo (Grenfell and Maykut, 1977).

In Grenfell (1991), the previous model is improved through the addition of multiple layers. The model also includes reflection and refraction of light at all layer boundaries which is considered especially important for bare sea ice (Perovich and Grenfell, 1981). Refraction at the snow-ice interface causes incident radiation to be redirected in a more normal direction allowing deeper penetration into the ice. Model results indicate that ignoring

refraction can lead to a significant overestimation of surface albedo, especially with bare ice at large solar zenith angles. Arrigo *et al.*,(1991) modelled the effect of biogenic material, like algae, on the optical properties of Antarctic sea ice. While considered important for the spectral transmissivity of sea ice (Arrigo *et al.*, 1991), the presence of biogenic material such as algae only affects the albedo of thin ice volumes and/or algae-contaminated snowcovers.

In summary, the albedo of bare sea ice is controlled primarily by the absorption coefficient of the volume's primary constituent, ice. Similar to snow, bare ice albedo is high at visible wavelengths, decreases rapidly in the near-infrared and levels off to a constant value throughout the rest of the infrared spectrum. Theoretical modelling of the optical properties of sea ice has highlighted the close relationship between the physical microstructure of the ice volume and its albedo. Specifically, the models reveal the importance of brine inclusions, vapour bubbles and solid salts in controlling extinction in the volume. These structures have been found to be sensitive to ice temperature and growth rate and are thus expected to vary on both a seasonal and annual scale. Shorter wavelength visible radiation capable of penetrating the ice volume is most sensitive to these microstructure changes. As a result, the visible albedo of bare sea ice has been shown to vary the most over the formation, cooling and warming of the sea ice volume. Since the attenuation of incident radiation increases rapidly at infrared wavelengths, the albedo in this region is determined by the physical characteristics of the surface layer.

3.1.3 Melt Ponds

The spring ablation of the overlying snow volume results in the pooling of melt water on the ice surface in melt ponds. The removal of the snowcover and the addition of the water layer affects sea ice albedo. Although not yet explicitly incorporated in sea ice radiative transfer models, melt ponds through their ubiquitous springtime presence are a significant influence on the regional albedo. Melt pond albedo is characterized as high in the shorter, visible wavelengths and rapidly decreasing in the 0.5 to 0.8 μm range. Since water is

transparent to the short visible wavelengths, the reflectance in this range is determined primarily by the optical characteristics of the underlying ice cover. However, at wavelengths greater than 0.5 μm, the absorption of the incident radiation by the melt water increases rapidly with wavelength. Above 0.8 μm, water absorption dominates and the resultant albedo approaches zero. An important factor in the albedo of melt ponds is the presence of biogenic and/or crustal material in the pond water. These can accumulate on the surface, pond bottom or even throughout the water column. These materials can reduce and change the spectral characteristics of the pond's albedo. Also notable is the formation of a thin layer of ice and/or slush on the pond surface during spring melt-freeze events. The ice cover usually increases both the visible and infrared albedo. Also relevant is the ability of this cover to support newly fallen or drifted snow which can dramatically increase melt pond albedo.

3.2 Field Observations of Sea Ice Albedo

The observation of sea ice albedo is a fundamental part of polar climate studies. However, unlike terrestrial climate observations, sea ice albedo cannot be recorded at continually manned weather stations. As a result, observations have been restricted to various surface programs that range in duration from days to a few months, often located in different parts of the Arctic Basin. Also significant is the fact that these measurements are often collected under varying atmospheric conditions and at different sun-target geometries. As a result, the record of sea ice albedo is spatially, temporally and methodologically inconsistent. This precludes a straightforward comparison of measurement results. However, in order to place the observations made during this investigation in context, it is useful to review previous field observations of sea ice albedo. The measurements examined here consist of both allwave and spectral albedo.

3.2.1 Allwave Albedo Measurements

Most of the recorded sea ice albedo measurements have been carried out over fast ice during the spring transition period of April to July, often in support of sea ice surface energy balance studies. In most instances, allwave sea ice albedo was measured by ratioing the response of two integrating pyranometers -- one pointed at zenith and the other normal to the surface. Pyranometers are capable of measuring and integrating incident solar radiation on a plane surface over a hemisphere usually in the spectral range 0.3 - 3.0 μm. Early albedo observations in the arctic (Marshunova, 1961; Chernigovisky, 1963; Bryazgin and Koptev, 1969) provided ice albedo values in the range of 0.2 over melt ponds to 0.75 over white ice (Grenfell and Maykut, 1977). Langleben used pyranometers suspended above the ice by high towers (1968) on Ellesmere Island (81° 25' N, 76° 50' W) and by aircraft (1971) in the Beaufort Sea (69° 26' N, 133° 02' W) to monitor the effects of melt on fast ice albedo. The Langleben studies found that pre-melt snow-covered sea ice albedo averaged around 0.7 and began to decrease with the onset of melt conditions. As daily mean temperatures exceeded 0°C, the surface transformed into a mixture of melt ponds, drainage channels and bare ice areas. The author determined that the dependence of allwave albedo on the presence of melt ponds can be expressed by the following linear model:

$$\alpha_A = 0.59 - 0.32 P_{mp} \qquad [3\text{-}4]$$

where P_{mp} is the percentage of ponded area (0-1). In the Ellesmere Island study, the surface melt albedo ranged from 0.49 (0% ponds) to 0.19 (100% ponds). Unfortunately the studies provide little quantitative information regarding the physical characteristics of the snow, ice and melt ponds.

3.2.2 Spectral Albedo Measurements

Although previous studies had considered the spectral characteristics of sea ice albedo (Thomas, 1963), the first extensive examination of the spectral characteristics of sea ice

albedo occurred over first-year fast ice (Point Barrow) and multiyear ice (Beaufort Sea: 84°N, 77°W) (Grenfell and Maykut, 1977). Examining sea ice albedo in the 0.4-1.0 μm range, the study found that albedo was highest in the 0.4-0.6 μm range and decreased at longer wavelengths at a rate likely determined by the liquid water content of the near-surface layers. Albedos at 0.5 μm ranged from 0.25 (mature melt pond) to 0.93 (dense dry snow). Bare ice albedo appeared sensitive to the physical properties of the upper surface of the volume. Multiyear bare ice albedo at 0.4-0.6 μm was found to be largely due to a decomposed surface layer consisting of tiny air bubbles that scatter light efficiently. The study showed melt pond spectra to exhibit a maximum at 0.4-0.5 μm due to efficient scattering by the underlying pond bottom and a rapid decrease at longer wavelengths, caused mainly by the absorption of incident radiation by the pond water.

Grenfell and Perovich (1984) performed a more extensive spectral albedo experiment in the fast ice off of Point Barrow, Alaska between mid-May and mid-June. Using a custom-built spectrometer with a spectral range of 0.4-2.4 μm, first-year and second-year sea ice were sampled under diffuse irradiance conditions. Of specific interest here is the temporal evolution of sea ice albedo with the onset of melt conditions. Overall, the albedo was found to decrease at all measured wavelengths with the spring melt. The spectral albedo of snow-covered sea ice appeared to be similar to that over terrestrial snow surfaces when the pack was optically thick or semi-infinite. As the snow aged, the investigation found that spectral albedo decreased at both the visible and infrared wavelengths. The rounding of ice grains and increases in grain size reduce the scattering efficiency of the volume. The largest changes were found in the infrared region where ice and water is moderately absorptive. Larger grain sizes and liquid water in the snow volume absorb more infrared radiation, thus lowering the albedo. The removal of the snowcover left a drained, white layer that scattered efficiently, thus maintaining an albedo just lower than the previous snowcover. The albedo of surfaces where melt ponds occurred were similar to those of the Grenfell and Maykut (1977) investigation.

Schlosser (1988) examined the spectral albedo of Antarctic sea ice under diffuse irradiance conditions using a coarse resolution spectrometer (0.05 μm) capable of sampling from 0.4-1.3 μm. Of interest is her measurements over thin ice types. As the ice thickens, the albedo was found to increase at all wavelengths. Largest increases were found in the visible spectral range. Schlosser also examined the monochromatic bidirectional reflectance of thin ice using a photometer and laboratory-grown sea ice. The study found that very thin ice (depth=6 mm) the reflectance is highly anisotropic (directional) in the forward direction and this anisotropy decreases with ice thickness. This decrease is likely due to the increased volume scattering within the ice due to increased grain sizes.

Perovich (1991) also examined the spectral albedo of thin sea ice as part of the Coordinated Eastern Arctic Experiment (CEAREX). The drift experiment began at 82°41' N, 32°32' E and took place between September through November, 1988. Using a SE-590 spectrometer (usable spectral range=0.4-1.0 μm), Perovich sampled 40 sites that represented new lead ice, second-year ice and multiyear ice. The study was enhanced by the collection of ice cores to aid in the interpretation of the collected spectra. Like Schlosser (1988), the study found the largest changes in albedo were found in leads where new ice was forming. The 0.4-0.7 μm surface albedo increased steadily from 0.1 (wind-roughened open water) to 0.38 (bare new ice, 20 cm thick). A 4 cm snowcover increased the albedo sharply to approximately 0.86. A limited set of bidirectional surface measurements were performed over a refrozen melt pond and a bare, new ice surface 20 cm thick. At detector zenith angles from 0°-60° the reflectance of both surfaces were fairly constant. Due to the specular reflection from the pond's smooth surface, reflectances increased sharply over the melt pond when the detector's relative azimuth was 0°, looking directly at the sun.

Perovich (1994) continued his examination of sea ice reflectance with a study outside Resolute, N.W.T. on snow-covered first-year fast ice during the onset of melt conditions. Added to this study was an examination of the polarization of reflected light. Albedo was found to decrease at all wavelengths with the onset of spring melt. The largest changes

were found at longer wavelengths where the albedo is most sensitive to the conditions of the near-surface layers of the volume. Using a 1° field-of-view, Perovich examined the anisotropy of the reflected radiation from the following ice surfaces: snow, glazed snow, bare ice, blue ice, and frozen melt pond.

3.3 Sea Ice Albedo Measurements During SIMMS

Probably the most limiting aspect of the sea ice observations described in the previous section is the absence of physical information regarding the conditions of the sea ice volume during measurement and the briefness of the observation period. In order to better understand sea ice albedo, it is necessary to identify how the physical characteristics of the sea ice volume changes on a seasonal basis and how these changes affect and are affected by surface albedo. This requires consistent measurements made over a relatively long period. The establishment of the annual Sea Ice Monitoring and Modelling Site (SIMMS) experiment in the Canadian Arctic Archipelago provided an opportunity to regularly measure sea ice albedo throughout the spring transition period (LeDrew and Barber, 1994). The location of the experiment afforded access to both fast first-year and multiyear ice covers. This section describes the collection, processing and analysis of surface albedo data collected during SIMMS. Using primarily surface data collected in the spring of 1993, the evolution of both first-year and multiyear icescape and the subsequent effects on surface albedo are described and examined. The following discussion expands on the investigation of De Abreu *et al.* (1994).

3.3.1 An Overview of the 1993 SIMMS Experiment

Before examining the measurement of albedo during SIMMS, it is useful to both summarize the project's scientific objectives and to describe the physical setting of the field program. The SIMMS project is a multiyear, multi-disciplinary field experiment with four major research themes (Misurak *et al.*, 1993):

- sea ice microclimate,
- numerical modelling of atmospheric processes,
- remote sensing of snow-covered sea ice, and
- ecosystem studies.

The measurement of sea ice albedo is considered important to all four themes. The SIMMS experiment was first staged in the spring of 1990 and continued on an annual basis up to 1995. The relative location of the SIMMS '93 study site and the experiment region is shown in Figure 3.8. An extensive overview of the 1993 experiment and the datasets collected can be found in Misurak *et.al.*(1993).

3.3.1.1 Climate Conditions of SIMMS '93 Experiment Area

The climate of the eastern portion of the Arctic Archipelago is controlled primarily by the solar radiation regime and the characteristics of surrounding synoptic systems. After April 28, twenty-four hours of daylight was available in the region. The mean and maximum incident solar irradiance measured at Atmosphere Environment Service's (AES) weather station Resolute is shown in Figure 3.9. As the season progresses, daily insolation increases until the June solstice. Values then begin to decrease. The noise in the radiation signal is due to the presence of cloud cover. Cloud cover increases dramatically in much of the arctic during spring. This is in contrast with the very clear skies experienced in the late winter and early spring. The appearance of cloud cover in the May and June months mark the waning influence of the cold, dry high pressure Arctic system that controls conditions for much of the polar year. Instead, the persistent low pressure maritime Atlantic system located over Baffin Bay now begins to dominate the synoptic characteristics of the region (Maxwell, 1980). As a result, warmer moister air masses bring warmer temperatures, increased precipitation and increased cloud cover in the months of May and June. The area can also come under the influence of warmer air masses originating from more southerly latitudes. Figure 3.10 shows the daily mean air

Figure 3.8 Location of SIMMS experiment region

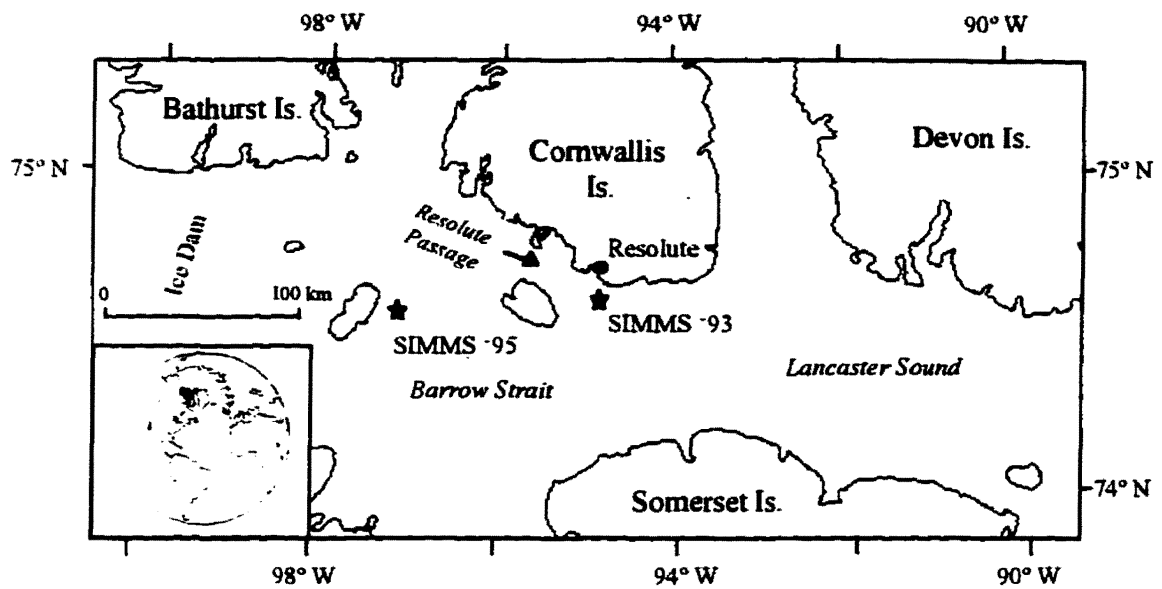
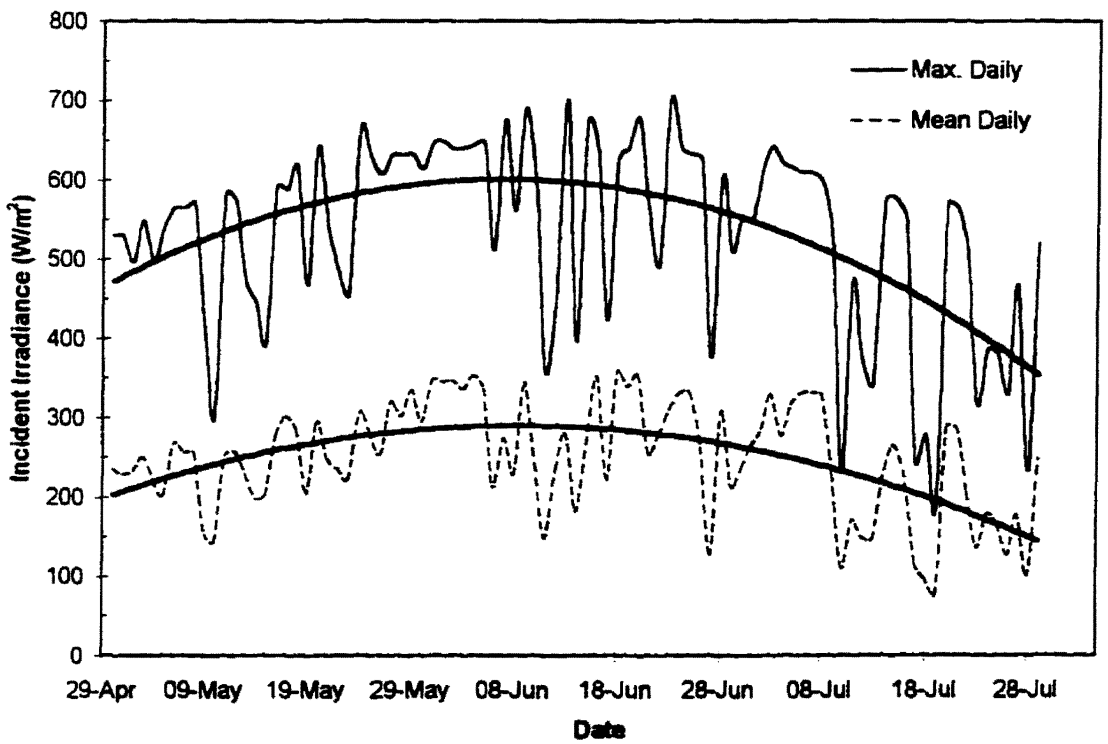
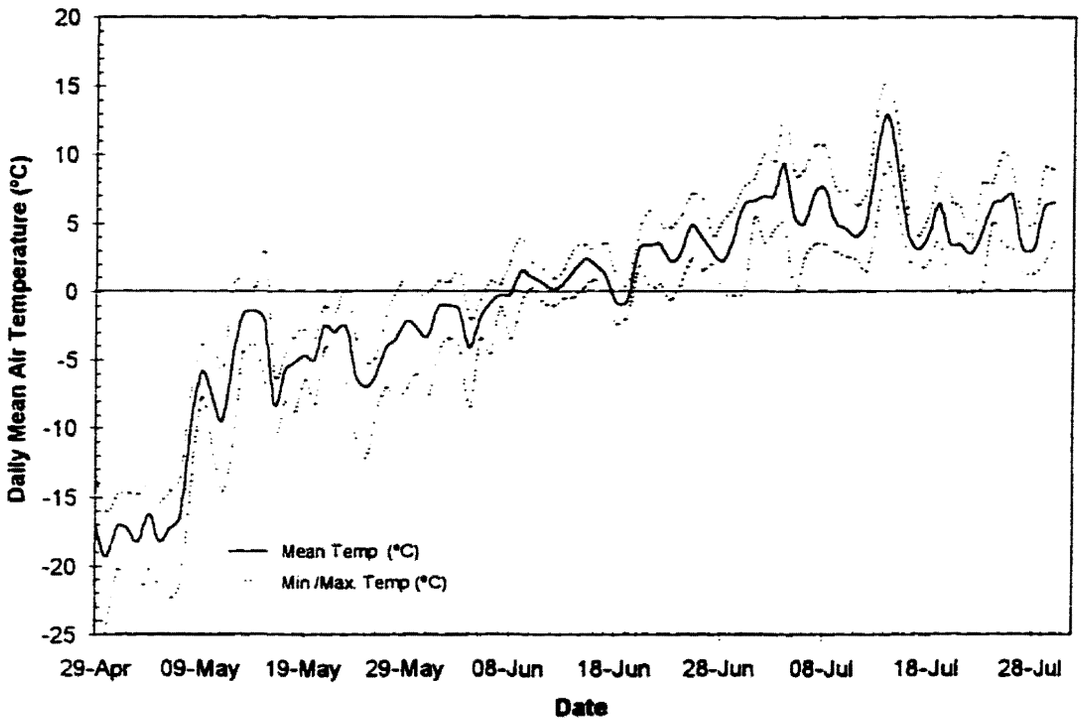


Figure 3.9 Seasonal change in solar irradiance measured at AES Resolute over study period. Seasonal trend lines are polynomial fits.



temperature measured at the SIMMS '93 first-year ice site. The seasonal increase in ambient temperature conditions is evident and its effect on the decay of the seasonal ice volume is paramount.

Figure 3.10 Daily mean air temperature during SIMMS '93.



3.3.1.2 Ice Conditions in the SIMMS '93 Experiment Area

Regional Ice Conditions

Each year the experiment has been situated in the Lancaster Sound/Barrow Strait region approximate to Resolute, N.W.T. This region is part of the Canadian Arctic Archipelago and for much of the year, it's waters are covered by a seasonal sea ice cover. The island system encourages the formation of a seasonal fast ice regime dominated by first-year ice.

Prevalent wind and ocean current patterns encourage the movement of ice from the Arctic Ocean, east through the arctic islands. Older multiyear ice types originating from the permanent ice pack in the Arctic Ocean move through the archipelago during the fall and occasionally are frozen fast within the region's first-year ice regime. The SIMMS experiment region is located in the middle of two different consolidation regimes: the Barrow Strait regime and the Lancaster Sound regime. The flow of ice through the Barrow Strait, Lancaster Sound route[5] is responsible for the largest influx of ice into northern Baffin Bay since it is open the longest and is the widest channel (Dey, 1981). This flow of ice is controlled by the annual formation of an ice dam in Barrow Strait south of Bathurst Island. The dam normally forms in December and breaks up in September. Thus there are only two to three months of unimpeded ice flow from the Arctic Ocean to Baffin Bay. After the formation of the dam, ice still forms east of the dam in Lancaster Sound and continues to move through the sound until freeze-up. Consolidation of this area can occur as late as early April. The eastern edge of the Barrow Strait ice dam is shown in Figure 3.8.

Local Ice Conditions

The SIMMS '93 experiment site was established on April 22 adjacent to a multiyear ice floe trapped in fast first-year ice at the eastern mouth of Resolute Passage (74.59° N / 94.71° W) (Figure 3.8). The site is located in the midst of an annual consolidation shear zone that separated two different consolidation regimes. To the west of the site, the ice in Resolute Passage often consolidates before January. In 1993, AES observations at the nearby Resolute weather station indicate that nearby Resolute Bay was completed covered with ice by October 14, 1992. On the east side of the ridge, the ice in eastern Barrow Strait consolidated substantially later in the year. ERS-1 imagery suggests that this regime was still unconsolidated at the end of February 1993. The consolidation zone consisted of very rough, pressure ridged ice caused by the movement ice along the consolidation boundary.

[5] This major Archipelago waterway is also known to as the Parry Channel

Local Physiographic Setting

The SIMMS experiment region is predominantly composed of first-year sea ice frozen fast against Cornwallis Is. and Griffith Is. (Figure 3.8). These land masses are largely unvegetated and consist of raised beach gravel and till. The passage side of Griffith Island is relatively steep with a maximum elevation of 625 ft. A.S.L.. The opposite side of the island gently slopes down to sea level. Across the passage, the shore of Cornwallis Is. is comprised off raised glacial beaches with some raised headlands. Unlike Griffith Is., the shore of Cornwallis Is. is marked with several bays. It is not uncommon for sea ice in these bays to survive a summers melt.

SIMMS experiments were timed to span much of the spring transition period when the ice surface transforms from a dry, snow-covered icescape to a flooded melt surface. In 1993, surface sampling began on April 22 and continued to June 22 resulting in eight weeks of surface observation. Figure 3.11 shows the dramatic changes in surface conditions that occurred over this sampling period at the FYI site. For much of the sampling period, changes occurred slowly within the sea ice volume. During this relatively stationary period, temperatures neared zero degrees and the ice surface resembled the conditions shown in Figure 3.11(a). As ambient temperatures neared zero, the ice volume began to change rapidly and ultimately resulted in the wet, heterogeneous surface shown in Figure 3.11(b).

The major objective of the surface sampling was to identify and quantify these changes over both first-year and multiyear ice types. To this purpose, intensive sampling sites were established on both first-year ice and multiyear ice within the rough shear zone. A Thematic Mapper (TM) image showing the location of the SIMMS '93 sampling sites is provided in Figure 3.12. The first-year ice (FYI) site was situated on flat, fast first-year ice with an ice thickness that ranged from 1.37-1.45 m over the experiment. Snow depths over the FYI site typically ranged from 10-15 cm (Misurak, 1993).

Figure 3.11 **Early spring (a) and late spring (b) FYI icescapes during SIMMS '93**

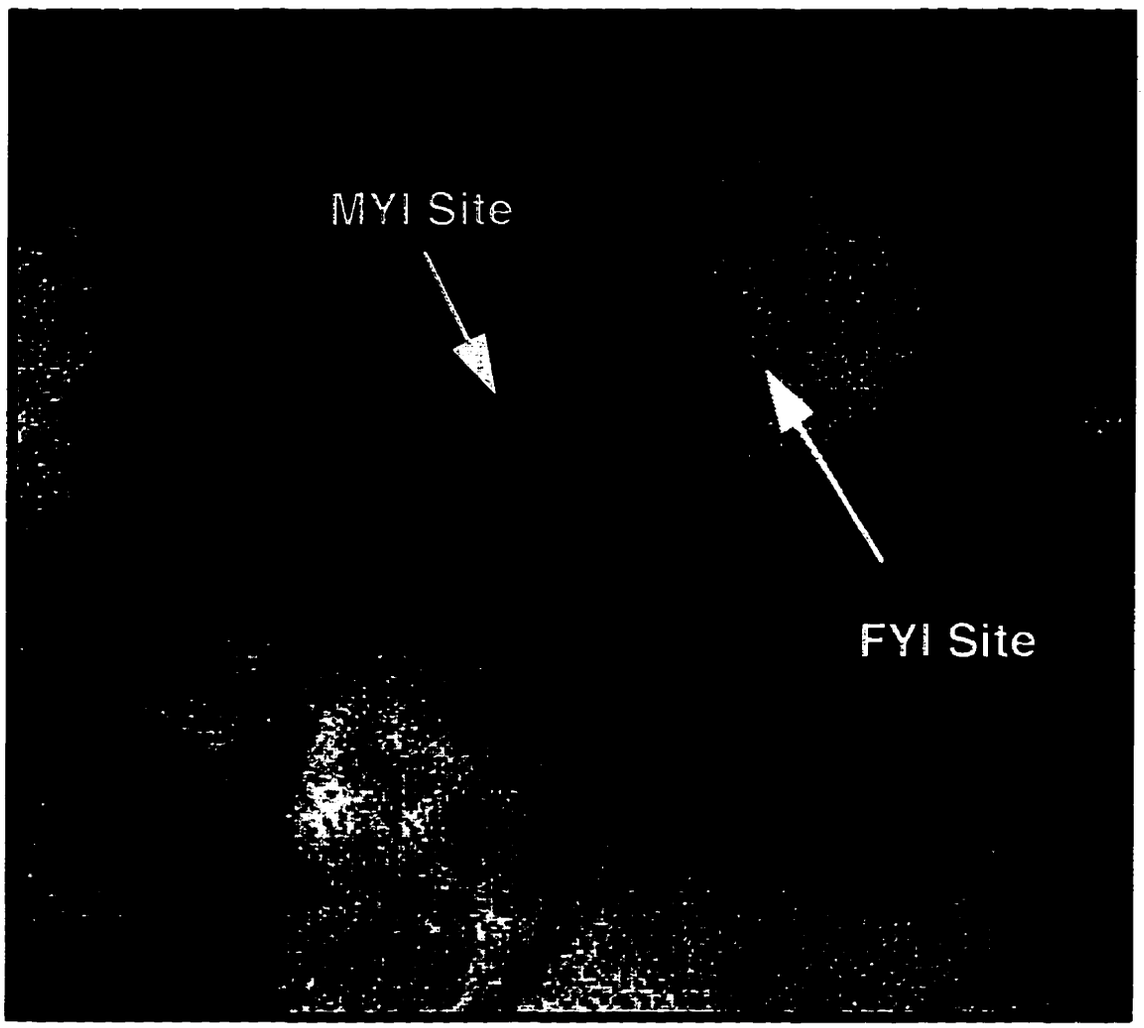
(a)



(b)



Figure 3.12 Location of SIMMS FYI and MYI site



TM Channel 4 June 4, 1993

A second site, the multiyear ice (MYI) site was located on an oval shaped multiyear ice floe approximately 2.5 km x 2.1 km in size. The hummocky topography of the floe was typical for a multiyear floe that appeared to be 4-5 years old. Ice thicknesses measured in melt pond areas ranged from 2.4-3.2 m, while those measured in hummock areas 4.1->5.9 m (Serreze *et al.*, 1993). Snow depths on the multiyear floe ranged from 0 cm on hummock tops to 88 cm in melt pond depressions.

3.3.1.3 Summary of SIMMS '93 Datasets and Sampling Strategy

In order to properly address the themes listed in Section 3.1, an extensive set of surface observations was collected during SIMMS experiments. Table 3.1 lists the snow, ice and microclimate variables measured and derived during SIMMS '93. Fully-equipped micrometeorological (micromet) towers were erected at both FYI and MYI sites and they operated into the third week of June when ice conditions forced their dismantling. Adjacent to each site's micromet towers, intensive snow volume observations were made in an area known as the "Crystal Pit Area". In these areas, a snow pit was dug on every third day and intensive snow pit profiles were performed. Snow grain structure through these profiles was recorded using 35 mm photography at the site. Prior to excavation of the snow pit, spectral albedo data were collected. In order to supplement these detailed yet spatially conservative measurements, large sampling grids were set up at each site where allwave albedo measurements (250 m transects) and less detailed snow pit measurements (300 m x 300 m grid) were performed. Further information on these measurements are available in Misurak (1993) and Serreze *et al.* (1993) respectively. Other surface measurements were made in support of various projects. These will be discussed where applicable to the goals of this investigation.

Table 3.1 Surface dataset collected during SIMMS '93

Component	Measured and Derived Variables
Snow Volume	depth density liquid water volume grain microstructure snow temperature profile transmissivity
Ice Volume	depth salinity temperature (incl. ocean) density dielectric constant microstructure surface roughness
Micro-climate	air temperature humidity wind velocity and direction incident and reflected short-wave radiation broadband albedo net radiation incident and reflected longwave radiation incident spectral irradiance spectral albedo cloud type, cover cloud base heights atmospheric soundings aerosol optical depth

One of the major objectives of SIMMS is the development of methodologies whereby remotely sensed data can be used to map environmentally significant variables in the arctic. To this purpose, both airborne and orbital remote sensing data were collected during

SIMMS '93. Table 3.2 identifies the various remote sensing datasets. These will be discussed in more detail in Chapter 4 and 5.

Table 3.2 Remote sensing datasets collected during SIMMS '93

Platform	Sensor	Type	Image Resolution*
Airborne	35 mm balloon photography	visible / infrared	< 1 m
	CV580 C/X band SAR	active imaging radar	6 m
Orbital	ERS-1	active imaging radar	25-30 m
	AVHRR 11, 12	visible / infrared / thermal	1.1 km
	Landsat TM	visible /infrared /thermal	30 m
	SSM/I	passive microwave	13 km

*Nominal resolution

3.3.2 Albedo Measurement Objectives

The objectives behind the measurement of sea ice spectral albedo during SIMMS '93 can be summarized as:

(1) characterize sea ice spectral albedo over first-year and multiyear ice surfaces during the spring transition,
(2) relate these characteristics to the physical condition of the ice volume(s), and
(3) provide *in situ* measurements for the interpretation of remotely sensed data.

Given these objectives, spectral albedo measurements were incorporated in the intensive sampling program. The linking of these measurements with the intensive snow pit

observations at the crystal pit sites was designed to address objectives 1 and 2 and was given measurement priority in the field. When conditions allowed, objective 3 was addressed through transect sampling. It should be noted that allwave albedo measurements were collected from the micromet towers for the duration of the experiment.

3.3.3 Instrumentation

Surface spectral albedo measurements were made in SIMMS '92-95 with an Analytical Systems Devices (ASD) Personal Spectrometer II radiometer. The instrument collects light from an external source through a fibre optics bundle. The captured light strikes a holographic grating which diffracts the incident light into its respective wavelengths and directs the light onto a silicon photo diode array detector. The silicon detector records light in the wavelength range 0.34-1.06 μm and stores it in 512 data elements with 12 bit precision (4096 counts). This results in a sampling interval of approximately 0.0014 μm. The radiometer has a mechanical shutter that allows for the measurement and later removal of dark current[6]. The exposure time of the array is controlled by a user-specified integration time. The radiometer is powered by one 9.6V battery. The radiometer's hardware interface is a IBM-XT compatible palmtop computer which sits on top of the radiometer. The computer is powered by two AA batteries. Its liquid crystal display provides real time display of signal spectra. Data are saved to one of two 1 megabyte PCMCIA flash memory cards. Each recorded spectra is saved as binary data file approximately 1500 bytes in size. The instrument supports the following field of views: 1°, 5°, 10°, 18° and 22°. A remote cosine receptor (RCR) provides the instrument with a hemispherical 180° view. The radiometer was quite portable (<10 lbs.) and performed well given the harsh environmental conditions. Appendix 2 shows a typical instrument setup during measurement.

[6] Dark current refers to the electrical charge that builds up on the device array. Since it is considered additive noise, it is usually removed from the measured current, leaving only the desired signal current.

It should be noted that the instruments response range, 0.34-1.06 μm, is only capable of measuring the visible and near-infrared surface albedo. Previous modelling and observational studies have shown us that, while snow albedo rapidly decreases outside the range of this detector, the infrared region is particularly sensitive to the morphological characteristics of the volume's surface layers (Grenfell and Perovich, 1984). Unfortunately, due to the limits of the internal detector, this portion of the albedo spectrum could not be observed in the field.

3.3.4 Spectral Albedo Measurements

In 1993, spectral albedo measurements were made possible with the incorporation of the RCR. Unlike bidirectional reflectance measurements made with narrow fields-of-view, spectral albedo data is readily incorporated into climate studies. The measurement procedure for spectral albedo can be described as follows:

1. Mount radiometer head equipped with RCR to 1 m tripod extension arm. Position tripod adjacent to target, opposite solar plane. Swing extension arm out over target and adjust instrument height to 0.75 m.
2. Orient sensor head normal to sky ceiling.
3. Set radiometer integration time to maximize use of dynamic range while avoiding signal saturation and measure/remove dark current signal.
4. Save scan of incident irradiance (E_λ).
5. Invert RCR, position normal to target surface and immediately take scan of reflected irradiance (M_λ).

Ten measurements of incident and reflected irradiance were taken in the crystal pit area and averaged. Each crystal pit was sampled every third day at solar noon. After measurement, the surface's spectral albedo (α_λ) was calculated as:

$$\alpha_\lambda = \frac{M_\lambda}{E_\lambda} \qquad [3\text{-}5]$$

Given the setup configuration, ninety percent of the reflected signal is from a surface area approximately equivalent to a circle with a diameter of 4.5 m.

3.3.5 Potential Error Sources

Several potential sources of uncertainty can be identified in the spectral albedo measurements:

(1) instrument calibration and signal-noise-ratio (*snr*),

(2) response of cosine receptor,

(3) instability of irradiance conditions, and

(4) field of view contamination.

Collecting spectral albedo data in polar regions requires special attention to these error sources. Overall, the measured albedo spectra presented here are considered accurate to 5% at visible wavelengths and 10% at infrared wavelengths. Probably the most serious source of error is the poor cosine response[7] of the remote cosine receptor (RCR). Most receptors perform acceptably for lower latitude measurements under low solar zenith angles. However, in polar regions, the high solar zenith angles require a receptor with very good cosine response. The following examines each of these potential sources of measurement uncertainty.

3.3.5.1 Instrument calibration and signal to noise ratio

Since albedo is a relative measurement, a calibrated instrument is not required. However, for absolute measurements such as incident irradiance or reflected radiance, a calibration is required to convert the instrument-measured voltages to absolute units. The radiometer

[7] A sensor with true cosine response weights incident radiance by the factor cos(source zenith angle) and integrates the resultant power over the upper hemisphere.

was calibrated before the 1993 field season by the manufacturer. The accuracy of the ASD radiometer is 1 nm at calibration temperatures (24°C) (precision 0.1 nm) and drops to 4 nm at temperatures between 0°C and 50°C. Since the instrument was often operated in the field at temperatures below 0°C, the accuracy is unknown, but conservatively estimated to be better than 10 nm (ASD Inc., personal communication). The sensor linearity is ±1% as measured by ASD Inc. As previously mentioned, dark current error was measured and subtracted before each spectra was saved.

The sensitivity of the silicon sensor in the ASD is reduced at infrared wavelengths. This loss in sensitivity, and the fact that the signal measured at these wavelengths is often low over sea ice surfaces, reduces the instrument's signal to noise ratio. This reduction manifests itself in the noise seen in the raw albedo spectrum shown in Figure 3.13. In order to reduce the effects of the noise, the data are truncated to 0.4-1.0 μm and smoothed using a robust, locally weighted regression technique - LOWESS. An example of the effects of the smoothing procedure is included in Figure 3.13.

3.3.5.2 Response of remote cosine receptor (RCR)

A significant source of error for albedo measurements recorded with the RCR is the collector's poor cosine response. Post field analysis revealed significant differences in the shape and magnitude of ice spectra taken under clear and diffuse sky conditions over identical targets. Under diffuse conditions, albedo spectra showed the proper wavelength dependence. However, clear-sky albedo spectra lacked the wavelength-dependent decrease expected at infrared wavelengths. Thus the ice spectra collected on clear days had a flatter appearance across the entire instrument range. The nature of this discrepancy pointed to an error in sensor response. Since the error only occurred under direct irradiance conditions, the cosine response of the RCR was identified as the likely source of error. Similar errors were alluded to by Grenfell and Perovich (1984) and corrected for in Seckmeyer and Bernhard (1993) and Grenfell *et al.* (1994). The construction and material of the RCR aperture can lead to significant wavelength-dependent departures from a true cosine response.

Figure 3.13 Raw vs. processed albedo spectra. Note: processed spectrum is offset for comparison.

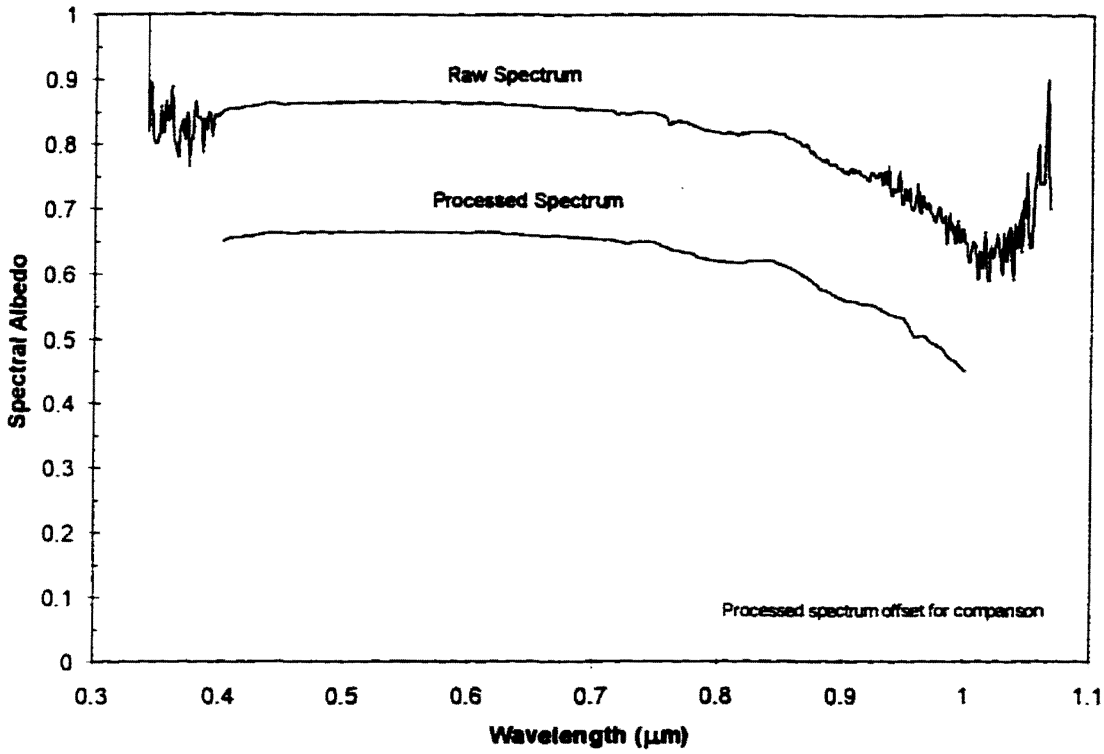
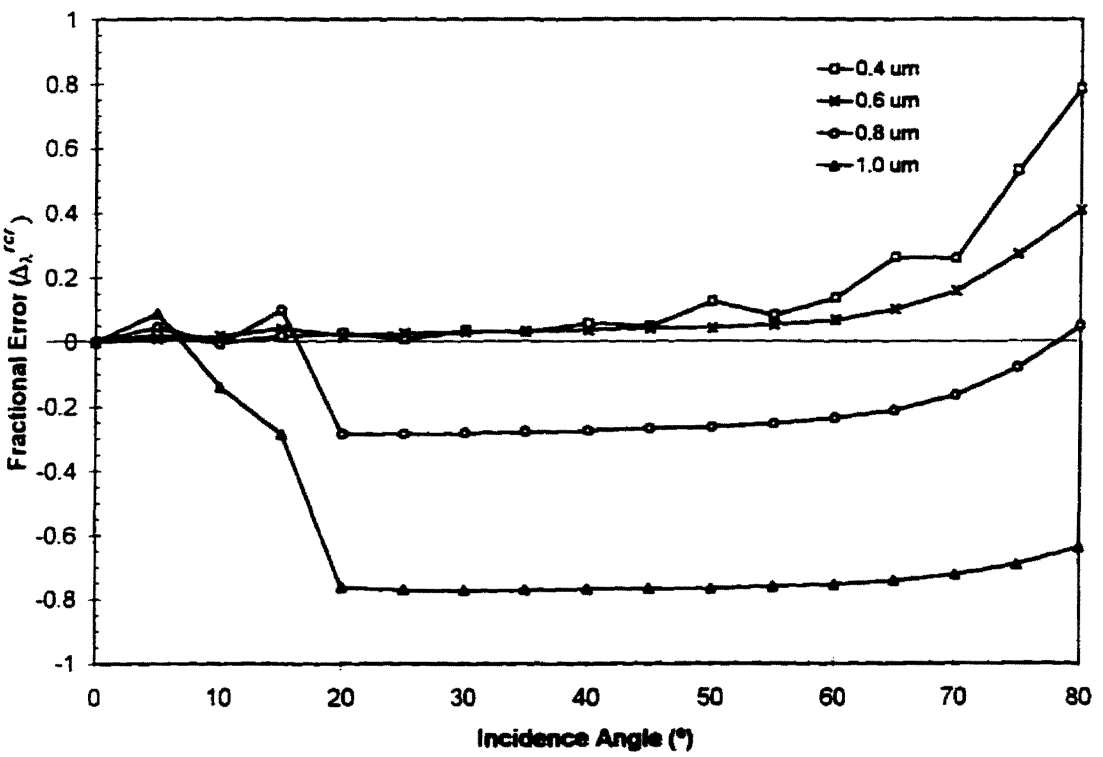


Figure 3.14 Fractional deviation in RCR cosine response



In view of this, the cosine response of the RCR was evaluated in a laboratory setting. A standard point source was used to illuminate the RCR and the incident angle of illumination was stepped at five degree increments from 5°- 90°. Deviation from a true cosine response (Δ_λ^{rcr}) as determined by comparing the measured signal of the instrument at a particular illumination angle ($S_\lambda(\theta)$) with the true cosine response expected at that angle, $\cos(\theta)\, S_\lambda(0°)$. A fractional deviation of cosine response was determined as follows:

$$\Delta_\lambda^{rcr} = \frac{S_\lambda(\theta) - \cos\theta(S_\lambda(0°))}{\cos\theta(S_\lambda(0°))} \qquad [3\text{-}6]$$

Figure 3.14 shows the fractional deviation for various wavelengths. The results show:

(1) the cosine response of the RCR degrades with an increasing incident illumination angle

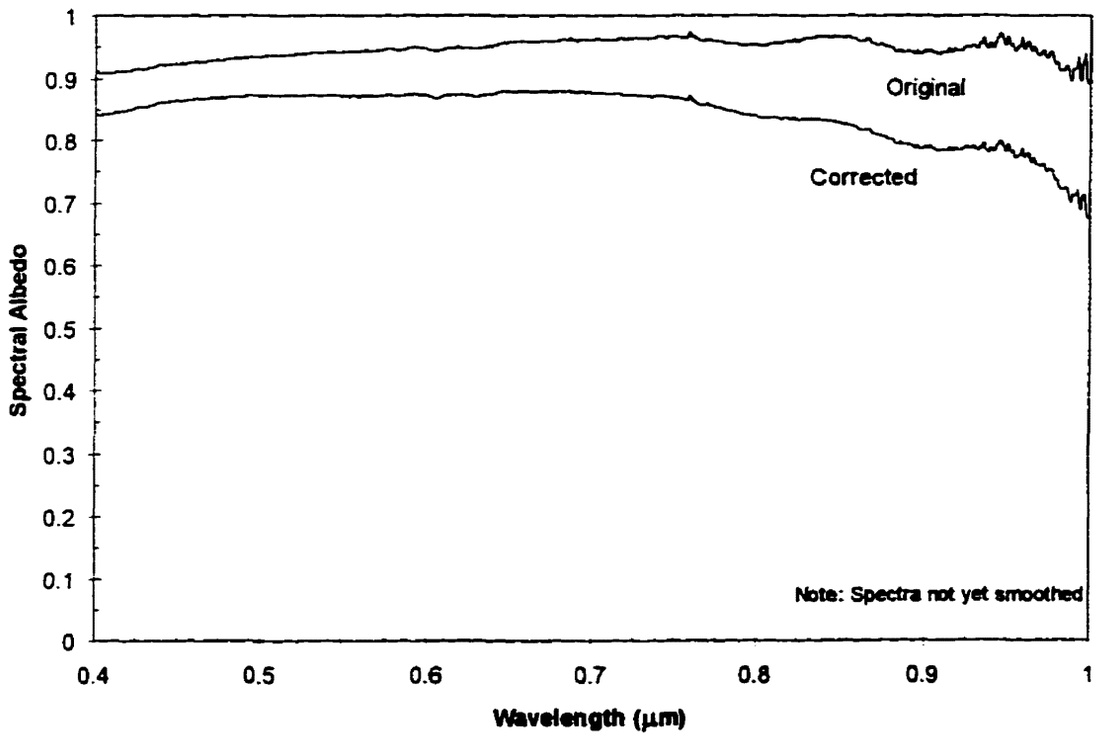
(2) the cosine response of the RCR degrades with increasing wavelength

At 0.4 μm and 0.6 μm, the cosine response of the instrument deviates slightly from a true cosine response. However at 0.8 and 1.0 μm, the RCR deviates significantly from a proper cosine response at larger illumination angles. In the range of incident angles measured in the field, 50°-60°, the cosine error is 12 % at 0.4 μm and at -25% at 0.8 μm. Grenfell and Perovich (1984) state that the cosine departure at infrared wavelengths may be due to the absorption characteristics of the plastic hemisphere diffuser. Overall, the response of the RCR was very poor. This has been acknowledged by the manufacturer and efforts are currently underway to design an RCR with proper cosine response. The steep dependence of the response error on illumination angle is of special concern for irradiance measurements made at the large solar zenith angles of the polar regions.

The most serious effect of this incorrect response on albedo measurements made in 1993 was a significant underestimation of the irradiance at infrared wavelengths under clear-sky conditions. This subsequently resulted in the flat spectral infrared albedo spectra noted

earlier. Cosine error correction of the clear-sky albedo data was performed using the lab-measured cosine response of the RCR and the correction procedure described in Seckmeyer and Bernhard (1993) and Grenfell *et al.* (1994). The correction procedure is described fully in Appendix 3. Assuming the direct and diffuse spectral irradiances at time of measurement is known, irradiances measured in the field can be corrected if the true cosine response of the RCR is determined. Figure 3.15 illustrates the effects of the RCR correction on the original spectra. The final overall correction ranges from a reduction in the original spectra of 6-25%. After correction, the albedo spectrum now shows proper wavelength dependence. Correction of this error severely restricted the albedo dataset in that only data collected under clear-sky conditions and/or totally overcast conditions could be utilized.

Figure 3.15 Effects of RCR calibration on field albedo spectra



3.3.5.3 Instability of irradiance conditions

Another source of uncertainty is the potential for irradiance conditions to change between the measurements of downwelling and upwelling irradiance. Depending on the type of change, this may lead to an underestimation or overestimation of surface albedo. The only way to avoid this possibility is to use two radiometers and measure the upwelling and downwelling flux simultaneously (Duggin, 1981; Milton, 1982). However, this is often not a feasible solution. In this study, a complete set of albedo measurements (upwelling and downwelling irradiance) usually required one minute after the instrument had been properly orientated and the radiometer had been adjusted. In order to minimize potential errors, albedo measurements were restricted to times when sky conditions were considered stable, i.e. clear skies or totally overcast, no solar disk. These requirements place severe restrictions on an albedo measurement program. However, given the sensitivity of albedo to irradiance conditions, it is a necessary precondition to measurement. It should be noted that even under apparently clear skies, irradiance conditions can fluctuate. In the arctic, the presence of high cirrus are especially difficult to detect visually, but do affect downwelling irradiance. Another step taken to minimize the effect of unstable irradiance conditions is the bracketing of the upwelling irradiance measurement with downwelling irradiance measurements. This allows one to ascertain whether downwelling irradiance conditions changed during measurement. If so, an average of the two irradiance measurements were used to calculate the albedo. Finally, since the ASD radiometer provided real time display of spectra, changing irradiance conditions often could be detected by observing the displayed irradiance spectra. Measurements were delayed until the displayed spectra appeared constant.

3.3.5.4 Field of view contamination

Kimes *et al.* (1983) point out that another potential source of error during field albedo measurements is the contamination of the incoming and reflected radiation field by nearby objects, such as the operator, vehicle and/or tripod. This interference can enhance the measured signal through reflection, or it can reduce the signal through shadowing. In

order to minimize these effects, instrument setup and operator position in relation to the sun was kept constant throughout the measurement season. This helped remove any random aspect of this error. Due to its large field of view, use of the cosine receptor required the instrument and operator to be as far removed from the site as possible. Fortunately, due to the 5 m length of the optical bundle, the operator and radiometer could be removed from the measurement area. When measuring incident irradiance, care was made to ensure that all objects were below the level of the RCR. As far as reflected irradiance, measurements in the field with and without a nearby operator (radiometer was controlled by a timer) showed a underestimation of albedo of approximately 1%. The shadowing effect of the tripod is estimated at 2% when the RCR is used. Under direct irradiance conditions (i.e. clear skies), the radiometer measurements were quite sensitive to leveling errors. Care was taken to ensure that the sensor head was normal to the target surface. Only flat target areas were selected and a leveling bubble on the sensor head was used to assist in the leveling.

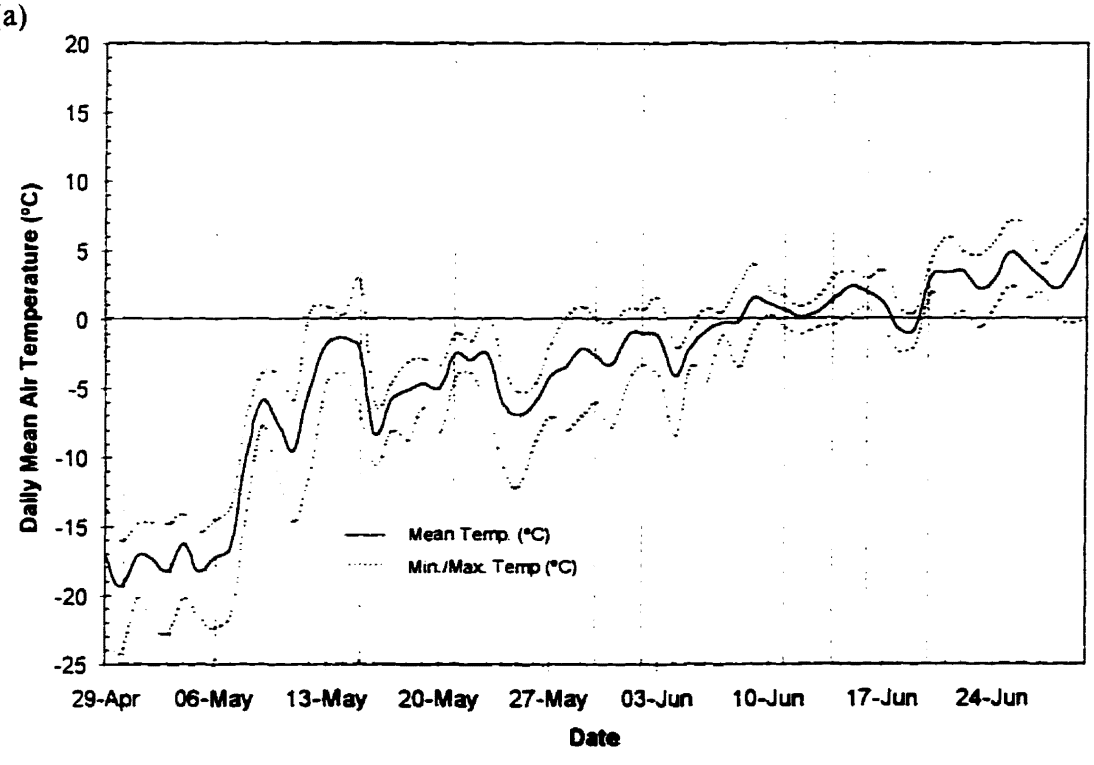
Of the various sources of uncertainty in the spectral albedo observations, the incorrect cosine response of the RCR under direct illumination is the most limiting factor in the utility of the seasonal dataset. Since there were no spectral measurements of diffuse radiation in 1993, there remained no method of correcting data that was collected under mixed irradiance conditions. Unfortunately, these data represented a large portion of the dataset. The data presented here are limited to those data collected under a clear sky (0/10 ths cloud) and cloudy sky (no solar disk visible, 10/10 ths cloud) conditions. These final sampled dates are shown for both ice types in Table 3.3 and Figure 3.16. Eleven sampling dates were available for the first-year ice site and seven dates for the multiyear ice site. While the first-year ice site is represented throughout the experiment period, a large gap between May 14 and June 4 exists for the multiyear ice site.

Table 3.3 Spectral albedo sampling dates

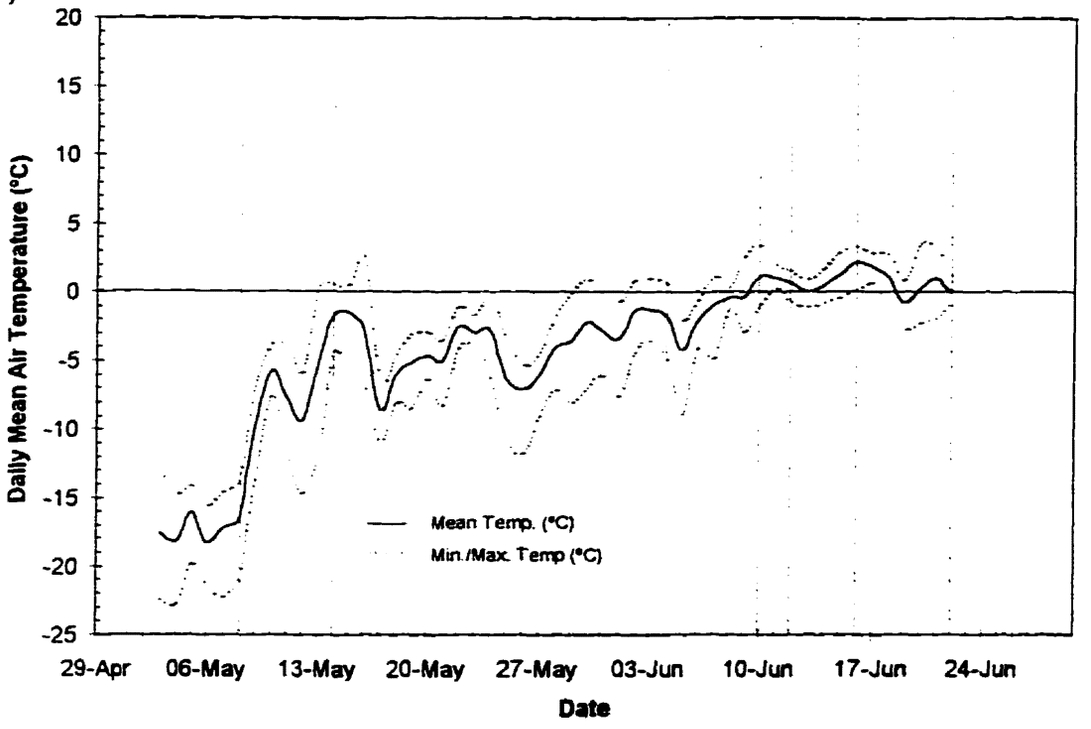
First Year Ice Site		Multi-year Ice Site	
April 30	May 3	May 8	May 14
May 6	May 15	June 4	June 10
May 21	May 30	June 12	June 16
June 2	June 11	June 22	
June 14	June 16		
June 20			

Figure 3.16 Sampling dates of (a) first year ice site and (b) multi-year ice site albedo data. Vertical lines identify sampled date. Daily mean air temperature (@ 5 m) over experiment period is included.

(a)



(b)



3.3.6 Ancillary Measurements

Subsequent to each albedo measurement, a detailed examination of the snow/ice volume was made via snow pit measurements. A snow pit consisted of a small rectangular excavation of approximately 0.5 m^2. Sampling was done at vertical intervals of 2 cm at the first-year ice site and 3 cm at the multiyear ice site on a shadowed pit wall. Snow wetness was measured using a capacitance plate (dielectric method). There was some question regarding the effect of snow salinity on snow capacitance measurements. While the wetness data appears correct, the accuracy or precision of this method has not been determined. Snow density was measured to ± 30 kg/m^3 using a gravimetric approach (Garrity and Burns, 1988) . *In situ* macrophotography was used to obtain snow grain photographs at each sampled depth. Snow grain size was determined automatically from the photos after digitization (Misurak, 1993). In this study, we consider the smallest disaggregated particle in the snowcover to be a snow grain. Snow grain radii in the crystal photos were determined by the following:

$$r = \frac{D_1 + D_2}{4} \qquad [3\text{-}7]$$

where D_1 and D_2 is the length of the major and minor axis of the grain respectively. Since snow grains were often aggregated when removed from the snowpack, the operator separated the crystals along visible grain boundaries for measurement. This likely introduced some subjective bias into the measurement. Unfortunately, crystal photography was stopped on June 7 due to the difficulty in keeping the samples from melting. Crude measurements of grain shape and diameter were continued by visual analysis of grain size and shape through the use of a magnifying glass and gridded paper. These measurements are considered accurate to ±500 μm. At time of measurement, solar zenith angles during the field season ranged from 50° to 60°. During SIMMS '93, daily average air temperatures ranged from -19 °C to 2 °C (Figure 3.16).

3.4 Seasonal Variation in the Visible and Near-infrared Albedo of Sea Ice.

The onset of melt conditions and the decay of the sea ice cover are accompanied by significant changes in the surface's spectral albedo. Since a multitude of factors control the evolution of the albedo of a particular ice surface, this section should not be considered definitive in terms of all sea ice types. For example, field observations have shown that the surface albedo of different parts of the same ice surface can be evolving at different stages due to slight differences in surface topography. Instead, by using the spectral albedo observations made during the SIMMS experiments, this section attempts to describe the principal stages in the transformation of sea ice visible and near-infrared albedo during the spring melt.

3.4.1 Assessment of Albedo Evolution With Time

The albedo dataset encompasses approximately the transition months of May and June. Figure 3.17 shows the spectral albedo of the FYI and MYI crystal pit snow/ice volumes for these dates. The seasonal transition in the magnitude and shape of the albedo spectra is evident. For comparison, the allwave albedo measured adjacent to the sampling area from 10 m high towers is shown in Figure 3.18. These data are not corrected for the shading effects of the tower or adjacent climate station infrastructure. As a result, the broadband albedos shown here are underestimated. The allwave albedo data follows the seasonal pattern of the visible and near-infrared albedo.

Since the focus of this investigation is on the visible (α_{vis}) and near-infrared albedo (α_{nir}) of sea ice, the albedo dataset is converted into broadband albedos by weighting the measured spectrum by the incident irradiance:

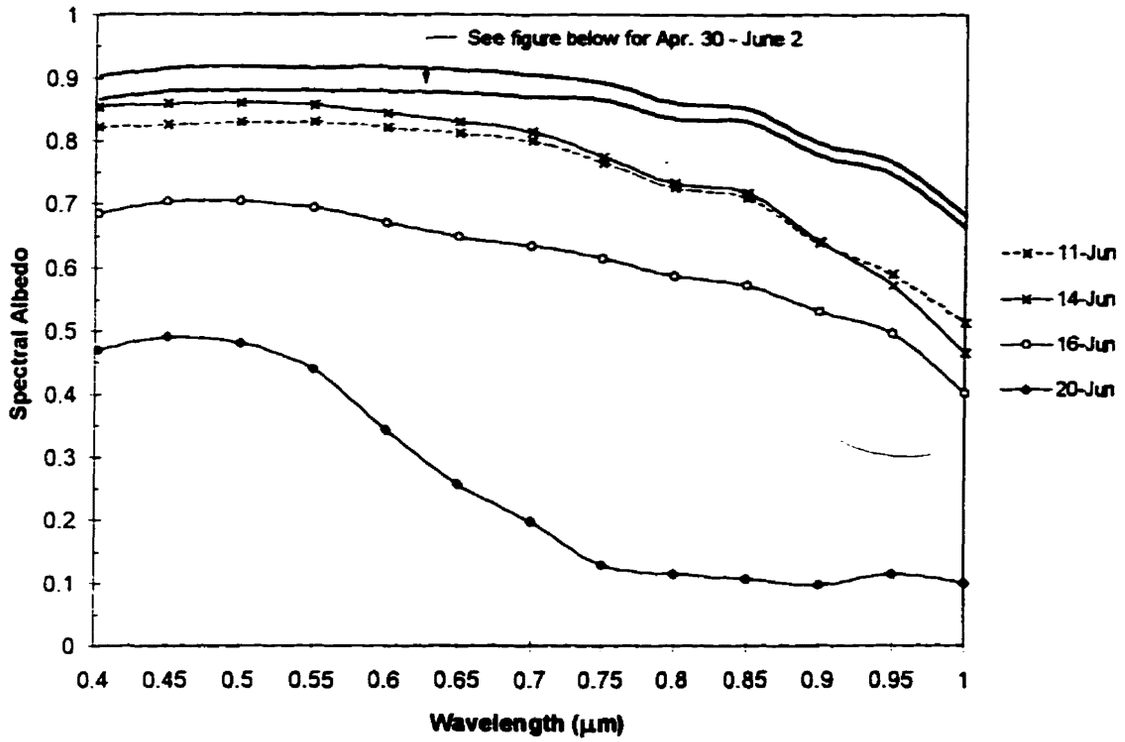
$$\alpha_{vis} = \frac{\int_{0.4}^{0.7} \alpha_\lambda E_\lambda d\lambda}{\int_{0.4}^{0.7} E_\lambda d\lambda} \qquad [3\text{-}8]$$

$$\alpha_{nir} = \frac{\int_{0.7}^{1.0} \alpha_\lambda E_\lambda d\lambda}{\int_{0.7}^{1.0} E_\lambda d\lambda} \qquad [3\text{-}9]$$

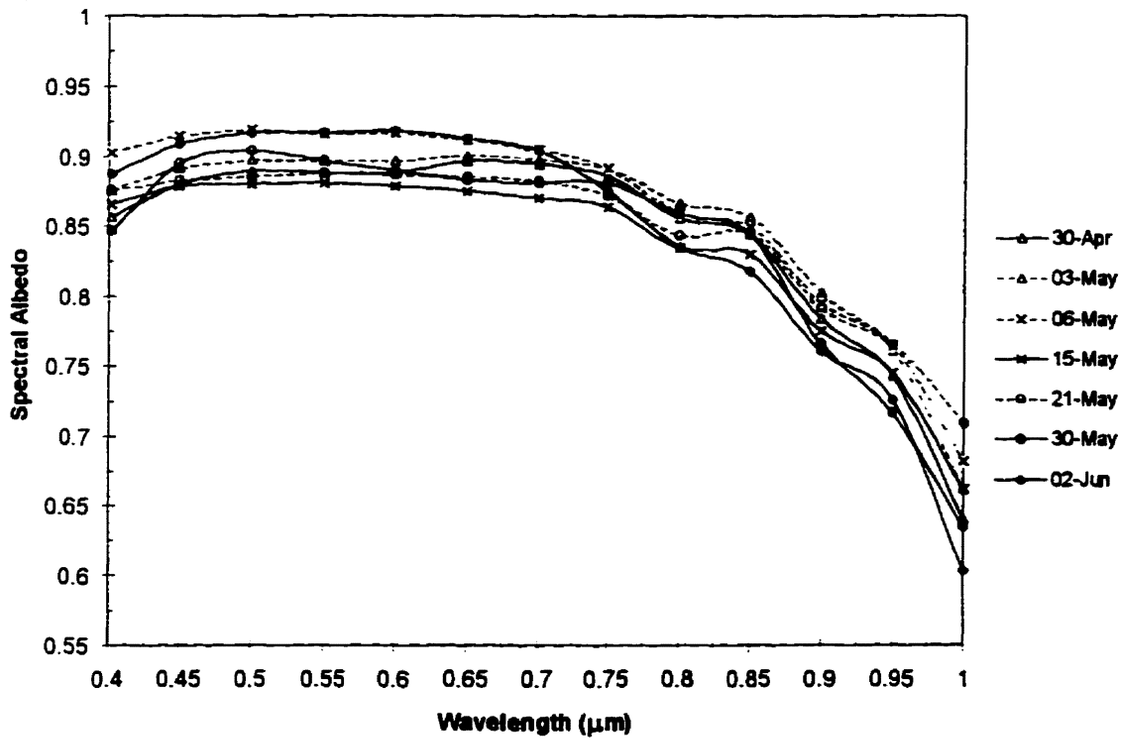
The resultant broadband albedos are shown in Figure 3.19 and Table 3.4 for each ice type. In order to aid in the description of the seasonal transition of albedo spectra, it is useful to identify those dates where spectra are similar and thus can be grouped together for examination. Upon examining Figure 3.19, dominant groupings of spectra are obvious for both first-year and multiyear ice sites.

Figure 3.17 Spectral albedo of (a) first year ice site and (b) multi-year ice site collected during SIMMS '93.

(a1)



(a2)



(b)

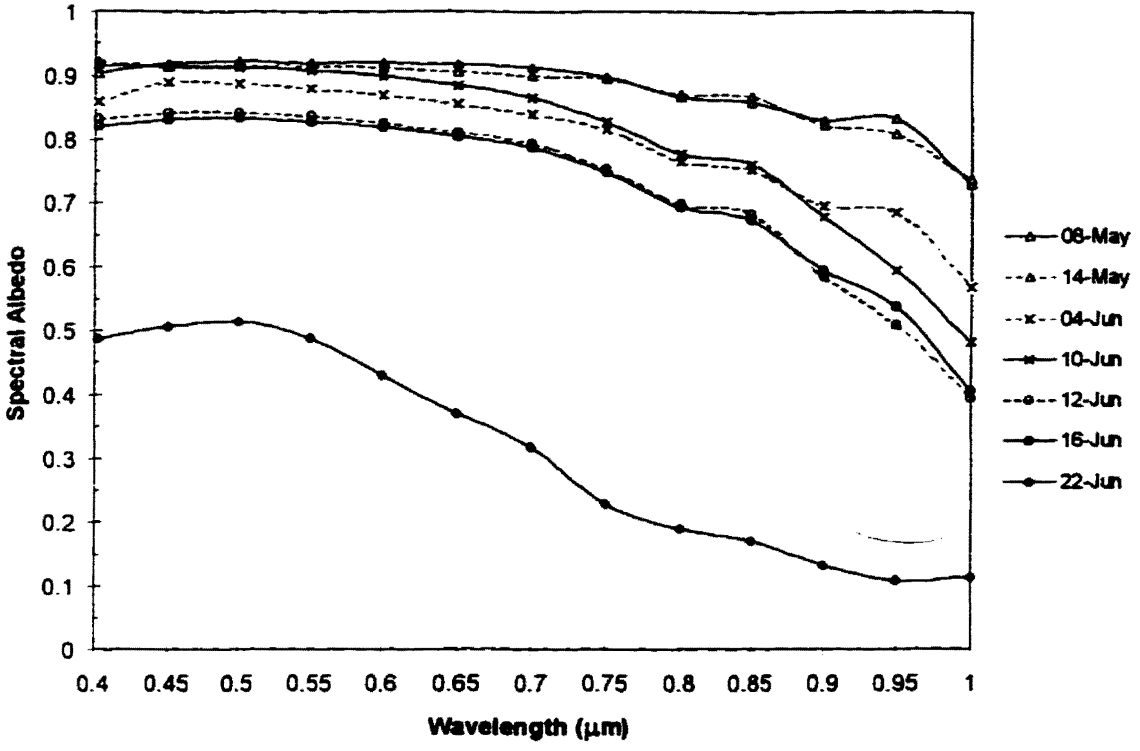


Figure 3.18 Seasonal change in allwave albedo observed at the first year ice and multi-year ice site.

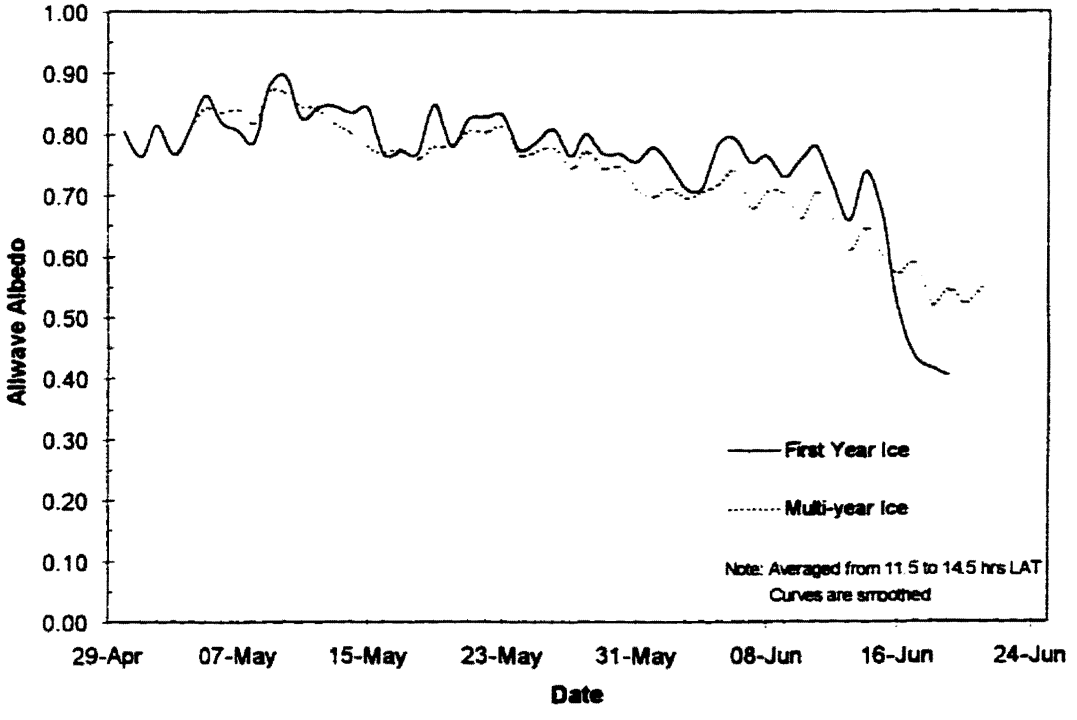
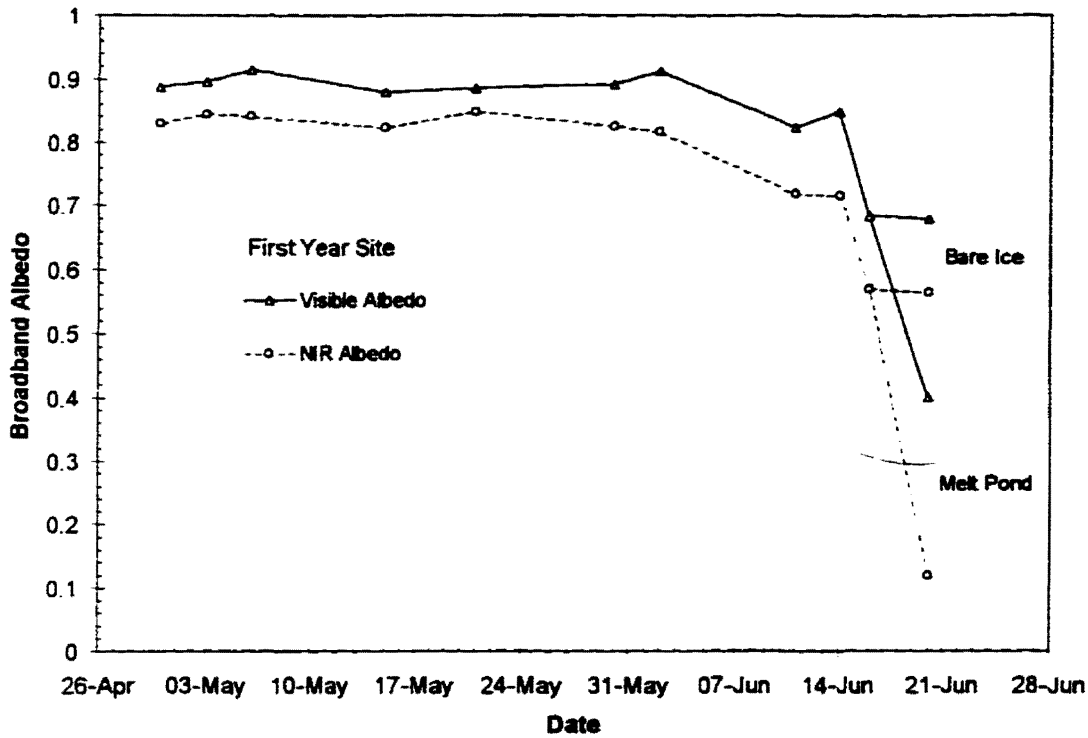


Figure 3.19 Seasonal change in visible and near-infrared broadband albedo observed at the (a) first year ice site and the (b) multi-year ice site.

(a)



(b)

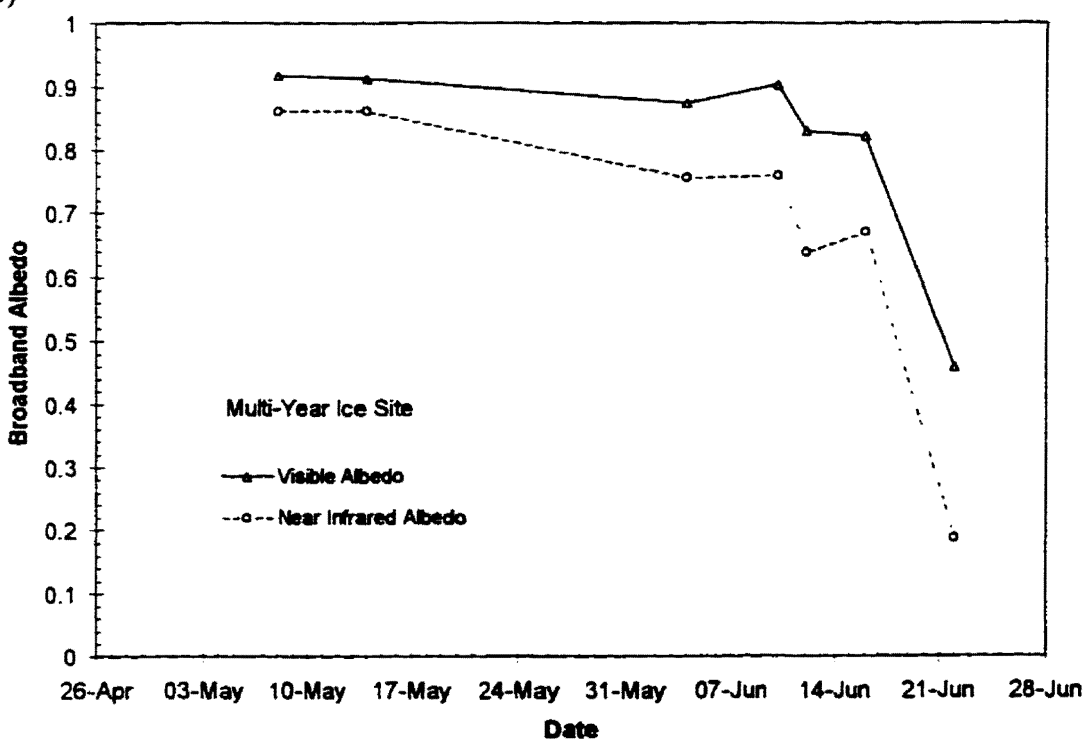


Table 3.4 Calculated broadband visible and near infrared albedo for (a) first year ice (b) multi-year ice. Albedo stages according to cluster analysis are grouped in boxes.

(a)

	First Year Ice	
Date	Visible α	Near Infrared α
Apr.30	0.887	0.829
May.3	0.895	0.843
May.6	0.914	0.841
May.15	0.878	0.824
May.21	0.885	0.849
May.30	0.891	0.827
Jun.2	0.912	0.817
Jun.11	0.823	0.718
Jun.14	0.849	0.716
Jun.16	0.683	0.569
Jun.20	0.400	0.120

(b)

	Multi-year Ice	
Date	Visible α	Near Infrared α
May.8	0.917	0.862
May.14	0.912	0.862
Jun.4	0.874	0.756
Jun.10	0.902	0.759
Jun.12	0.830	0.639
Jun.16	0.821	0.670
Jun.22	0.458	0.188

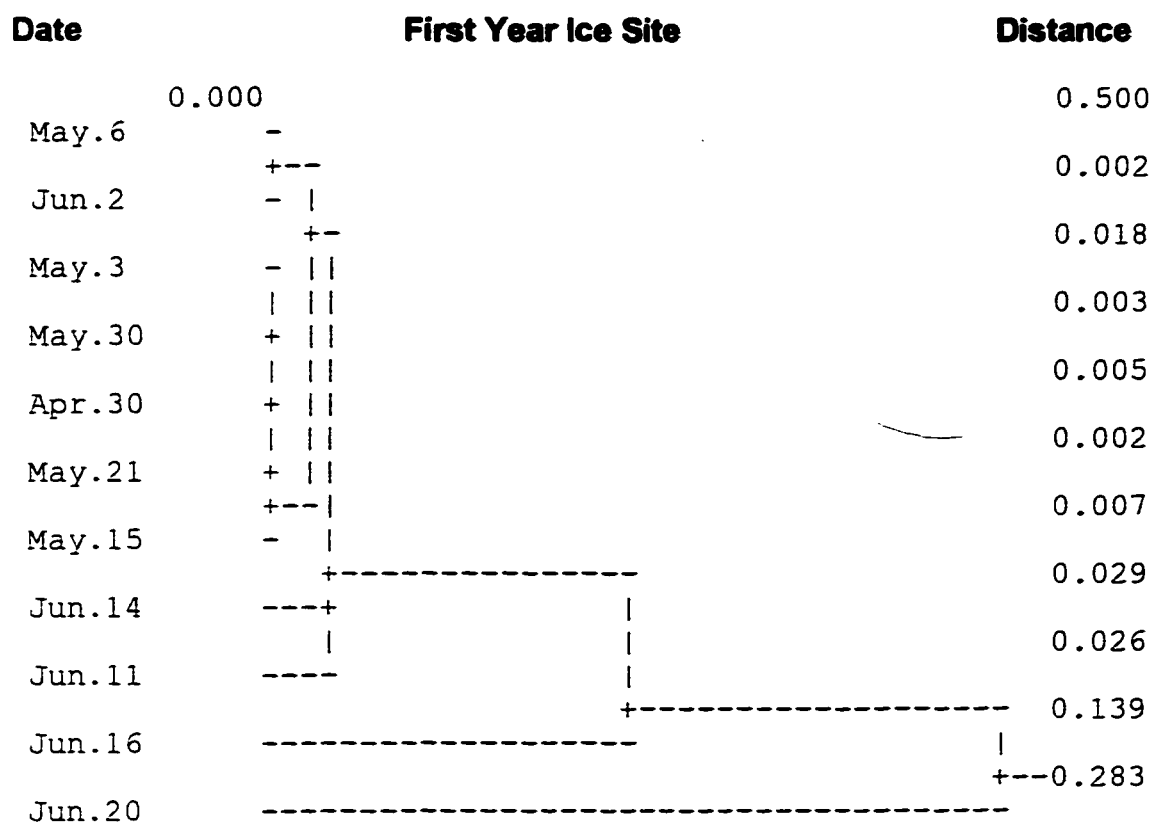
In order to assist in identifying these natural groups of data, cluster analysis is applied to the visible and infrared albedo for each ice type. A Euclidean distance metric is used to assess the similarity between dates. Using these distances, various methods were used to link the data into groups. Since all of these methods were found to result in comparable clusters, the data were finally grouped using the most intuitive approach -- the nearest neighbour (single linkage) method . Figure 3.20 contains dendrograms which show the results of the cluster analysis for both visible and near-infrared albedo. Dates with similar albedos are expected to cluster quickly and result in lower distances. Dissimilar spectra will cluster at larger distances. Since there are no robust, truly objective methods of determining the number of clusters (Everitt, 1980), the determination of cluster groups was based here on a subjective interpretation of the dendrograms. In the following discussion, the evolution of spectral albedo in 1993 will be examined within the context of these clusters.

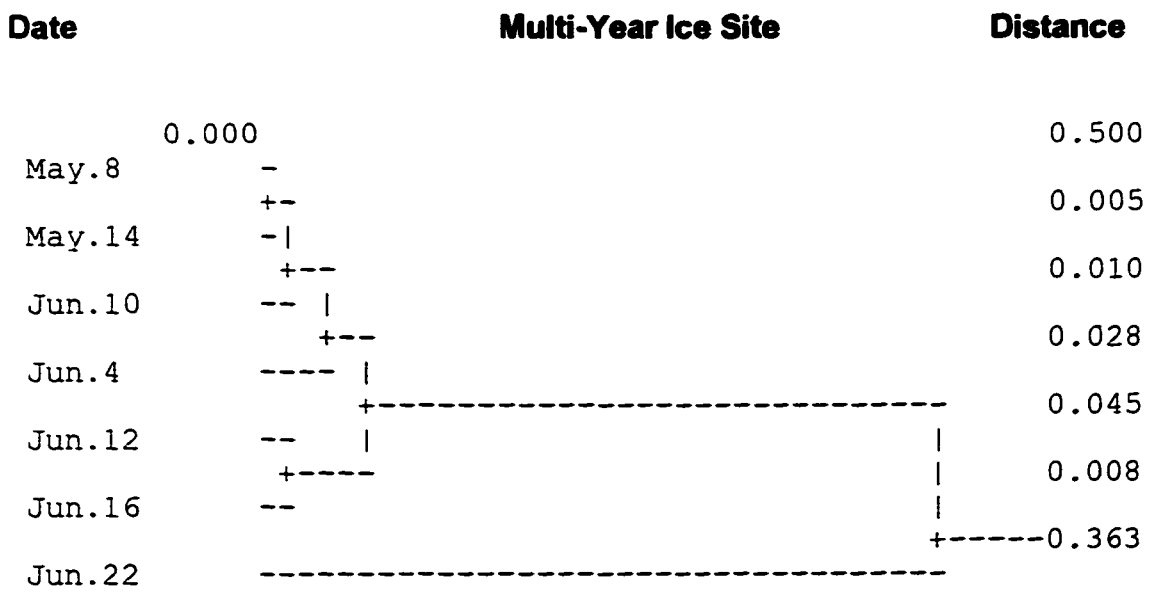
The albedo spectra were grouped into the clusters outlined in Table 3.4 and Figure 3.21. In terms of visible albedo on the first-year ice site, there appears to be three major groups -- April 30 to June 14, June 16 and June 20. The first large group represents the albedo of snow-covered sea ice. The second group, June 16, is the albedo of bare, white ice and the final group represents melt pond albedo. The first snow group can be divided into two sub-groups: April 30 to June 2 and June 11 to June 14. These represent early snow and late snow conditions respectively. Near-infrared albedo data collected at the first-year ice site cluster identically to the visible albedo if you include the two snow subgroups.

Unlike the first-year ice site, the visible albedo on the multiyear ice site separates into only three major clusters: May 8 to June 10, June 12 to June 16 and June 22. The white ice stage does not occur in multiyear ice melt pond areas. Based on the available data, this indicates that the albedo of multiyear ice melt pond area evolved through fewer stages than the first-year ice site over the sampled period. Like the first-year ice site, the first multiyear ice cluster represents snow-covered ice. In terms of visible albedo, this cluster represents the first four albedo dates.

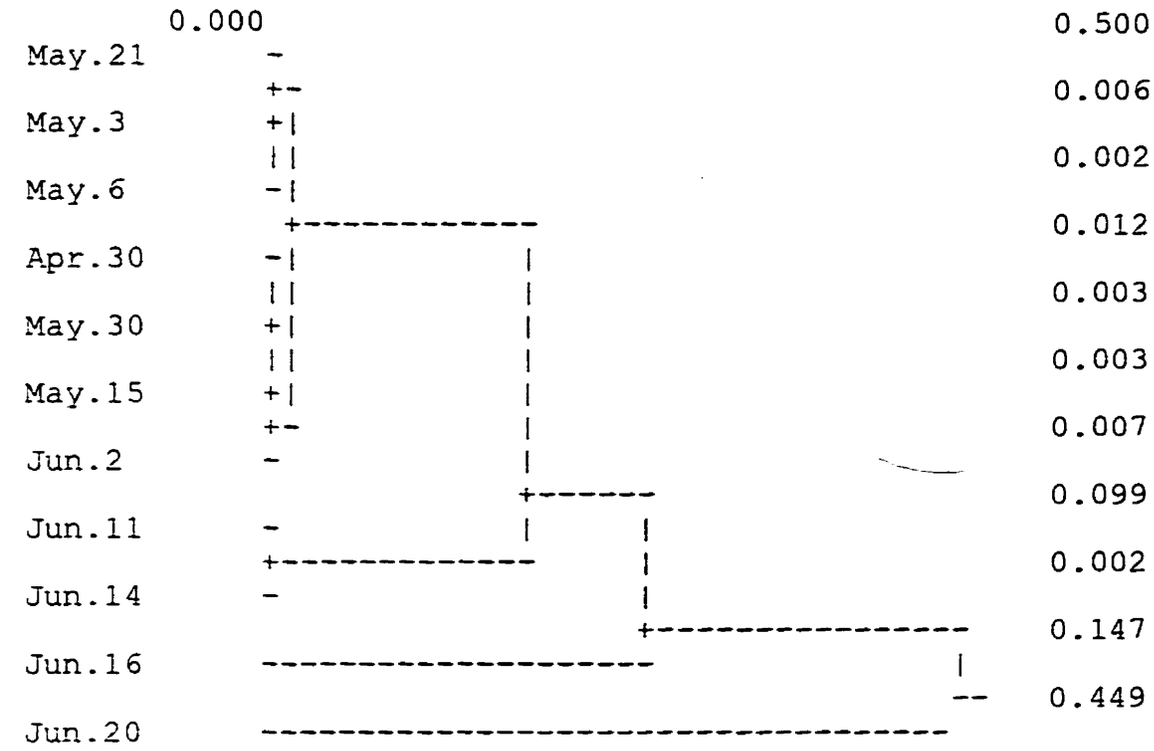
Figure 3.20 Dendrograms for (a) visible albedo and (b) near-infrared albedo. (Note: similiarity distances not drawn to scale)

(a) Visible albedo





(b) Near infrared albedo



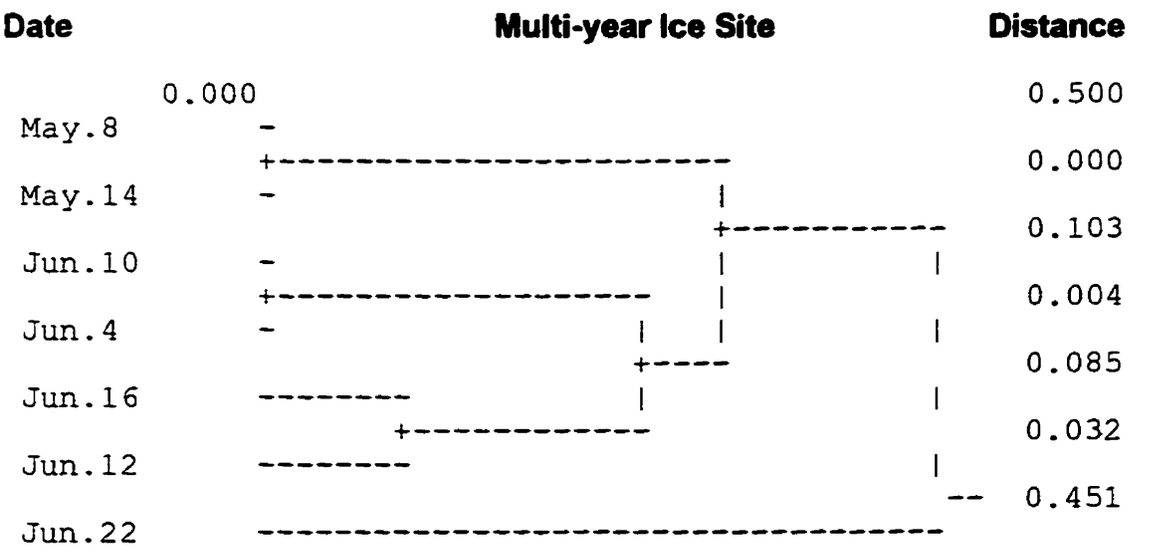
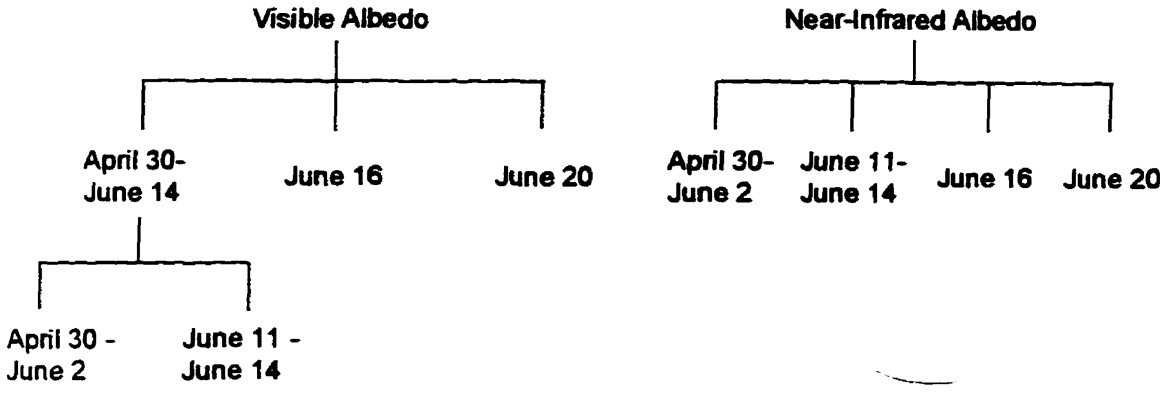
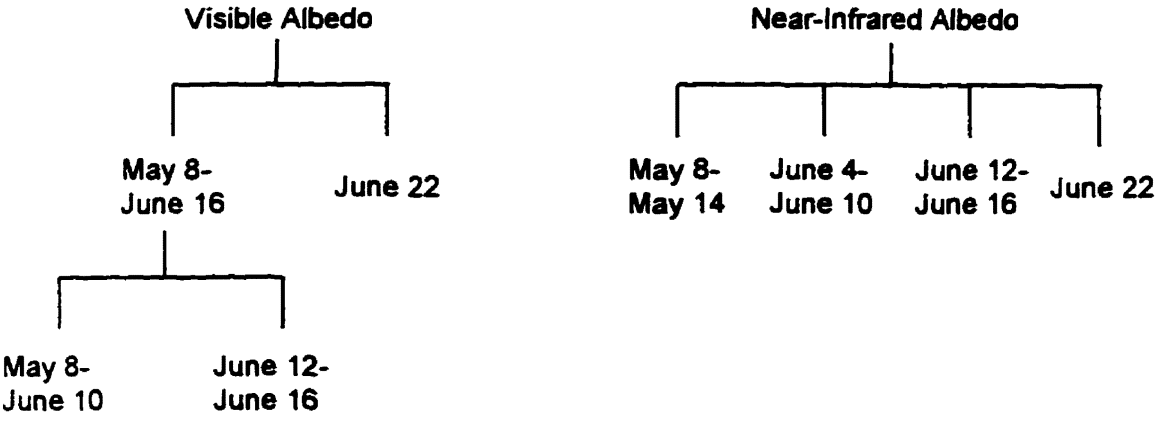


Figure 3.21 Visble and near infrared albedo groupings for (a) the first year ice site and (b) the multi-year ice site.

(a) First year ice site



(b) Multi-year ice site



However, this same period constitutes two distinct clusters for infrared albedo data. Like the first-year ice site, the late snow period June 12-June 16 represents another albedo stage for both visible and infrared data. The final distinct period is the melt pond data collected on June 22.

3.4.2 Spring Transformation of Visible and Near-Infrared Sea Ice Albedo

The results of the cluster analysis indicate that the seasonal transition of sea ice visible and near infrared albedo spectra can be divided into somewhat similar stages for both first-year and multiyear ice in 1993. For the purposes of discussion, the observed albedo for both first and multiyear ice types are divided into five major transition stages:

(1) Dry Snow - Cold
(2) Dry Snow - Warm
(3) Wet Snow
(4) White Ice
(5) Melt Ponds

As will be shown, all stages are not applicable to both ice types. In the following section, these stages will be defined and the characteristics of the volume's visible and near-infrared albedo will be described for each of these stages. Of specific interest is the relationship between measured albedo and the physical nature of the sea ice volume during each stage. It should be noted that the SIMMS surface observational record ends when the ice is flooded with melt water. Normally, melt water drains from the ice leaving a white, porous layer. While this stage should be considered a natural part of the late stage in albedo evolution, it is not included here due to lack of observational data. Figure 3.22 summarizes schematically the physical characteristics of the first-year ice and multiyear sea ice volume during each of the albedo stages. Included on the figure are the calculated visible and near-infrared albedo for each stage. The physical volume data presented Figure 3.22 represent conditions averaged over each of the stages. Again, these data were collected at the crystal pit, subsequent to each albedo measurement.

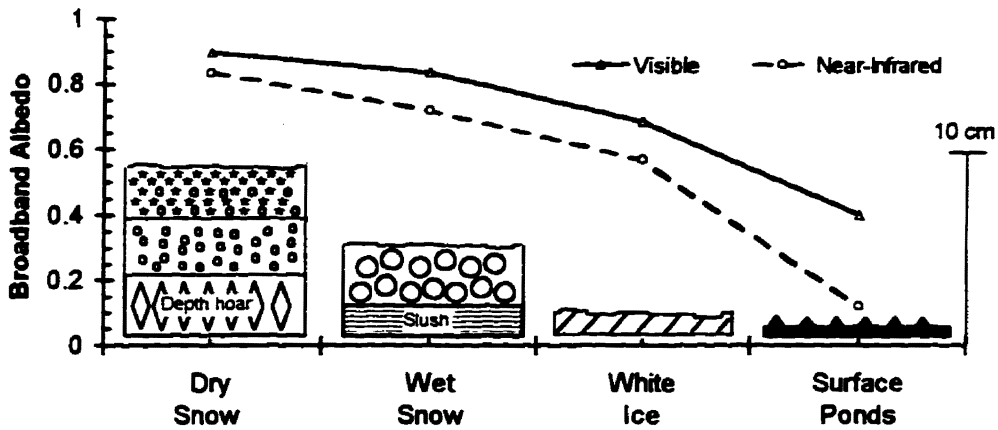
3.4.2.1 Dry Snow

The Dry Snow stage encompasses albedo data collected between April 30 and June 10. During this stage, the mean daily air temperate at both sites averaged -9 °C and for the

Figure 3.22 The seasonal tranformation of the sea ice snow volume and broadband albedo for (a) first year ice site and (b) multiyear ice site.

(a)

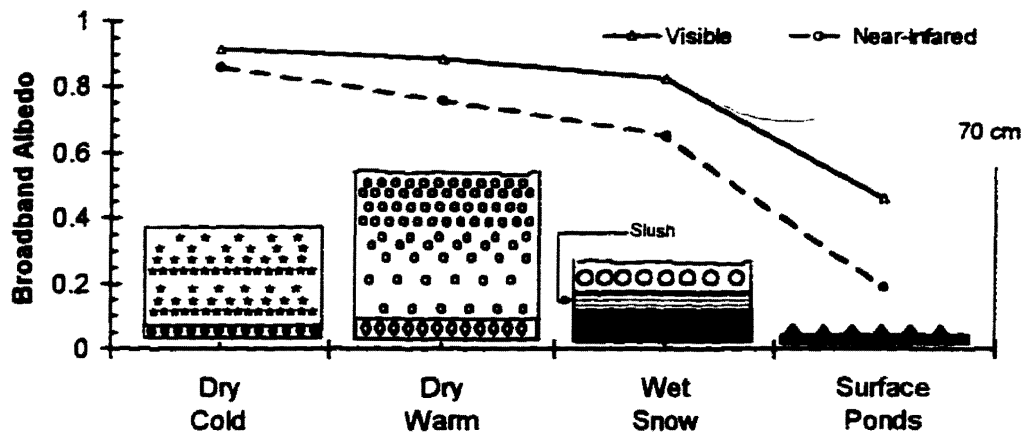
	Dry Snow	Wet Snow	White Ice	Melt Pond
Snow Depth (cm)	9.5	5	1.5	0***
Snow Density (kg/m^3) *	360(300)	380		
*Grain Size** (μm)	297(676))	2750	1500	
*Snow Wetness*** (% LBV)	2.7	5.6		
Air Temp. (°C)	- 9.0	1.1	2	3.25



* Upper layer / bulk volume
** Upper layer
*** 11 cm of water
LBV - Liquid water by volume

(b)

	Dry Snow I	Dry Snow II	Wet Snow	Melt Ponds
Snow Depth (cm)	37.5	68.5	10	0*
Snow Density (kg/m^3)	263(327)	373	383(452)	
*Grain Size** (μm)	237(500)	700	1500	
Snow Wetness (% LBV)	0.8	1.1	6.3	
Air Temp. (°C)	- 9.1	-0.26	1.42	1.03



* 15 cm of water

most part stayed well below zero degrees (Figure 3.16). Since the surface was covered by snow, the albedo at this stage is influenced by the optical characteristics of the overlying snowpack. The extent of this influence is largely dependent on the physical characteristics of the snow volume. In the Dry Snow stage, the volumes are in a predominantly pendular range, i.e. where the distribution of free water in the pack ranges from covering ice grains with a thin film of water to being held in the interstices of snow grains (Denoth, 1980). Thus, the use of the term "dry" here is not meant to imply an absence of liquid water in the pack.

First-year Ice Site

The Dry Snow stage for the first-year ice site includes data measured from April 30 to June 2. Over this period, the daily mean temperature averaged -9.0 °C and never rose above zero degrees (Figure 3.16). The average snow depth at the FYI crystal pit site was 9.5 cm -- much shallower than previous years (1990-1992). Using data from April 30, May 15, May 27 and June 2, the vertical variation in snow density and grain radii during this period is shown in figures 3.23 and 3.24 respectively. The layer depth is normalized by the depth of the volume. Again, snow grain photography ceased at the end of May. The data shown in Figure 3.24 were extracted from the grain photographs.

Snow grain properties and snow density varied widely over the shallow first-year ice snow volume. The density of the April 30 volume decreases with depth throughout the 6 cm volume. The density profile of May 15 and June 2 are C-shaped indicating a low density top layer overlying a slightly denser middle layer. Density then decreases with depth.

Figure 3.23 Snow density of FYI snow volumes during Dry Snow period.

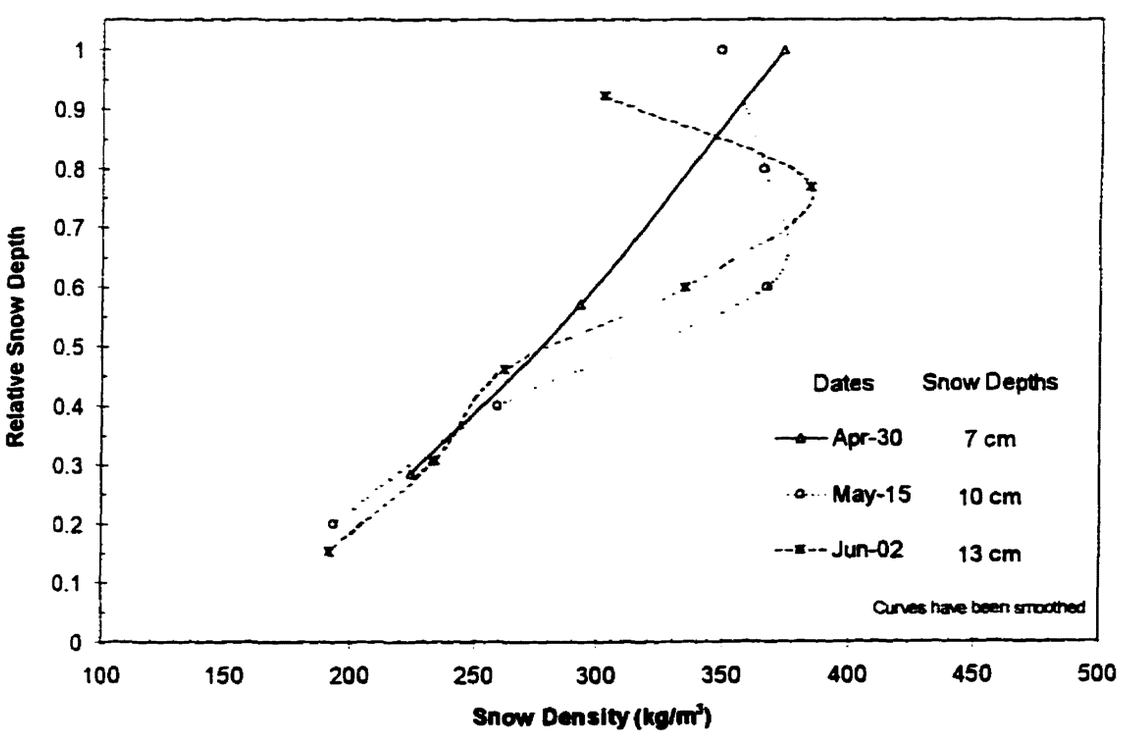
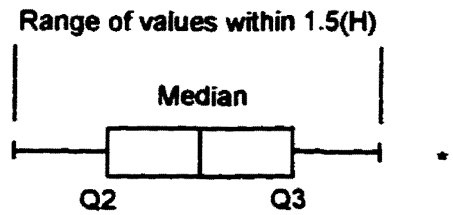
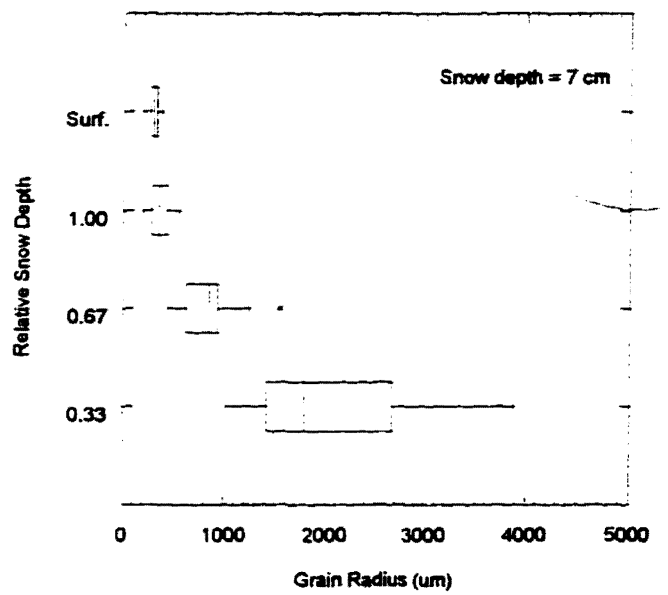


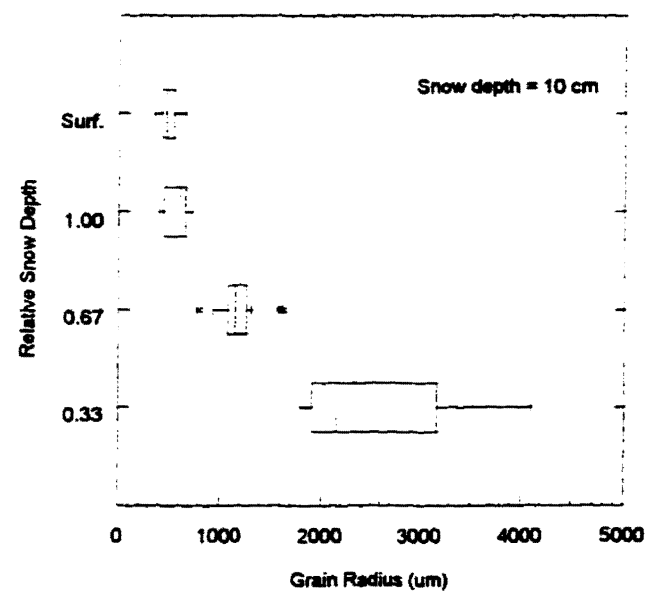
Figure 3.24 Variation of first year ice snow grain radi with depth for (a) April 30, (b) May 15 and (c) May 27.



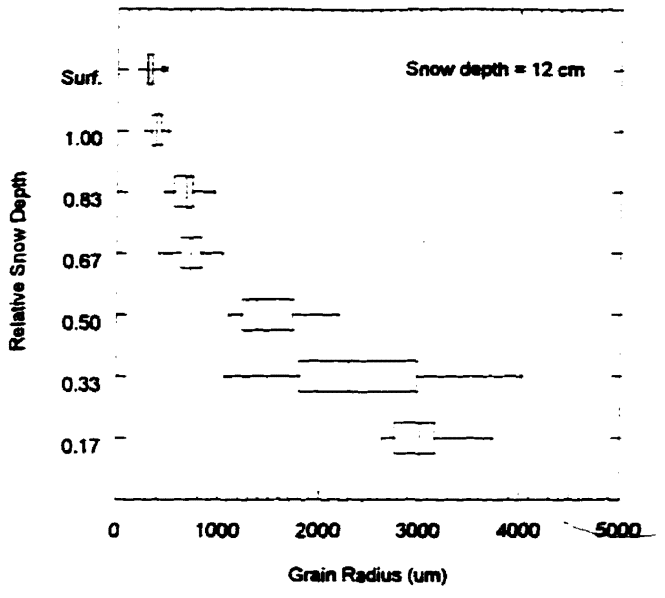
(a)



(b)



(c)



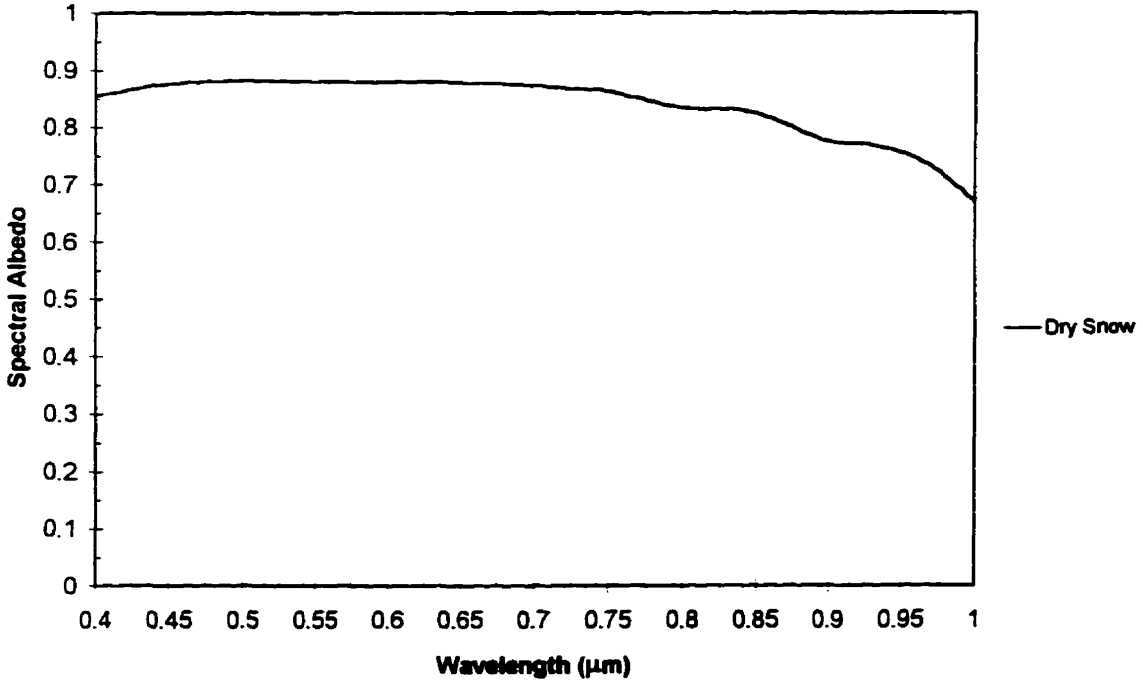
All volumes possess a low density bottom layer. Snow grain size and variability increased with depth. In the top third of the snow volume, snow grain radii averaged 483 μm while at the surface it averaged 363 μm. The upper layer in the April 30 snow volume consists of wind packed snow which likely originally fell the previous fall. The lower density and grain sizes of the upper layers of the May 15 and June 2 volumes suggest a mixture of this old snow and new spring snow which fell in May. Visual observations of grain size on June 2 indicate the formation of polycrystalline grains with an estimated grain radii of 1000 μm. The formation of these clusters follow closely the arrival of warm temperatures and the subsequent increase in liquid water in the pack. Colbeck (1979) explains that this type of clustering results as the grains attempt to minimize surface free energy.

In the middle layer, snow grain size increased and density decreased. This transitional layer primarily consisted of larger, older, rounded crystals with an average radius of 1030 μm for the month of May. The low density bottom layer consisted mainly of depth hoar crystals. These large, faceted crystals grow normal to the ice surface in response to a

significant negative temperature/vapour gradient within shallow snowcovers during the winter and early spring (Gray and Male, 1981).

The mean albedo spectra for this stage is shown in Figure 3.25. The corresponding visible and near-infrared albedo was 0.895 ($\sigma = 0.014$) and 0.833 ($\sigma = 0.012$) respectively. The high albedo indicates that, during this stage, much of the incident solar radiation is scattered out of the snowpack. The albedo spectra for this stage is relatively constant at visible wavelengths and begins to increasingly decrease with wavelength. This is consistent with previous theoretical and observational studies. Again, the visible and infrared characteristics of snow spectral albedo are largely controlled through the wavelength-dependent absorption characteristics of pure ice (Figure 3.1). The flat appearance and the magnitude of the visible portions of the observed spectra suggest that the snowcover may not have been pure and/or semi-infinite.

Figure 3.25 Average first year ice albedo spectra for Dry Snow stage



In order to assess whether the underlying ice volume contributed to the surface albedo, albedo spectra from May 15 is compared to the modelled pure snow diffuse albedo for a

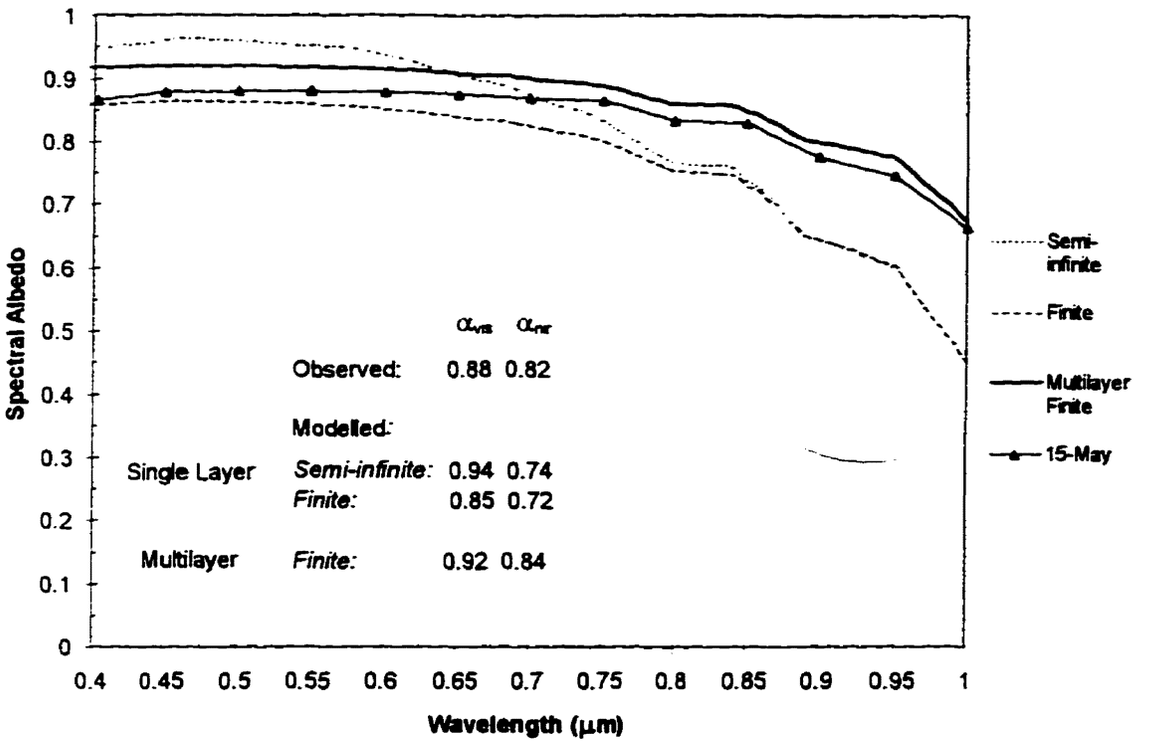
single layer and multilayer finite and semi-infinite volume. The albedo spectra on this date are closest to the average albedo for this period. In the single layer simulation, the model is initialized with the May 15 bulk volume properties. In terms of the multilayer simulation, the snow volume is divided into three equal and distinct levels and the physical properties from each level are used to initialize the snow albedo model. These data are summarized in Table 3.5. The albedo of white ice measured on June 20 was used as the albedo of the underlying surface for the finite volume.

Figure 3.26 compares the modelled albedo with the May 15 albedo. Included in the figure are the calculated visible and near-infrared broadband albedos. The visible albedo of the May 15 data (0.88) is well below that expected from a pure, semi-infinite snow volume (0.94) of comparable composition. At short wavelengths, the observed spectra agrees better with the modelled finite snow volumes, especially the single layer model value (0.85). This suggests that the snow volume in this period was finite. Indeed, based on the bulk characteristics of the volume, 55 cm of snow would be required to make this snowcover optically thick. Unlike the single layer model, the multiple layer approach appears to closely replicate the shape of the visible albedo spectrum. However, the visible albedo is 0.04 too high. This discrepancy might be offset by assuming that soot or another absorber is present in the volume.

Table 3.5 Input parameters for snow albedo model

Model	Layer	Grain Size (μm)	Snow Density (kg/m^3)	Snow Depth (cm)
	Top	236	349	2
3-Layer	Middle	525	366	4
	Bottom	1860	226	4
Single	n/a	1001	307	10

Figure 3.26 Comparison of May 15 albedo to modelled albedo for a semi-infinite and finite snow volume. Model initialized using field-observed volume characteristics.



While the presence of visible snowpack impurities were noted in the field, no measurement of soot content was made. The proximity of camp, snow machines and the Resolute Airport suggest that soot contamination is a strong possibility. Clearly without accurate information regarding snowpack impurity content, it is difficult to resolve the differences between the field spectra and the modelled results in the visible portion of the solar spectrum.

As expected, the near-infrared albedo is lower and much more wavelength-dependent than the visible albedo. The closest modelled result, the multilayer finite volume, is 0.02 higher than the observed albedo. Since the infrared albedo is highly sensitive to grain size at the surface of the volume, the use of a single layer model and a bulk volume grain size will usually lead to an underestimation of infrared albedo. This is confirmed by the single layer

modelled results in Figure 3.26. As Grenfell and Warren (1994) illustrated, infrared snow albedo is very sensitive to the grain characteristics of the upper surface layer. Simulations show that if the modelled snow grain radius is increased by 100 μm, the observed and finite-multilayer infrared spectra then match. This grain size increase falls within the accuracy range of the layer estimate. Another possible reason for an underestimation of grain size is the effect of liquid water in the pack. A storm on May 9 and May 10 brought warm temperatures from the south (Figure 3.16). The liquid water content of the upper snow layer on May 15 was 4% indicating that the snow was wet during this storm period. This is supported by the grain photography which showed that the grains were indeed wet. This increase in liquid water can further increase the optically-effective grain size by filling pore spaces and coating grains (Dozier *et al.*, 1981). This is a plausible reason for the discrepancy between the two spectra.

Multiyear ice Site

The Dry Snow period at the multiyear ice site included data collected from May 8 to June 10. Like the first-year ice site, the multiyear ice crystal pit site was covered by a snow volume throughout the period. However, the snowcover on the multiyear ice site was considerably deeper (27-75 cm) owing to the hummocky surface topography of the floe being favorable to the catchment of snow. Figure 3.27 and 3.28 show the snow volume's density and vertical distribution of grain size for May 8, May 17 and June 1. The erratic density profile is likely indicative of several submerged surface layers. Detailed grain size data was only available for the multiyear ice site to June 1. Multiyear snow volume is considerably more vertically homogeneous in grain structure than the first-year volume. Grain growth appears to be greater within lower layers of the pack and grain size increases with snow depth. Surface grain radii for the three days averaged 230 μm -- smaller than the grain sizes of the first-year ice layer. Over the top half of the volume, the average grain radii over these dates was 264 μm (σ =74 μm) and the average density was 326 kg/m^3. Over these three dates, the upper layer of the snow volume was dry with liquid water contents less than 1%. Visual observations of surface grain radii for June 4 and June 10 indicate sizes of 650 μm and 750 μm respectively.

Figure 3.27 Snow density of MYI snow volumes during Dry Snow stage

(a)

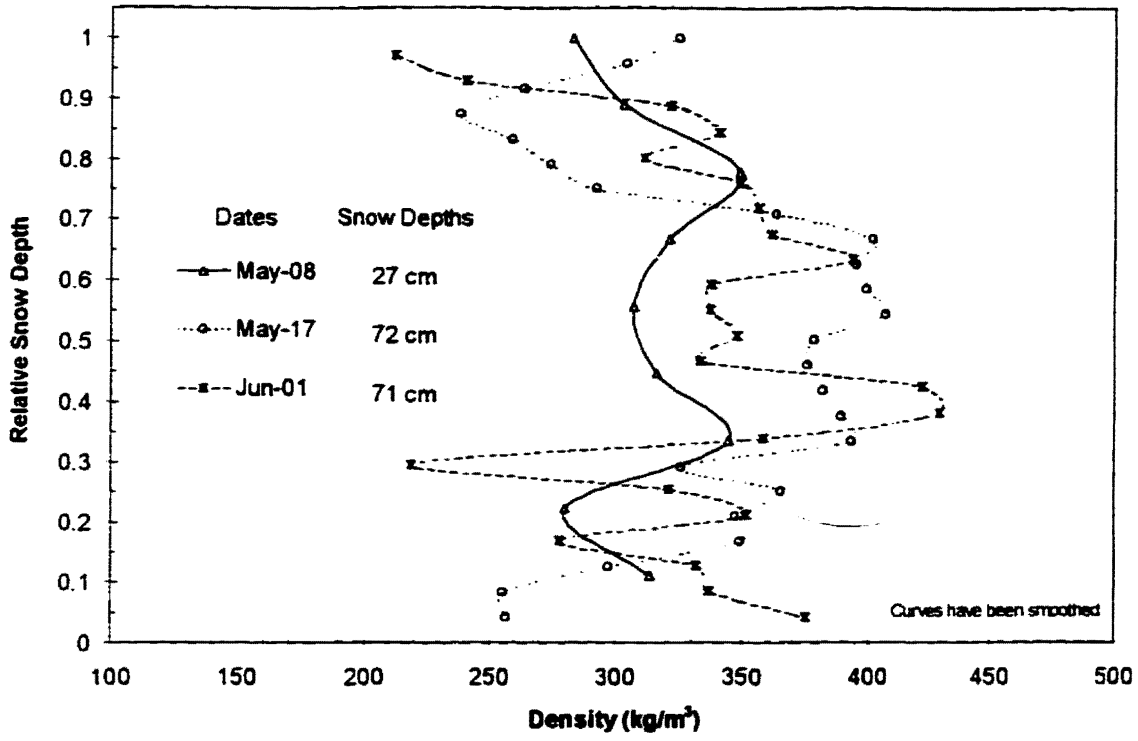
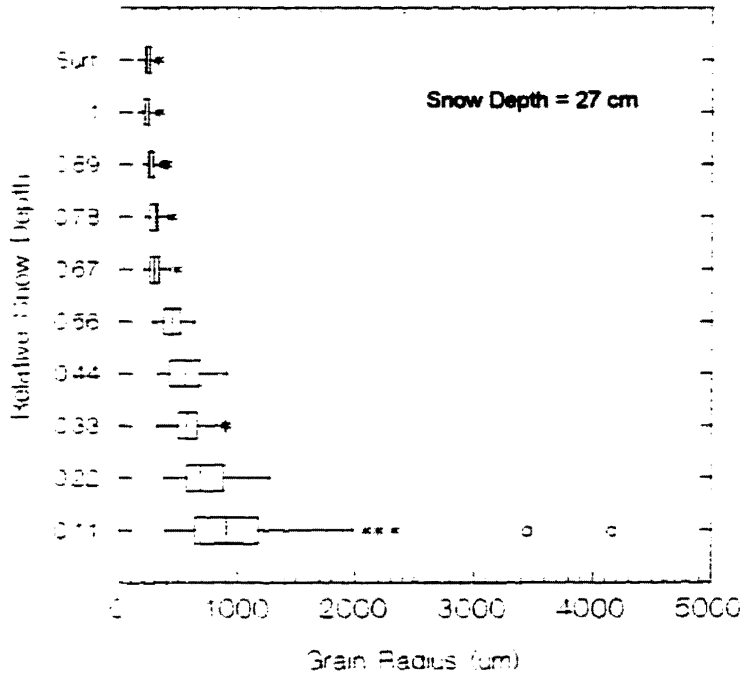
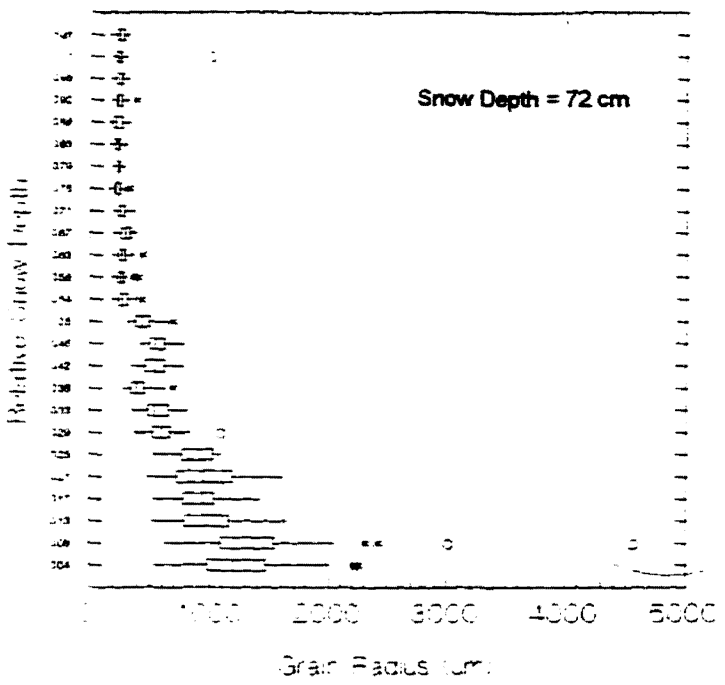


Figure 3.28 Variation of multi-year ice snow grain radi with depth for (a) May 8, (b) May 17 and (c) June 1.

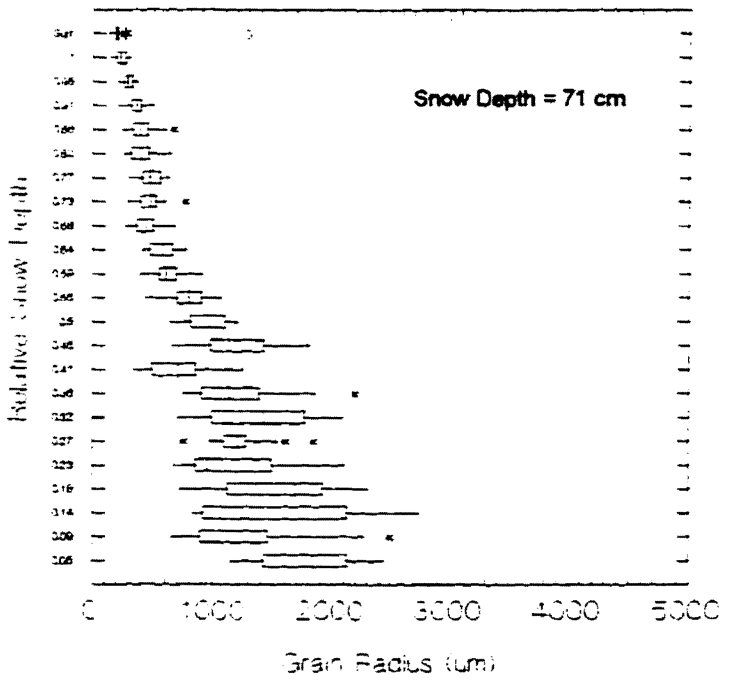
(a)



(b)



(c)

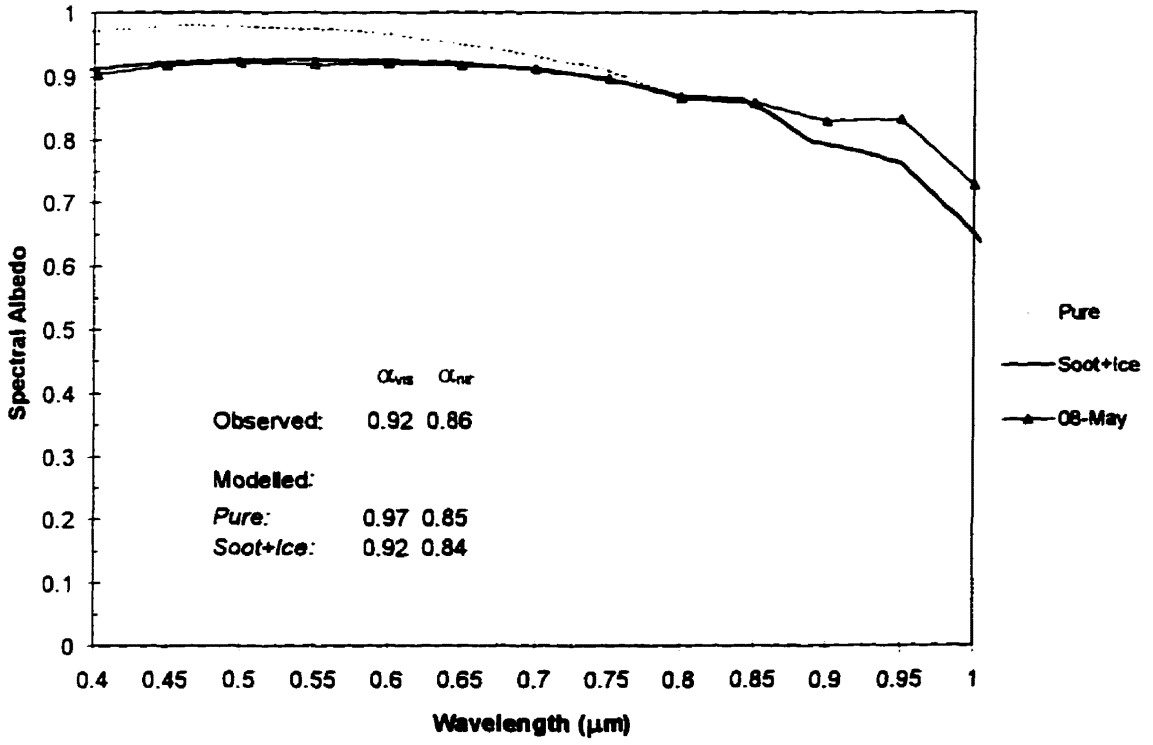


This rapid increase in size may be partly due to the switch to less accurate visual estimates. However, this increase in grain size is expected due to the formation of poly-crystalline aggregate grains in the upper layers of the snow volume. Liquid water contents increased

to greater than 1% within the first week of June. Night-time refreezing of this free water at low solar elevations and lower ambient temperatures results in the formation of these complicated crystal structures in the near-surface layers.

The average visible albedo during the early stage was 0.92 and showed little variation from May 8 to June 10. The deep snowcover suggests that the volume was optically thick and the albedo is representative of the overlying snow volume. However, the 0.92 albedo appears to be lower than would be expected from a pure, semi-infinite snowpack (Wiscombe and Warren, 1980). Figure 3.29 compares the albedo spectrum from May 8 to a modelled semi-infinite albedo spectrum. The model is initialized with the average grain radii and density of the first half of the volume. The homogeneity of these variables over this layer suggests a one-layer model may be appropriate.

Figure 3.29 Comparison of May 8 albedo to modelled albedo for a pure semi-infinite and soot-contaminated semi-infinite snow volume. Model is initialized using field-observed volume characteristics (depth=27 cm, r=276 um and density=312 kg/m^3). Soot is assumed to have a density of 1g/cm^3 , internally mixed, a refractive index of m=1.8-0.5i and a volume fraction of 5x10^{-8}.



The modelled result indicates that the visible albedo of a pure, semi-infinite snowpack with a grain size of 276 μm and a density of 312 kg/m^3 would be 0.97. This is 0.05 albedo units higher than the observed data. Since the snow volume was semi-infinite, it is plausible that snow pack contaminants reduced the visible albedo. This possibility is explored by recalculating the modelled albedo by first assuming that soot is present within ice grains with a volume fraction of 5×10^{-8}. Chyleck *et al.* (1983) state that this fraction is similar to that needed to explain Grenfell and Maykut's (1977) snow albedo measurements at T-3. The resultant soot-ice albedo is compared to the observed data in Figure 3.29. The addition of soot results in a match between the modelled and observed visible albedos. Again the presence of soot and/or other impurities in the observed snow volumes cannot be confirmed. However, the depression of the visible albedo results suggest that they were indeed present.

Cluster analysis indicates that the infrared albedo for this stage can be split into two periods. They are referred to here as Dry Snow-Cold and Dry Snow-Warm. In the first group, both May 8 and May 14 have a near-infrared albedo of 0.86. A month later, data collected on June 4 and June 10 indicate that this albedo had dropped 12 % to 0.76. Unlike the visible albedo, it appears that over this early Dry Snow stage, the near infrared albedo is less stationary. The large decrease between the near-infrared albedo between these two groups is attributable to the dramatic increase in grain size at the snow surface. In the Dry Snow-Cold period, measured surface grain sizes for May 8 and May 17 were similar measuring 226 μm and 243 μm respectively. This is supported by their near identical near-infrared albedos. Visual grain size estimates for June 4 and June 10, the Dry Snow-Warm period, indicate a significant increase in surface grain radii to 650 μm and 750 μm respectively. In the volume's upper layer, increased solar insolation and warmer ambient temperatures increased the amount of liquid water in the pack. This encouraged the growth of snow grains through melt-freeze events. These larger surface grains absorbed more incident radiation and thus decreased the longer wavelength albedo during this period. It is evident that in terms of a deep, optically thick snowcover, changes in the

snow's grain structure had little effect on the amount of visible radiation reflected out of the volume at this stage.

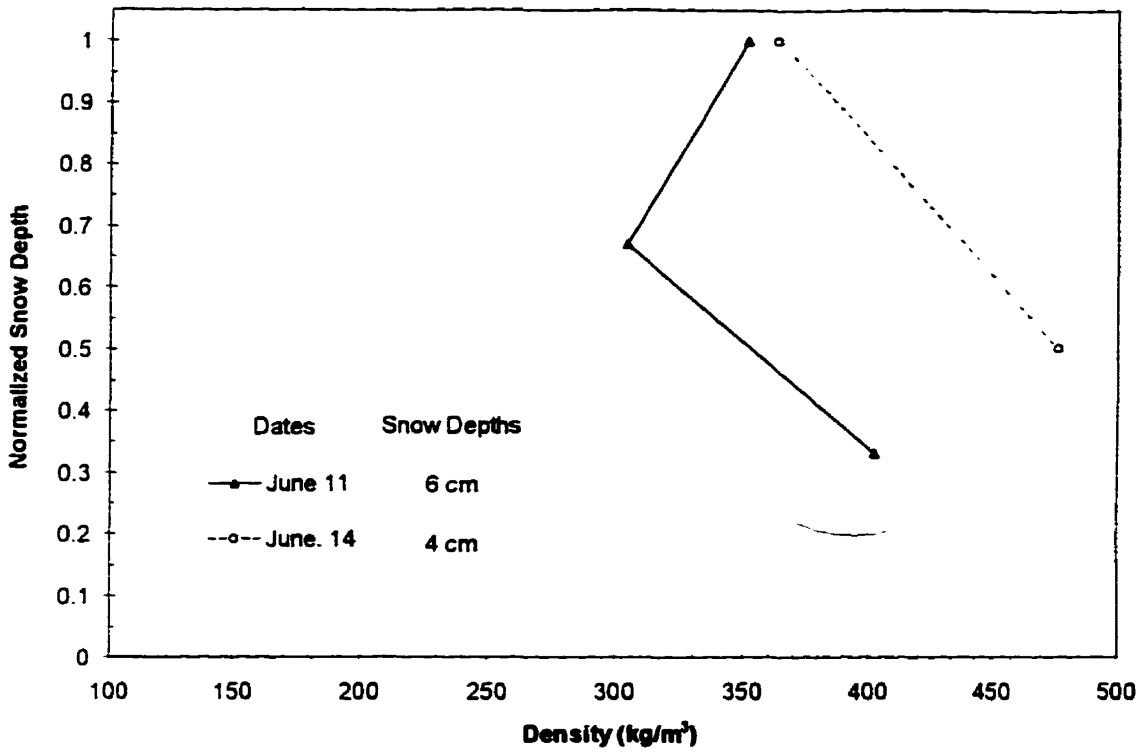
3.4.2.2 Wet Snow

In the Wet Snow period, the icescape is still covered by a measurable snow layer. However, unlike the snow volume of the previous period, the snowpack in the Wet Snow period has reached the funicular stage, i.e. free liquid water is draining through the pack through complicated water structures (Denoth, 1980). The onset of this stage coincides with the arrival of positive daily average air temperatures (Figure 3.16). As the pack approaches saturation in response to the warmer ambient conditions, its albedo decreases at all wavelengths.

First-year Ice

Compared to the earlier stage, the spectra collected on June 11 and June 14 show a decrease in both the visible and near-infrared albedo (Figure 3.17(a1)). This decrease is larger in the infrared than the visible. The air temperature data in Figure 3.16 show that during this period, the daily average air temperature was positive ranging from 0 to 2 °C. Snow depths for June 11 and June 14 were 6 cm and 4 cm respectively as positive air temperatures accelerated the ablation of the remaining snow volume. The measured liquid water content of the snowpack was 6-9% indicating that the volume had moved from a relatively low water state to a saturated, freely-draining volume. The saturation of the snow volume resulted in the formation of dense slush at the basal layer. As shown in Figure 3.30, this results in a reversal in the snow volume's density profile. Visual examination of surface grain size indicate that snow grains clustered to form large, polycrystalline aggregate structures. Grain radii for June 11 and June 14 was estimated at 2000 μm and 3500 μm respectively.

Figure 3.30 Snow density of FYI snow volumes during Wet Snow stage.



The decrease in the visible albedo during this period is in response to the larger contribution made by the underlying darker, ice volume and/or slush layer to the surface's overall albedo. As the snowcover became thinner and grain size increased, the snow volume became more transparent. Another reason for the decrease in the visible spectrum is the possibility of volume contamination by crustal material transported from nearby landforms. During this period, the snow on nearby land disappeared. Without the blanketing effect of snow, crustal material is easily picked up by winds and deposited on the nearby ice surfaces. Although this contamination was seen predominantly in near shore areas, it was visible in the experiment area. However, it was not evident in the crystal pit sampling area. It is conceded however that contamination by very small dust particles may have occurred in sampled snow volume and subsequently reduced the sampled visible albedo.

Over this period, infrared albedo continued to decrease in response to increasing grain sizes in the volume's upper layers. Near-infrared albedo decreased from 0.83 to 0.72. Initializing the snow albedo model with the observed surface grain size of 2000 μm results in a spectrum significantly lower than the June 11 spectra. By decreasing the effective optical grain size to 1000 μm, the modelled spectra matches the observed spectra. This suggests that the optically equivalent sphere radii for the volume was significantly less than the observed grain size. Part of this large discrepancy in grain size may be due to sampling error or the fact that the optically effective grain size is usually smaller than the observed grain size.

Multiyear ice

At the multiyear ice site, melt pond snowcovers exhibited a dull colour as they approached saturation levels. Within the melt ponds, freely draining melt water accumulated within lower snow layers creating a darker sub-surface slush layer. During this stage, travel on the multiyear ice floe was very difficult due to the heavy, wet snow in melt pond areas. Snow volumes during this stage consisted of a snow layer, an underlying slush layer and a basal water layer. The volume on June 12 was only 25 cm deep (hummock side) -- 10 cm of wet, large grain (1500 μm) snow overlying 15 cm of dark blue slush. The volume on June 16 was 39 cm deep -- 10 cm of snow overlying 3 cm slush and 26 cm of basal water. Measured snow wetness of the surface layer was 6% on both days.

While the depth of the volumes on June 12 and June 16 differed substantially, Figure 3.17(b) shows that the albedo for the two volumes are identical. This is consistent with the fact that both volumes had 10 cm of snow overlying a slush layer. In this period, the thin overlying snowcover allowed incident visible radiation to interact with the lower albedo slush layer decreasing visible albedo to 0.83. The infrared albedo continues to decrease with increased grain growth in the surface layer. The doubling of the grain size to 1500 μm reduced the albedo 14 % to 0.65. Overall, the appearance of a saturated snow surface in the Wet Snow stage caused albedo to decrease across the instrument range, the largest decrease being at near-infrared wavelengths.

3.4.2.3 White Ice Stage

The June 16 spectra (Figure 3.17(a)) represents the albedo of white ice at the first-year ice site. The term *white ice* is used here to refer to the remnant ice surface found after the ablation of the snow volume. Void of any measurable snow layer, the ice at this stage was not as dark and as smooth as found early in the season at the bottom of excavated snow pits. Instead, the ablation of the snowcover and the refreezing of the melt water left a thin, dense, grey-white ice surface. At time of measurement, the layer was estimated to be 1-2 cm deep. Reviewing previous experiments, this albedo stage appears to be unique to the first-year ice site of SIMMS '93. Due to the shallow snow volumes at the 1993 site, the amount of snow melt water was small. Ponding on first-year ice is caused by meltwater pooling within dense, remnant snow drifts on the surface. At the 1993 first-year ice site there was little snow resulting in little snow melt water and minimal surface drifting. Thus when the snowcover melted, the small amount of melt water did not pool, but thinly spread over the ice surface and quickly refroze. In comparison, due to its deeper snow volumes, first-year ice in nearby Resolute Passage was dotted by numerous melt ponds at this stage.

During this White Ice stage, the site albedo decreased at all wavelengths, more so in the visible spectrum. The measured visible albedo and near-infrared albedo were 0.68 and 0.57 respectively. Although this ice layer scatters light less efficiently than the ablated snow volume, it still gives the sea ice volume a relatively high albedo. The surface's greyish appearance suggests that the darker underlying consolidated ice volume was partly contributing to the visible albedo along with the surface snow-ice layer. The 21% decrease in near-infrared albedo is in response to the replacement of granular snow volume with a denser, more absorptive ice layer. Compared to the modelled bare ice spectra shown in Figure 3.6, this surface layer reduces the sharp wavelength dependence of bare ice albedo, resulting in higher albedo over the solar spectrum and the whiteness of the surface. Field observations indicate that this period is relatively short as this snow-ice layer and underlying ice cover melts and a thin layer of surface water begins to accumulate on the surface.

3.4.2.4 Melt Pond Stage

In the final stage observed in 1993, both first-year and multiyear ice surfaces evolved into a heterogeneous mix of standing melt water and bare snow/ice surfaces as air temperatures stayed consistently above 0 °C. The unique topography of multiyear ice floes, having encouraged the accumulation of deep snowcovers, led to the formation of water-filled melt ponds interspersed among the floe's hummocks. In comparison, less snow, increased melt water drainage and flatter topography at the first-year ice site prevented the formation of deep water-filled melt ponds at the study site. Instead, surface water formed a network of shallow melt sheets. The 1993 field season concluded with the appearance of surface melt water. In 1994 and 1995, more extensive melt pond studies were undertaken (Morassutti and LeDrew, 1995; De Abreu, 1995). Results from these studies will be used to complement the limited melt pond data from 1993.

First-year Ice

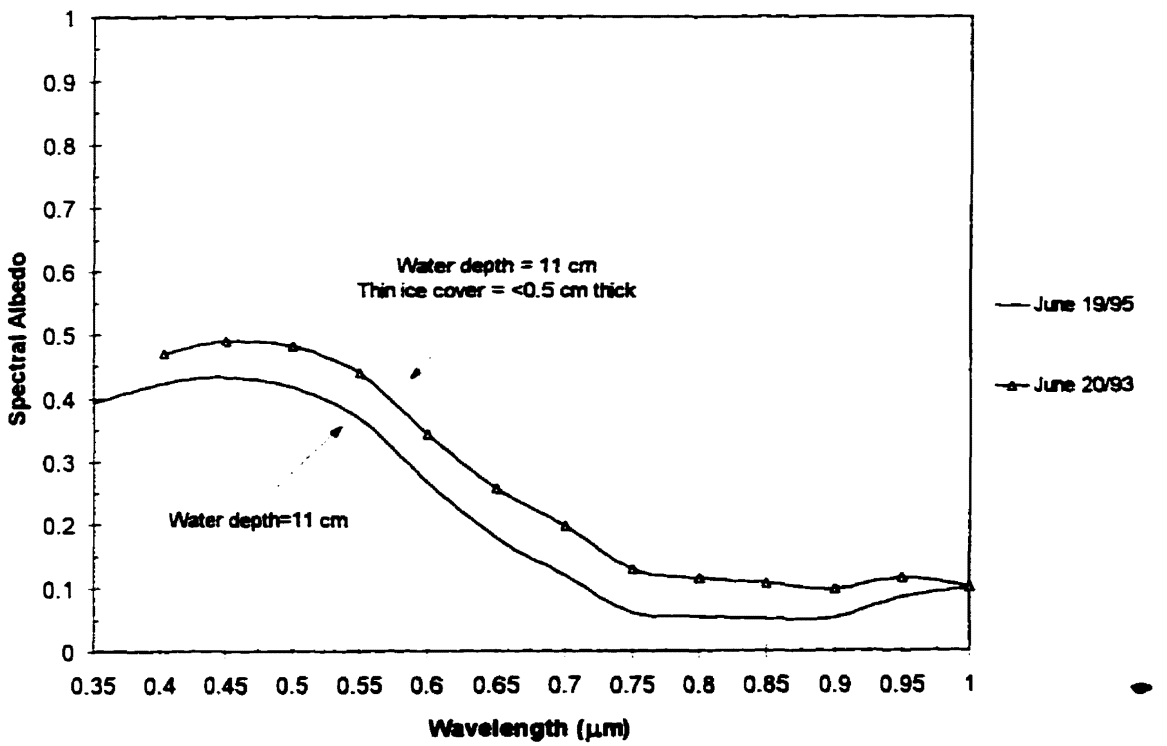
The depth and distribution of surface ponding on first-year ice is controlled by the amount of deposited snow and the topography of the ice surface. Deeper snow volumes result in more meltwater and the local ice topography determines the depth of the snow volume and the collection this water. Over rough first-year ice, snow and meltwater accumulate in ridged/rafted ice areas. On smooth first-year ice surfaces, melt ponds usually form in the interstitial areas of wind-hardened snow drifts. In the arctic, pond water depths are modulated by drainage into nearby ridge areas or through seal holes. In SIMMS '94, extensive sampling of melt ponds showed that pond depths on first-year ice were predominantly in the range of 10 to 15 cm (Morassutti and Ledrew, 1995).

Figure 3.31 contains melt pond albedo measured on June 20, 1993 and June 19, 1995 over first-year ice[8]. Both ponds were 11 cm deep and light blue in colour. The pond's surface in 1995 was covered by a thin (<0.5 cm) transparent ice cover. At the beginning of the surface ponding stage, melt pond surfaces often freeze as temperatures dip below the

[8] Since the instrument's signal to noise ratio was much better in the 1995 dataset, usable data is available at wavelengths less than 0.4 μm.

freezing point. The ablation of the white ice layer reduced the visible albedo to 0.46. Again, since water is transparent to visible light, the bulk of the visible albedo represents light scattered by the underlying ice volume. This is especially true for wavelengths less than 0.5 μm, a fact that gives the ponds a blue colour. The albedo of first-year ice is expected to decrease throughout the melt pond stage as the ice decays. More specifically, as the ice begins to warm, the brine volume of the underlying ice volume increases. Brine pockets enlarge, connect and collect released air bubbles. This reduces scattering within the ice and thus reduces the albedo of first-year ice (Perovich *et. al.*, 1986). The effect of the ice cover on the pond albedo in 1993 was minimal due to its apparent transparency at visible wavelengths. However, as pointed out earlier, by providing a solid surface for snow deposition, these ice covers have the potential to affect sea ice albedo for short periods.

Figure 3.31 First year ice melt pond albedo. 1995 melt pond spectrum included for comparison. Note wavelength range extended to 0.35 μm.



The appearance of surface water has the most effect on albedo at infrared wavelengths. Again, water is very absorptive at longer wavelengths. Its presence on sea ice effectively reduces the infrared albedo to near zero. By covering the absorptive water surface, the thin surface ice cover in the 1993 data increased the infrared albedo. However, the measured pond albedo at wavelengths greater than 0.75 μm appears to be overestimated by approximately 0.05. This may be due to the large field-of-view of the RCR. As such, nearby snow areas surrounding the melt ponds may be contributing to the measured albedo. In this case, the albedo at all wavelengths would be slightly overestimated. Also, the RCR correction procedure assumed that the upwelling irradiance was diffuse (Appendix 3). This assumption is likely violated over the specular water surface of a melt pond under direct incident irradiance. This lends some uncertainty to the melt pond data that may explain its overestimation of infrared albedo.

Multiyear ice

The hummocky topography of multiyear ice and the deep snow volumes are conducive to the development of melt ponds. Unlike the sheet-like melt features of first-year ice, multiyear ice melt ponds often have discernible boundaries and shapes and are capable of holding more melt water. The aerial photo in Figure 3.32 was taken during SIMMS '95 from a tethered balloon (Piwowar, 1995). It shows the contrasting shapes of melt ponds on first-year and multiyear ice. In this stage, warm ambient conditions transformed the deep snowcover in the crystal pit area to a water filled melt pond.

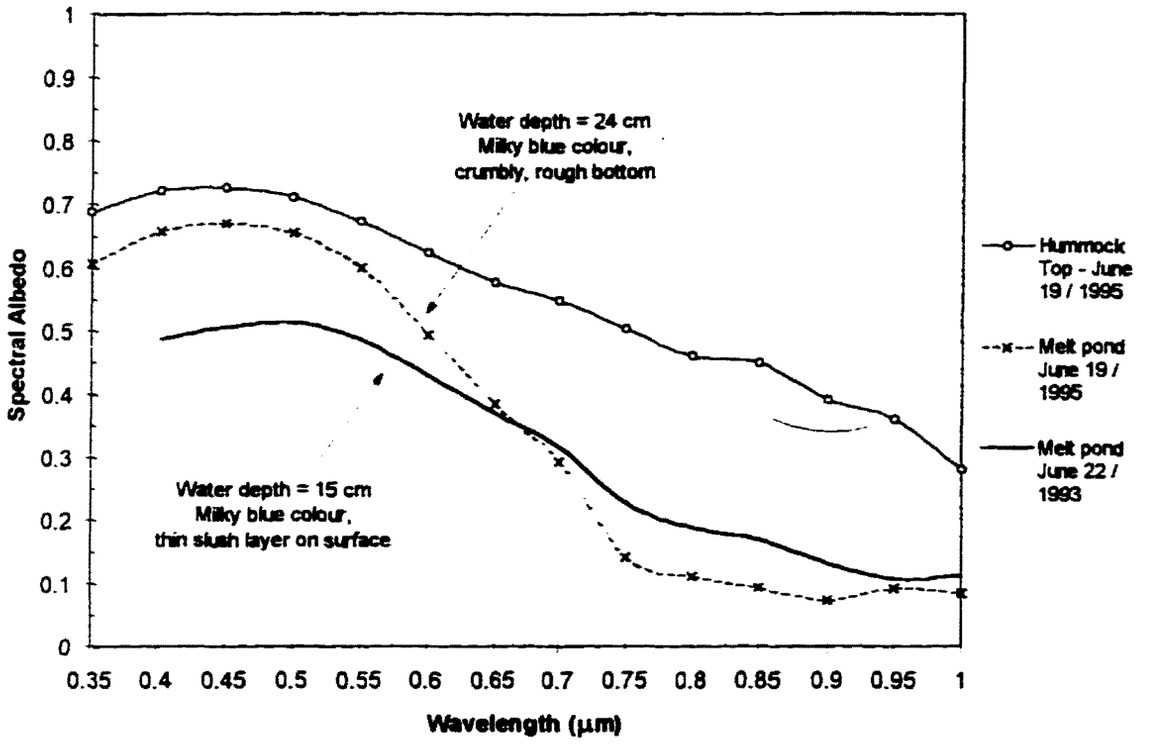
Figure 3.33 shows the melt pond albedos collected on multiyear ice on June 22, 1993 and June 19,1995. Like the first-year ice site, the June 22 pond is covered by a thin surface, this time a translucent slush layer (<1.0 cm). The albedo is very similar in magnitude (α_{vis}=0.46, α_{nir}=0.19) and shape to that of the ice covered first-year ice melt pond. However, preliminary analysis of the albedo observations in SIMMS 1995 indicate that early melt pond visible albedo differs between first and multiyear ice types.

Figure 3.32 Contrast in FYI and MYI late season ponding measured via balloon photography.



June 16, 1995 Central Barrow St. Altitude=300 m

Figure 3.33 Multi-year ice melt pond albedo. 1995 melt pond spectrum included for comparison. Note wavelength range extended to 0.35 μm.



The June 19, 1995 melt pond in Figure 3.33 is typical of the several multiyear ice melt ponds measured in 1995. The 1995 melt pond data indicates that the visible albedo of multiyear ice ponds was approximately 0.1 albedo units higher than sampled first-year ice ponds. This is consistent with the observations of melt pond observations of Grenfell and Maykut (1977) (their figure 1). The higher visible albedo of multiyear ice ponds is due to presence of air bubbles in the near-surface ice layers. These air bubbles are efficient scatterers and thus increase volume albedo. Field observations indicate that this bubbly layer was absent from first-year ice surfaces, thus resulting in a lower albedo.

Although the melt pond crystal pit site was the sampling focus at the multiyear ice site, hummock ice surfaces were the predominant surface type on the floe. Five years of observations have shown that while these features change slowly over the melt season, they exhibit a wide range surface characteristics. Usually, a hummock top consists of blue

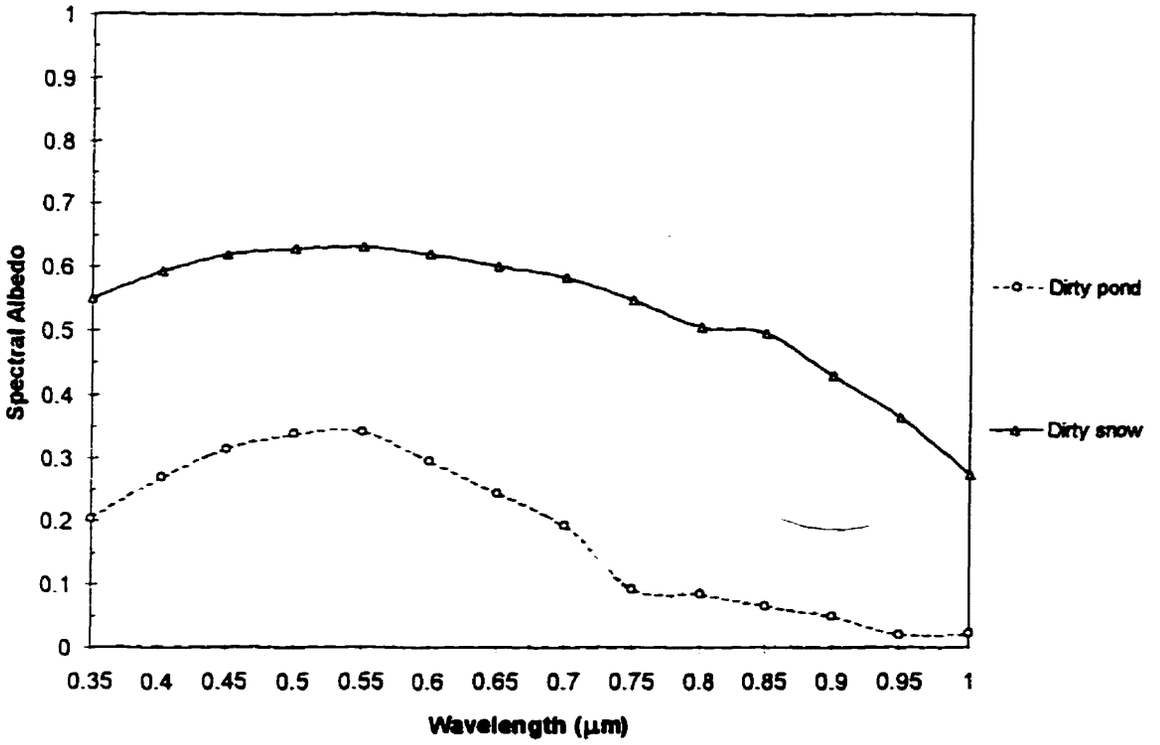
ice overlain by a crusty, porous white layer which varies in depth. This ice layer is very similar to the white ice of first-year ice site occasionally found before pond formation. Early in the season, hummocks can be covered by a thin layer of snow which eventually decomposes and contributes to this white surface layer. This porous layer scatters light efficiently given these features a high albedo relative to melt ponds. The hummock spectrum in Figure 3.33 was measured over a white ice-topped hummock in SIMMS 1995 on June 19. In SIMMS '90, this drained white layer was absent from the sampled multiyear floe. Instead, the hummock tops were bare and bright blue in colour. Since this inaugural experiment ended before surface melt, it is not known whether surface melting eventually transformed these bare blue tops.

Figure 3.34 shows the effect of both eolian debris on the albedo of a multiyear ice pond (depth=15 cm) and a snow volume (depth=4 cm). The material in the melt pond appeared to be predominantly crustal, with some biological matter. Suspended matter in the pond water and on the surface absorbed much of the radiation in the blue portion of the spectrum, thus leaving the pond with a grey-green colour. The pond bottom was pocked by debris pits or *cryoconites* as this absorbed radiation melts the pond's bottom. Snowcover adjacent to the dirty pond was also contaminated. The snow spectrum shows the absorptive effects of the gigantic crustal particles nestled between the snow grains of the volume's upper layer. This type of contamination is always a possibility for sea ice in the island regions like the arctic archipelago. This is especially true for multiyear ice floes that travel through the region throughout the year. Again, fast, first-year ice is more likely to become contaminated by crustal materials when snow disappears from nearby land masses.

3.5 Conclusions

In SIMMS '93, the first-year ice site transformed from a high-albedo snow-covered surface to a low-albedo water-covered surface. The most dramatic changes occurred at near-infrared wavelengths. The high-albedo of snow-covered sea ice was reduced when

Figure 3.34 Spectral albedo of debris-laden multi-year ice melt pond and snow cover.



reductions in the snow volume's depth and enlargement of snow grains allowed incident radiation to interact with the darker, underlying ice surface. The time of season when this critical depth is reached will vary depending on the ambient temperature and, most importantly, snow depth. The spring snow depth is dependent on the frequency of snowfall, which can serve to increase snow depth and reduce the volume's snow grain size, and the opportunity for catchment to facilitate significant snow depths. The infrared sea ice albedo responded to seasonal changes in the surface layers of the volume. When a snowcover was present, the seasonal growth of snow grains into polycrystalline units in the near-surface layer of the pack decreased infrared albedo. When surface water was present, the sea ice surface was a radiation sink at infrared wavelengths. It should be noted that the SIMMS '93 experiment did not encompass the full melt season. With the appearance of the cracks in the ice, this first-year ice surface drained and likely revealed a higher albedo ice surface (Grenfell and Perovich, 1984).

Like first-year ice, the multiyear ice floe in SIMMS '93 transformed from a high- to low-albedo surface with the progression of the spring melt. Unlike the first-year ice site, at full melt conditions the multiyear ice site was less homogenous due to the presence of the white hummocks interspersed among the melt ponds. The floe's overall albedo is thus dependent on its hummock to melt pond ratio. It was evident that this ratio decreased as melt conditions progressed over the experiment period. Early in the melt season, the floe's melt pond areas were filled with an optically thick snowcover which resulted in an albedo higher than the first-year site with thinner snow volumes. The infrared albedo was more sensitive to microstructure changes occurring in the snowpack's upper layers. The visible albedo stayed constant until increased water volumes in the pack resulted in the saturation of the cover's lower layers. As this slush layer grew and approached the snow/air interface, incident visible radiation scattering through the remaining snow layer is absorbed, consequently lowering the surface visible albedo. With the appearance of surface melt water, both the visible and infrared albedo are reduced considerably. The shorter wavelength visible radiation interacts more with the pond's bottom and underlying ice microstructure. Almost all of the incident infrared radiation is absorbed within the melt water, likely leading to the ablation of the pond's ice bottom and sides.

While the crystal pit measurements were valuable in the understanding of the relationships between the seasonal change in albedo and the decaying sea ice volume, the sampling clearly lacked the spatial component needed to fully comprehend the variability of this important climate variable. Traverses throughout the experiment region via helicopter and snow machine made this fact evident. Climate studies require accurate albedo information resolved over regional scales at a temporal resolution capable of capturing the variable's critical variance. The most efficient way of accomplishing this is through the incorporation of remotely sensed data. The next chapter describes how visible and near-infrared satellite data can be utilized to map sea ice albedo.

4 ESTIMATING SURFACE ALBEDO FROM AVHRR 1 AND 2

4.1 Introduction

Satellite remote sensing is the only viable means of measuring climatically significant variables over the spatial and temporal scales necessary for the development, initialization and validation of climate models. While much attention has been given to the collection of these data over lower-latitude terrestrial surfaces, comparatively little study has been invested in the use of this technology for monitoring important climate variables over high-latitude sea ice surfaces. One of the most consistent and extensive satellite datasets of the Arctic Basin is NOAA's Advanced Very High Resolution Radiometer (AVHRR) archive.

AVHRR has been providing polar coverage continually since 1978. Although AVHRR was designed to provide timely meteorological information, efforts are underway to evaluate the utility of this global archive for providing Earth-atmosphere (E-A) information important for the long-term simulation of this planet's climate (Gutman *et.al.*, 1995). AVHRR's extensive polar coverage give it the potential to resolve key spatial and temporal polar features critical to the modelling of the atmosphere-ice-ocean. However little attention has been given to the application of AVHRR data to these types of polar scientific problems (Steffen *et al.*, 1993). Obvious obstacles to the general application of these data to polar regions are the frequent summer cloud cover and its dependence on solar illumination. Also the lack of *in situ* measurements important to evaluating the utility of these data is a significant hurdle to the utility of these data.

The visible and infrared channels of AVHRR have the potential to directly measure those energy fluxes that control the energy balance of the marine cryosphere. Among these fluxes, the importance of measuring sea ice albedo has been established. Under clear-sky conditions, AVHRR's visible channel (AVHRR 1) and near-infrared channel (AVHRR 2) have the potential to measure sea ice surface albedo over regional scales readily adaptable to larger scale climate models. However, there is no established methodology regarding the inversion of these data from orbital AVHRR data. Moreover, no attempt has been made to assess the potential accuracy of sea ice surface albedo data derived from AVHRR.

This chapter describes a methodology for extracting surface visible and infrared albedo from AVHRR 1 and AVHRR 2 clear-sky data. The chapter begins by describing the AVHRR sensor and briefly reviewing previous studies that have utilized shortwave imagery to extract surface albedo over snow and ice surfaces. The theory of using orbital measurements collected in solar spectrum for measuring surface albedo is discussed. The methodology used to extract visible and infrared surface albedo from AVHRR 1 and AVHRR 2 is described and validated. The sensitivity of the derived albedos to input parameters is examined and a detailed error analysis is performed.

4.2 Sensor and Platform Description

Regular satellite coverage of the polar regions is currently provided by the National Oceanographic and Atmospheric Administration (NOAA) 11, 12 and 14 satellites equipped with the AVHRR sensor. Designed to provide meteorological information to aid in operational weather forecasting, the TIROS-N satellites have provided uninterrupted service since 1978. NOAA 11 was launched on September 24, 1988, NOAA 12 was launched May 14, 1991 and NOAA 14 was launched on December 30, 1994. NOAA 13 was lost due to malfunction.

Table 4.1 describes NOAA 12's AVHRR sensor and the parameters of the TIROS NOAA platform. The parameters of this satellite have been relative constant since NOAA 6. Even numbered satellites have daylight (7:30 A.M.) north-south equatorial crossing times and the odd numbered platforms have nighttime (2:30 A.M.) crossing times (Lillesand and Kieffer, 1987). The orbit and large swath width (2400 km) allows all locations to be sampled at least twice a day at a nominal instantaneous field of view (IFOV) of approximately 1.1 km at nadir (Kidwell, 1991). At high polar latitudes, orbits overlap providing coverage several times a day. The sensor's IFOV becomes larger with distance from nadir to a maximum of 2.4 km at the far edge of the swath. The data are recorded and archived at full resolution (Local Area Coverage or LAC) or at a degraded resolution of 4 km (Global Area Coverage or GAC).

The AVHRR sensor consists of one visible channel (1: 0.58-0.68 μm), one near-infrared channel (2: 0.73-1.1μm) and three thermal infra-red channels (3: 3.55-3.93 μm; 4: 10.3-11.3 μm; 5: 11.5-12.5 μm). There is a very small reflected component in channel 3 and some researchers have found it useful in cloud detection schemes (Key and Barry, 1992). Channels 1 and 2 are calibrated pre-launch and the thermal channels are continually calibrated with an onboard thermal source. The spectral response of channels 1 and 2 are shown in Figure 4.1. These two channels measure solar radiation reflected from the Earth and atmosphere within these two broad bands.

4.3 Previous Investigations

There has been very little attention given to the extraction of sea ice surface albedo using sensors that operate within the solar spectrum. The reasons for this are varied. On a whole, the utilization of any type of satellite data for mapping climatically-significant surface variables in the polar regions is still relatively recent. More specifically, the use of optical sensors is restricted to clear-sky events during the spring and summer months when solar illumination is available. While there are a significant

number of clear-sky events in April and May, increasing cloudcover in the remaining spring and summer months limits the availability of usable imagery. Another related problem is the detection of cloud cover over high-albedo snow/ice surfaces (Key and Barry, 1989). Despite this, previous studies have shown that visible satellite data have the potential to provide useful information regarding surface sea ice albedo over various spatial and temporal scales.

Table 4.1 Characteristics of AVHRR on NOAA 12

Parameter	NOAA 12
Launch Date	May 14, 1991
Altitude (km)	» 833
Orbital Period (min.)	102
Orbits per day	»14
Scan angle from nadir	±55.4°
IFOV at nadir (km)	1.1
IFOV off nadir, maximum (km)	2.4 - 6.9
Swath width (km)	2400
Coverage	Every 12 hr.
AVHRR spectral channels† (μm)	
1	0.58 - 0.68
2	0.73 - 1.10
3	3.55 - 3.93
4	10.3 - 11.3
5	11.5 - 12.5

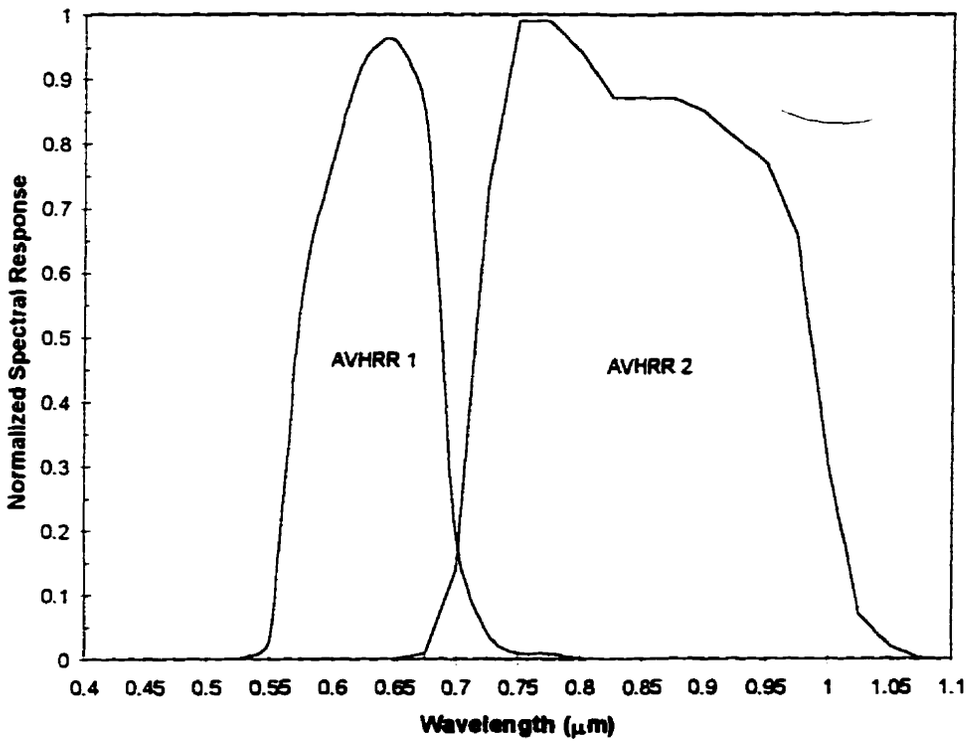
† Based on half power widths

Source: Adapted from Lillesand and Kiefer(1987)

Raschke *et al.*'s (1973) study claims to be the first high resolution study of the Earth's annual global radiation budget. Using Nimbus-3 data (0.2-4.8 μm), the study found

albedo values of 0.50-0.70 over snow and ice surfaces in the polar regions. The authors attributed variations of sea ice albedo in the Arctic to snow melt patterns and "formations of fractures in the ice and water cover on the ice". Preuss and Geleyn (1980) used Raschke *et al.*'s data to derive global estimates of surface albedo which include measurements of sea ice albedo. The authors inverted surface albedos using a radiative transfer approach.

Figure 4.1 AVHRR Channel 1,2 Normalized Spectral Response



Probably the most extensive study of the use of visible imagery to map sea ice albedo is the work of Robinson *et al.* (1986, 1992). The Operational Line Scanner (OLS) system onboard the Defense Meteorological Satellite Program (DMSP) satellite was used to map surface broadband albedo and snow melt in the Arctic for the first time by Robinson *et al.* (1986) for the years 1977 and 1979 and again by Robinson et al. (1987) for 1977, 1979, 1984 and 1985. The Arctic was divided into five study

regions: Central Arctic, Beaufort/Chukchi Seas, east Siberian/Laptev seas, the Kara/Barents seas and northwest North Atlantic. The Canadian Arctic Archipelago was not included in the study.

The OLS system operates in the spectral range 0.4-1.1 μm, and for these studies, a degraded image resolution of 2.7 km was utilized. Within both studies, the authors report that at least one cloud free scene per three day interval was available over more than 80% of the basin from May to mid-August. The data were manually classified into four brightness classes representing different surface conditions. Surface albedos for each class were based on a simple parameterization based on brightness levels and previously measured albedo values. The brightest pixels in the study grid were assigned an albedo of 0.79 until late June when the value was decreased to 0.69 to account for snow melt. The darkest pixel which was assumed to be open water was given an albedo of 0.12. These *tie*-point values were based on published albedo values. Surface albedos of all intermediate pixels were then linearly interpolated based on these two values and the surface class was assigned a mean value. The study minimizes the effect of the specular nature of sea ice reflectance by claiming that it is "minimal over snow, ice and water surfaces" according to Taylor and Stowe (1984). Closer examination of Taylor and Stowe's results in this chapter will show that, while the anisotropy of sea ice may be less relative to other natural surfaces, it is still considerable in a climatological sense. As a result, variability in DMSP pixel brightness may be a function of viewing geometry and not albedo. However, this effect was likely reduced due to the monthly averaging over the study's ten year period.

The regional and seasonal variability in surface albedo for the Arctic Basin is presented in Table 4.2. During the spring and summer, the Arctic sea ice albedo ranged from 0.80 in the Central Arctic in May to 0.23 in the Kara/Barents seas in August. The variability among arctic regions is evident and is ascribed to varying rates of surface melt which ultimately determine ice surface conditions (i.e. snow-covered ice vs.

ponded ice). Some of this variability may be due to the spatial variability of low-albedo open water and thin ice within the ice classes. The authors acknowledge this possibility and assume that these effects were minimized through averaging.

Table 4.2 Monthly mean parameterized regional sea ice (>10% ice cover) surface albedos in the Arctic Basin derived from Robinson *et.al.* (1987).

Month	Central Arctic	Beaufort/ Chukchi	Laptev/ E. Siberian	Kara/ Barents	NW North Atlantic
May	0.8	0.76	0.78	0.7	0.71
June	0.74	0.62	0.62	0.55	0.62
July	0.54	0.44	0.44	0.34	0.47
August [+]	0.51	0.39	0.38	0.23	0.44

[+] Values for first half of month only.

It should be noted that this study employed AVHRR imagery when DMSP imagery was not available. Morassutti (1992) subsequently developed a methodology to split these DMSP broadband albedos into visible and near-infrared albedos.

Schweiger *et.al.* (1993) compared the 10 year Arctic parameterized albedo dataset of Robinson *et.al.* (1992) with surface albedos derived from AVHRR 1 data processed by the International Satellite Cloud Climatology Program (ISCCP) algorithm. The ISCCP C-2 dataset contains cloud amount, cloud optical depth, surface temperature, atmosphere constituent profiles and surface reflectivity at 0.6 μm (Rossow and Schiffer, 1991). The ISCCP narrowband 0.6 μm albedo was used to estimate the spectral reflectance of typical sea ice surfaces over the solar spectrum. A radiative transfer model was then used in conjunction with derived spectral albedo to calculate broadband surface albedo. The spatial patterns of surface albedo derived from the ISCCP data agreed well with the DMSP dataset. A concentric pattern of decreasing

surface albedo progressing towards the south was found in both datasets. Schweiger *et.al.* 's (1993) surface albedo was systematically lower by 0.1 than the OLS dataset in May and June and higher in July. The likely reason for this discrepancy will be addressed later.

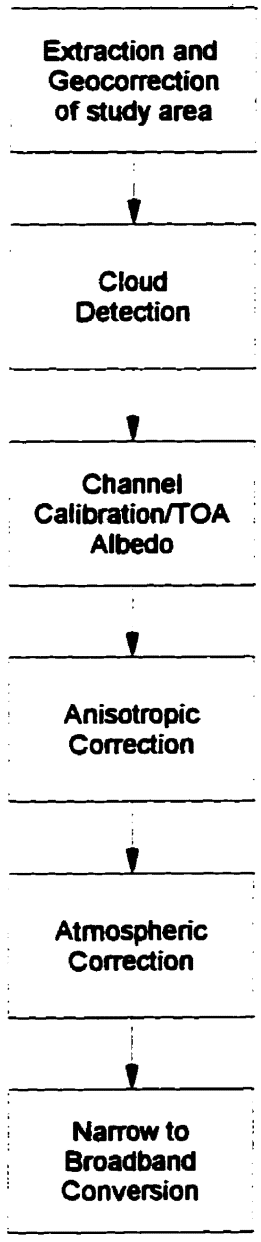
Recently, De Abreu *et al.* (1994) and Lindsay and Rothrock (1993, 1994) examined the use of AVHRR for mapping arctic sea ice albedo. Unlike earlier studies, these investigations attempted to map surface albedo by directly inverting the satellite-measured radiances. De Abreu *et al.* (1994) investigated the applicability of a simple inversion methodology for deriving broadband surface albedo over snow-covered fast ice in the SIMMS study area in 1993. The inversion methodology was similar to the method proposed in this investigation. The study was supported by *in situ* surface and atmospheric observations. Using four AVHRR scenes collected on the same day, the authors found that satellite-derived broadband albedo were within 0.01 albedo units of surface broadband albedo measurements when effects of surface anisotropy and atmospheric attenuation were accounted for.

Lindsay and Rothrock (1993) used a very similar methodology to measure surface albedo with AVHRR data of the Chuckchi Sea in March, 1989. Like Robinson's and Schweiger's study, no surface validation of the results was available. In Lindsay and Rothrock (1994), the authors expanded the scope of their study to include much of the Arctic Basin for March to September 1989. The authors calculated a mean monthly broadband albedo of the central Arctic range from 0.76 in April to 0.47 in August. These studies will be examined more closely within the context of this investigation.

In this chapter, a multi-step inversion methodology is used to derive surface albedo from AVHRR channel 1 and 2 satellite measurements. Figure 4.2 is a schematic diagram describing the general methodology used in this investigation. The inversion process estimates visible (0.3-0.7 μm) and infrared albedo (0.7-4.0 μm) from AVHRR 1 and

AVHRR 2 respectively. The method is appropriate for clear-sky AVHRR 1 and 2 data of spring sea ice surfaces.

Figure 4.2 Surface albedo inversion methodology



4.4 Data Extraction and Cloud Detection

The AVHRR data used in this study were provided by the Atmospheric Environment Service (AES). AES downlinks and archives AVHRR data in support of its varied forecasting operations. Using cloud cover observations from SIMMS '93 and AES weather station Resolute, potential clear-sky dates between April 1 and July 31 were identified. AES TeraScan® software was used to extract all available AVHRR NOAA 11 and 12 data for these dates. In order to minimize image distortion and atmospheric effects, only images with solar zenith angles less than 70° and satellite zenith angles less than 45° were selected. 280 x 280 km^2 LAC sectors from the complete orbital swath were extracted and registered to a rectangular map (256 x 256 pixels) centered on 75° N 93.5 W. Each datafile consisted of five channels of image data (AVHRR 1-5) and five channels of ancillary information stored on a pixel by pixel basis: latitude, longitude, relative azimuth, satellite zenith angle and solar zenith angle.

One of the more serious obstacles to routine employment of optical satellite imagery to measure polar surface features and energy fluxes is the blocking and attenuation effects of clouds. Cloud detection and mapping procedures developed for lower latitude environments do not work well over polar surfaces and atmospheres (Key, 1989). The most difficult aspect is the inability to distinguish between clouds and snow/ice surfaces, both of which have similar reflectances. Methods under study are generally based on spectral or textural approaches (Key and Barry, 1989; Welch *et al.*, 1992; Ebert, 1992, Rossow and Schiffer, 1992). Although this is a very active research area at the moment, no accepted or fully reliable automated method exists for cloud detection in the polar regions. Thus for the purposes of this investigation, a manual approach was taken to ensure the study areas were cloud-free.

Image analysis software was used to display the raw shortwave channels and the calibrated thermal channels of each potential clear-sky image. Using channels 1 and 2, images where

cloud obviously obscured the experiment area were excluded from analysis. At this first level of detection, water clouds (stratus, stratocumulus) were detected primarily through their shape, texture and coverage. Fortunately, unlike the Arctic Basin, land surfaces are present in the archipelago thus providing image contrast that assisted in the detection of cloudcover. When in doubt, the difference between AVHRR 3 and AVHRR 4 was used to detect clouds. This method takes advantage of the difference in brightness temperatures between the two channels during sunlit conditions (Yamanouchi and Kawaguchi, 1992). Difference images (AVHRR 3 - AVHRR 4) were compared to AVHRR 4 images to identify cloud contaminated pixels. The remaining images were considered to be cloud-free.

The appearance of ice fog in advanced melt conditions is another source of image contamination. This often ubiquitous, low-lying fog is restricted to the ice surface and thus may give the impression that the image is clear due to the cloud-free appearance of surrounding land surfaces. In this dataset, ice fog presence was detected using visual textural differences in AVHRR 1 and 2. Ice fog tends to result in a smooth sea ice image, devoid of the higher variability in pixel brightness expected in advanced melt conditions. Also, the occurrence of ice fog was monitored by surface observers.

The dataset assembled for processing and analysis after screening is summarized in Table 4.3. The eight image dates available encompass much of the spring melt. In order to trace the transformation of AVHRR raw data into surface albedo, the brightness values averaged over a 7x7 pixel area centered in Resolute Passage will be summarized at the conclusion of each processing step.

Table 4.3 Sun-target-sensor geometry of AVHRR dataset

Date	Local Time (approx.)	Solar Zenith	Satellite Zenith	Relative Azimuth
April 30	11:30	61	18	159
May 3	10:45	63	8	18
June 4	11:00	55	2	161
June 9	17:50	61	22	150
June 16	13:30	51	40	157
June 20	13:30	51	41	157
July 7	11:00	56	6	15
July 29	12:30	56	37	160

4.5 Calibration and Conversion to TOA Reflectances

4.5.1 Calibration

On request, AES calibrated the three thermal channels and provided AVHRR 1 and AVHRR 2 data in their raw digital number (DN) format. The digital numbers of each image pixel were converted to TOA radiances (L_i) ($Wm^{-2}\ sr^{-1}\ \mu m^{-1}$) for each channel (i) through [4.1] according to Holben *et al.* (1990):

$$L_i = \delta_i (DN_i - C_i) \qquad [4\text{-}1]$$

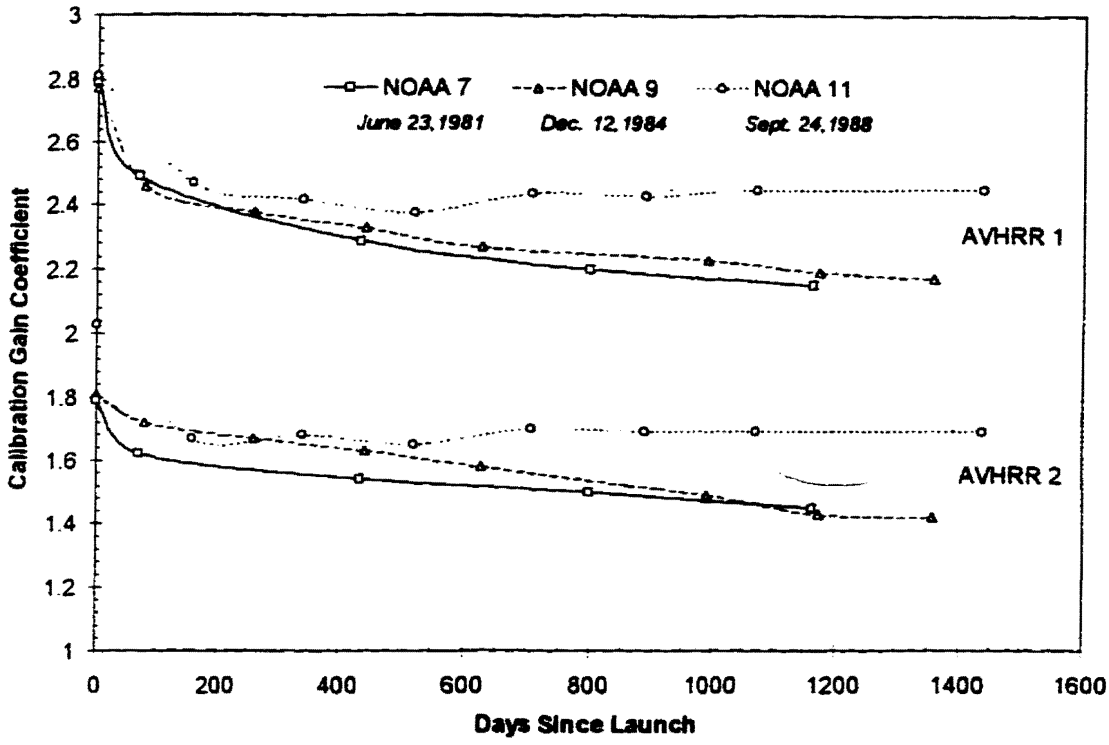
where $\delta_i = 1/G_i$, is the channel gain (counts/$Wm^{-2}\ sr^{-1}\ \mu m^{-1}$) and C_i is the channel offset (counts). The channel offset and gains are determined by a pre-launch calibration (Teillet *et al* (1994).

NOAA AVHRR channels 1 and 2 are routinely calibrated with a standard light source before each satellite launch. However it has been shown that this calibration may change during pre-launch storage, during launch and during space flight (Holben *et al.*, 1990). Since there is no in-flight calibration of these channels, a concerted effort has been launched to monitor and upgrade the pre-launch calibrations of operating AVHRR sensors (Price, 1987; Brest and Rossow, 1992; Vermote and Kaufman, 1995; Rao and Chen, 1995). These techniques range from observing large, homogeneous surfaces (desert, ocean, cloud) of known reflectance to using coincident calibrated airborne or orbital data. Teillet and Holben (1994) have taken these results and compiled a database containing time-dependent calibrations for NOAA 6-11. While the calibration offset is considered consistent with pre-launch values, investigators have found significant changes to the gain coefficients of both channels. Figure 4.3 shows the drift in the calibration gain for NOAA 7, 9 and 11 as determined by desert calibration. Typically, AVHRR 1 and 2 experience a large degradation immediately following launch. The rate of degradation then slows and, as shown by AVHRR 11, can level out.

Unfortunately, no known calibration update is available for NOAA 12's AVHRR sensor[9]. In order to account for degradation in AVHRR 12's visible and near-infrared channel, this investigation utilized coincidental surface albedo measurements in concert with the 6S radiative transfer code[10] to predict the at satellite radiance for AVHRR 1 and AVHRR 2. Surface and satellite data from April 30 is chosen as the calibration dataset. On this date, the reflectance of the sea ice surface appeared to be spatially homogeneous. As a result, the measured crystal pit surface albedo is considered here to be representative of the albedo over an AVHRR pixel.

[9] The lack of calibration updates is typical of the even-numbered NOAA platforms which possess early morning equator crossings. Note: the loss of NOAA 13 has reversed this rule.
[10] The 6S radiative transfer code is explained in detail in a following section.

Figure 4.3 Change in calibration gain for NOAA 7, 9, and 11 AVHRR as determined by desert calibration. Launch date shown in italics.



Source: Teillet and Holben, 1994

In order to initialize the 6S model, the surface albedo measured by the AVHRR instrument must be determined. The surface albedo measured by a filtered radiometer such as AVHRR (α_1, α_2) is a function of the solar irradiance incident within the sensor channel, the surface albedo and the spectral response of the instrument measuring the reflected radiation (ϖ). The spectral albedo measured by AVHRR 1 and 2 was determined by

$$\alpha_{1,2} = \frac{\int_{b1}^{b2} E_s \alpha_s \varpi_{1,2} d\lambda}{\int_{b1}^{b2} E_s \varpi_{1,2} d\lambda} \qquad [4\text{-}2]$$

where the limits *b1* to *b2* are the spectral range of the AVHRR channel, i.e. 0.57-0.70 μm for AVHRR 1 and 0.70-1.1 μm for AVHRR 2. The resultant emulated AVHRR 1 and 2 surface albedos for April 30 were 0.89 and 0.84 respectively.

The 6S code required that the derived April 30 channel albedos be expressed as a bidirectional surface reflectance measurement. Since sea ice is an anisotropic reflector, i.e. its reflectance is a function of solar incidence angle and viewing geometry, the measured sea ice albedo cannot be considered equivalent to that viewed by the satellite sensor. Perovich (1994) sampled the bidirectional reflectance distribution function (BRDF) of various sea ice covers in Resolute Passage. The 1991 study derived spectral anisotropic reflectance factors[11] (ARFs) (f_λ) which relate bidirectional reflectance (ρ_λ) measurements to albedo (α_λ) through the following

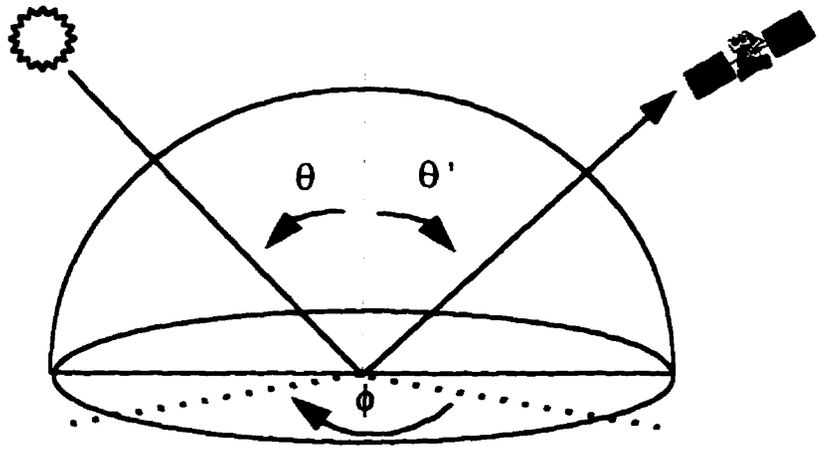
$$f_\lambda(\theta,\theta',\phi) = \frac{\rho_\lambda(\theta,\theta',\phi)}{\alpha_\lambda} \qquad [4\text{-}3]$$

where θ is the solar zenith angle, θ' is the satellite zenith angle, and ϕ is the relative azimuth angle between the sun and the satellite measured at the surface (Figure 4.4). A perfectly isotropic surface would have an ARF of unity. Given the measured spectral albedo and the target's ARF, [4.3] can be rearranged to convert surface albedo to a bidirectional reflectance:

$$\rho_\lambda(\theta,\theta',\phi) = \alpha_\lambda f_\lambda(\theta,\theta',\phi) \qquad [4\text{-}4]$$

[11] Anisotropic reflectance factors are discussed in depth in a following section

Figure 4.4. Typical geometry of sun-target-sensor



The spectral ARFs closest to the scene geometry for the April 30 overpass were integrated over the channel bandpass and weighted by the incident irradiance to determine the appropriate conversion factors. These factors were then used to convert the surface spectral albedo to a bidirectional reflectance. Table 4.4 shows the derived AVHRR surface albedos, the channel ARFs and the resultant AVHRR surface reflectances used to initialize the radiative transfer model.

Table 4.4 Determination of TOA radiance as viewed by NOAA 12 on April 30 overpass.

Channel	Surface Albedo[†]	Anisotropic Reflectance Factor[††]	Surface Reflectance	TOA Radiance[†††] ($W/m^2/sr/\mu m$)
1	0.89	0.95	0.85	174.53
2	0.84	0.96	0.81	110.23

† Measured at FYI crystal pit April 30
†† Taken from Perovich (1994) ARF measurements for snow covered sea ice
††† Determined by 6S radiative transfer code

A reasonably accurate radiative transfer code popular in the remote sensing community is the *Second Simulation of the Satellite Signal in the Solar Spectrum* or 6S (Vermote *et.al.*, 1994). Compared with the previous version 5S, 6S employs a more accurate scattering method for solving the radiative transfer equation thus extending its former limitation to solar zenith angles of less than 60 degrees to at least 70 degrees (D. Tanre, personal communication). However, the accuracy of the solution decreases as the solar zenith angle approaches this limit. The derived channel reflectances were input into the 6S model along with *in situ* estimates of the atmospheric conditions during the overpass on April 30. These atmospheric inputs (aerosol optical depth, ozone and water vapour amount) are discussed in more depth in later sections. The 6S code predicted that, based on the surface reflectances in Table 4.4, the atmospheric conditions on April 30 and the sun-target-sensor geometry, the TOA radiance measured by AVHRR 1 and 2 should be 174.53 $W/m^2/sr/\mu m$ and 110.23 $W/m^2/sr/\mu m$ respectively.

A four pixel subarea (2 x 2) including the SIMMS data site was extracted from the April 30 overpass for AVHRR 1 and AVHRR 2. The location of the subarea was chosen to exclude the multiyear ice floe. The extracted DNs shown in Table 4.5 reveal that the site reflectance appeared homogenous. By rearranging [4.1], employing the TOA DNs and assuming that the channel offsets have not changed[12], the updated gain coefficients for AVHRR 1 and AVHRR 2 were determined to be 1.71 and 2.21 respectively. Over approximately two years, this signifies an 8.6 % and a 25.1 % degradation in the sensitivity of AVHRR 1 and 2 respectively. While the decrease in AVHRR 1 response is comparable to previous platforms (Figure 4.3), the NOAA 12's AVHRR 2 degradation appears to be more serious. Given the experience with NOAA 11, it is quite possible that the gain for both channels will begin to stabilize. If not, the decrease in sensitivity is expected to slow with time. In this study, these new gain coefficients were applied to the NOAA 12 data with the assumption that the gain does not decrease over the three month study period.

[12] The channel offsets or *deep space counts* change very slowly with time and are typically very close to prelaunch values (Teillet and Holben, 1994)

Table 4.5 Adjustment of NOAA 12's AVHRR 1 and 2 calibration gain. Included are the TOA digital numbers averaged over SIMMS study site for April 30 overpass.

Channel	Mean Subarea DNs[†]	Pre-launch Gain	Adjusted Gain	% Change
1	340 (0.5)	1.87	1.71	-8.6
2	283 (2.1)	2.95	2.21	-25.1

[†] Brackets contain st. deviation of DNs over subarea

4.5.2 TOA Reflectance Conversion

The TOA radiance was converted to a TOA reflectance (ρ_{TOA}) by dividing by the filtered exoatmospheric solar irradiance within each channel (E), adjusted for the sun-Earth distance (d) and normalized by the cosine of the solar zenith angle (θ) at time of data acquisition[13]:

$$\rho_{TOA} = \frac{\pi L * d^2}{\cos\theta E} \qquad [4\text{-}5]$$

Table 4.6. provides the calculated TOA reflectance based on the pre-launch and the updated calibration coefficients listed in Table 4.5. The results indicate ignoring the calibration drift would significantly underestimate the TOA reflectance and subsequently the surface albedo.

[13] The channel subscript i is assumed for all subsequent relations unless otherwise specified

Table 4.6. Comparison of TOA reflectances determined by pre-launch and updated calibration gain coefficients. Note: DNs averaged over 7x7 subarea in Resolute Passage.

Date	AVHRR 1			AVHRR 2		
	DN	Pre-Launch	Updated	DN	Pre-Launch	Updated
30-Apr	340.69	0.66	0.72	282.43	0.52	0.70
03-May	315.96	0.63	0.69	259.51	0.50	0.66
04-Jun	381.47	0.64	0.70	281.41	0.45	0.60
09-Jun	330.12	0.63	0.69	246.53	0.44	0.59
16-Jun	378.45	0.58	0.63	258.69	0.37	0.49
20-Jun	290.98	0.43	0.47	180.35	0.24	0.32
07-Jul	207.47	0.32	0.35	137.59	0.18	0.25
29-Jul	86.82	0.09	0.09	67.78	0.05	0.07

4.6 Anisotropic Correction

The reflectance measured by a satellite is considered bidirectional, or in other words, representative of an individual view direction at a certain solar zenith and solar azimuth angle. It may or may not be representative of the total amount of energy reflected by the Earth-atmosphere system. Over isotropic surfaces, a sensor's bidirectional measurement is considered representative of the surface's albedo. Since most natural surfaces display some level of anisotropy, bidirectional satellite reflectance measurements cannot be considered representative of albedo until this anisotropy is addressed.

The degree of anisotropy of an object's reflectance, in this case the reflectance of the Earth's surface and atmosphere, is commonly expressed by the following anisotropic reflectance factor (ARF) (f):

$$f(\theta,\theta',\phi) = \frac{\rho_{TOA}(\theta,\theta',\phi)}{\alpha_{TOA}} \qquad [4\text{-}6]$$

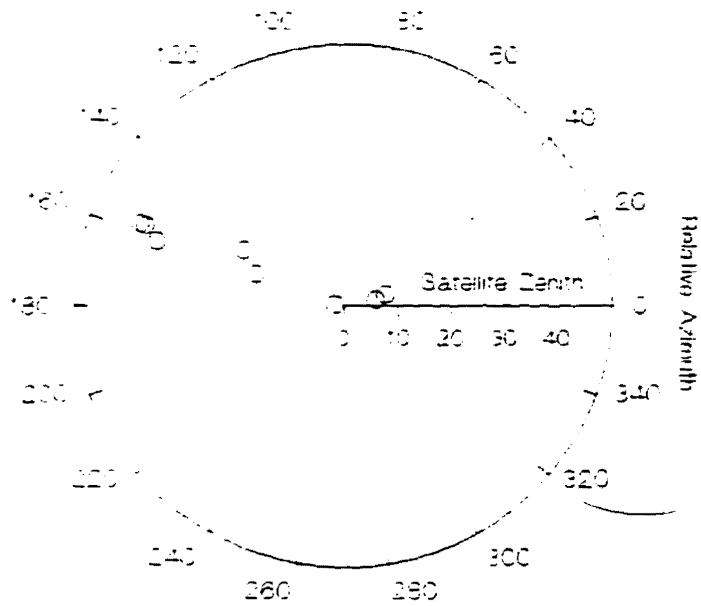
where α_{TOA} is the albedo measured at the top of the atmosphere. A perfectly isotropic surface[14] would have an ARF of unity. Given the TOA-measured reflectance and the target's ARF, [4.6] can be rearranged to convert a bidirectional reflectance measurement (ρ_{TOA}) to a TOA albedo:

$$\alpha_{TOA} = \frac{\rho_{TOA}(\theta,\theta',\phi)}{f(\theta,\theta',\phi)} \qquad [4\text{-}7]$$

In terms of polar studies, it has been accepted that the reflectance of sea ice surfaces is not isotropic, but in fact, directional in nature. In most cases, this *anisotropy* is wavelength-dependent and strongly dependent on the physical characteristics of the surface (Perovich, 1993). In the case of an orbital or airborne sensor, surface anisotropy can be modulated by the overlying atmosphere (Koepke and Kriebel, 1987; Kondratyev *et al.*, 1992). Thus, in order to facilitate comparison of multi-temporal satellite data of TOA radiation data collected at different sun-sensor geometries, the anisotropy of the surface and atmosphere should be considered. This is especially true for sensor's like AVHRR that collect data at a variety of times during the day and at varying satellite zenith angles. Due to AVHRR's wide swath (56° from nadir), the same point on the surface can be viewed on two or more consecutive days with wide variations in the sun-target-sensor configurations (Roujean *et al.*, 1992). Figure 4.5 indicates the variation of the sun-target-sensor geometry of the each AVHRR image in this dataset. It is apparent that the viewing directions are close to the solar plane, i.e. 0° and 180°.

[14] An isotropic surface is often termed a Lambertian surface. i.e. reflectance from the surface will follow Lambert's cosine law -- varying with the cosine of the source zenith angle.

Figure 4.5 Satellite-sun geometry of study dataset



Note: Sun at 0° Azimuth

Unfortunately, appropriate BRDF models to derive sea ice ARFs are unavailable. Outside of those described earlier (Schlosser, 1988; Perovich, 1994), measurements of the surface BRDF of sea ice are rare. These surface measurements, however, cannot account for the anisotropy of the overlying atmosphere. Caution should be exercised when solely basing the anisotropy of TOA satellite reflectance on surface-measured anisotropic characteristics. This is especially true when the radiance is recorded at large zenith angles or above turbid atmospheres where the opportunities for atmospheric scattering and absorption are large. In order to utilize surface ARF values, the TOA reflectance measurement should be first corrected for atmospheric effects.

Ideally, a spaceborne sensor that can view the Earth at several angles at once is required to develop appropriate BRDF models for various surface types and overlying atmospheres. The Multi-angle Imaging Spectro-Radiometer (MISR) planned to be launched on the EOS AM-1 platform in 1998 has been designed for this purpose and

promises to provide the data necessary to construct and validate BRDF models appropriate for satellite remote sensing. Until this time however, the derivation of surface albedo from bidirectional satellite measurements is compromised due to lack of sea ice-atmosphere BRDF models. Presently, the derivation of reflectance patterns by Taylor and Stowe (1984) using Earth Radiation Budget Experiment (ERBE) data is the only major source of ARF information for sea ice and other surface types.

4.6.1 Taylor and Stowe Anisotropic Reflection Factors

Using 61 days of Nimbus-7 ERBE data, Taylor and Stowe (referred here on as T&S) (1984) developed an atlas of reflectance patterns for various geotypes: *ocean, land, snow, clouds and sea ice*. For each surface type and sun-sensor geometry, the atlas provides anisotropic correction factors (ARF) capable of converting bidirectional satellite reflectance data to TOA albedos factors through [4.7].

In the absence of scene identification, the sea ice model is more appropriate for polar regions since it represents the widest range of surface conditions. For example, Lindsay and Rothrock (1994) used the sea ice model exclusively in their long term study of surface albedo over the Arctic Basin. In terms of this dataset, the predominant surface types from April to July include snow, meltponds, bare ice and open water. In situ observation allowed the identification of the predominant surface type at image acquisition and thus manual selection of the appropriate ARF model[15]. Given this, three ARF models are applied in this investigation: snow, sea ice and ocean. Table 4.7 lists the image dates paired with their appropriate model.

For those image dates that required the snow and ocean models, the appropriate ARF was selected from the atlas tables provided in Taylor and Stowe (1984). The ARFs are determined by the sun-sensor geometry at time of data acquisition. A single ARF is

[15] In situ observations were not available for July 7 and July 29. Scene types were estimated.

determined for each scene based on the sun-sensor geometry of the central pixel in the image and applied to each pixel in the image. Since the study area is relatively small, the sun-sensor geometry remains relatively constant over the image. In the case of two dates that required the sea ice model, a parameterization based on the T&S sea ice ARF dataset developed by Lindsay and Rothrock (1994) was applied on a pixel by pixel basis. The view geometry of each pixel was input into the following model:

$$f = \beta_0 + \beta_1 x + \beta_2 y + \beta_3 u + \beta_4 x^2 + \beta_5 y^2 + \beta_6 yu \qquad [4\text{-}8]$$

where

$$\begin{aligned} x &= \sin\theta' \cos(\pi/2 - \phi) \\ y &= \sin\theta' \sin(\pi/2 - \phi) \\ u &= \cos\theta \end{aligned} \qquad [4\text{-}9]$$

and the β_i are weighted least squares regression coefficients (β_0=0.681, β_1=-0.185, β_2=-0.222, β_3=0.310, β_4=0.413, β_5=0.608, β_6=0.338). The residual standard error in the model is given as 0.084. For each image date, the ARFs were applied to the TOA reflectance data to produce TOA albedos. The same ARF was applied to both channel 1 and channel 2 data. The validity of this application will be addressed later.

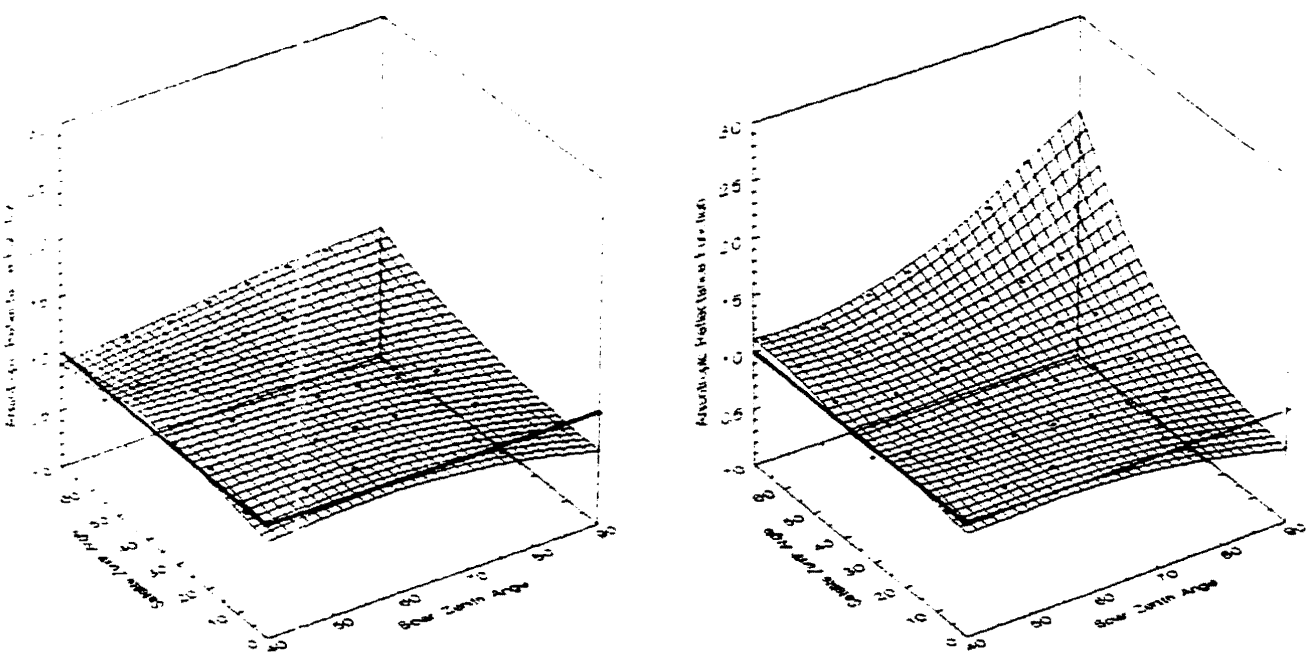
Table 4.7 Distribution of T&S ARF models

Date	Selected ARF Model	Surface Conditions
April 30	snow	Dry snow
May 3	snow	Dry snow
June 4	snow	Wet snow
June 9	snow	Wet snow
June 16	sea ice	Melt Ponds, wet snow
June 20	sea ice	Melt Ponds
July 7	sea ice	Melt Ponds, bare ice, open water
July 29	open water	Open water, bare ice

As shown in Figure 4.5, the two main sensor views for NOAA 12 can be summarized as: 15-20° relative azimuth (looking with the sun) and 155° relative azimuth (looking into the sun). Figure 4.6 shows the T&S snow, sea ice and ocean ARF models for these two view geometries. A distance-weighted least squares smoothed surface (McLain, 1974) has been applied and the ARF=1 line has been added to the data. TOA reflectances collected at satellite-sun geometries which intersect this line are considered representative of TOA albedos and no anisotropic correction is necessary. Data points in the ocean model where ARF>3.0 have been truncated to preserve axis scale.

Figure 4.6. Taylor and Stowe (1984) Sea Ice Anisotropic Reflection Factor Models

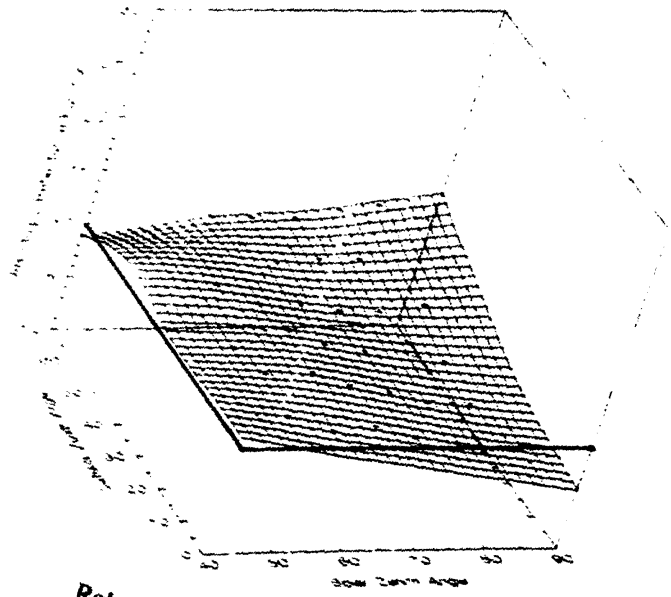
(a) Snow Model



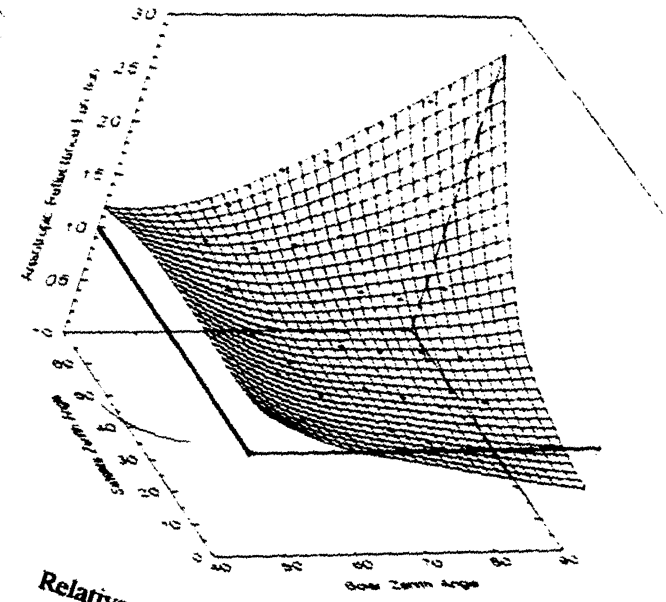
Relative Azimuth = 20°

Relative Azimuth = 155°

(b) Sea Ice Model

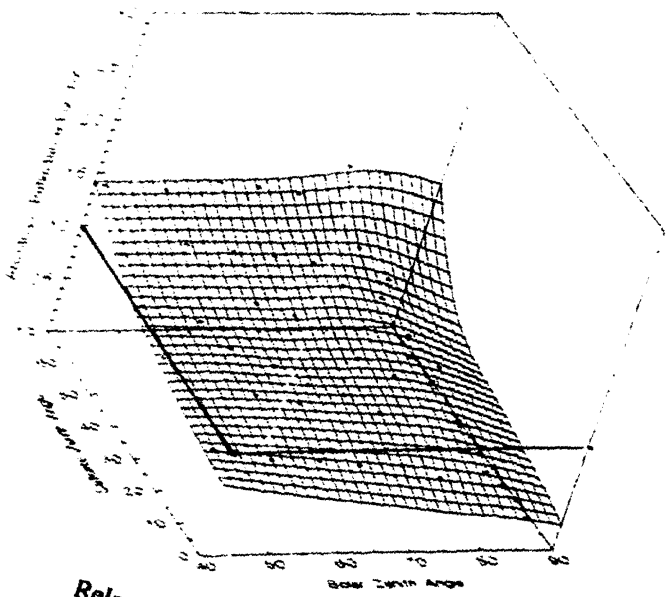


Relative Azimuth = 20°

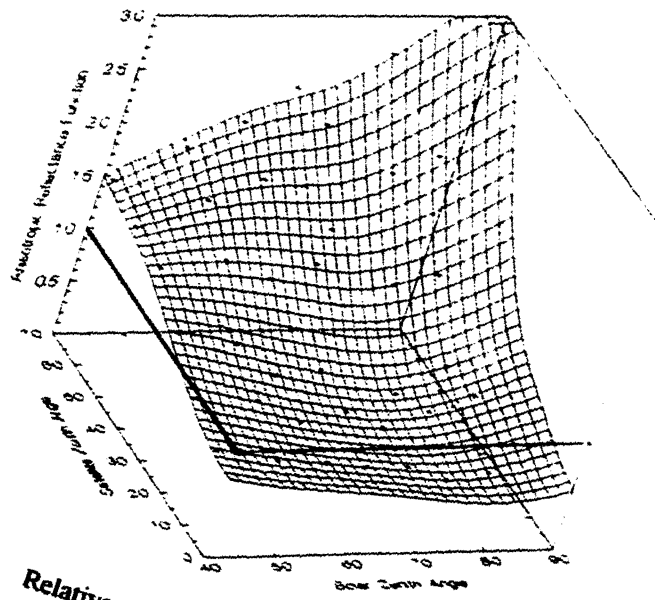


Relative Azimuth = 155°

(c) Ocean model



Relative Azimuth = 20°



Relative Azimuth = 155°

As expected, T&S's results show the similarity between the anisotropy of snow and sea ice surfaces. Sea ice appears to scatter light more strongly in the forward direction compared to the snow surface. This is likely due to the anisotropic effects of bare ice and melt pond surfaces within the sea ice model results. Snow appears to be the most isotropic reflector of the three surfaces (Figure 4.6(a)). In fact, of all surfaces examined by Taylor and Stowe (1984), snow was indeed the least anisotropic. It is apparent from Figure 4.6. that all three surfaces are strong forward-scatterers. When the sensor is facing directly into the sun (ϕ=180°), the surface-reflected radiation contains a large specular component. This effect, though lessened, is evident in the ARF values for a relative azimuth of 155° -- when the satellite zenith angles approach the angle of reflection of the direct solar beam. In the case of the ocean model, the specular characteristics of water surfaces are well known. Also, both snow and ice have been characterized as strongly forward scattering media. In this sun-sensor geometry, the satellite-derived TOA reflectance of these surfaces often are significantly larger than the TOA albedo. The level of anisotropy also appears to increase with solar zenith angle.

The results of the anisotropic correction are shown in Table 4.8 and Figure 4.7. In this investigation, the anisotropic correction is significant in cases, ranging from +17% to -46% of the TOA reflectance for the low albedo July data. The average ARF over the dataset was 1.06. For all snow images, regardless of viewing geometry, the TOA reflectance underestimates the TOA albedo. The opposite is true for the two June sea ice images since the sensor was looking into the sun. The largest ARF (f=1.84) was for the July 29 image (ocean model) where the sensor was facing into the sun's direction.

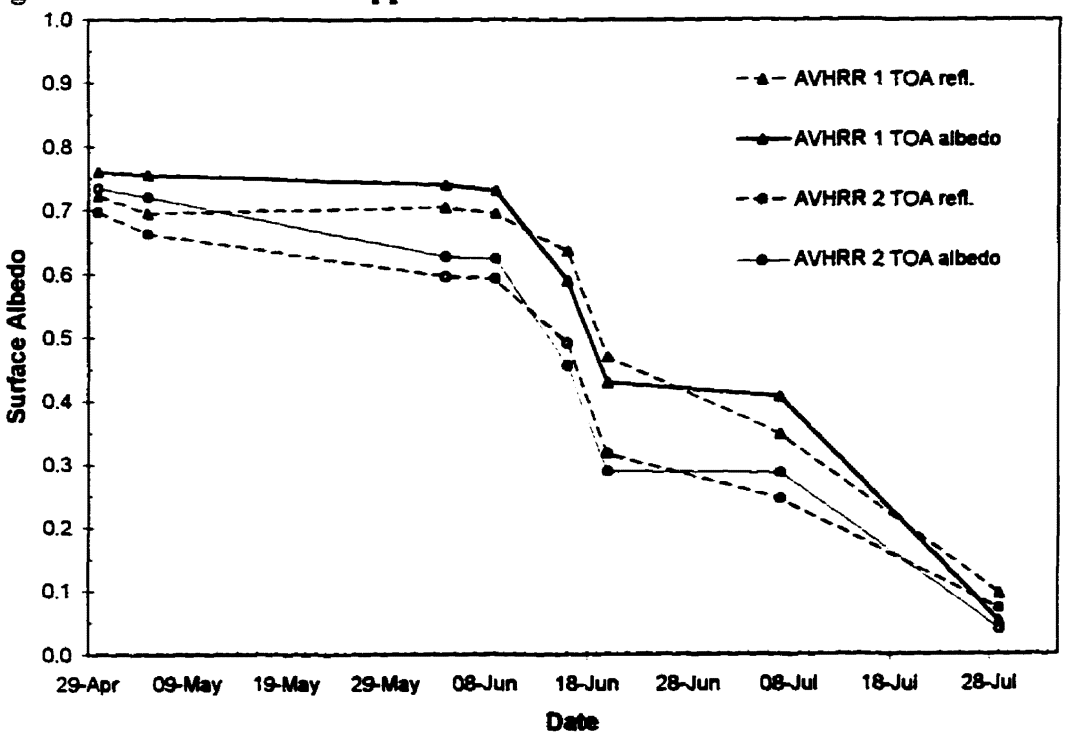
Although these factors were designed to correct data used to measure the Earth's radiation budget at scales of 2.5° x 2.5°, they have been applied to TOA reflectance data collected over non-uniform surfaces by other sensors operating within the solar spectrum at finer resolutions (Koepke and Kriebel, 1987; De Abreu, 1993; Lindsay and Rothrock, 1994). This is true of this investigation and as expected, there are caveats regarding the

Table 4.8 Conversion of AVHRR 1 and 2 TOA reflectance to TOA albedo via anisotropic correction factors. TOA reflectances from dates with positive difference underestimate TOA albedo.

Date	TOA Reflectance		f [+]	TOA Albedo		Diff / % Diff. [++]	
	1	2		1	2	1	2
30-Apr	0.72	0.70	0.95	0.76	0.73	0.04 / 5.3	0.04 / 5.3
03-May	0.70	0.66	0.92	0.76	0.72	0.06 / 8.7	0.06 / 8.7
04-Jun	0.70	0.60	0.95	0.74	0.63	0.04 / 5.3	0.03 / 5.3
09-Jun	0.69	0.59	0.95	0.73	0.62	0.04 / 5.3	0.03 / 5.3
16-Jun	0.64	0.49	1.08	0.59	0.46	-0.05 / -7.3	-0.04 / -7.3
20-Jun	0.47	0.32	1.09	0.43	0.29	-0.04 / -8.7	-0.03 / -8.7
07-Jul	0.35	0.25	0.86	0.41	0.29	0.06 / 16.8	0.04 / 16.7
29-Jul	0.09	0.07	1.84	0.05	0.04	-0.04 / -45.7	-0.03 / -45.7

[+] Same anisotropic reflectance function used for channel 1 and 2
[++] Difference (Diff.) = TOA Albedo - TOA Reflectance
% difference (% Diff.) = Abs. Diff / TOA Albedo*100

Figure 4.7 Effects of ARF application to TOA AVHRR 1 and 2 reflectances



application of the dataset to AVHRR sea ice data. These will be discussed in a later section.

4.7 Atmospheric Correction

Since the Earth's atmosphere is most transparent in the visible part of the solar spectrum, the most obvious use of satellite data is the observation of the Earth's surface at visible wavelengths (Lenoble, 1993). However attenuation mechanisms of the intervening atmosphere can significantly perturb the reflected signal as it travels back to the sensor. As a result, the flux measured by a satellite at the TOA should be considered representative of the surface and the atmosphere. Thus, in order to utilize TOA measurements to estimate surface variables, the attenuation of the overlying atmosphere must be accounted for and removed. This process of removing atmospheric effects, which essentially converts a TOA-measured flux to a surface flux, is commonly referred to by the remote sensing community as *atmospheric correction.* In previous work, the remote sensing community has attempted to bypass atmospheric correction of AVHRR data by constructing channel indices (Vermonte *et al.*, 1995). These indices, like the Normalized Difference Vegetation Index (NDVI), normalize image data and thus reduce atmospheric effects. Further reductions were garnered through image compositing techniques (Cihlar *et al.*, 1994). However, in order to derive accurate values of surface radiation budget variables, such as albedo, atmospheric correction is a necessary pre-analysis step.

The following section begins by briefly describing the two atmospheric attenuation mechanisms relevant to the atmospheric correction of AVHRR visible and near-infrared data -- scattering and absorption by atmospheric constituents. The theory behind atmospheric correction is illustrated using analytical expressions that approximate the interaction of incident and reflected radiation with an atmosphere under a sensor at the TOA. The implementation of atmospheric correction in the AVHRR sea ice dataset is described and the results are presented.

4.7.1 Atmospheric Attenuation

This section briefly introduces the concept of atmospheric scattering and atmospheric absorption. In the visible/near-infrared spectrum, these are the two mechanisms that attenuate incident and reflected solar radiation. Of specific interest is the effect of these mechanisms on the transmissivity of the atmosphere within the spectral bandpass of AVHRR 1 and AVHRR 2.

4.7.1.1 Atmospheric Scattering

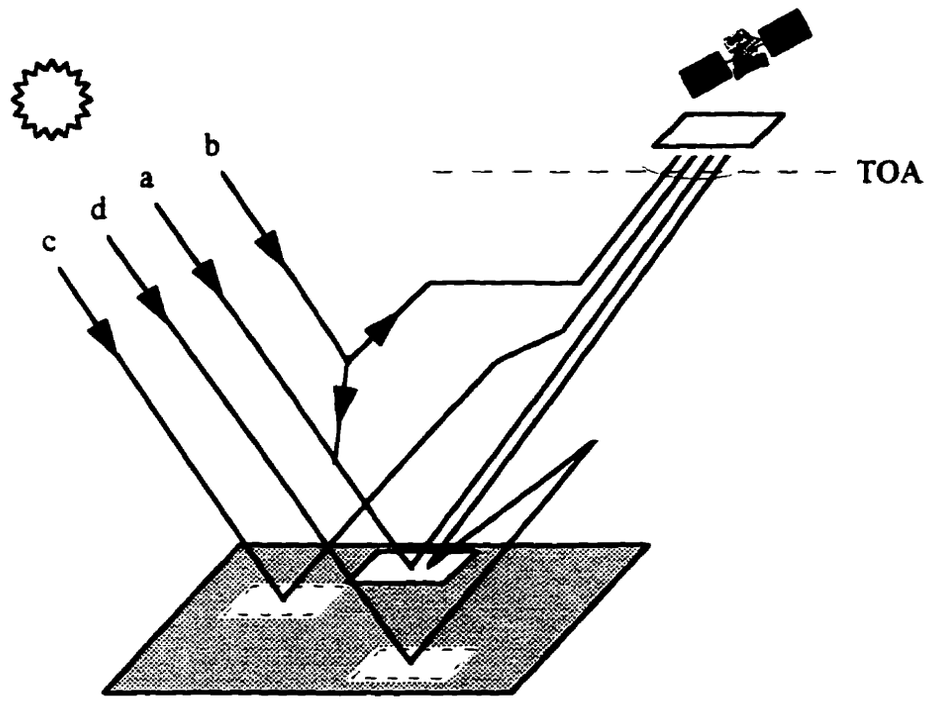
Radiation propagating through the atmosphere interacts with particles as small as molecules and as large as raindrops. When this interaction changes the direction of propagation of the incident radiation, or diffuses it, without changing its frequency, this mechanism is referred to as scattering. Scattering is dependent on the following (Slater, 1980):

(1) the size distribution of the scattering elements,
(2) the composition and concentration of the scatterers, and
(3) the wavelength of the radiant flux incident on the elements .

Radiation traveling along the sun-surface path and the surface-sensor path is scattered by the Earth's atmosphere. Figure 4.8 illustrates the potential effects of scattered radiation on the signal recorded by a TOA satellite sensor. Vector *a* represents the direct solar and reflected flux that does not experience scattering. Vector *b* represents the diffuse solar radiation that is scattered out of the atmosphere and into the path of the sensor. Also shown is down-scattered flux that can contribute to the direct solar flux (vector a). Vector *c* represents radiation that is reflected by adjacent surfaces into the surface-sensor path. This environmental effect can be ignored if the surface is homogeneous, but is considered a perturbation to the signal if the surface is heterogeneous in nature. Finally

vector *d* represents radiation backscattered by the atmosphere and ultimately contributes to the illumination of the target. The main effect of atmospheric scattering on satellite data occurs along vector b, the addition of scattered radiation to the recorded radiance. The major cause of this scattering is the presence of air molecules (Rayleigh scattering) and aerosols.

Figure 4.8. Scattering processes in the atmosphere



Rayleigh's theory is commonly used to describe the scattering of solar radiation by air molecules. This theory assumes that scattering particles are less than 1/10th the wavelength of incident light. Rayleigh scattering occurs generally in the first 8 km of the atmosphere and is easily accounted for given the sun-satellite geometry and elevation of the target (Iqbal, 1989). Rayleigh-scattered radiation is distributed evenly in the forward and backward directions.

An aerosol is defined here as a small solid or liquid particle that is suspended in the atmosphere and follows the motion of the air (Iqbal, 1989). These particles commonly reside in the lower troposphere and stratosphere. The material content, concentration, size, and distribution of aerosols vary widely making their distribution extremely difficult to predict. Aerosol radii and concentration cover ranges of 8 and 30 orders of magnitude respectively (Jaenicke, 1984). Aerosols scatter incident solar radiation in a manner that is dependent on their optical characteristics.

4.7.1.2 Atmospheric Absorption

Atmospheric absorption describes the process whereby radiant energy incident on an atmospheric particle is absorbed and emitted as thermal radiation. In remote sensing, incident or reflected radiation propagating through the atmosphere is absorbed by gases and aerosols within the intervening atmosphere. The major absorbing gases within the solar spectrum are oxygen (O_2), ozone (O_3), water vapour (H_20), carbon dioxide ($C0_2$), methane (CH_4) and nitrous-oxide (N_20) (Vermote et al., 1994). The atmospheric gases O_2, CO_2, CH_4 and N_2O are considered constant and uniformly mixed in the atmosphere. Conversely, O_3 and H_2O are considered to be spatially and temporally variable and thus more difficult to characterize. Most sensors are designed to avoid collecting data at wavelengths where gaseous absorption is prevalent. However, as will be shown with AVHRR, some sensors are affected by atmospheric absorption.

The other potential absorbers of solar radiation in the atmosphere are aerosols. Most tropospheric aerosols consist of non-absorbing material (Bohren and Huffman, 1983) and thus are usually not considered a major absorption agent in remote sensing operating in the solar range. However, particles that contain carbon, such as soot, are very absorptive in the solar spectrum and as will be shown, their presence must be considered when correcting satellite data for atmospheric attenuation.

4.7.2 Theory of Atmospheric Correction

Simply stated, atmospheric correction attempts to reconstruct the original radiance leaving the surface in the direction of the satellite sensor by accounting for the major attenuating mechanisms along the atmospheric path to the sensor. The following section uses analytical expressions taken from Vermote *et.al.* (1994) to theoretically describe the attenuation of the reflected satellite signal and the determination of surface albedo from TOA radiance measurements over a lambertian surface.

A satellite sensor at the top of the atmosphere records radiation reflected from the Earth-atmosphere (E-A) system. The use of satellite TOA radiances to measure surface albedo is based on the assumption that the signal received at the sensor is composed largely of radiation reflected from the surface and that the perturbing effects of the atmosphere can be adequately separated from this surface signal. Symbolically, the radiance recorded at the satellite (L_{TOA}) can be decomposed into two contributing terms:

$$L_{TOA}(\theta,\theta',\phi) = L_a(\theta,\theta',\phi) + L_s(\theta,\theta',\phi) \qquad [4\text{-}10]$$

where L_s is the radiance reflected from the target surface and L_a is radiation scattered from the atmosphere. L_a is commonly referred to as *path radiance*[16]. By assuming the surface to be a uniform lambertian reflector, the target surface radiance can be expanded as follows:

$$L_{TOA}(\theta,\theta',\phi) = L_a(\theta,\theta',\phi) + \frac{E_{TOA}u\rho_s(\theta,\theta',\phi)T}{\pi[1-\rho_s(\theta,\theta',\phi)s]} \qquad [4\text{-}11]$$

[16] Although not explicitly stated, all variables in this discussion are assumed a function of spectral channel.

where E_{TOA} is the solar spectral radiance incident at the top of the atmosphere integrated over the sensor channel, u is the cosine of the solar zenith angle ($\cos\theta$), $\rho_s(\theta,\theta',\phi)$ is the surface reflectance within the sensor channel, T is the total (direct and diffuse) two-way transmittance of the atmosphere due to scattering and absorption, and s is the reflectance of isotropic light entering from the base of the atmosphere.

In terms of scattering, the total transmittance (T) along an atmospheric view angle (θ') is a product of the direct (T_D) and diffuse (T_d) transmittance:

$$T(\theta') = T_D(\theta') + T_d(\theta') \qquad [4\text{-}12]$$

The variation of direct atmospheric transmittance with viewing angle can be expressed according to Bouguer's law, :

$$T_D(\theta') = e^{-\tau_A \cdot \cos\theta'} \qquad [4\text{-}13]$$

where τ_A is the total optical thickness of the atmosphere. In terms of the Earth's atmosphere, the optical thickness can be subdivided into the following components (Saunders, 1990):

$$\tau_A = \tau_a + \tau_r + \tau_g \qquad [4\text{-}14]$$

where τ_a, τ_r and τ_g are the mean aerosol optical depth, the Rayleigh optical depth and the mean optical depth due to gaseous absorption respectively. τ_g includes absorption due to water vapour, mixed gases and ozone.

By combining [4.10] and [4.11] and by normalizing [4.11] by the incident solar radiance ($E_{TOA}\,u$), the satellite reflectance at the TOA (ρ_{TOA}) can be expressed:

$$\rho_{TOA}(\theta,\theta',\phi) = T_g\left[\rho_a(\theta,\theta',\phi) + \frac{T_t\rho_s(\theta,\theta',\phi)}{[1-\rho_s(\theta,\theta',\phi)s]}\right] \qquad [4\text{-}15]$$

where ρ_a is the atmospheric reflectance measured at TOA. In the above formulation, scattering and absorption effects are decoupled into T_t, the two-way transmittance due to scattering and T_g, the two-way transmittance due to gaseous absorption. In fact, these processes are somewhat interdependent. Since the Vermote *et. al.* (1994) formulation used here is designed for operational atmospheric correction, this coupling cannot be explicitly considered in lieu of a time-consuming, full radiative transfer algorithm. This decoupling and its consequences are examined in detail by Tanre *et al.*, (1992) and Tanre *et al.* (1995). The error is considered to be less than one percent with solar zenith angles less than 84°. In the process of this decoupling, the gaseous transmission function is only evaluated for sun-target-satellite direct paths.

Re-arranging [4.15], the surface reflectance can be expressed by:

$$\rho_s = \frac{y}{[1 + y \cdot s]} \qquad [4\text{-}16]$$

where

$$y = \frac{\frac{\rho_{TOA}(\theta,\theta',\phi)}{T_g} - \rho_a(\theta,\theta',\phi)}{T_t} \qquad [4\text{-}17]$$

Thus, given the satellite-measured TOA reflectance, the inversion of surface reflectance requires specification of the reflectance of the atmosphere and the two-way transmittance of the atmosphere at time of satellite overpass. In the following section, the atmospheric factors that effect the transmissivity of the atmosphere to incident and reflected radiation in the wavelength ranges of AVHRR 1 and 2 are examined.

4.7.2.1 Atmospheric Transmissivity for AVHRR 1 and 2

In order to examine the factors affecting TOA radiances measured by AVHRR 1 and 2, the effects of ozone, aerosols and water vapour on atmospheric transmissivity are modelled. Similar experiments can be found in Saunders and Edwards (1989) and Tanre *et al.* (1992) with different radiative transfer models constrained by different atmospheres. The LOWTRAN 7 radiative transfer model (Kneizys *et al.*, 1988) was used to model the atmospheric transmissivity within AVHRR 1 and 2. By using a wide range of atmospheric models, LOWTRAN is capable of calculating path radiances, atmospheric transmissivity and direct spectral irradiance under a variety of atmospheric conditions at a spectral resolution of 20 cm^{-1}. The model's sub-arctic atmospheric profile was selected with a solar zenith angle of 60 degrees. The code was run for both summer and winter seasons. These two model seasons approximate the range of water vapour content and ozone content similar to that found in this investigation. The simulations were constrained by the aerosol conditions described in Table 4.9. The winter lower troposphere (0-2 km) aerosol model was customized to reflect arctic haze conditions using aerosol optical properties provided in Shaw *et al.* (1993). Within AVHRR 1 and 2, the haze model corresponds to aerosol optical depths of 0.53 and 0.34 respectively.

Integrated transmittances based on the AVHRR 1 and 2 filter functions were calculated for each attenuator in the atmosphere. The resultant channel transmittances for the most significant attenuators -- air molecules (Rayleigh), aerosols, ozone and water vapour -- are provided in Table 4.10. The results are shown graphically in Figure 4.9. A transmittance of 0 refers to a totally opaque atmosphere and a transmission of 1 refers to a totally transparent atmosphere. It is apparent that atmospheric transmissivity and the controlling mechanisms vary between the two channels and between the two seasons.

In AVHRR 1 aerosol scattering and to a lesser extent, aerosol absorption are the most significant extinction mechanisms. Ozone absorption and Rayleigh scattering also decrease AVHRR 1 transmissivity. Rayleigh scattering and ozone absorption are for the

most part seasonally invariant and spatially conservative. Therefore, of these three attenuators, they are the most easily accounted for. Water vapour has very little effect in AVHRR 1 and can be ignored. Seasonally, winter haze events can significantly decrease atmospheric transmissivity in both channels. The effects of haze will be discussed further in following sections.

Table 4.9 Aerosol Models used in Transmissivity Modelling

Layer	Winter	Summer
Lower Troposphere	arctic haze	tropospheric
Upper Troposphere	tropospheric	tropospheric
Stratosphere	moderate/aged volcanic	moderate/aged volcanic

Table 4.10 Atmospheric transmittances integrated over AVHRR Chn. 1 and 2

Mechanism	AVHRR Channel			
	1		2	
	Winter	*Summer*	*Winter*	*Summer*
Rayleigh	0.89	0.89	0.96	0.96
Ozone	0.94	0.94	1.00	1.00
Water Vapour	0.99	0.98	0.94	0.87
Aerosols	0.59	0.73	0.71	0.80
TOTAL *	0.49	0.60	0.62	0.65

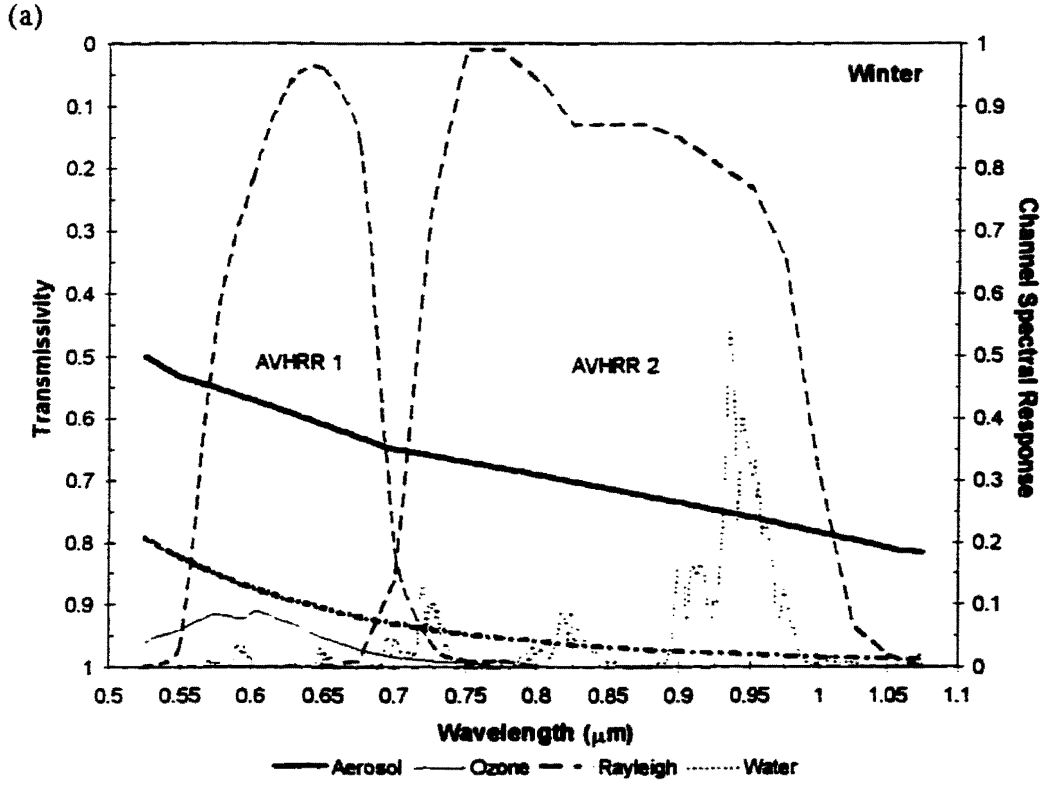
* Represents all attenuators in the atmosphere, i.e. includes attenuators not included in table

Source: Modelled via LOWTRAN 7: Sub-Arctic profile, solar zenith angle=60°, spectral resolution 20 cm-1; O_3 amount: winter=0.32 cm NTP, summer=0.27 cm NTP; H_2O content: winter=0.65 g/cm^2, summer=3.3 g/cm^2; aerosol type = *winter*: lower troposphere (0-2 km) - haze (after Shaw *et al.*, 1993), upper troposphere - tropospheric, stratosphere - moderate/aged volcanic; *summer*: troposphere-tropospheric, stratosphere - moderate/aged volcanic.

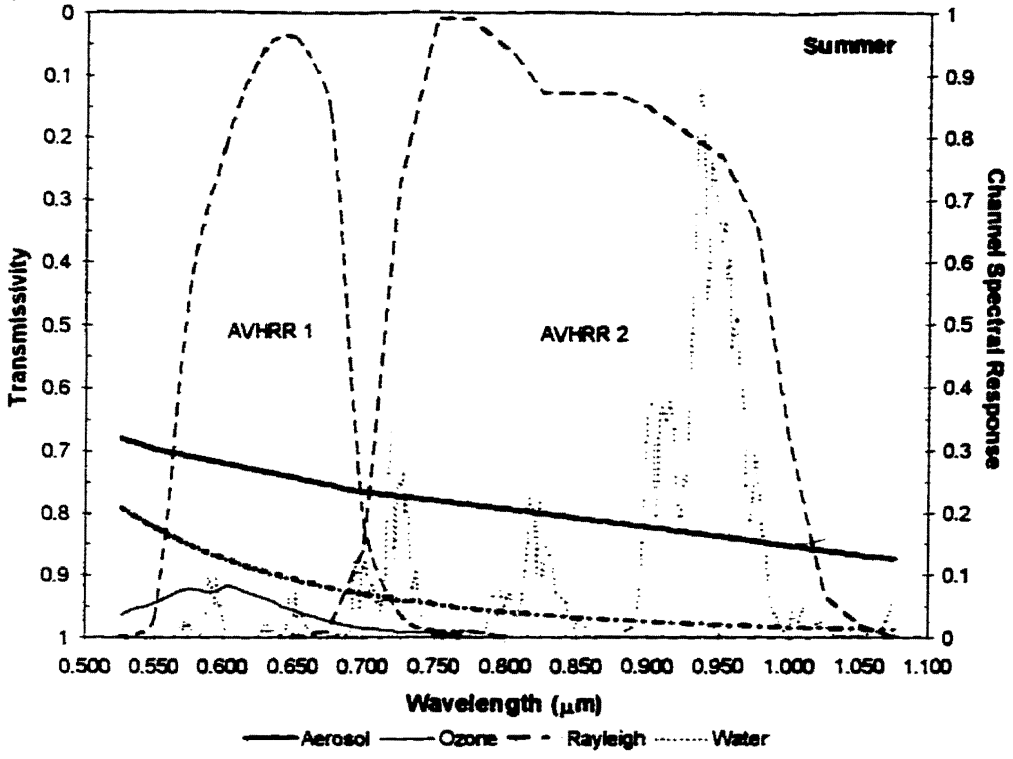
Within AVHRR 2, water vapour absorption and aerosol attenuation are the primary mechanisms controlling atmospheric transmissivity. Since Rayleigh and aerosol scattering are proportional to wavelength, their influence decreases in AVHRR 2. The influence of ozone is negligible in this channel. The atmosphere's transmissivity due to water vapour varies inversely with the seasonal water vapour content in the arctic atmosphere. Transmission is higher during the winter months when the atmosphere is drier and decreases significantly in the summer months when the atmosphere's water content is higher.

Ozone, water vapour and aerosols are significant factors controlling the extinction properties of the atmosphere in the spectral regions of AVHRR 1 and 2. For the most part, the transmissivity of the atmosphere decreases with increasing solar zenith angle. The long path lengths that accompany large solar zenith angles increase the opportunity for atmospheric attenuation.

Figure 4.9. Atmospheric Transmission within AVHRR Channels 1 and 2



(b)



The success of atmospheric correction is dependent on the procedure's ability to accurately estimate the magnitude and characteristics of these atmospheric attenuators during image acquisition. The following section describes the methods used in this investigation to estimate ozone, water vapour and aerosol content of the atmosphere during satellite overpass times. Since Rayleigh scattering is predictable and easily accounted for, it is not considered further.

4.7.3 In Situ Atmospheric Measurements

Critical to atmospheric correction of image data is the availability of a priori information regarding the following:

(1) illumination and viewing geometry (preferably for each pixel), and

(2) atmospheric conditions for the scene (ozone amount, aerosol optical depth and water vapour amount).

The acquisition geometry information is often included in the satellite's data stream and easily accessible. In the case of this AVHRR dataset, these ancillary data were available on a pixel by pixel basis.

In Teillet (1992) and Tanre *et al.*(1992), various sources of atmospheric information for correction of AVHRR images are recommended. Optimally, these data should be acquired from the satellite scene itself. Unfortunately, methods for extracting such data are few, often inappropriate for polar regions and most require further validation. Future sensors like MODIS will utilize scene-based atmospheric data derived from its own bands for atmospheric correction. Today, atmospheric correction schemes commonly utilize either coincidental ground-based measurements or more likely, climatological data of the required atmospheric variables. In this investigation, *in situ* atmospheric measurements coincidental to the image acquisition will be used as initialization data for the atmospheric correction. The following section describes the measurement of ozone amount, aerosol optical depth and water vapour content. The final inputs to the atmospheric correction schemes are presented in Table 4.11.

4.7.3.1 Ozone Amount

Although dependent on latitude and season, compared to water vapour and aerosols, atmospheric ozone content can be considered relatively invariant. Ozone is currently measured by a world-wide network of monitoring stations and climatological ozone information is readily available. While satellite information on ozone is also available (Keating *et al.*, 1989), the benefits of incorporating such data would have to be weighed against the processing effort, the accuracy of the dataset and the overall importance of

ozone in the correction scheme. The sensitivity of AVHRR-derived surface albedos to ozone amount will be assessed later.

Total column ozone amount is measured twice daily at the AES Resolute weather station. These data, along with similar data from stations around the world, are published annually in *Ozone Data For the World* (AES, 1993). Ozone data for overpass events were extracted from the 1993 dataset and are included in Table 4.11. As shown in Table 4.11, arctic ozone values peak in the winter and early spring and begin to decrease in the spring.

Table 4.11 Inputs to Atmospheric Correction

Date	Water Vapour (cm precipitable H_2O)	Ozone (column Amt. - cm NTP)	Aerosol Optical Depth (@ 0.55 μm)
April 30	0.29	0.410	0.14
May 3	0.38	0.402	0.14
June 4	1.10	0.339	0.09
June 9	1.18	0.354	0.10
June 16	1.53	0.349	0.10
June 20	1.73	0.338	0.10
July 7	2.05	0.307	0.05
July 29	2.74	0.279	0.05

4.7.3.2 Water Vapour Content

The transmission modelling in 4.9(b) suggests that in order to estimate surface albedo in channel two, an estimate of the water vapour content of the atmosphere at time of image acquisition is desirable. Teillet (1992) reviews various sources of regular information suitable for the correction of water vapour in AVHRR data. These sources can be broadly classified as climatological, radiosonde and satellite data. Climatological datasets provide

seasonal, latitude-dependent data. Radiosonde data provides information on the vertical distribution of water vapour in the atmosphere. Unfortunately, the world wide network is irregular, sparse and data retrieval can be cumbersome. Tanre *et al.* (1992) suggest a climatology derived from GCM modelled results based on radiosonde data, but acknowledges that the accuracy of such an approach would be poor given the scarcity of data over remote regions.

The ability to extract water vapour amounts from satellites is attractive. Carelton (1991) provides a thorough review of the satellite retrieval of atmospheric water vapour. Justice *et al.* (1991) utilize an empirical relationship between the difference between AVHRR channel 4 and 5 and water vapour content. The approach is highly sensitive to location and its applicability to polar regions remains to be investigated. The TIROS platform which carries the AVHRR also carries the TOVS (TIROS-N Operational Vertical Sounder) sensor which includes both an infrared (HIRS/2) and microwave (MSU) sounding instrument. TOVS commonly provides information on water vapour patterns only in the mid to upper troposphere. Microwave instruments with their penetrating capabilities are more capable of providing moisture information at all column levels, thus making them more useful in the correction of satellite data (Prabhakara *et al.*, 1982)

In order to estimate the atmospheric water vapour content on overpass days, this investigation utilizes radiosonde data collected twice daily (00:00 and 12:00 hours GMT) at the nearby AES Resolute, N.W.T. weather station (Figure 3.8). Temperature and relative humidity data were extracted from AES radiosonde data for the 12:00 GMT launch (0700 hrs local time) on overpass days. A common way of expressing the amount of water vapour in a column of air is the calculation of precipitable water (w). Precipitable water can be described as the thickness of the liquid water that would be formed if all of the water vapour in a vertical column were condensed at the surface of a unit area (Iqbal, 1983). Precipitable water can range from 0.1 cm for a very dry atmosphere to 5 cm for a humid atmosphere. Since data beyond the altitude of 12 km were inconsistent between overpass dates and given that very little water vapour exists beyond this level, the

precipitable water was calculated for the 0-12 km column. Data for this column were extracted and the precipitable water amount (w) for the vertical column was calculated by:

$$w = \int_0^{12} \vartheta_v dz \qquad [4\text{-}18]$$

where ϑ_v is the absolute humidity (mass of water vapour per unit volume of air) in kg/m^3 and z is the height of the layer. The precipitable water amounts for each overpass day are shown in Table 4.11.

The calculated precipitable water amounts illustrate the wide seasonal variability of atmospheric water vapour in the Arctic Archipelago. Early in the spring, the atmosphere was very dry with precipitable water vapour amounts around 0.35 cm. Melting sea ice and the injection of moist air from southerly latitudes increased water vapour amounts in June to approximately 1.5 cm. In July, when the ice had broken up and open water was ubiquitous, water vapour amounts climbed to > 2 cm.

4.7.3.3 Aerosol optical depth

Due to its high degree of variability in radiative characteristics and distribution, the effect of aerosol attenuation is the most difficult atmospheric variable to estimate for the atmospheric correction of satellite data. The amount and characteristics of stratospheric aerosols are considered to be relatively static compared to those inhabiting the troposphere. The tropospheric aerosols in the first 2 km display the widest range of variability in content and type. As a result, this regime is the hardest to characterize. The amount of aerosols in an atmospheric layer is often expressed in terms of extinction, that is as the aerosol optical depth of the layer. Clear-sky aerosol optical depths can range from 0.05 for a very clear, non-turbid atmosphere to greater than 0.4 for a hazy, turbid atmosphere.

An optimal atmospheric correction strategy would require scene-based identification and knowledge of the following characteristics of aerosols present in the intervening atmosphere: optical thickness, phase function and single scattering albedo. Future sensors may incorporate such schemes, but present day schemes are forced to rely on climatological aerosol information. These types of data are scarce for much of the world, but especially so for tropical and polar regions. Regardless, the use of climatological information is questionable given the variant effects of aerosol masses in both the Arctic's troposphere and stratosphere. As will be shown, the influence of aerosols on AVHRR 1 and 2 data is large and thus requires close attention in atmospheric correction schemes. This section begins by briefly describing the Arctic aerosol regimes that have the potential to affect AVHRR measurements of surface albedo. The method employed here to estimate aerosol content for the correction of the 1993 AVHRR dataset is described. The resultant aerosol optical depths for the overpass dates are presented in Table 4.11.

4.7.3.3.1 Arctic Aerosol Regimes

Freund (1983) identified three major regimes of arctic aerosols -- all found to be relevant to this investigation. The first regime is the spring loading of the lower troposphere (< 2 km) by anthropogenic particles originating from lower latitudes. The second regime, also tropospheric, is a result of airborne crustal material appearing when snowcover melts from the surrounding land masses in the archipelago. The final regime is the background or stratospheric regime that has been regarded as optically thin ($\tau_a = 0.05$) and invariant. Volcanic activity this decade has proved this characterization to be false. Another arctic aerosol regime, not identified by Freund (1983) but potentially relevant to this investigation, is lower tropospheric ice crystals or "diamond dust" which form within the lower 2 km of the atmosphere.

Arctic Haze

Although once thought of as a pristine environment in terms of atmospheric conditions, the opacity of the Arctic's springtime atmosphere has been shown to occasionally rival that of a large urban centre. This seasonal loading of the atmosphere presents significant obstacles to the correction of satellite data collected during these episodes. Studies have shown that during the winter and spring, the arctic aerosol is composed of significant amounts of anthropogenic material, primarily soot (graphitic carbon) (Barrie *et al.*, 1981; Shaw, 1982). The source of this seasonal increase in atmospheric soot is lower-latitude industrial regions. The layered characteristics of the aerosol's distribution and the resultant reduction in visibility has led to this annual phenomenon to be labeled *arctic haze*. During the winter and spring, the clear-sky atmospheric aerosol optical depth is commonly 0.1-0.3, a range more typical of urban environments. This range is consistent with those shown in Table 4.11. This regime begins to dissipate with the onset of melt conditions (May and June). The reasons for this decrease are likely twofold. Increased springtime precipitation, especially drizzle from low level stratus clouds, scavenges out aerosols, thus decreasing its load (Barrie *et al.*, 1981). Also, the establishment of a more zonal (latitudinal) flow in the northern hemisphere as summer approaches reduces the exchange of aerosols from turbid centres in the south (Smirnov *et al.*, 1994).

Of particular significance to this study is the opacity of soot to visible radiation. While most atmospheric aerosols have single scattering albedos[17] (SSA) approaching unity at visible wavelengths, soot is considered a strong, wavelength-dependent absorber with a SSA of <0.2 (Blanchet, 1989). The overall effect of soot is to decrease the aerosol's overall SSA in an amount that is proportional to its relative mass. The optical properties of arctic aerosols have been determined through observation (Clarke et al., 1984; Barrie et al., 1981) and theoretical modelling (Blanchet and List, 1984). The airborne observations of Clarke et al. (1984) have shown that the SSA range for dry air arctic aerosols in the first 5 km of the atmosphere is 0.77-0.93 (at 550 nm). This mean of 0.86 agrees with

[17] Single scattering albedo (0-1) refers to the probability that a photon intecepted by a particle will be scattered rather than absorbed.

modelled results for dry air (Blanchet, 1989) and with observed and modelled results at Resolute N.W.T. (McGuffie *et al.*, 1985).

Background Stratospheric

In comparison to the highly variable tropospheric aerosol masses, aerosols in the stratosphere (background aerosols) appear relatively invariant. However, in the last 15 years, volcanic activity and new observational techniques has shown the optical properties of the upper atmosphere to be far from static. The eruption of volcanoes, like El Chichon in 1982 and Mount Pinatubo in 1991, inject large quantities of SO_2 straight into the stratosphere. The injected material reacts directly with incident irradiation changing the radiative balance of the E-A system. The presence of volcanic material increases the background optical depth in the Arctic. Airborne photometer measurements collected during the 1992 Lead Experiment (LEADEX) in the Beaufort Sea revealed stratospheric optical depths of approximately 0.1, which is a magnitude higher than normal. These larger than normal optical depths are attributed to suspended volcanic ash in the lower stratosphere that originated from the 1992 eruption of Mt. Pinatubo in the Philippines (Stone et al., *in press*). The reduced transparency of the atmosphere is thought to be responsible for the global cooling experienced after the eruption.

Figure 4.10 shows a time series of polar aerosol optical depths from 2 km and upwards measured by SAM II (Stratospheric Aerosol Measurement II). The immediate and long term effects of volcanic activity is evident. Aerosol optical depths returned to pre-1979 background levels 8 years after the 1982 El Chichon eruption (McCormick *et al.*, 1994). Given that the Mt. Pinitubo eruption injected three times as much material into the atmosphere in 1991, it is reasonable to say that this aged volcanic material continues to augment the aerosol optical depths measured today and in 1993, the year of data collection. Episodic sources of aerosols, like volcanic activity, warrant caution when applying background values of Arctic aerosol optical depths based on climatological values.

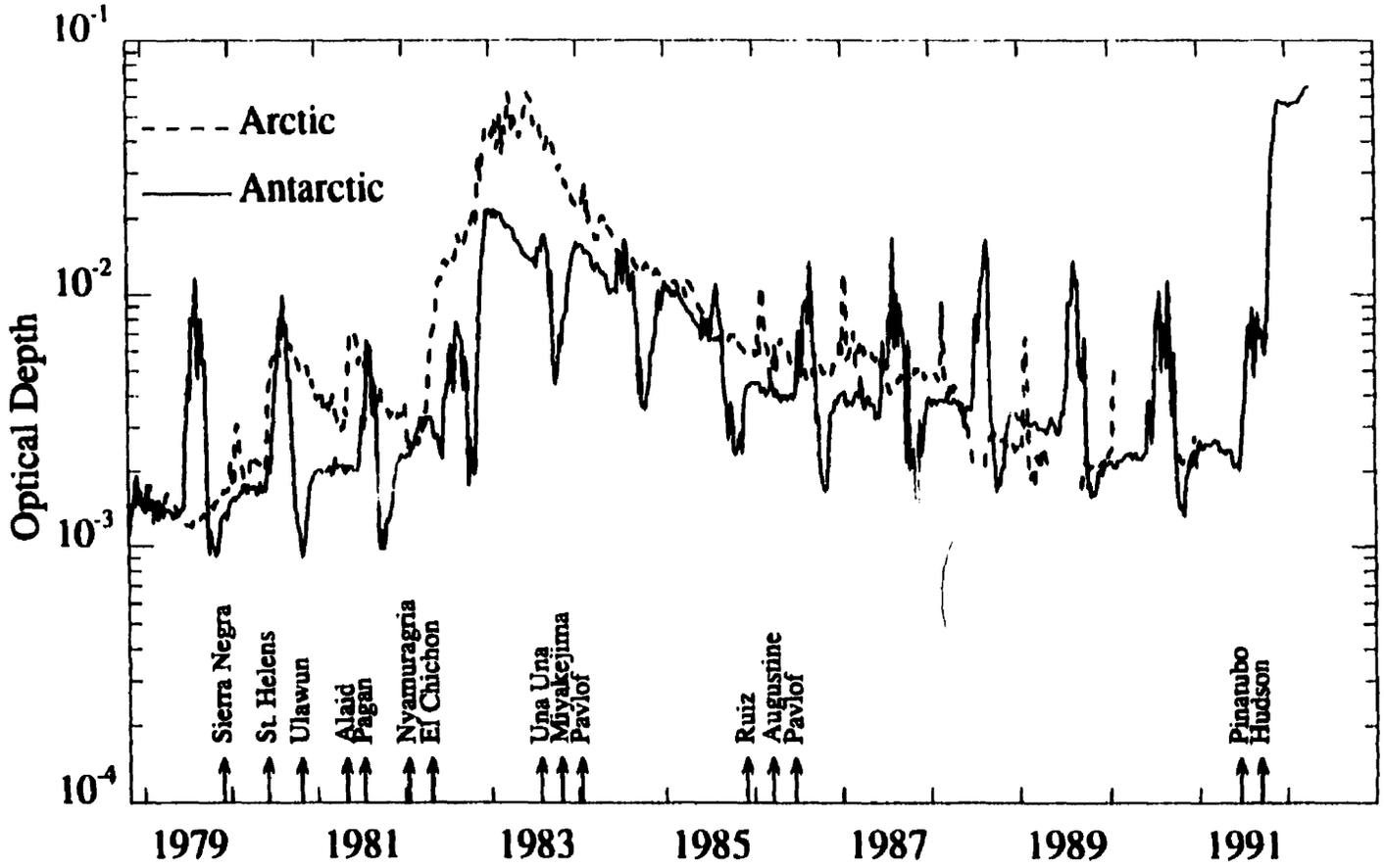


Figure 4.10 SAM II weekly average aerosol optical depths @1.0 μm at high latitudes. Arrows indicate volcanic eruptions throughout period. Source: McCormick *et al.*, (1993).

Lower Atmosphere Ice Crystal Precipitation

During the cold half of the year in polar regions, ice crystal precipitation commonly occurs within the lower troposphere. Ice crystal precipitation (ICP) has been observed to have a winter frequency of approximately 50% and to occur primarily within 1 km from the surface (Curry et al., 1990) ICP or "diamond dust" forms mainly as a result of isobaric cooling in atmospheres with temperatures lower than -15° to -20° C (Wilson et al., 1993). ICP events were regularly observed during SIMMS '93 under clear-sky conditions in April and early May. While the effect of ice crystal precipitation on the surface energy balance (Overland and Guest, 1991) and on satellite response in the thermal channels (Stone and Key, 1993) has been investigated , little attention has been given to its effect on shortwave satellite imagery.

Crustal Material

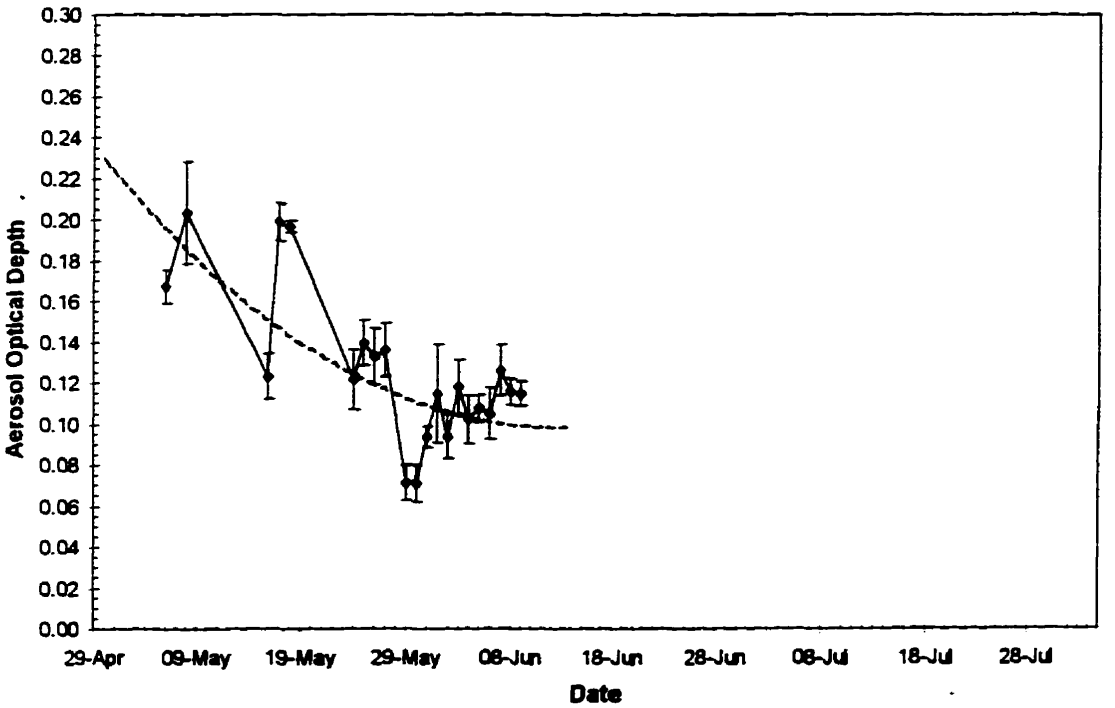
Snow free land of archipelago land masses in the Arctic is a significant source of aerosols in the warmer spring and summer months. Wind-blown crustal material contributes to the aerosol mass in the lower troposphere. While their residence time is low, this terrestrial aerosol source may prevent optical depth levels from returning to low background levels after the Arctic haze effects have dissipated in late spring.

4.7.3.3.2 Sun photometer measurements

Sun photometers are used to measure direct solar irradiance, often with the purpose of retrieving total atmospheric optical depth. These instruments usually consist of a silicon photoelectric detector in a tube capable of collimating incident light. Filters are usually employed to focus measurements in wavelength intervals free from gaseous absorption (*atmospheric windows*). The measurement of direct incident irradiance allows the estimation of atmospheric extinction and relatedly, total atmospheric optical depth. Theoretically, by accounting for the Rayleigh and ozone optical depths, the residual extinction is attributed to aerosols and serves as an estimate of aerosol optical depth.

In SIMMS '93, Serreze *et al.* (1993) collected sun photometer measurements at two wavelengths, 0.38 μm and 0.50 μm, during clear-sky events between May 6 and June 9. Measurements consisted of a sample of six to ten photometer readings. The instrument was re-calibrated after returning from the field and it showed no drift from its absolute calibration at Mauna Loa, Hawaii. The total optical depth measurements were corrected for Rayleigh scattering, ozone absorption and changes in relative airmass. Figure 4.11 shows the variation of daily average aerosol optical depth within the time period spanned by the AVHRR coverage. These optical depth values are estimated by Serreze *et al.* (1993) to be accurate to 0.02 or less than 10% of the values.

Figure 4.11 ***In situ*-measured daily average aerosol optical depths at 0.5 μm**



Note: Error bars = +/- one standard deviation

There is considerable day to day variability in the depth measurements, especially in May. This variability could be due to the movement of different synoptic systems in and out of the region. A trajectory analysis of dominant systems during the period may reveal the

cause of this variability in optical depths (Smirnov *et al.*, 1994). The simple trend line fitted to the data helps to show the general decrease in aerosol optical depth throughout the spring period. The increased presence of clouds and occurrences of precipitation in the late spring effectively remove aerosols from the atmosphere. Also increased synoptic activity improves the exchange of turbid air in the Arctic. In July, the aerosol optical depth is expected to level off at background stratospheric levels.

The measured data are compared in Table 4.12 with the results of previous studies of aerosol optical depths at Resolute, N.W.T. (Freund, 1983; McGuffie *et al.*,1985). These studies utilize pyranometer measurements to estimate aerosol optical depth using a simple transfer equation. The values presented in Table 4.12 have been adjusted to 0.55 μm according to the method described in the following section. Although limited in time, the surface measurements of spring 1993 for the most part are comparable with the results of the climatological studies. It should be noted that these climatological studies occurred prior to the volcanic activity discussed in the previous section and thus may not be representative of current conditions in the Arctic.

Table 4.12 Monthly average aerosol optical depths (0.55 μm) at Resolute, N.W.T.

Month	Freund (1983) 1978-1980	McGuffie et al. (1985) 1970-1979	SIMMS '93
April	0.15	0.19	
May	0.13	0.16	0.13
June	0.09	0.08	0.10*
July		0.04	

*based on June 1 to June 9

Aerosol depths derived from the sun photometer measurements were coincidental to the acquisition of the June 4 and June 9 AVHRR data. As shown in Figure 4.11, the optical

depth measurements only cover the middle of the spring season. There are no coincidental photometer measurements available for the rest of the AVHRR data. As such, the optical depth measured on May 6 is used for April 30 and May 3. Aerosol optical depths for June 16 and June 20 are assumed to be 0.1 based on the climatological studies and the values measured in the earlier part of the month. The aerosol depth values for July 7 and 29 are assumed to be 0.05 based on McGuffie *et al.*'s (1985) estimate. Although the value is likely low due to the residual effects of volcanic activity, it is accepted here in lieu of data to the contrary.

4.7.3.3.3 Spectral Adjustment of Aerosol Optical Depths

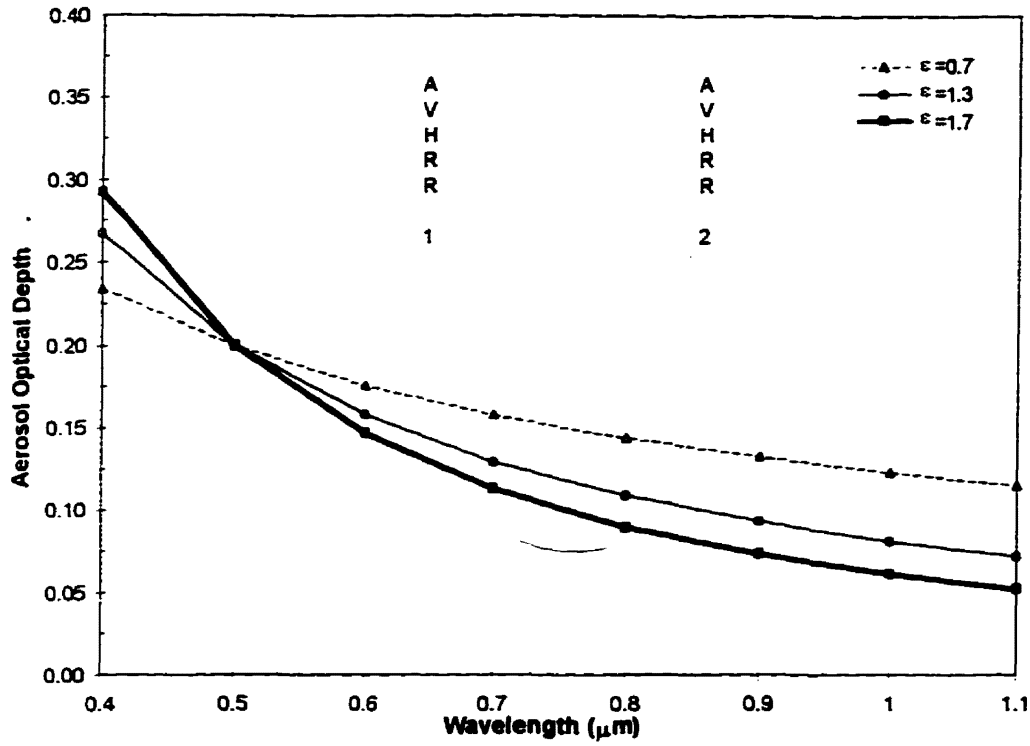
As with most atmospheric correction schemes, the aerosol optical depth is often required to be specified at one wavelength, usually 0.55 μm. In this investigation, aerosol optical depths are determined at 0.5 μm through observation. Therefore, some adjustment is necessary before these depths can serve as input to atmospheric correction schemes.

In Shaw (1982), the wavelength dependency of Arctic (and Antarctic) aerosol optical depth are empirically found to follow a power law relationship of the form

$$\tau_a(\lambda) = Q\lambda^{-\varepsilon} \qquad [4\text{-}19]$$

where Q is a constant and values of ε were found to range from 0.9 to 1.7 based on multiple wavelength sun photometer measurements. Based on an aerosol optical depth of 0.2 at 0.5 μm, Figure 4.12 shows the relationship between aerosol optical depth and the wavelength of incident radiation using ε coefficients of 0.9, 1.3 (midpoint of observed range) and 1.7. The effective centre wavelengths of AVHRR 1 and 2 are also identified. Since Shaw (1982) provides little information regarding the ε coefficient range, the midpoint value of 1.3 will be used. All calculated depths will be adjusted for a wavelength

Figure 4.12 Spectral Adjustment of Aerosol Optical Depth



of 0.55 μm using an ε of 1.3. The final aerosol optical depths at 0.55 μm for use in the atmospheric correction of the AVHRR data are included in Table 4.11.

4.7.4 Implementation of Atmospheric Correction

A wide variety of atmospheric correction techniques for visible and infrared satellite data have been developed over the years. The method and application of such schemes is dependent on the scope of data, the availability of a priori information regarding the state of the surface and overlying atmosphere, the availability of the acquisition geometry and finally, processing restraints. Theoretically, given the availability of the necessary ancillary information and a code that simulates radiative transfer of light through the atmosphere, [4.16] could be solved for each pixel in each image scene. Although possible for small scenes, such an approach requires considerable computing overhead for large scenes and multiple images.

A more common approach is to solve [4.16] for a variety of view geometries, atmospheric conditions and surface reflectances. A simple linear relationship describing the relationship between the TOA albedo to the surface albedo is then developed for a variety of atmospheric and view conditions. The required multiplicative and additive coefficients can be stored in multi-dimensional look-up tables for quick access. The appropriateness of such a scheme is dependent on the similarity between the atmospheric and surface conditions used to constrain the radiative transfer model from which the model coefficients were derived.

In this investigation, two methods for atmospheric correction were utilized:

(1) *Koepke Method*: a simple linear model relating AVHRR surface albedo to TOA albedo. Coefficients for the model are taken from Koepke's (1989) radiative transfer model results for various Earth surfaces under varying atmospheric conditions and at variable solar zenith angles;

(2) *Second Simulation of the Satellite Signal in the Solar Spectrum* or 6S radiative transfer code in inverse mode. After being initialized by an appropriate atmospheric and aerosol model, the 6S code provides surface albedo for a given TOA measured AVHRR albedo.

Both methods were used to correct the TOA albedos calculated in Section 4.6 to surface albedo by correcting for atmospheric effects.

4.7.4.1 Koepke Method

In Koepke (1989), a simple procedure to remove atmospheric effects from AVHRR 1 and 2 data is presented. The method takes advantage of the following linear relationship commonly used to estimate between TOA albedo (α_{TOA}) and surface albedo (α_s) (Chen and Ohring, 1984):

$$\alpha_{TOA} = a + b\alpha_s \qquad [4\text{-}20]$$

and vice versa:

$$\alpha_s = \frac{\alpha_{TOA} - a}{b} \qquad [4\text{-}21]$$

Since anisotropic correction has been applied to the satellite TOA reflectances (ρ_{TOA}), these are now equivalent to TOA albedos. Koepke and Kriebel (1987) point out that essentially the coefficient a describes the path radiance and b represents the mean effective two-way transmittance. Given the appropriate coefficients and the TOA albedo, surface albedo in each channel is economically calculated on a pixel by pixel basis.

The atmospheric model utilized in Koepke (1989) to determine the AVHRR coefficients is described in detail in Koepke and Kriebel (1987). The model accounts for all orders of scattering in the atmosphere and calculates radiances at wavelengths with $\Delta\lambda$=0.05 μm over the entire solar range. The radiances are integrated over the spectral response functions of AVHRR 1 and 2. The computation accuracy is better then 1.5% and the spectral radiances are calculated with an accuracy less than 1%. For each atmospheric case, the channel radiances are calculated at 25 zenith angles and 80 azimuth angles and integrated over the hemisphere to produce irradiances. Using band-weighted spectral irradiances (Neckel and Labs, 1981) and the calculated flux densities, the channel albedo at the top and bottom of the atmosphere is calculated. These albedos are calculated for a set of model atmospheres and the coefficients a and b are determined as intercept and slope of a linear regression. The model atmospheres represent both clear (τ_a=0.05 at 0.55 μm) and turbid (τ_a=0.4 at 0.55 μm) conditions and the total amount of ozone in the atmosphere is varied with values of 0.24 and 0.36 cm at normal temperature and surface pressure (NTP). Two aerosol types are considered: continental and marine. Both aerosol types are considered to be slightly absorbing. The water vapour content in each of the models is varied with precipitable water content values of 0.5, 2 and 5 g/cm^2 -- a range that represents the natural range of water vapour in the atmosphere. The variability of the Earth's surface is accounted by the incorporation of the following BRDFs: clean fresh snow, pasture land, savannah and coniferous forest.

Essentially, the coefficients developed by Koepke (1989) represent the extremes of atmospheric conditions and a general surface reflectivity model. The applicability to sea ice surfaces in the Arctic is thus unknown. These coefficients have been used to derive of sea ice surface albedo in De Abreu *et al.* (1993) and Lindsay and Rothrock (1993, 1994). In De Abreu *et al.* (1993), the authors found that AVHRR broadband albedos derived with Koepke's coefficients (and Taylor and Stowe's (1984) anisotropic correction factors) compared well with *in situ* observations of broadband albedo. However, since only one scene was utilized in the study, the applicability of the approach to a wide range of atmospheric and surface conditions was still questionable. Although Lindsay and Rothrock's (1993,1994) studies also resulted in reasonable surface albedos, surface validation of the results was unavailable.

Koepke (1989) supplies coefficients for AVHRR 1 in a look-up table defined by solar zenith angle (0-80°, 10° increments), two aerosol optical depths (0.05 and 0.4) and two ozone amounts (0.24 and 0.36 cm NTP). Coefficients for AVHRR 2 are based on the same variables except that ozone is replaced by three water vapour amounts (0.5, 2 and 4 cm precipitable water). Table 4.13 summarizes these models. Ozone absorption is only considered for AVHRR 1 and water vapour absorption is restricted to AVHRR 2. This is a logical simplification given the modelled transmissivities shown in Figure 4.9. In order to determine coefficients intermediate to the supplied zenith angles, a fourth order polynomial equation was applied to each look-up table variable (r^2>0.99). This equation was used to derive coefficients at one degree intervals.

Figure 4.13 shows the Koepke coefficients for AVHRR 1 and AVHRR 2 for the solar zenith angles 0-80°. Recalling that the *a* coefficient is anomalous to path radiance, Figure 4.13 indicates that as the atmosphere becomes more turbid and the optical path length increases, the more the atmosphere contributes to the measured TOA signal through increased path radiance. This is more evident in channel 1 where scattering is more prevalent. An increase in ozone and water vapour amounts results in increased absorption

in channel 1 and channel 2 respectively. As a result, path radiance and atmospheric transimissivity is reduced. Both coefficients display a strong dependency on solar zenith angles greater than 50°. Large zenith angles result in longer path lengths for radiation in the atmosphere. This increases the opportunity for absorption and scattering of photons. This is particularly relevant in polar regions where large zenith angles (>50°) are common.

Table 4.13 Atmospheric parameters for Koepke model

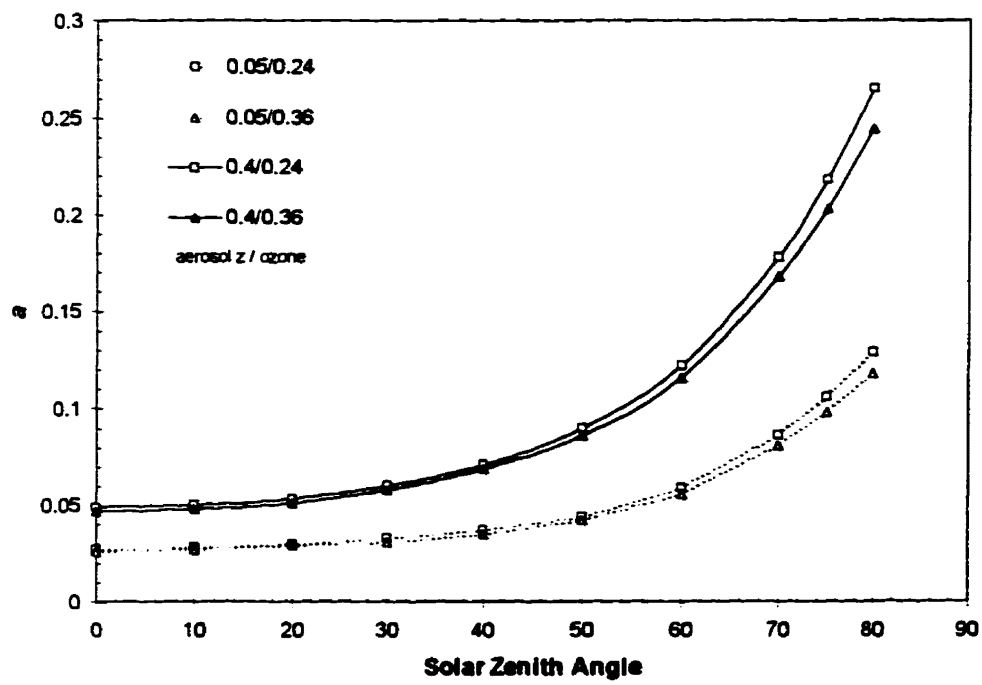
Channel	Ozone (cm NTP)	Water Vapour* (cm)	Aerosol Optical Depth
Channel 1	0.24, 0.36	n/a	0.05, 0.4
Channel 2	n/a	0.5, 2, 5	0.05, 0.4

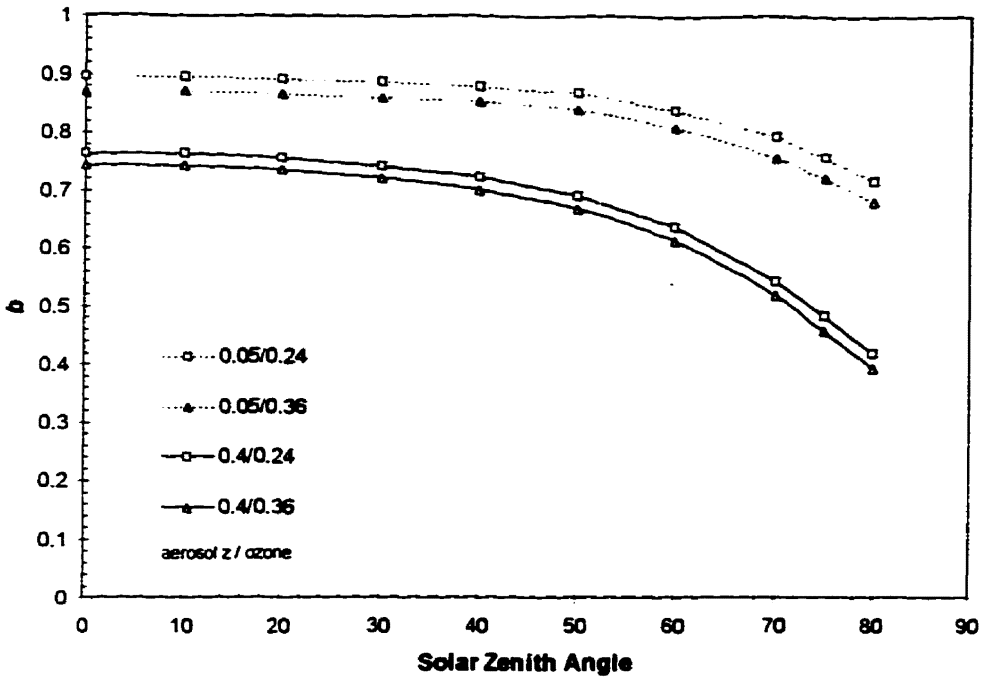
* Measured in precipitable water

Figure 4.13 Koepke Coefficients for (a) AVHRR 1 and (b) AVHRR 2

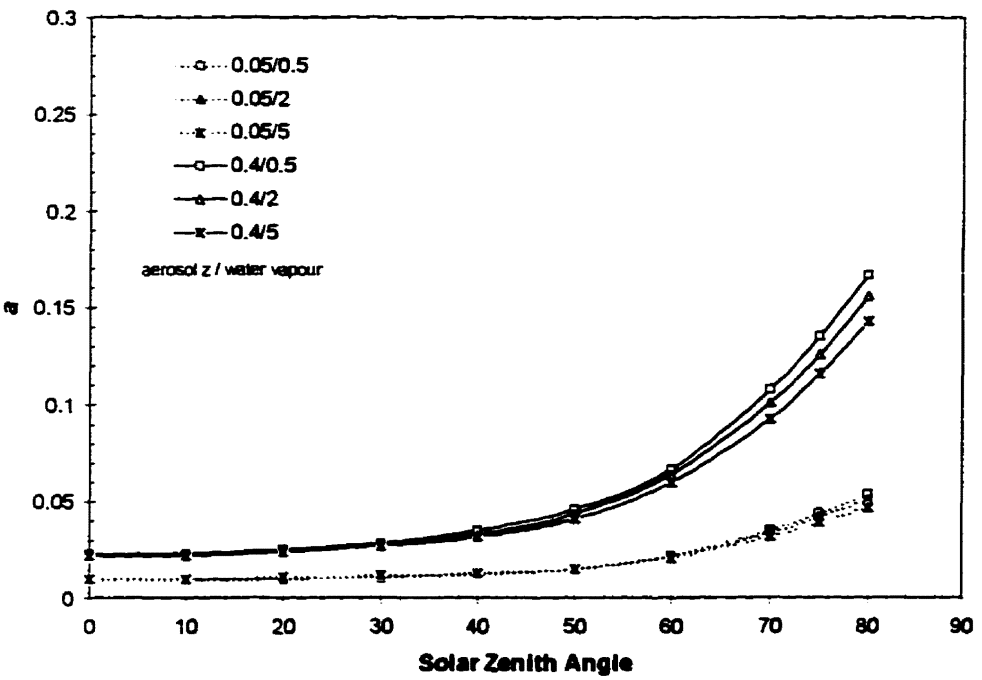
Source: Koepke (1989)

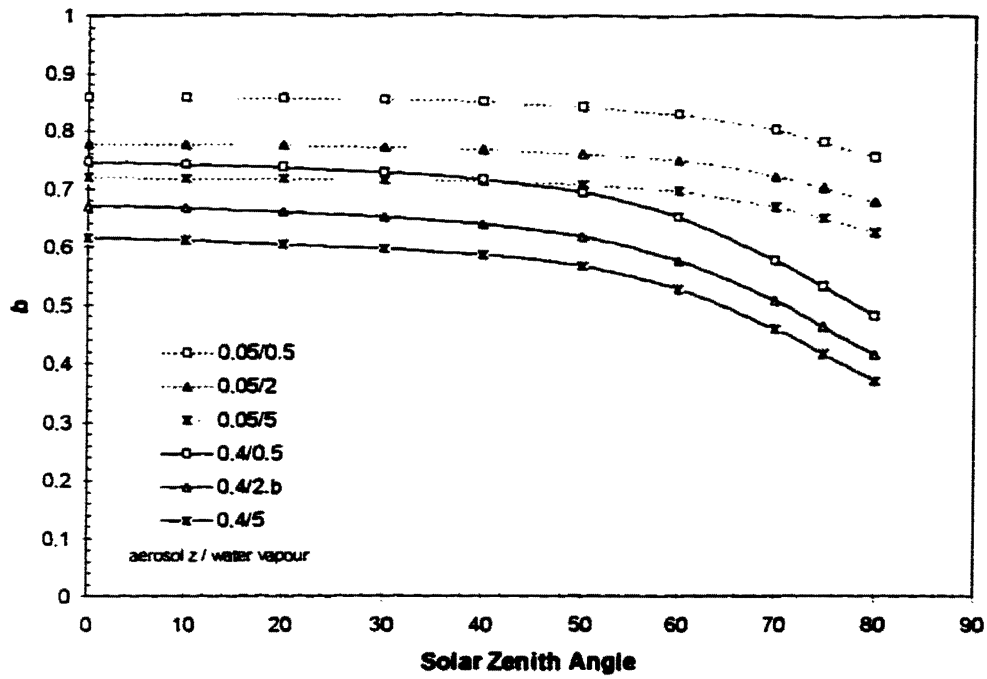
(a)




1
0.9
0.8
0.7
0.6
0.5
0.4
0.3
0.2
0.1
0
0.05/0.24
0.05/0.36
0.4/0.24
0.4/0.36
aerosol z / ozone
0
10
20
30
40
50
60
70
80
90
Solar Zenith Angle

(b)


0.3
0.25
0.2
0.15
0.1
0.05
0
0.05/0.5
0.05/2
0.05/5
0.4/0.5
0.4/2
0.4/5
aerosol z / water vapour
0
10
20
30
40
50
60
70
80
90
Solar Zenith Angle



Using Koepke's atmospheric correction coefficients, the following procedure was used to convert AVHRR TOA albedos to surface albedos on a pixel by pixel basis.

1. *Define atmospheric state for each image.*

Each image was assigned an aerosol optical depth, a water vapour amount and an ozone amount based on the values calculated in section 4.73. It is assumed that these quantities do not vary significantly over the small study area and are thus valid for each image pixel.

2. *Extract solar zenith angle for each pixel.*

This data is provided in the AVHRR data stream upon collection and readily available as an ancillary data file with the same dimensions as the image data.

3. *Determine correction coefficients (a,b) for each image pixel.*

Using a lookup table, correction coefficients corresponding to the atmospheric state variables (step 1) and solar zenith angle (step 2) were determined. Looking at the

atmospheric state values in Table 4.11, it is apparent that most of the atmospheric values fall within or just outside the ranges provided by Koepke (Table 4.13). For observational values intermediate to the Koepke values, the correction coefficients were derived from simple linear interpolation. There were instances where the observational data were outside the range used by Koepke to derive the model coefficients. In the case of ozone data where values were greater than 0.36 cm NTP, the coefficients were determined by linear extrapolation based on the values of 0.24 and 0.36 cm NTP. In the case of the water vapour data, values less than 0.5 cm precipitable water were extrapolated using a second order polynomial (r^2=1) based on the values 0.5, 2 and 5 cm precipitable water. These extrapolations are made over small excursions from the data ranges and are considered reasonable.

4. *Apply atmospheric correction.*

Using the TOA albedos determined in section 4.6 and the appropriate atmospheric correction coefficients, [4.21] is applied to each image pixel to convert TOA albedo values to surface albedo values.

Table 4.14 and Figure 4.14 contain the results of the atmospheric correction on the TOA albedos. Since the effects of the overlying atmosphere have been removed, the TOA albedos can now be referred to as surface albedos.

4.7.4.2 6S Method

The atmospheric correction of AVHRR data is based on the calculations and solutions of atmospheric radiative transfer formulations. Given an external source (e.g. the sun's emission), the reflective and emissive properties of the Earth's surface, and the atmosphere's characteristics, radiative transfer models can predict the direction and magnitude of radiance at any wavelength (Lenoble, 1993). The remote sensing community commonly employ these models in what is termed *direct* and *inverse* mode. In direct mode, the surface reflectance can be supplied to the model as a boundary condition.

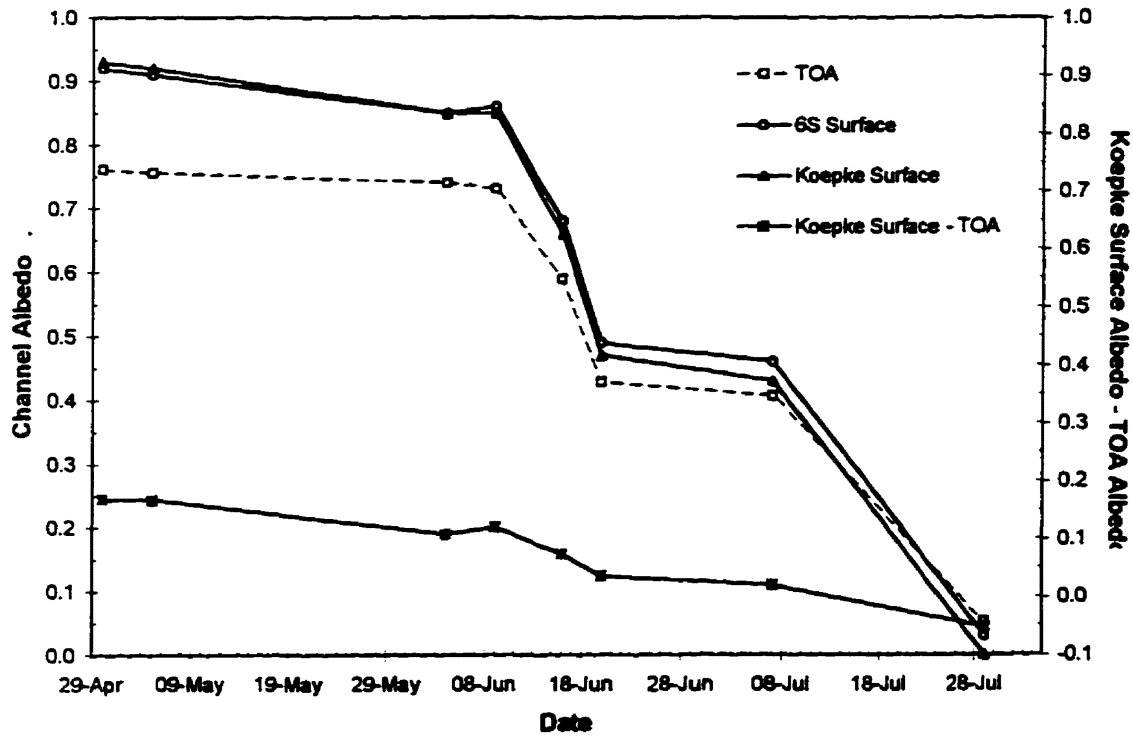
Table 4.14 Conversion of AVHRR 1 and 2 TOA albedo to surface albedos via Koepke Method.

Date	TOA Albedo		Surface Albedo		Diff / % Diff. †	
	1	2	1	2	1	2
30-Apr	0.76	0.73	0.93	0.88	0.17 / 22.4	0.14 / 19.5
03-May	0.76	0.72	0.92	0.87	0.17 / 22.2	0.15 / 20.5
04-Jun	0.74	0.63	0.85	0.77	0.11 / 14.7	0.14 / 22.5
09-Jun	0.73	0.62	0.85	0.77	0.12 / 16.6	0.15 / 24.3
16-Jun	0.59	0.46	0.66	0.57	0.07 / 12.7	0.11 / 24.8
20-Jun	0.43	0.29	0.47	0.36	0.04 / 8.4	0.07 / 23.2
07-Jul	0.41	0.29	0.43	0.35	0.02 / 5.1	0.07 / 23.5
29-Jul	0.05	0.04	0.00	0.03	-0.05 / -100	-0.01 / -31.3

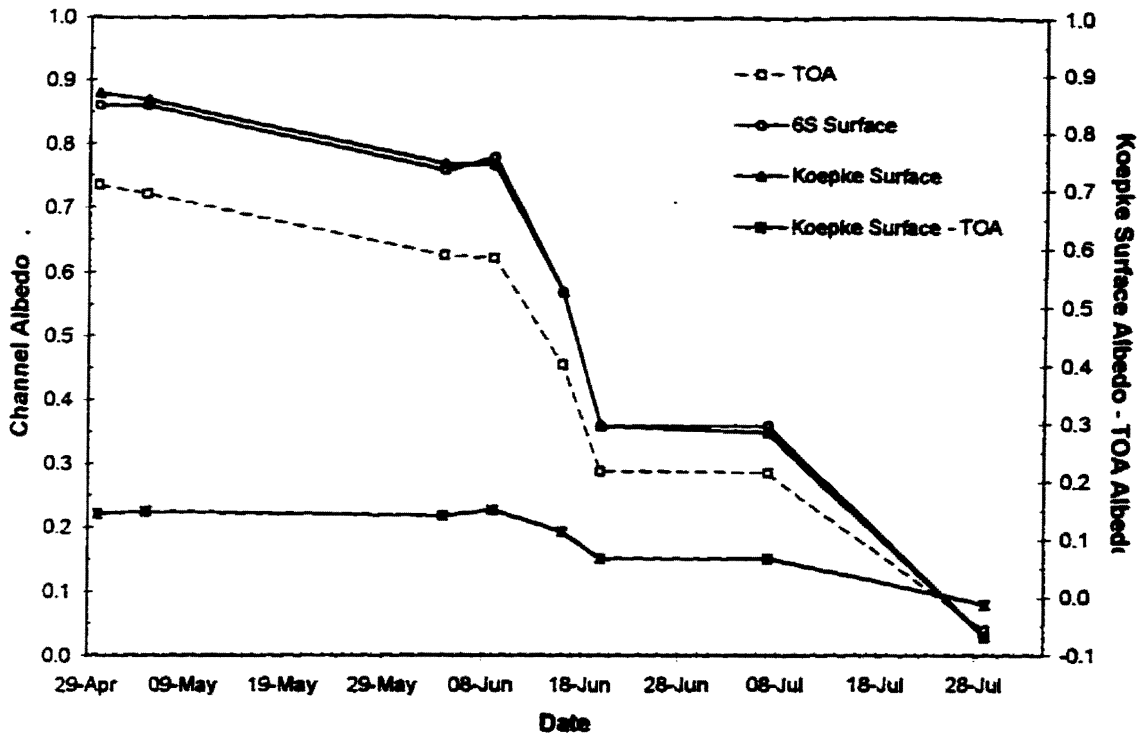
† Difference (Diff.) = TOA Albedo - TOA Reflectance
% difference (% Diff.) = Abs. Diff / TOA Albedo*100

Figure 4.14 AVHRR surface albedos determined via Koepke coefficients and 6S code. Difference between Koepke surface albedos and TOA albedos also shown.

(a) AVHRR 1



(b) AVHRR 2



By allowing the atmospheric characteristics to vary, the TOA radiance (or reflectance) measured by a sensor operating at a specific wavelength over different atmospheric conditions can be predicted. In the more common inverse application, the TOA radiance (or reflectance) is known and the unknown quantity is a characteristic of the atmosphere or of the surface. It is agreed upon that compared to the direct application of the model, the inverse problem is much more complex. 6S supports both direct and inverse applications.

In order to compare the results of the Koepke method to those derived from a more rigorous approach, the 6S model was used to invert surface albedos using the TOA albedos in Table 4.8. The model was initialized with the same atmospheric parameters used in the Koepke correction. The program's continental aerosol model was chosen to define the aerosol type. The code was initialized with the TOA albedos for each overpass day and run in inverse mode to produce a surface albedo for each channel. The results are

compared to the results from the Koepke approach in Table 4.15 and Figure 4.14. The 6S-derived surface albedos are very close to those calculated from the simpler Koepke approach. This validates the use of the Koepke's linear model and coefficients in the atmospheric correction procedure for this study set.

Table 4.15 Comparison of AVHRR 1 and AVHRR 2 surface albedos derived via 6S code and Koepke coefficients.

Date	6S Method		Koepke Method		Difference†	
	1	2	1	2	1	2
30-Apr	0.92	0.86	0.93	0.88	-0.01	-0.02
03-May	0.91	0.86	0.92	0.87	-0.01	-0.01
04-Jun	0.85	0.76	0.85	0.77	0.00	-0.01
09-Jun	0.86	0.78	0.85	0.77	0.01	0.01
16-Jun	0.68	0.57	0.66	0.57	0.02	0.00
20-Jun	0.49	0.36	0.47	0.36	0.02	0.00
07-Jul	0.46	0.36	0.43	0.35	0.03	0.01
29-Jul	0.03	0.03	0.00	0.03	0.03	0.00

† Difference = 6S - Koepke

4.7.5 Results

The results of the atmospheric correction indicate that the attenuation effects of the atmosphere are indeed large over sea ice surfaces. The time series in Figure 4.14 show that the albedos in AVHRR 1 and 2 steadily decreased from a very high value in early spring to near zero as the ice cover disappears. In terms of AVHRR 1, the TOA albedo is on average 12% lower than the respective surface albedo. Similarly, AVHRR 2 TOA albedo underestimates surface albedo on average 19%. The differences between the surface albedos and TOA albedos are provided in Table 4.14 and Figure 4.14. The attenuation effects of the overlying atmosphere significantly decreases both the flux

incident at the surface and the reflected flux along the path to the sensor. Both result in the TOA albedo underestimating surface albedo.

Atmospheric transmissivity in AVHRR 1 increases with the seasonal decrease in aerosol optical depth. Also, the seasonal decrease in solar zenith angles decrease the opportunity for atmospheric attenuation thus increasing atmospheric transmissivity. Thus, the difference between the surface and TOA AVHRR 1 albedo decreases with time over the season. There was less change in the difference between AVHRR 2 surface and TOA albedo as the season progressed. Early in the season, like AVHRR 1, this channel's transmissivity is controlled by aerosols. However, the seasonal decrease in aerosol optical depth is countered by a sharp increase in water vapour content in June and July. Since the transmissivity in AVHRR 2 is also affected significantly by water vapour absorption, the transmissivity does not increase in the late spring and the atmospheric correction is still significant in this channel throughout most of the period examined here.

After being initialized with the identical atmospheric optical variables, Koepke's linear coefficients produced surface albedos consistent with those derived from the more rigorous 6S model. While this may be more an indication of the similarity between the radiative transfer model used by Koepke and the 6S model, these results do validate the use of the simpler linear model for this dataset. As mentioned, computationally, the simple linear model is most easily implemented for large datasets. Also, the similarity in the results support the use of simple linearly interpolated Koepke coefficients for atmospheric variable values intermediate to the model cases. Before widespread application to other polar surfaces, the sensitivity of these results to larger solar zenith angles (i.e. >70°) should be investigated. Again the performance of 6S and other radiative transfer models over these long atmospheric path lengths is considered poor. While Koepke provides coefficients up to 80°, their validity is unknown. Also, it is not known whether the results of the two approaches diverge in these viewing conditions.

4.8 Narrow-to-Broadband Conversion

Climate studies often require surface albedo information integrated over large portions of the solar spectrum. Since satellite surface albedos often represent energy reflected in narrow bands of the solar spectrum, a procedure to convert a narrowband albedo to broadband albedo is required before these data can be utilized for climate studies. Much work has been concentrated on developing simple models that relate narrowband satellite measurement to a broadband climatological measurement (Koepke, 1982; Stum *et. al.*, 1985, Pinty *et. al.*, 1985). These studies take advantage of the strong linear relationship between narrowband and broadband measurements found over most surfaces. Until now, most of the development and application of these schemes has concentrated on deriving an allwave (0.15-4.0 μm) albedo (α_A) or outgoing allwave flux estimates from narrowband satellite radiance measurements. In these studies, theoretical and empirical approaches use bivariate analysis to produce linear models that relate the narrowband measurement to the broadband climatological measurement. In the theoretical approach, radiative transfer models simulate both the narrowband and broadband flux given a particular channel response function. These data then serve as input to a regression analysis. In empirical studies, satellite or surface radiometer observations provide the required narrowband and broadband observational data.

Sea ice studies have utilized the work of Wydick *et al.* (1987) and Li and Leighton. Both studies used TOA ERBE broadband data to create algorithms for estimating TOA allwave albedo using AVHRR 1 and 2 data. Wydick *et al.* (1987) used a radiative transfer model to derive the following linear model for deriving broadband albedo from AVHRR 1 and 2 TOA albedo data for snow surfaces:

$$\alpha_A = 0.0047 + 0.440\alpha_1 + 0.43\alpha_2 \qquad [4\text{-}22]$$

Lindsay and Rothrock (1993) used this model to convert AVHRR 1 and 2 sea ice data to allwave surface albedos. Strictly speaking, this model was derived for TOA albedos. However, the authors assume that they are applicable to surface albedo values in clear-sky conditions.

Li and Leighton (1987) compare TOA ERBE broadband satellite data to AVHRR 1 and 2 data to develop a similar narrow to broadband model for allwave snow and ice albedo:

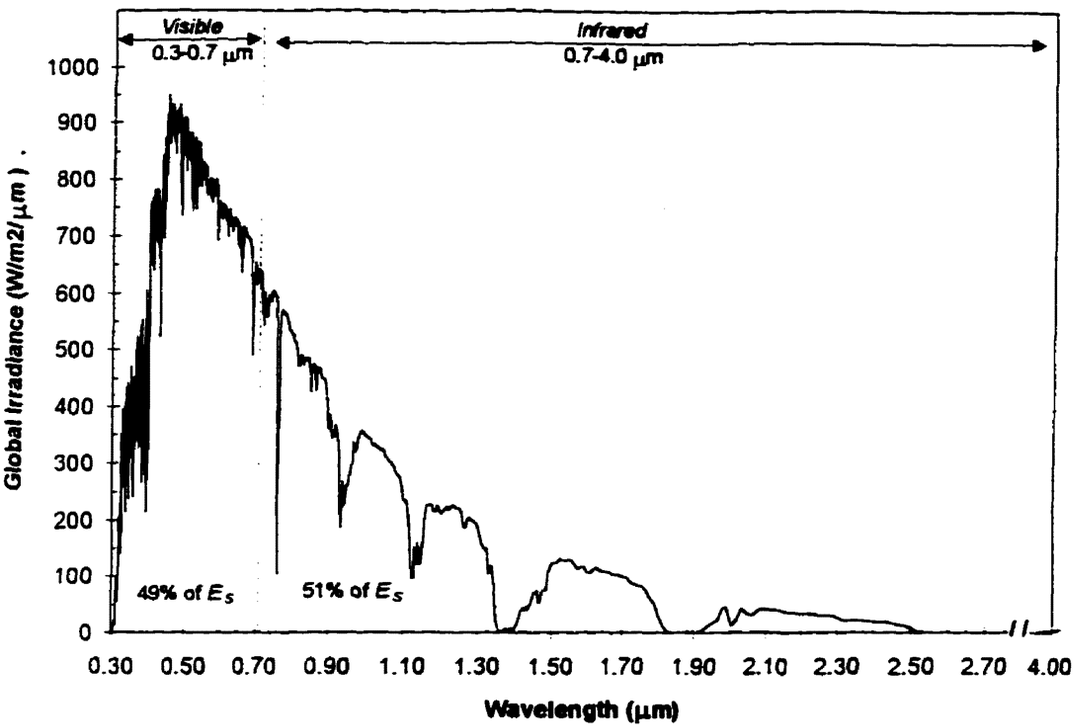
$$\alpha_A = 0.0453 + 0.389\alpha_1 + 0.452\alpha_2 \qquad [4\text{-}23]$$

On average, Li and Leighton's model produce broadband albedos approximately 5% higher than Wydick *et al.* 's conversion. This model was used by De Abreu *et al.* (1993) to convert sea ice AVHRR 1 and 2 surface albedo data to broadband albedo data. The authors also assumed that this TOA model could be extended to surface narrowband data. In Lindsay and Rothrock (1994), the authors utilize the following conversion scheme for snow-covered sea ice based on albedo measurements in Antarctica by Allison *et al.* (1993):

$$\alpha_A = 0.43\alpha_1 + 0.47\alpha_2 \qquad [4\text{-}24]$$

Many of today's climate models no longer require an allwave albedo. Instead, the solar spectrum is often divided into two portions representing the visible and infrared regions. The surface global irradiance for a typical, clear-sky day is shown in Figure 4.15. The visible and infrared regions of the solar spectrum appear to form two nearly equal regions. Today's climate models require an estimate of the surface visible (0.15-0.70 μm) albedo (α_{vis}) and infrared (0.7-4.0 μm) albedo (α_{ir}). In this investigation, a theoretical approach similar to that of Wydick *et al.*, (1987) is used to develop a model that allows the estimation of visible and infrared surface albedo from surface albedos derived by AVHRR 1 and AVHRR 2 respectively.

Figure 4.15 Visible and infrared broadband regions of the surface global irradiance.



Note: Spectrum is modelled irradiance of clear sky (τ_a=0.08) and dry atmosphere (ω=0.66 g/cm^2)

4.8.1 Data

The estimation of broadband albedo from a narrowband channel, requires an understanding of their functional relationship and how this changes as a function of environmental conditions. Discrepancies between a narrowband and broadband satellite albedo are due to differences in:

(1) the surface albedo within and outside of the channel, and/or
(2) the distribution of irradiance both across the broadband and within the channel.

These two factors interact to define the functional relationship between narrowband and broadband albedo. Depending on conditions, these factors can compensate each other to minimize albedo differences, or conversely, together they can increase the difference between narrow and broadband albedos. It is safe to say that the wider the satellite band,

the more likely it is to be representative of the broadband albedo. Theoretically, by simulating the response of AVHRR 1 and 2 under various irradiance and surface albedo conditions, a linear function can be fit to the calculated narrowband and broadband albedos.

Towards this, the first step requires the calculation of narrowband and broadband albedo measurements observed for typical sea ice and atmospheric conditions. To facilitate this, a radiative transfer model is used to simulate surface spectral irradiances representative of an early spring and late spring Arctic atmospheres. Modelled and observational spectral albedo data were then used to characterize the wide range of surfaces observed in the springtime Arctic. Together these data are used to simulate the narrowband and broadband albedos of each surface type under the different irradiance conditions. From this database, regressions analysis based on least squares optimization was conducted to relate the simulated narrowband albedo with its broadband counterpart.

4.8.1.1 Global Spectral Irradiance at the Surface

In order to assess the influence spectral irradiance may have on the conversion of narrowband AVHRR albedo to broadband albedo, global irradiances on a horizontal surface for the following four atmospheric states were modelled for a solar zenith angles of 50°, 60° and 70°:

- Dry/Clear - a clear dry atmosphere,
- Dry/Hazy - a hazy dry atmosphere,
- Wet/Clear - a clear moist atmosphere, and
- Wet/Hazy - a hazy moist atmosphere.

The Dry/Clear and the Dry/Hazy atmospheres are considered typical of early spring conditions, while the Wet/Clear atmosphere is typical of a late spring atmosphere. The

Wet/Hazy atmosphere is atypical of spring Arctic conditions, but is included here for purposes of comparison. In terms of this investigation, conditions in 1993 are best approximated by the Dry/Hazy atmosphere for the months of April and May and the Wet/Clear atmosphere for June and July. Further details on each atmosphere is provided in Table 4.16.

Table 4.16 Modelled atmosphere for narrow to broadband conversion

Label	Atmosphere Model [†]	Water Vapour (g/cm^2)	Ozone (cm NTP)	Boundary Layer Aerosol Model	Aerosol Optical Depth [††]
Dry/Clear	Winter	0.66	0.319	Tropospheric	0.08
Dry/Hazy	Winter	0.66	0.319	Arctic haze	0.36
Wet/Clear	Summer	3.30	0.270	Tropospheric	0.1
Wet/Hazy	Summer	3.30	0.270	Arctic haze	0.39

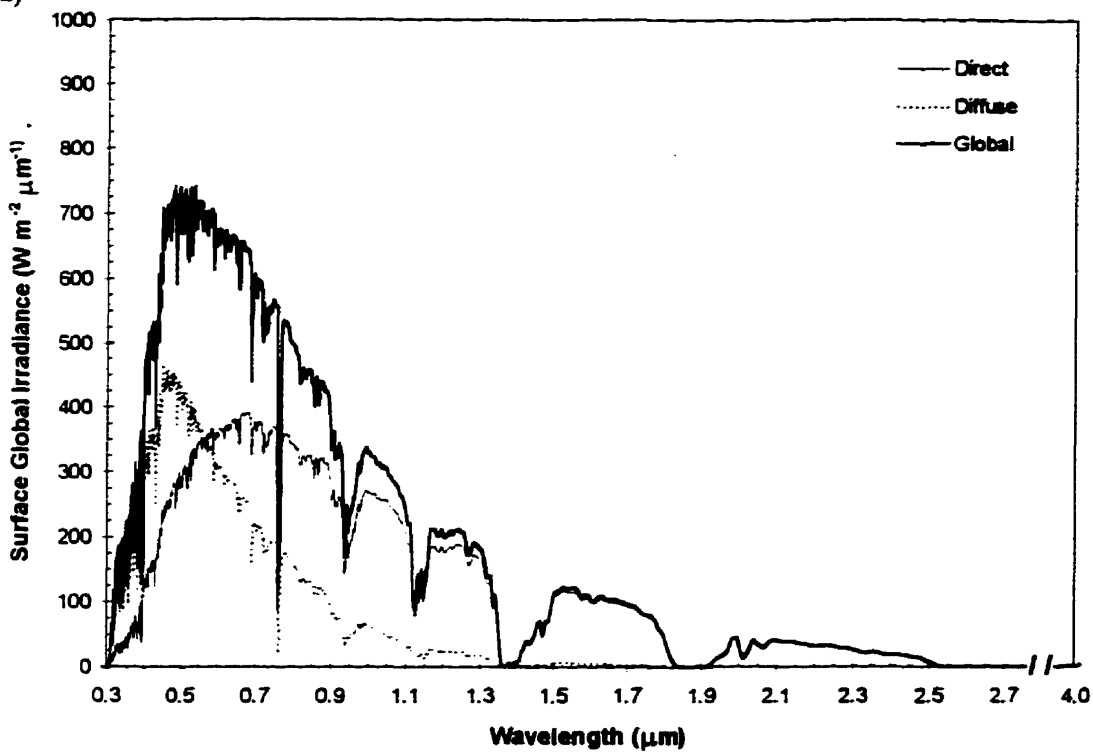
[†] Sub-arctic atmospheric model [††] specified at 0.55 μm

The procedure used to model the surface irradiances is described in Appendix 4. In brief, LOWTRAN 7 was used to provide transmission functions for the two atmospheres. The sub-arctic atmospheric model was used along with two aerosol models: tropospheric and arctic haze. The diffuse component was estimated using a simple two-stream approximation provided in Iqbal (1983). Since the magnitude of the diffuse component is partially dependent on multiple reflections between the surface and atmosphere, the magnitude and distribution of global irradiance is dependent on the surface albedo. Recognizing this, individual irradiance spectra were generated for each of the surface types described in the next section.

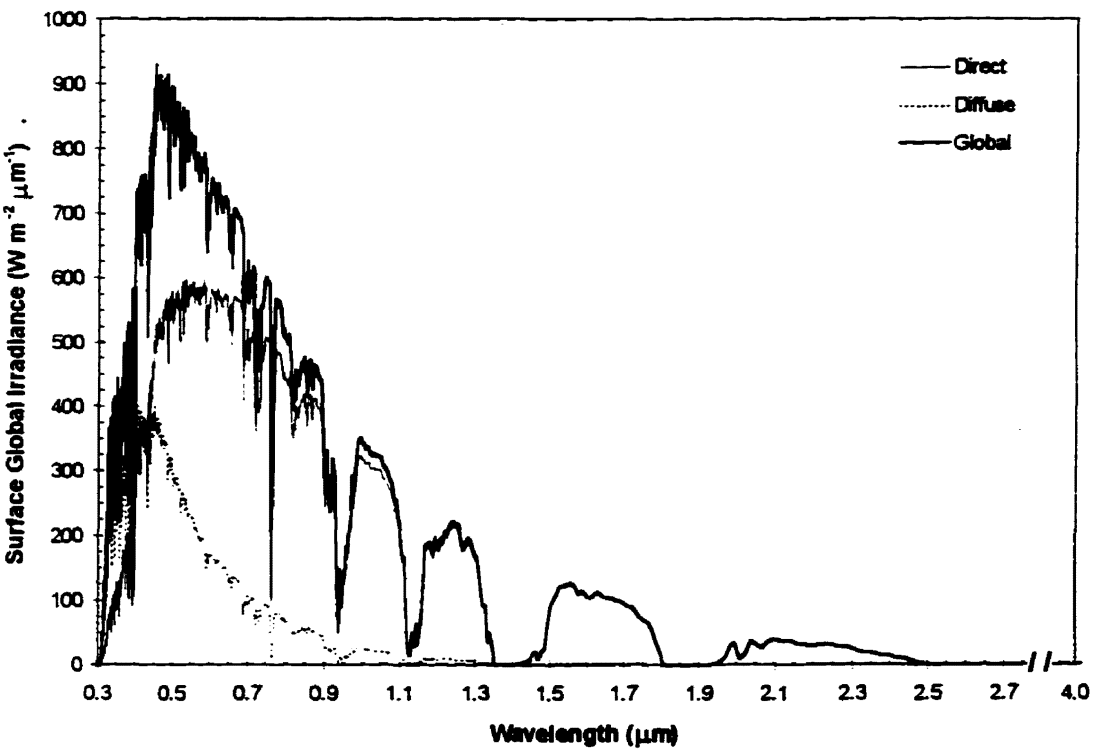
Figures 4.16 shows the modelled irradiance components for the dry/hazy atmosphere and the wet/clear atmosphere over a new snow surface. Global irradiance is considerably less in the hazy atmospheres due to aerosol absorption of primarily direct radiation. The wet/clear atmosphere shows the effects of water vapour absorption at water vapour

Figure 4.16 Modelled surface irradiances for (a) hazy, dry atmosphere and (b) clear, wet atmopshere. Both atmospheres over a new snow surface and solar zenith angle of 60°.

(a)



(b)



absorption bands (e.g. 0.95 μm and 1.15 μm). Of significance here is the distribution of incident irradiance and how it changes with atmospheric conditions. The direct component is centered at longer wavelengths since much of the very shortwave direct radiation is scattered out of the direct beam. As seen in these simulations, this resultant diffuse component can be significant over high-albedo polar surfaces due to the multiple reflections between the typically high-albedo sea ice surfaces and the long optical path lengths in polar regions. Since scattering of radiation is essentially inversely proportional to wavelength in the visible spectrum, the diffuse component peaks at very short wavelengths.

4.8.1.2 Sea Ice Surface Spectral Albedo

In order to develop a conversion model appropriate for sea ice surfaces, the spectral albedos of six typical spring sea ice surfaces were calculated:

- new snow (no impurities),
- dry snow (soot present),
- thin wet snow (underlying ice visible)
- melting FYI bare ice
- late ponded - 60% melt ponds / 40% melting FYI
- breakup - 50% FYI bare ice / 50% open water

The albedo spectra are shown in Figure 4.17(b) and Figure 4.18(b) and described in Table 4.17. The snow albedos were modelled after Wiscombe and Warren's (1980) finite and semi-infinite approaches (Appendix 1). The model runs were initialized by *in situ* observations collected in SIMMS'93. Albedos were generated for solar zenith angles 60° assuming that 25% of global incident irradiance consisted of diffuse radiation. This proportion was found to be consistent with AES Resolute shadowband measurements at a solar zenith angle of 60° on a clear day. The addition of soot to the snowcover is based on

the internal mixing approach of Chylek *et.al.*, (1983). This approach produces snow albedos more consistent with field observations than the external model used by Warren and Wiscombe (1980). The volume fraction of soot used here is consistent with that measured by Grenfell and Maykut (1977) on the Arctic ice island T3. The bare ice albedo was taken from Grenfell and Perovich (1984) measurements in the Southern Beaufort Sea of FYI melting ice. A late season ponded surface representing a complex surface consisting of melt ponds and melting FYI was calculated. The melting FYI albedo spectra previously mentioned was combined with FYI melt pond spectra measured during SIMMS '95 (De Abreu, 1995). The albedo for the mixed (*m*) surfaces (α_m) were determined as follows:

$$\alpha_m = \left((1 - P_{mp})\alpha_s\right) + \left(P_{mp}\alpha_{mp}\right) \qquad [4\text{-}25]$$

where P_{mp} is the proportion of the surface covered by melt ponds (0-1), α_s is the albedo of the old snow surface and α_{mp} is the melt pond albedo. The maximum pond coverage of 60% is appropriate for much of the arctic. The breakup spectra was created using [4.25] by combining the open water albedo spectra with that of melting FYI. The open water spectra from 0.4-1.0 μm was taken from Allison *et al.*'s (1993) ship-based measurements in the Indian Ocean off Antarctica. Both the melt pond and open water albedo was extrapolated from 1.0 to 4.0 μm by assuming an albedo of 0.05 across this range.

Figures 4.17 and 4.18 show the irradiance and spectral albedo in the visible and infrared spectrums respectively. The location of AVHRR 1 appears to represent a significant portion of the visible irradiance (approx. 30-35 %) and the surface albedo in AVHRR 1 albedo is very similar to the albedo of the broadband. This suggests a strong relationship between AVHRR 1 albedo and visible albedo. Like AVHRR 1, AVHRR 2 also represents a large portion of the incident irradiance (approx. 30-35 %). However, the surface albedo for all of the sea ice surfaces are higher than the albedo over the rest of the infrared spectrum. This indicates that on its own, AVHRR 2 albedo overestimates sea ice infrared albedo.

.Figure 4.17 Visible spectrum: (a) spectral irradiance in AVHRR 1 relative to the visible spectrum and (b) typical sea ice albedos within visible spectrum

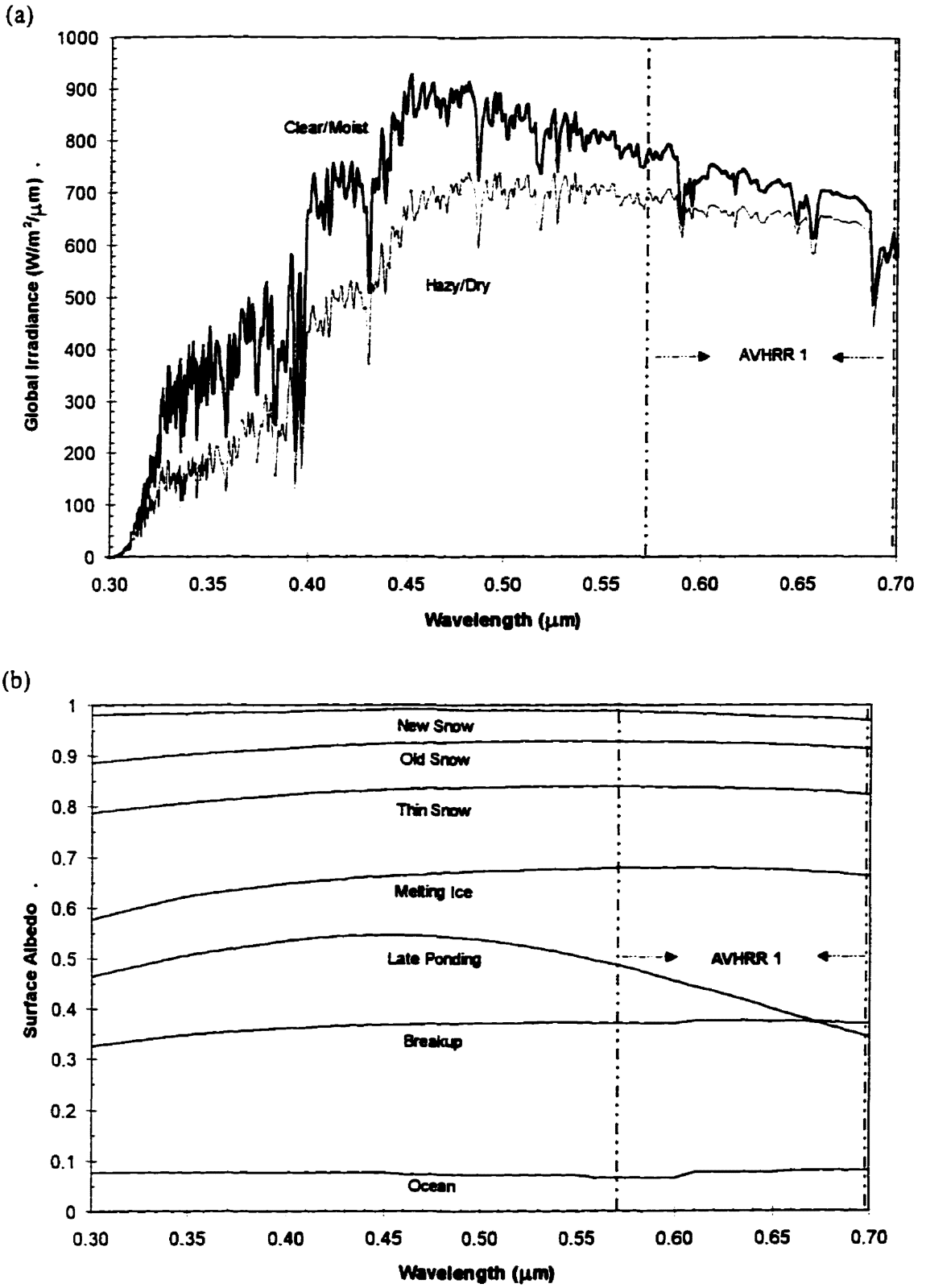
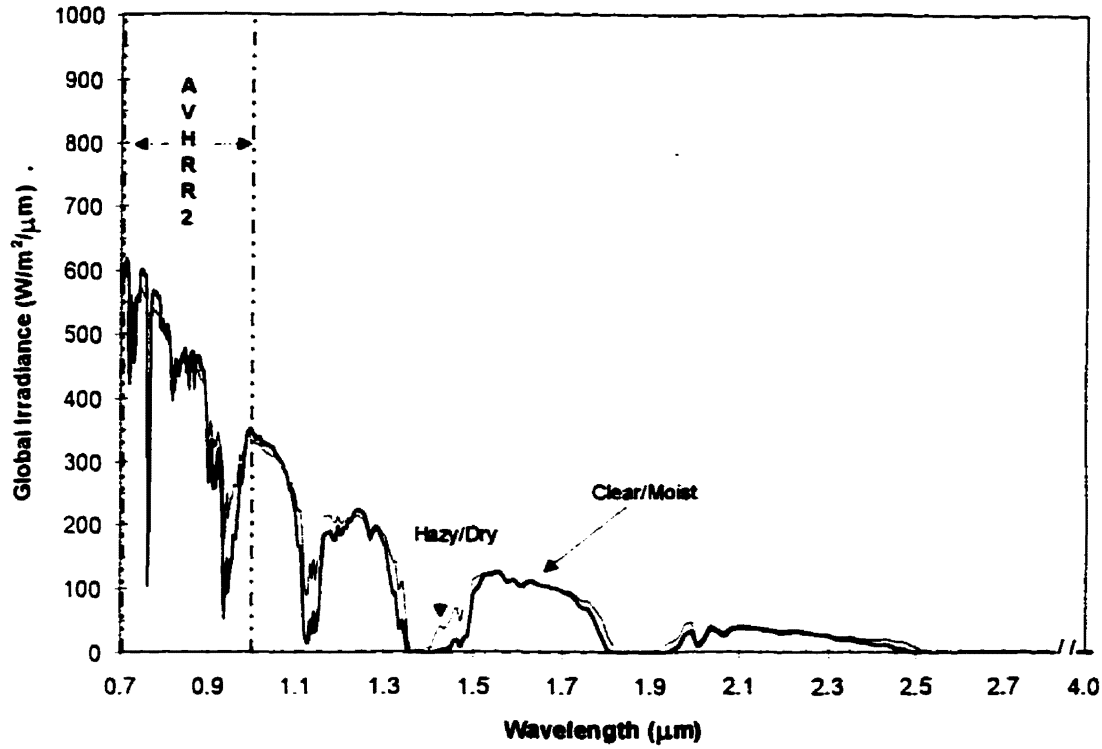


Figure 4.18 Infrared spectrum: (a) spectral irradiance in AVHRR 2 relative to the infrared spectrum and (b) typical sea ice albedos within infrared spectrum

(a)



(b)

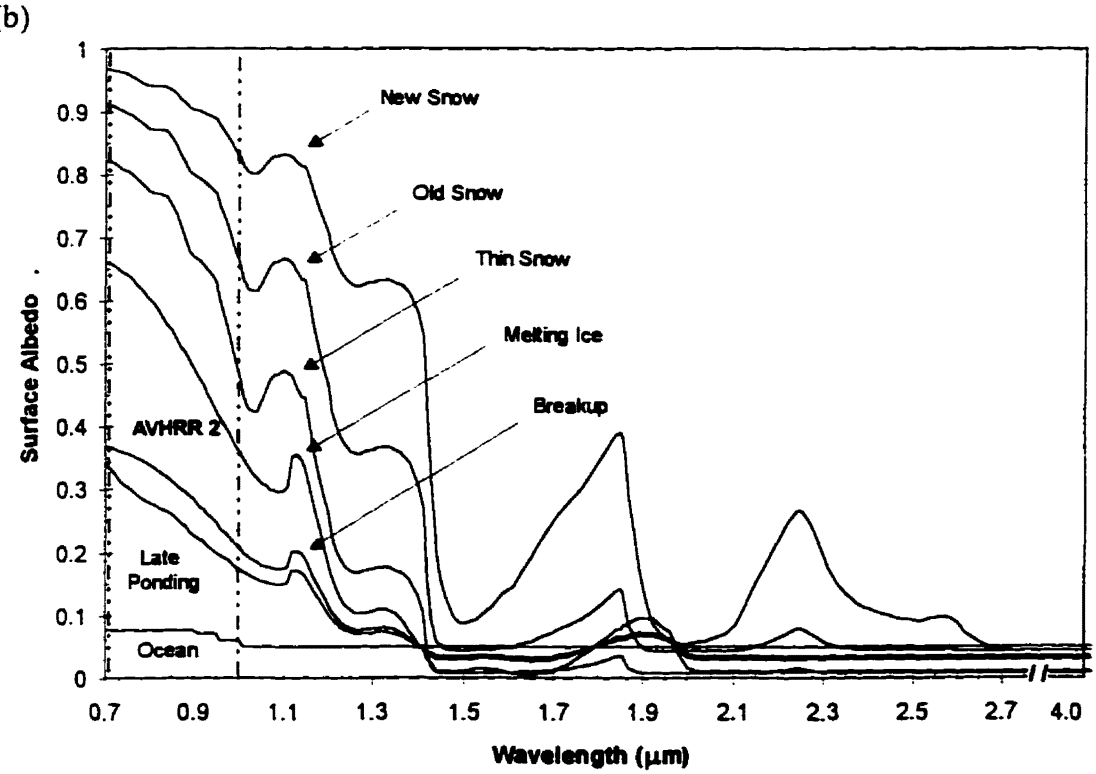


Table 4.17 Spring sea ice surfaces observed in SIMMS '93 used in narrow to broadband modelling

Surface	Description
new snow	depth=30 cm, grain radius=100 μm, density=100 kg m^{-3}
old snow	depth=30 cm, grain radi=500 μm , density=350 kg m^{-3}, soot volume fraction=$5x10^{-8}$
thin snow	depth=10 cm, grain radi=1000 μm, density=450 kg m^{-3}, soot same as above, underlying ice has 1.5 cm crumbly surface layer
melting ice	FYI ice covered by 1.5 cm crumbly layer consisting of grain radi=2.5-5 mm with small scale irregularities
late ponding	60 % FYI melt pond, depth=9 cm, 40% melting ice
breakup	50% open ocean, 50% melting ice

4.8.2 Method

Using the simulated data described in the previous section, visible and infrared broadband albedos are calculated for each surface under each atmosphere by

$$\alpha_{vis,ir} = \frac{\int_{\lambda 1}^{\lambda 2} E_\lambda \alpha_\lambda d\lambda}{\int_{\lambda 1}^{\lambda 2} E_\lambda d\lambda} \qquad [4\text{-}26]$$

where λ_1 and λ_2 are the spectral boundaries of the broadband albedo. Surface AVHRR 1 and 2 channel albedos are calculated with [4.2].

Bivariate analysis was then used to examine the relationship between AVHRR 1 and visible albedo, and AVHRR 2 and infrared albedo under a range of atmospheric conditions. The objective is to develop a scene-independent method of converting narrowband AVHRR 1 and 2 albedo to their climatological broadband counterparts.

4.8.3 Results

4.8.3.1 Visible Albedo

The simulated visible albedos and their corresponding AVHRR 1 albedo for the most representative atmospheric scenarios are presented in Table 4.18 for the seven surfaces and four atmospheres for the solar zenith angles of 50° and 70°. The scatterplot in Figure 4.19 compares AVHRR 1 albedo to visible albedo for two atmospheres at a solar zenith angle of 60°. It should be noted that a similar plot with empirically derived data would show much more scatter as it incorporates more of the natural variability of the measurement. The results in Table 4.18 show that, with the exception of the late ponded surface, the difference between the narrowband and broadband albedo estimate is less than 0.01 absolute albedo units. Included in Table 4.18 is the root mean square error (*rmse*) when AVHRR 1 is used to estimate visible albedo. The error statistic is expressed in albedo units and calculated as follows:

$$rmse = \left[\frac{1}{n} \sum_{i=1}^{n} \left(\alpha_{vis,i} - \alpha_{1,i} \right)^2 \right]^{1/2} \qquad [4\text{-}27]$$

where n is the number of surface/atmosphere combinations and i represents each surface, solar zenith angle, atmosphere combination. As predicted, AVHRR 1 albedo appears to provide a good estimate (*rmse*=0.024-0.028) of visible albedo over all surfaces, except for the late ponding case.

The variability in the error statistic between cases is due to atmospheric influences, more specifically, the variation in the proportion of incident visible irradiance within AVHRR 1. AVHRR 1 appears to provide a slightly better estimate of visible albedo in hazy conditions, especially at larger solar zenith angles. This is due to the larger proportion of incident radiation contained in AVHRR 1 under these conditions. Increased atmospheric absorption in hazy conditions results in a reduction of incident radiation primarily at wavelengths shorter than AVHRR 1. Figure 4.20 shows how the proportion of incident visible radiation within AVHRR 1 changes with atmospheric conditions and solar zenith

Table 4.18 Comparison of AVHRR 1 albedo with corresponding visible albedo under early spring hazy conditions and late spring clear conditions (SZA=60°).

Surface	Early Spring Hazy			Late Spring Clear		
	Vis. Albedo	AVHRR 1	Difference	Vis. Albedo	AVHRR 1	Difference
new snow	0.986	0.981	0.005	0.986	0.981	0.005
old snow	0.923	0.924	-0.001	0.921	0.924	-0.003
thin snow	0.832	0.835	-0.003	0.831	0.835	-0.004
melting ice	0.668	0.675	-0.007	0.666	0.675	-0.009
late ponding	0.483	0.414	0.068	0.487	0.415	0.072
breakup	0.370	0.374	-0.004	0.369	0.374	-0.005
open water	0.073	0.074	-0.002	0.073	0.074	-0.001
		r.m.s.e	*0.03*		*r.m.s.e*	*0.03*

Figure 4.19 Comparison of AVHRR 1 albedo with corresponding visible albedo under early spring hazy conditions and late spring clear conditions (SZA=60°).

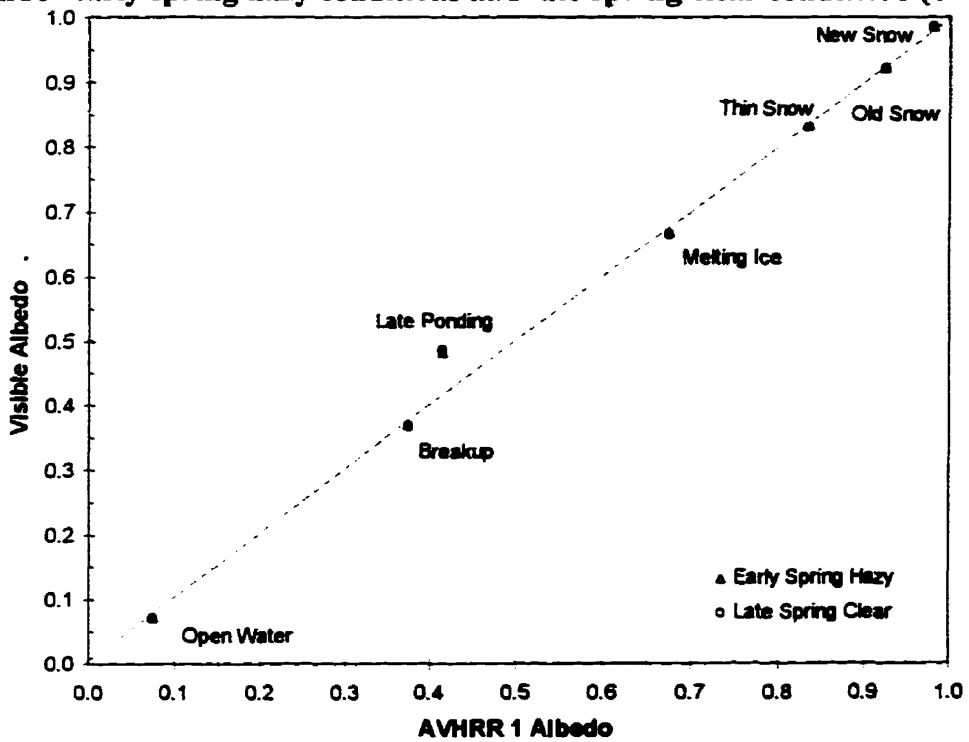
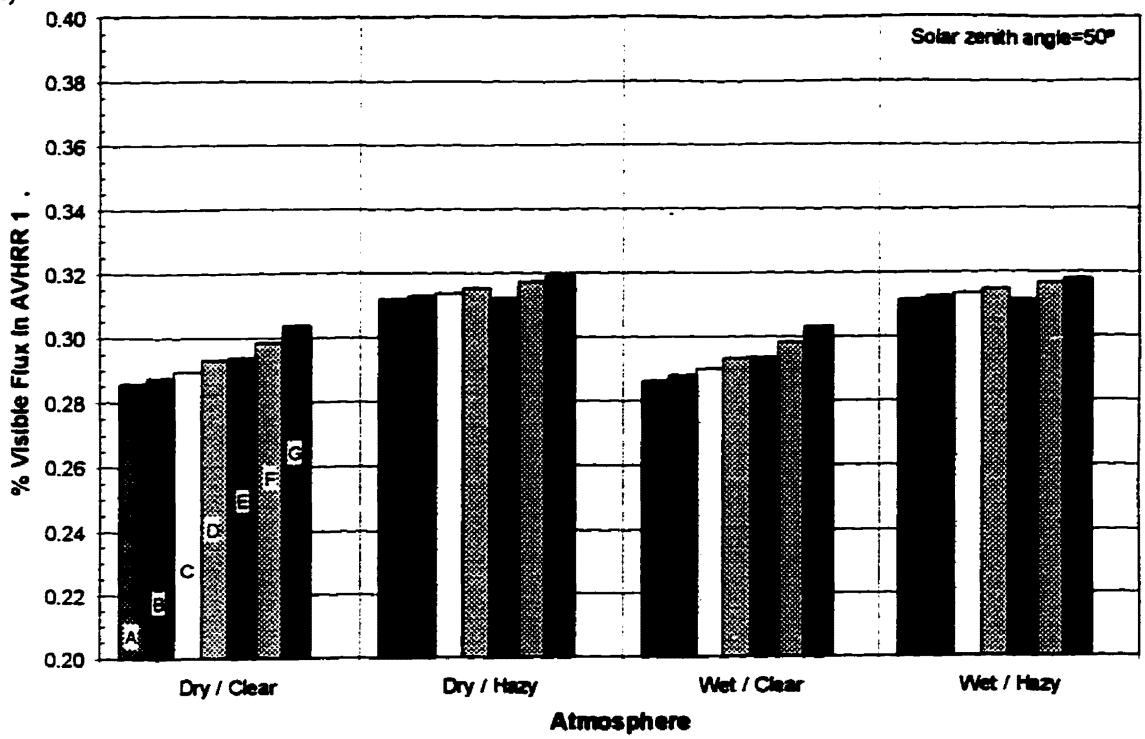


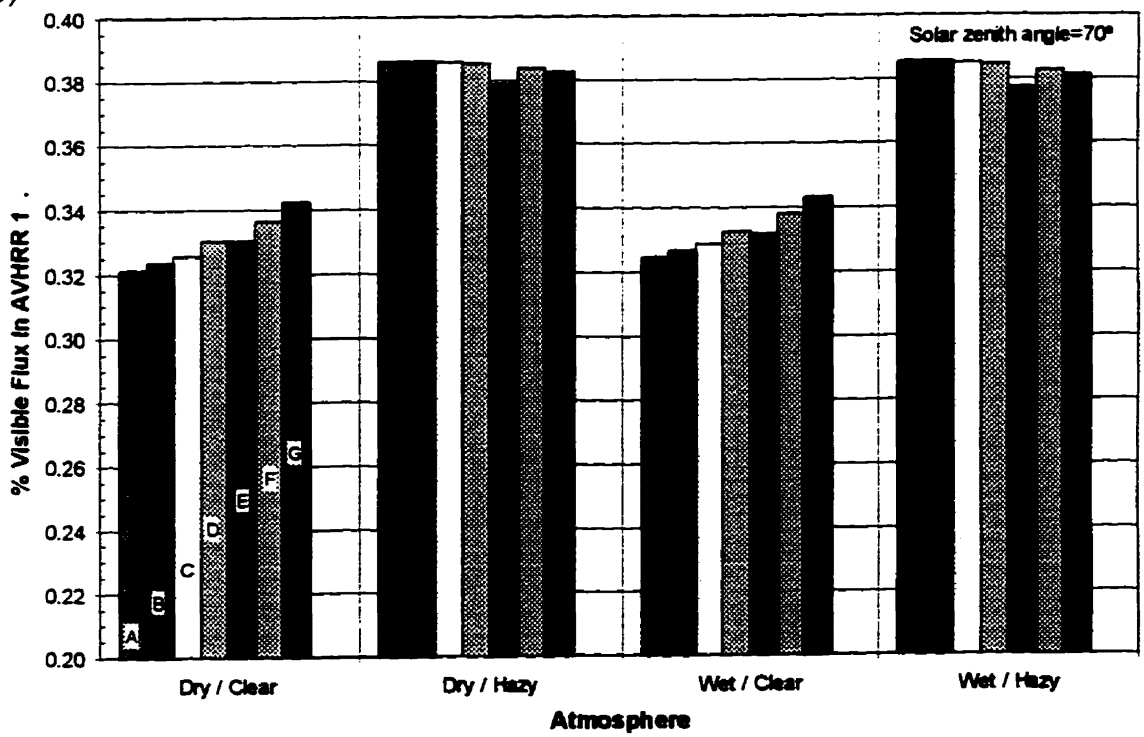
Figure 4.20 Proportion of visible flux within AVHRR 1 for (a) a solar zenith angle of 50° and (b) a solar zenith angle of 70°.

(a)



Note: Surfaces: A=new snow, B=old snow, C=thin snow, D=melting ice, E=late ponding, F=breakup, G=open water

(b)



angle. This atmospheric effect is enhanced over the longer atmospheric path lengths and thus much more obvious at larger solar zenith angles. Again, however, the differences between cases are minor.

Figure 4.17(b) shows that the albedo of a melt pond surface tends to be higher at shorter wavelengths and declines rapidly within the AVHRR 1 channel. As expected, AVHRR 1 underestimates visible albedo of the late melt pond surface by approximately 0.07. Since the ponded surface simulated here represents the peak coverage of melt ponds, AVHRR 1 albedo measurements of surfaces with a lower percentage of melt ponds are expected to provide a better estimate of visible albedo than the results shown here. These results suggest that over most surface and atmosphere conditions, AVHRR 1 provides an acceptable estimate of visible albedo. Given this, no narrow-to-broadband transformation will be applied to AVHRR 1 data in this investigation.

4.8.3.2 Infrared Albedo

The calculated AVHRR 2 and infrared albedos are shown in Table 4.19 and compared in Figure 4.20. Over snow and ice surfaces examined here, AVHRR 2 overestimates infrared albedo by 0.24-0.26. The *rms* error is large (0.191-0.212) when AVHRR 2 is used to estimate infrared albedo without adjustment. The two albedo values become more similar as the surface water appears and the wavelength-independent albedo of water becomes more dominant. This results in the curvi-linear relationship between AVHRR 2 and infrared albedo shown in Figure 4.21.

The simulated data indicates that 31-36 % of infrared irradiance falls within AVHRR 2, a similar proportion as AVHRR 1 in the visible spectrum. AVHRR 2 albedo provides a slightly better estimate of infrared albedo in clearer, moist atmospheres. Figure 4.22 shows that in moist atmospheres, AVHRR 2 represents a larger proportion of incident

Table 4.19 Comparison of AVHRR 2 albedo with corresponding infrared albedo under early spring hazy conditions and late spring clear conditions (SZA=60°).

Surface	Early Spring Hazy			Late Spring Clear		
	IR. Albedo	AVHRR 2	Difference	IR. Albedo	AVHRR 2	Difference
new snow	0.705	0.936	-0.231	0.725	0.938	-0.213
old snow	0.582	0.860	-0.278	0.604	0.864	-0.259
thin snow	0.461	0.753	-0.292	0.484	0.758	-0.274
melting ice	0.339	0.570	-0.231	0.359	0.575	-0.217
late ponding	0.169	0.267	-0.099	0.179	0.270	-0.092
breakup	0.198	0.321	-0.124	0.209	0.325	-0.115
open water	0.060	0.074	-0.013	0.062	0.074	-0.012
		r.m.s.e	*0.21*		*r.m.s.e*	*0.19*

Figure 4.21. Comparison of AVHRR 2 albedo with corresponding infrared albedo under early spring hazy conditions and late spring clear conditions (SZA=60°).

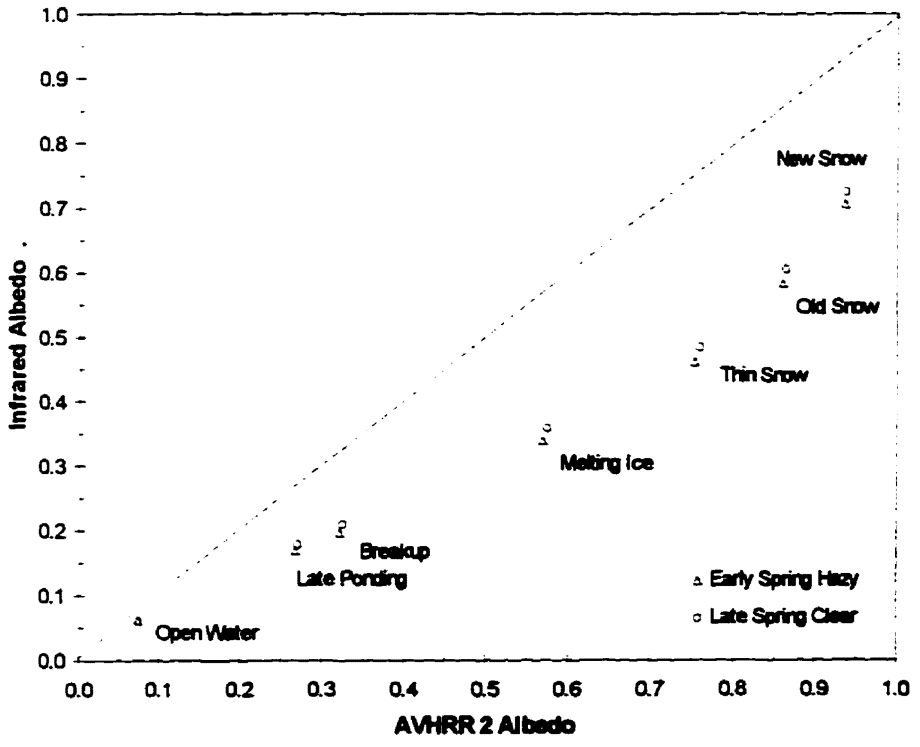
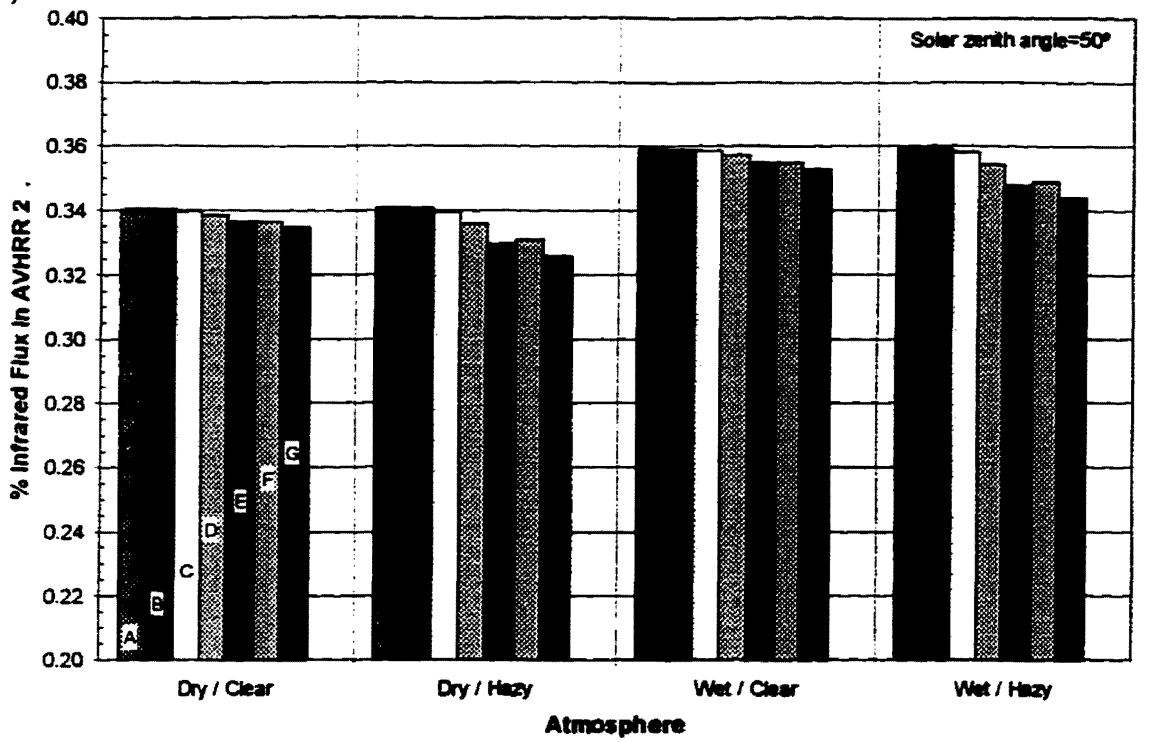


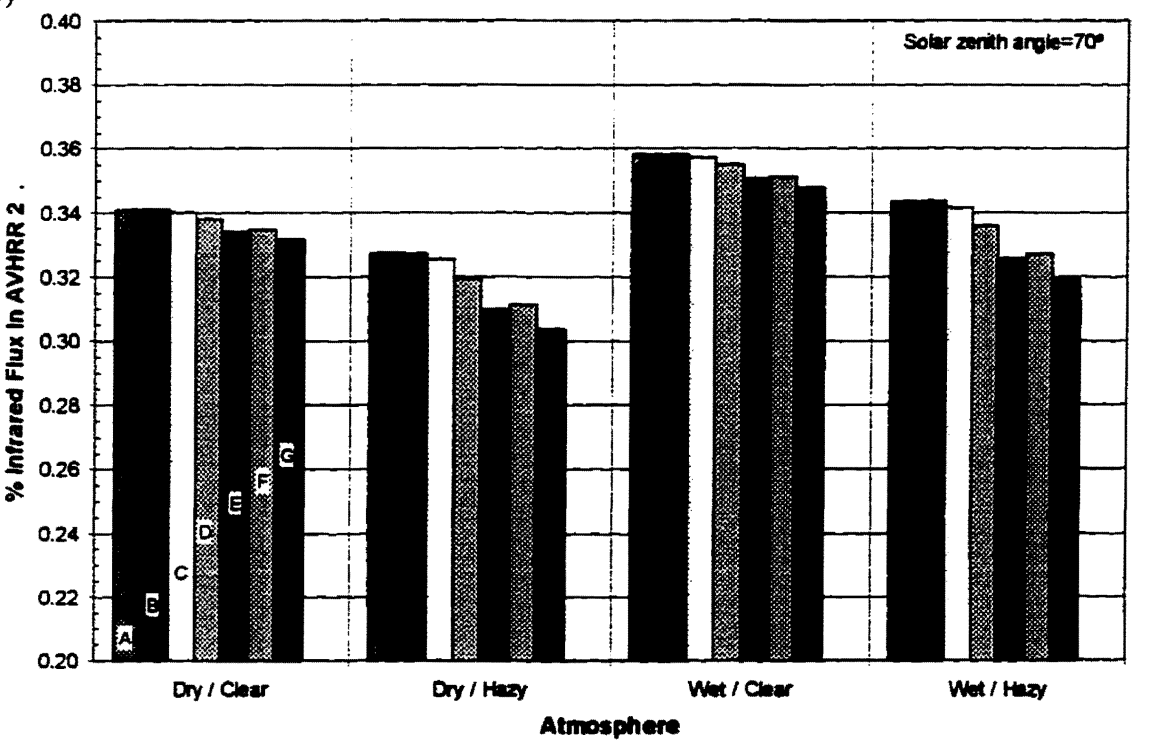
Figure 4.22 Proportion of infrared flux within AVHRR 2 for (a) a solar zenith angle of 50° and (b) a solar zenith angle of 70°.

(a)



Note: Surfaces: A=new snow, B=old snow, C=thin snow, D=melting ice, E=late ponding, F=breakup, G=open water

(b)



infrared irradiance due to water vapour absorption occurring primarily at longer wavelengths outside of the channel. This gives more weight to the channel albedo resulting in a closer infrared albedo estimate. At infrared wavelengths, the effects of atmospheric haze appear only significant at large solar zenith angles. Attenuation effects reduce the amount of incident irradiance within AVHRR 2, which ultimately results in an overall poorer estimation of the broadband infrared albedo.

Unlike AVHRR 1, AVHRR 2 cannot directly be used to estimate infrared albedo without a large error. Some type of conversion is required. It is preferable to implement a scheme independent of surface, atmospheric and solar conditions. Furthermore, to ease interpretation and implementation, the simpler the method, the better. Towards this, regression analysis was used to relate infrared albedo (dependent variable) to AVHRR 2 (independent variable) using the simulated dataset. Analysis is run on three atmospheric datasets:

(1) Dry/Hazy - from here on referred to as "Early Spring",
(2) Wet/Clear - referred to from here as "Late Spring", and
(3) Combined - a combination of both the above atmospheres.

The first two atmospheres are most representative of the conditions during acquisition of the 1993 AVHRR dataset and are considered typical of spring Arctic conditions. Each dataset represents albedo of the seven typical sea ice surfaces simulated for three zenith angles -- 50°, 60° and 70°.

A simple linear model relating AVHRR 2 albedo and infrared albedo is attractive due to its simplicity in application and interpretation. As mentioned however, the relationship shown in the scatterplot in Figure 4.21 appears to be non-linear, thus suggesting that a simple linear model may be inappropriate for these data. An acceptable alternative is the transformation of the of the dependent, independent or both variables of the dataset in an

attempt to linearize a non-linear regression function (Tukey *et.al.*, 1977). The dependent variable, infrared albedo, was transformed as follows

$$\alpha'_{ir} = \sqrt{\alpha_{ir}} \qquad [4\text{-}28]$$

The results of the transformation on the dependent variable is shown in the scatterplot in Figure 4.23. The relationship between the two variables now appears linear making a simple linear model suitable. The transformed regression function is now given as

$$\tilde{\alpha}'_{ir} = b_0 + b_1\alpha_2 \qquad [4\text{-}29]$$

where $\tilde{\alpha}'_{ir}$ is the best estimate of infrared albedo corresponding to an AVHRR 2 albedo (α_2). or, expressed in the original albedo units

$$\tilde{\alpha}_{ir} = (b_0 + b_1\alpha_2)^2 \qquad [4\text{-}30]$$

Statistical software was used to calculate the regression functions for the early spring hazy data, the late spring data and for both atmospheres combined. The calculated regression parameters and fitted functions are shown in Table 4.20 and Figure 4.23 respectively. Analysis of the model's residuals and regression parameters show that the linear model utilized is apt. There seems to be no large difference between the models derived for individual atmospheres and the combined atmosphere. For that reason, the following combined atmosphere model is adopted for the conversion of the AVHRR 2 albedos derived in this investigation

$$\tilde{\alpha}_{ir} = (0.222 + 0.646\alpha_2)^2 \qquad [4\text{-}31]$$

The accuracy of new predictions derived from the model in [4.34] was estimated to be ±0.05 after the approach of Neter *et al.*, (1985). The calculated broadband visible and infrared albedos are shown in Table 4.21 and Figure 4.24.

Table 4.20 Derived regression parameters for infrared NTB model.

Atmsophere	Constant (b_0)	Slope (b_1)	Coeff. of Determination (r^2)	Standard Error of Model	Confid. Level (0.95) New Prediction*
Early Spring	0.219	0.641	0.992	0.0189	±0.046
Late Spring	0.225	0.650	0.991	0.0195	±0.048
Combined	0.222	0.646	0.991	0.0197	±0.046

*Calculated for a new AVHRR 2 observation equivalent to mean of independent variable and given here in original units (albedo).

Figure 4.23 Same data as figure 4.21 except infrared albedo transformed ($\sqrt{\alpha_{ir}}$).

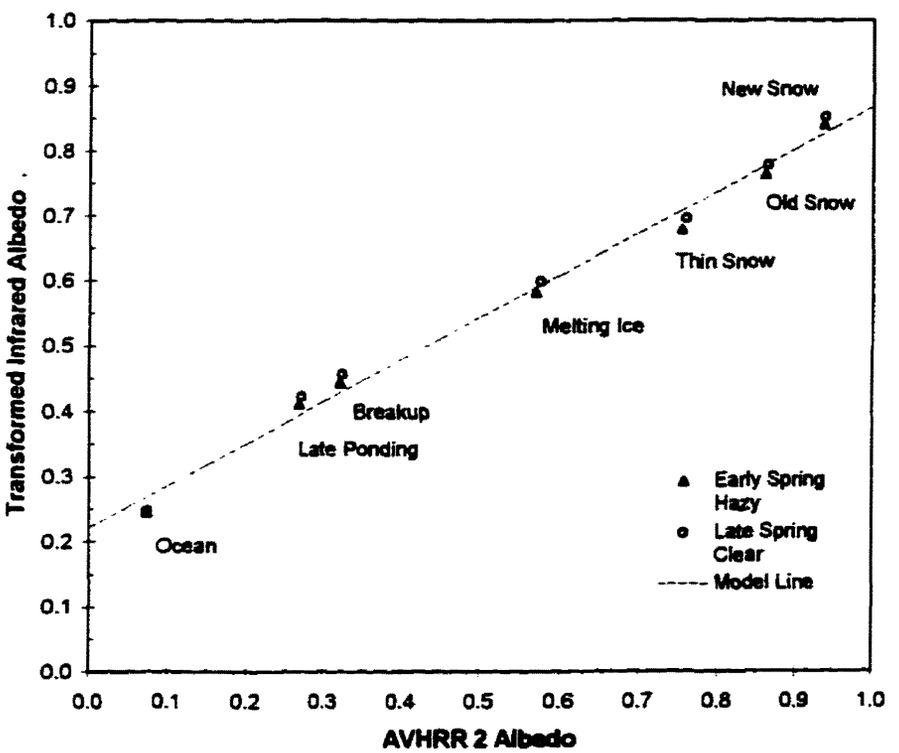
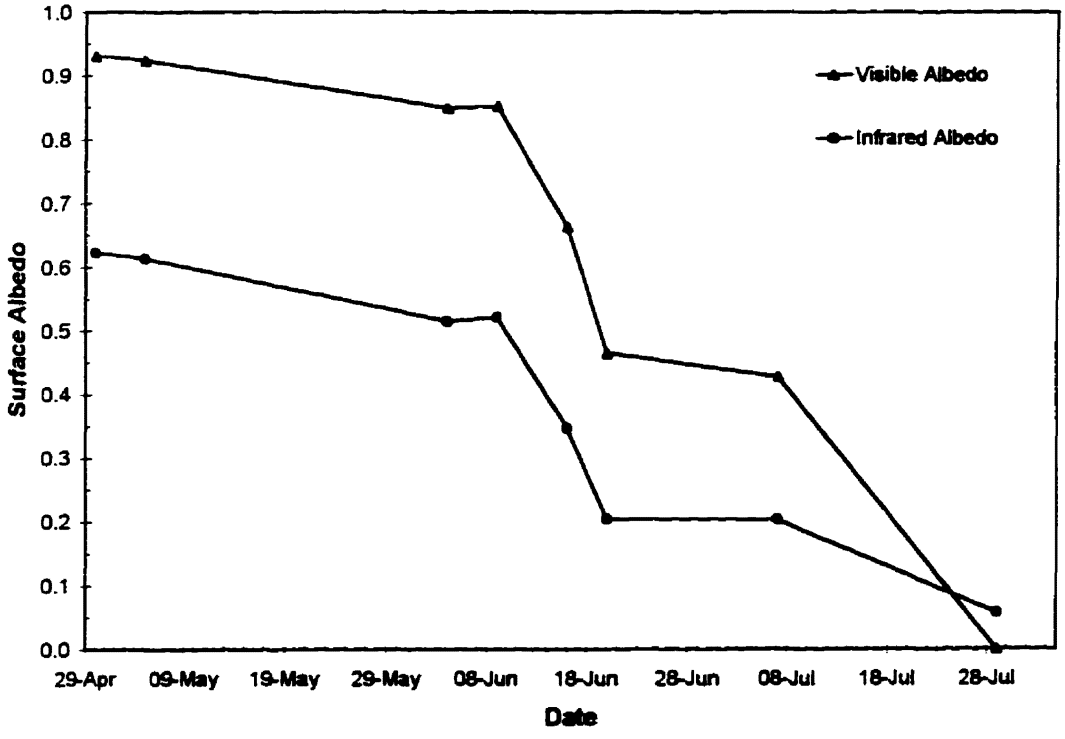


Table 4.20 Conversion of narrowband channel albedos to broadband albedos

Date	AVHRR Surface Albedo		Broadband Surface Albedo	
	1	2	Visible	Infrared
30-Apr	0.93	0.88	0.93	0.62
03-May	0.92	0.87	0.92	0.61
04-Jun	0.85	0.77	0.85	0.52
09-Jun	0.85	0.77	0.85	0.52
16-Jun	0.66	0.57	0.66	0.35
20-Jun	0.47	0.36	0.47	0.20
07-Jul	0.43	0.35	0.43	0.20
29-Jul	0.00	0.03	0.00	0.06

Figure 4.24 Visible and infrared surface albedo



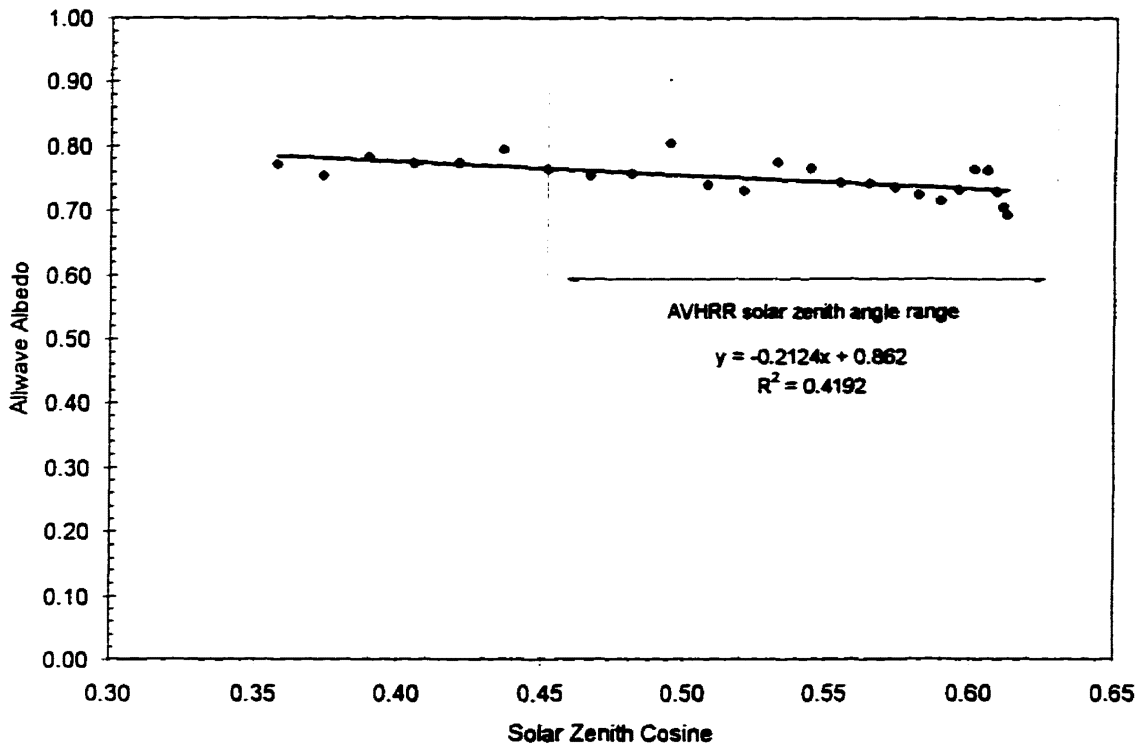
4.9 Solar Zenith Angle Normalization

Observations have shown that, at high solar zenith angles, the allwave albedo of snow, and hence snow-covered sea ice, increases as the sun's elevation decreases (Liljequist, 1954; Carrol and Fitch, 1981). As the solar zenith angle increases, there is an increased probability that incident radiation will begin scattering closer to the surface. This increases the opportunity for the scattered radiation to scatter out of the snowpack and thus increase the surface albedo (Wiscombe and Warren, 1980). Theoretically then, clear-sky snow albedo data collected at different solar zenith angles require normalization before comparison. Lindsay and Rothrock (1994) used a fit to Liljequist's (1956) albedo data for Antarctic snow to normalize their clear-sky AVHRR albedos to a solar zenith angle of 70°. Using this approach, the corrections to this dataset would be less than 0.01 after normalizing the results to the median solar zenith angle of 56°.

However, Warren (1982) states that this issue is somewhat controversial since the magnitude of this dependence is still unknown given the wide range of uncertainty in field observations and the complex effects of surface roughness on this relationship. Using measurements made from the first-year ice climate tower on June 4 under clear skies, Figure 4.25 compares allwave albedo with the cosine of the solar zenith angle. Solar zenith angles in the AVHRR data ranged from 51-61°. A least squares fit is applied to the data. There is considerable scatter around the line and the correlation coefficient (r^2) is low. Nevertheless, the June 4 data show a slight dependence on zenith angle consistent with the findings reported elsewhere (Warren, 1982). However, the applicability of these results to this AVHRR dataset is questionable given the wide range of surface conditions over the scene and through the melt season. For example, this correction is typically for smooth surfaces, therefore its application to rubble ice areas is likely inappropriate. Similarly, the zenith angle dependence of melt pond and bare ice albedo is likely more pronounced than a snow surface. However, there is no data to confirm this. Also, the dependence is likely more pronounced for the infrared albedo due to increased surface anisotropy, but again, no empirical data exists to confirm this. In light of these

uncertainties and the small range of solar zenith angles sampled here, the final AVHRR albedo data were not normalized to a common solar zenith angle.

Figure. 4.25 Dependence of allwave albedo on solar zenith angle



4.10 Sources of Uncertainty

Of obvious concern to potential users of this method is the precision at which surface sea ice albedo can be derived from AVHRR data. Precision is defined here as the smallness of range of statistical error, or in other words, freedom from random error (Lyon, 1970). It is expressed here as the fractional uncertainty ($\delta\alpha_s$) or

$$\delta\alpha_s = \frac{\Delta\alpha_s}{|\alpha_s|} \qquad [4\text{-}32]$$

where $\Delta\alpha_s$ is the uncertainty or error in the satellite derived surface albedo. Essentially the error in surface albedo is equivalent to summation of the error in the determination of TOA reflectance (*TOA*), the anisotropic correction (*anis*) and the atmospheric correction (*atm*) and the narrow to broadband conversion (*nb*), or

$$\Delta\alpha_s = \Delta\alpha(TOA) + \Delta\alpha(anis) + \Delta\alpha(atm) + \Delta\alpha(nb) \qquad [4\text{-}33]$$

The uncertainties in these terms can enhance each other or cancel each other out depending upon their sign (Koepke and Kriebel (1987). In terms of the determination of visible albedo, the inversion equation is

$$\alpha_{vis} = \frac{\rho_{TOA} - af}{bf}\eta \qquad [4\text{-}34]$$

where all terms of the equation have been defined previously except for η, which refers to the narrow to broadband conversion factor. In the case of AVHRR 1, $\eta = 1$. In the case of the infrared albedo, the inversion equation is

$$\alpha_{ir} = \left[c_1 + c_2\left(\frac{\rho_{TOA} - af}{bf}\right)\right]^2 \qquad [4\text{-}35]$$

where c_1 and c_2 refer to the regression coefficients. Using the law of the propagation of errors, the total uncertainty in both expressions can be expressed as a function of errors in each of the parameters. Thus for visible albedo, the following equation applies:

$$\Delta\alpha_{vis} = \frac{\partial\alpha_{vis}}{\partial\rho_{TOA}}\Delta\rho_{TOA} + \frac{\partial\alpha_{vis}}{\partial f}\Delta f + \frac{\partial\alpha_{vis}}{\partial a}\Delta a + \frac{\partial\alpha_{vis}}{\partial b}\Delta b + \frac{\partial\alpha_{vis}}{\partial\eta}\Delta\eta \qquad [4\text{-}36]$$

where Δ refers to the difference between the true and estimated value or the error. In terms of the total error in the infrared albedo, the following expression applies:

$$\Delta\alpha_{ir} = \frac{\partial\alpha_{ir}}{\partial\rho_{TOA}}\Delta\rho_{TOA} + \frac{\partial\alpha_{ir}}{\partial f}\Delta f + \frac{\partial\alpha_{ir}}{\partial a}\Delta a + \frac{\partial\alpha_{ir}}{\partial b}\Delta b + \frac{\partial\alpha_{ir}}{\partial c_1}\Delta c_1 + \frac{\partial\alpha_{ir}}{\partial c_2}\Delta c_2 \qquad [4\text{-}37]$$

Assuming the errors stated in [4.36] are independent and random, the total error in the derived visible albedo can be determined by solving the following differential equation

$$\Delta\alpha_{vis} = \left[\left(\frac{\partial\alpha_{vis}}{\partial\rho_{TOA}}\Delta\rho_{TOA}\right)^2 + \left(\frac{\partial\alpha_{vis}}{\partial f}\Delta f\right)^2 + \left(\frac{\partial\alpha_{vis}}{\partial a}\Delta a\right)^2 + \left(\frac{\partial\alpha_{vis}}{\partial b}\Delta b\right)^2 + \left(\frac{\partial\alpha_{vis}}{\partial\eta}\Delta\eta\right)^2\right]^{1/2} \quad [4\text{-}38]$$

where $\Delta\eta$ refers to the error in the narrow to broadband conversion. The corresponding equation for the infrared albedo is

$$\Delta\alpha_{ir} = \left[\left(\frac{\partial\alpha_{ir}}{\partial\rho_{TOA}}\Delta\rho_{TOA}\right)^2 + \left(\frac{\partial\alpha_{ir}}{\partial f}\Delta f\right)^2 + \left(\frac{\partial\alpha_{ir}}{\partial a}\Delta a\right)^2 + \left(\frac{\partial\alpha_{ir}}{\partial b}\Delta b\right)^2 + \left(\frac{\partial\alpha_{ir}}{\partial c_1}\Delta c_1\right)^2 + \left(\frac{\partial\alpha_{ir}}{\partial c_2}\Delta c_2\right)^2\right]^{1/2} \quad [4\text{-}39]$$

[4.38] and [4.39] were used to estimate the total uncertainty in the derived surface albedo for each study date based on the precision of the input parameters to the inversion process for that day. The average relative uncertainty of the method over the study period for extracting the visible and infrared albedo was 21% (σ =6%) and 16% (σ =4%) respectively. The poor precision is due mainly to the large uncertainty in the anisotropic correction of the TOA reflectances. In the following sections, this and other sources of uncertainty in the inversion methodology are closely examined.

In the following sections, the solutions of [4.38] and [4.39] were used to assess the sensitivity of the error in surface albedo to the uncertainties of each of the input parameters. For example, solving [4.36] for visible albedo results in:

$$\Delta\alpha_{vis} = \frac{1}{bf}\Delta\rho_{TOA} + \frac{-\rho_{TOA}}{bf^2}\Delta f + \frac{-1}{b}\Delta a + \frac{af - \rho_{TOA}}{fb^2}\Delta b + \alpha_{vis}\Delta\eta \qquad [4\text{-}40]$$

In order to include the role of surface albedo in the sensitivity analysis, the preceding expression was modified and simplified to:

$$\Delta\alpha_{vis} = \frac{1}{bf}\Delta\rho_{TOA} + \frac{a + b\alpha_{vis}}{fb}\Delta f + \frac{-\Delta a - \alpha_{vis}\Delta b}{b} + \alpha_{vis}\Delta\eta \qquad [4\text{-}41]$$

The preceding expression is identical to that found in Koepke and Kriebel (1987) except for the inclusion of the $\Delta\rho_{TOA}$ and $\Delta\eta$ here[18]. By assuming no error in the other terms, the sensitivity of surface channel albedo to errors in each of these variables was assessed. If the error is positive, the derived/assumed value is too low. If the error is negative, the opposite is true. In the following sections, the errors in each of these terms are examined in detail.

4.10.1 Calculation of TOA Reflectance

One of the most serious obstacles to AVHRR sensors measuring absolute surface albedo is the uncertainty in the calibration of the visible and infrared channel and the subsequent calculation of TOA reflectance. Even after correction for sensor drift, the channels only have an accuracy of ±7% (Che and Price, 1992). On its own, this inherent error precludes the use of this sensor to provide highly accurate albedo information.

Ignoring the drift in the channel calibration will result in a systematic error in the calculated albedos. Table 4.6 shows that reflectances derived from radiances based on the pre-launch calibration will be underestimated on average 0.05 for AVHRR 1 and 0.14 for AVHRR 2[19]. This uncertainty is somewhat lessened by post-launch calibration

[18] In Koepke and Kriebel (1987), it was assumed that there was no error in the determination of the TOA albedo and narrow to broadband conversion was not applicable.
[19] These average errors represent the R.M.S.E.

experiments that help detect the magnitude of sensor drift. In this investigation, an attempt was made to reduce this uncertainty by updating the prelaunch calibration by employing surface albedo measurements and the 6S radiative transfer code. The TOA radiances based on the updated calibration is considered to have a relative uncertainty of 7%. It appears that the uncertainty in this calibration method is just slightly less than the drift in AVHRR 1 and thus, this method is unlikely capable of correcting for drifts in this channel less than 7%. Teillet *et al.*, (1990) found that a similar calibration method was incapable of tracking AVHRR calibration changes less than 10%.

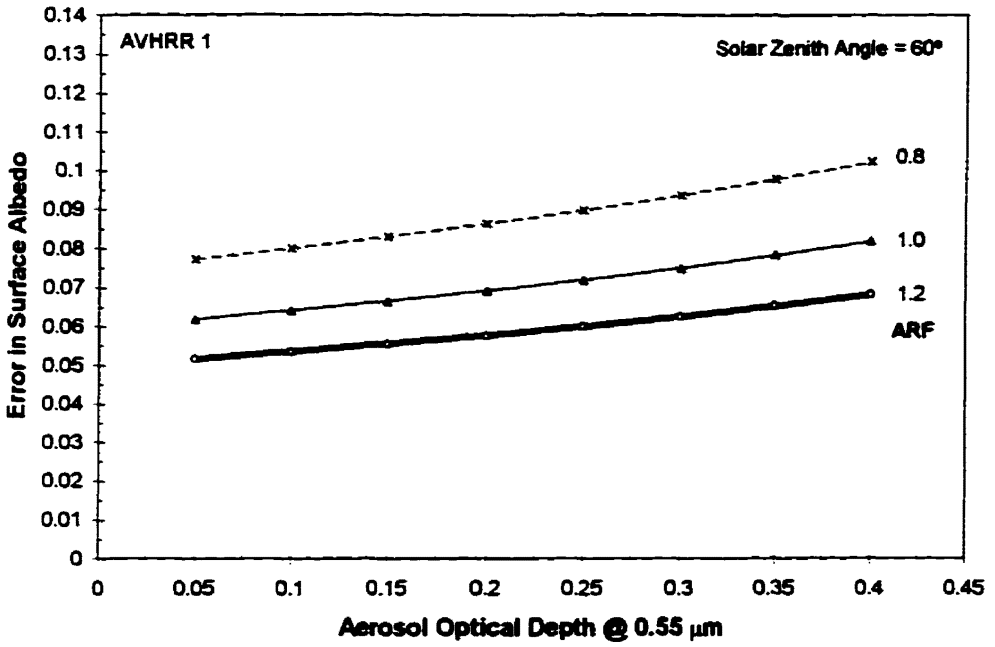
The sensitivity of error in the determination of ρ_{TOA} is assessed using [4.41]. Assuming that there is no error in the derivation of the other parameters, the error in surface albedo due to error in the calculation of TOA reflectance is inversely proportional to b, which essentially represents the transmissivity of the atmosphere, and the anisotropic correction factor. This dependence is shown in Figure 4.26 where the transmissivity of the atmosphere is represented by aerosol optical depth. Since the atmospheric transmissivity is always less than one, a positive error in TOA reflectance will be amplified over a surface where the ARF is less than or equal to one. Since an ARF greater than unity indicates that the TOA albedo is initially overestimated, the masking effect of the atmosphere can be compensated and the effect of the error on the surface albedo can be dampened to some degree. Figure 4.26 illustrates both the importance of a properly calibrated instrument in the derivation of surface albedo and the compensatory relationship of some errors in the inversion process.

4.10.2 Anisotropic Correction

The anisotropic correction is the largest source of error in the inversion process. In order to correct for the anisotropy of the surface and atmosphere, this study applied anisotropic correction factors derived from ERBE data (Taylor and Stowe, 1984). These factors were chosen based on the sun-target-sensor geometry at the subarea's central pixel. The anisotropic correction factors were derived for angular bins with an angular

resolution of 12° for the zenith angles and 30° for the azimuth angle. The variability of the ARFs can be described by the relative dispersion of radiances in each angular bin

Figure 4.26 Error in calculated visible albedo due to 0.05 error in the derivation of TOA reflectance for varying atmospheric turbidity and based on different ARFs. Note: Ozone amount fixed at 0.35 cm NTP.



expressed as a percentage (standard deviation of radiances in each bin divided by the bin average). This variability is likely due to errors in scene identification, field of view contamination, surface type contamination and finally the natural variability of the surface category and overlying atmosphere (Taylor and Stowe, 1984). Although snow and ice surfaces had the smallest dispersions of all representative surfaces in the dataset, they are still substantial. Based on the sea ice model and the predominant view angles of AVHRR shown in Figure 4.5, the average dispersion for a particular sun-target-sensor configuration for solar zenith angles between 45° and 78° is 23%. Taylor and Stowe (1984) state that the large dispersions in the database do not compromise the quality of their results and they believe that the anisotropic factors are realistic and are within expected limits. However, clearly the variability in these values reduce the precision of the methodology used here.

The high level of variability for individual view configurations may be due to cloud contamination of the target scene. The capability of the cloud detection algorithm used in the T&S study is questionable (Lindsay and Rothrock, 1994). Specifically, the technique had difficulty detecting low cloud (Taylor and Stowe, 1984). This deficiency is particularly relevant in the case of the sea ice model, since low stratus clouds are prevalent over arctic sea ice for much of the spring and summer season. On the other hand, the dispersion in the ARFs may represent the true seasonal variability of sea ice anisotropy. Taylor and Stowe's (1984) ARFs were based on measurements made from Nov. 17, 1978 to Sept. 12, 1979, thus representing most of the annual cycle of sea ice growth. The ARFs in each view bin represents an average of the anisotropy of a mixture of snow, bare ice and melt water surfaces. Perovich's (1984) ARF results for various sea ice surfaces are summarized in Table 4.22.

Table 4.22 Variability of sea ice ARFs over various view configurations for (a) 0.45 μm and (b) 0.95 μm. Based on ARFs measured in Perovich (1994).

(a) 0.45 μm

Solar Zenith	Relative Azimuth	Snow	Glazed Snow	Bare Ice	Blue Ice†	Melt Pond	*Mean*	*St. Dev.*
90	-	0.99	1.18	0.91	0.93	0.93	*0.99*	*0.11*
60	180	1.06	1.41	0.99	1.12	1.04	*1.12*	*0.17*
60	90	0.97	1.14	0.95	0.96	0.84	*0.97*	*0.11*
60	0	0.96	1.14	0.95	0.91	0.86	*0.96*	*0.11*
30	180	1.36	1.77	2.16	1.66	1.42	*1.67*	*0.32*
30	90	0.96	1.14	1.01	1.02	0.89	*1.00*	*0.09*
30	0	0.82	0.53	0.56	0.83	0.83	*0.71*	*0.15*

†Blue ice refers to bare ice with bluish colour due to minimal bubbles in ice's upper layer

(b) 0.95 μm

Solar Zenith	Relative Azimuth	Snow	Glazed Snow	Bare Ice	Blue Ice	Melt Pond	*Mean*	*St. Dev.*
90	-	0.97	1.03	0.63	0.79	0.29	*0.74*	*0.30*
60	180	1.07	1.48	0.86	1.36	0.64	*1.08*	*0.35*
60	90	0.96	1.2	0.8	1.01	0.31	*0.86*	*0.34*
60	0	0.95	1.03	0.75	0.76	0.29	*0.76*	*0.29*
30	180	1.58	2.38	3.12	2.39	1.47	*2.19*	*0.68*
30	90	0.95	1.19	0.87	1.01	0.2	*0.84*	*0.38*
30	0	0.86	0.26	0.27	0.64	0.2	*0.45*	*0.29*

The large variability within view configurations indicates that for a particular configuration, the anisotropy of sea ice can vary substantially. The degree of variability in Perovich's results compare well with the variability in Taylor and Stowe's sea ice ARFs. It should be noted that the variability in the Taylor and Stowe dataset may also be due in part to the anisotropy of the atmosphere. Airborne particulates such as ice crystals likely affect the anisotropy of the surface viewed from space. It is apparent that, due to the large annual range of sea ice anisotropy, the use of a seasonally-independent ARFs in the determination of TOA albedo, as done in this and other investigations, severely curtails the precision of the derived data.

The estimated error in the ARFs employed here are based on the dispersion in the final coefficients as supplied by Taylor and Stowe (1984). However, there remains unknown uncertainty regarding the use of T&S's ARFs to correct AVHRR data. Since there are inherent differences between ERBE and AVHRR data, the application of ARF models derived from ERBE measurements to AVHRR-derived reflectances ultimately results in uncertainty in the derived surface albedo data. This uncertainty in the ARF arises primarily due to the differences between the sensors' spatial, temporal and spectral dimensions. In terms of the sea ice model, the T&S ARF dataset represents the anisotropy

of ERBE pixels spectrally integrated over the entire solar spectrum, spatially averaged over a 90 km^2 pixel area (nominally), geographically averaged over both poles and temporally averaged over much of the sea ice growth cycle. Of course, the more similar the sampling of AVHRR is to ERBE, the less potential for uncertainty in the results. Towards this, the following will examine the sources of uncertainty when applying T&S ARFs to this AVHRR data by examining the spatial and spectral sampling inconsistencies between the datasets.

4.10.2.1 Spatial Differences

The T&S study attempted to ensure that each of the surface models were constructed from uniform areas. However, due to the coarseness of the ERBE sensor's spatial resolution, the ARF models are likely representative of a variety of surface types captured within an pixel area of minimum size of 90 km^2 (250 km^2 out to the horizon). Thus, in some cases, the models can be considered a mixed reflectance function derived from a number of surface features of who's individual contributions to the function is not known and is averaged over the sampling period. Since the snow model is based primarily on images of Antarctica and Greenland, contamination of the model by other surface types is unlikely (Taylor and Stowe, 1984a). Thus, in this regards, application of the snow model to smaller AVHRR pixels of snow-covered ice is appropriate. Similarly, applying the ocean model to finer resolution sensors like AVHRR is not likely a source of uncertainty since the variability of ocean reflectance is low.

In contrast, the application of the sea ice model is less straightforward. In the case of sea ice surfaces, the intra-pixel feature composition is seasonally and geographically dependent. The T&S factors were based on measurements made from Nov. 17, 1978 to Sept. 12, 1979, thus representing most of the annual cycle of sea ice growth. For much of the annual cycle, the ice surface is snow-covered and relatively homogeneous. The derived sea ice ARFs can thus be considered to be biased towards this type of surface type

and thus more appropriate for early spring periods. Also, the availability of a larger number of clear-sky days in early spring strengthens this bias towards snow-covered sea ice. However, warmer spring and summer temperatures replace the snow-covered icescape with a heterogeneous surface dotted with melt ponds and dissected by open water leads. Each of these surface types (snow, bare ice, melt ponds, ridged ice and open water) have different ARFs (Perovich, 1994). Taylor and Stowe (1984) point to this feature variability for the higher variability found in sea ice ARFs compared to snow ARFs.

Since most of these sea ice features are small and thus not resolved in the AVHRR's 1.1 km nominal pixel size, a coarse resolution model like T&S's seems appropriate. Caution should be exercised, however, when applying these coarse resolution ARFs to TOA reflectances measured by sensors capable of resolving these individual features. On the two dates where the sea ice ARF model is applied, June 16 and June 20, *in situ* observations reveal that over the area of an AVHRR pixel, the surface consisted of a mixture of melt ponds, wet snow and bare ice. Since the sea ice model is likely weighted towards snow surfaces, application to these image dates is a source of uncertainty. Since the anisotropy is considered to be greater over these melt surfaces, the use of T&S's sea ice model likely underestimates the TOA albedo to some small degree on these dates. For heterogeneous surfaces, Koepke and Kriebel (1987) advocate the use of a mixed ARF derived from the ARFs of homogeneous areas and weighted by the pixel fraction each surface type occupies. Such an approach, however, requires information regarding the spatial distribution of surface features over each pixel. There is a potential here for high resolution imagery, such as TM or SAR, to provide this feature information.

Finally, the course resolution of the ERBE sensor leads one to question whether the variability in derived ARFs is due to the surface's anisotropy or atmosphere's anisotropy. It is possible that over such a large area, inhomogeneities in the surface anisotropy may cancel out, thus leaving the atmosphere as the primary source of variability (Lee, 1990; Pinker and Stowe, 1990). This is may be especially true over the long optical path lengths

inherent in polar imagery. If this is the case, application of these factors to data from a higher resolution sensor capable of resolving variability in surface anisotropy may lead to error.

4.10.2.2 Spectral Differences

Compared to AVHRR 1 and 2, the ERBE instrument used to build the ARF models operated over a wider spectral range (one band: 0.2-4.5 μm). Since the ARFs were derived from a sensor operating over the entire solar spectrum, care must be taken when applying these correction factors to individual, narrower spectral bands within this wavelength range. Of specific interest here is the application of the T&S ARFs to both AVHRR 1 and 2. This approach assumes that the anisotropy of radiation reflected by the three model surfaces and the overlying atmosphere is constant with wavelength over the visible and near-infrared AVHRR channels. This assumption has been made in previous albedo studies (De Abreu *et al.*, 1993; Lindsay and Rothrock, 1994).

In terms of the snow model, given the wavelength-independence of the anisotropy of radiation reflected from snow surfaces (Figure 4.6(a)), the applicability of these broadband factors to both the visible and near-infrared AVHRR channel seems appropriate for snow-covered sea ice surfaces. In contrast, the anisotropy of water is wavelength dependent and the application of the ocean ARF to both AVHRR 1 and 2 is a source of uncertainty. However, given the low flux of radiation reflected by ocean surfaces, the overall magnitude of error is considered minor in terms of the energy balance of the surface. A similar application of the sea ice model is not as straight-forward.

As pointed out earlier, the sea ice model is a composite of the anisotropy of various sea ice surface types and is most representative of snow-covered sea ice. Over snow-covered sea ice, the application of one ARF to both AVHRR channels, as done in De Abreu (1993) and Lindsay and Rothrock (1994) is acceptable. However, as shown in Table 4.22, sea ice

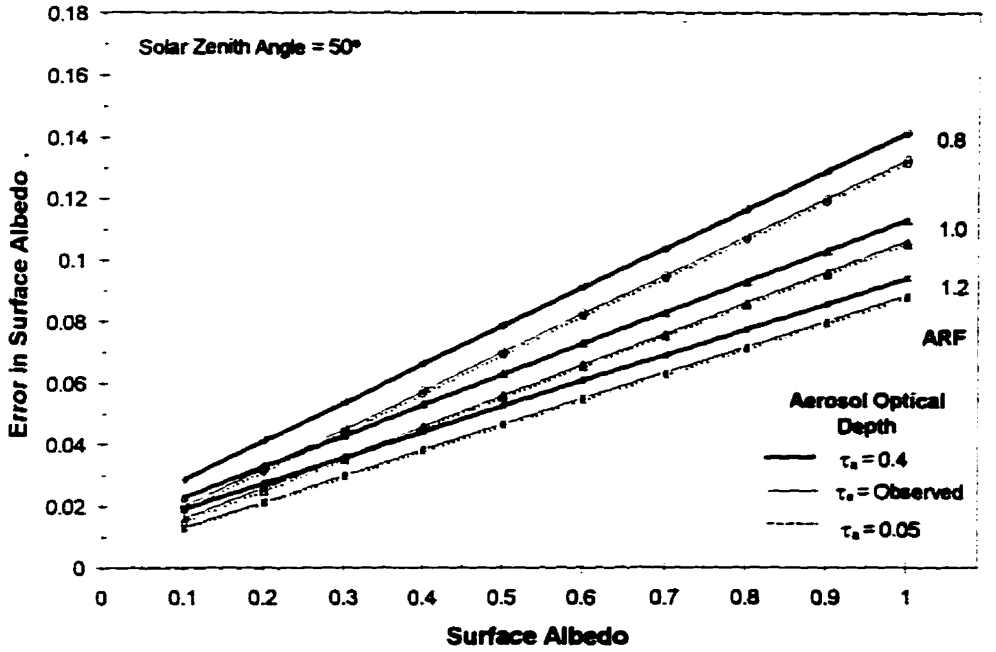
ARFs are not wavelength-independent. The effect of adding an atmosphere above the surfaces measured in Perovich (1994) on the wavelength-dependence of his surface-measured ARFs is unknown, but it is unlikely to entirely mask this wavelength dependence. Thus application of one ARF to both channels is likely a source of uncertainty, but which channel is it more representative of? Over a sea ice surface, the incident and reflected radiation is heavily weighted towards the visible wavelengths. The broadband ERBE ARF is thus likely more representative of the anisotropy of visible radiation, or in terms of AVHRR, channel 1. Since the near-infrared ARFs are consistently lower (approx. 10%) than the visible ARFs over sea ice melt surfaces (Perovich, 1994), the application of T&S's broadband ARF to the near-infrared channel 2 data likely underestimates the TOA infrared albedo.

Figure 4.27 and Figure 4.28 show the error in calculated surface albedo for a 0.1 error in the anisotropic correction factor for a range of aerosol optical depths, surface albedos and solar zenith angles for AVHRR 1 and 2 respectively. Within each graph, the results are grouped by the correct ARF. The data indicate that the calculated surface albedo is very sensitive to errors in the anisotropic correction factor. Based on the observed average atmospheric conditions observed here, a surface with an albedo of 0.9 and an ARF of 1 will have 0.12 error in AVHRR 1 surface albedo when the ARF is in error by 0.1. The error for AVHRR 2 is 0.09. AVHRR 1 appears more sensitive to errors in the ARF than AVHRR 2. This is logical given its greater sensitivity to atmospheric scattering. Based on the range of ARFs examined here and the mean observed solar zenith angle, the error in surface albedo ranges from 0.012 to 0.145 for an error of 0.1 in the prescribed ARF. The level of error increases linearly with surface albedo, indicating that over sea ice surfaces there is a greater need for accuracy in the specification of ARF. Errors in surface albedo are largest for turbid conditions and larger solar zenith angles.

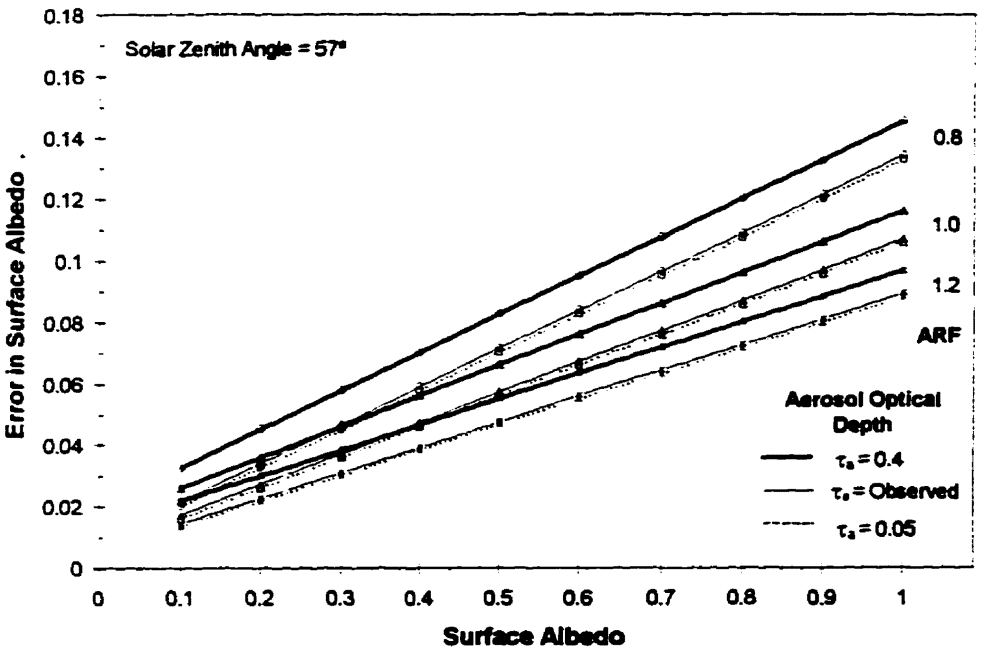
The following equation can be used along with the data in figures 4.27 and 4.28 to estimate the required accuracy of the ARF (Δf) required to achieve a certain accuracy in surface albedo ($\Delta \alpha_s$) at a specific surface albedo:

Figure 4.27 Error in calculated visible albedo to due to 0.1 error in anisotropic reflectance factor based on true factors of 0.8, 1.0 and 1.2. Results are given for a range of aerosol optical depths: turbid (τ_a=0.4), mean observed (τ_a=0.1) and clear (τ_a=0.5) and solar zenith angles. Note: the atmopsheric correction is assumed to be correct.

(a)



(b)



(c)

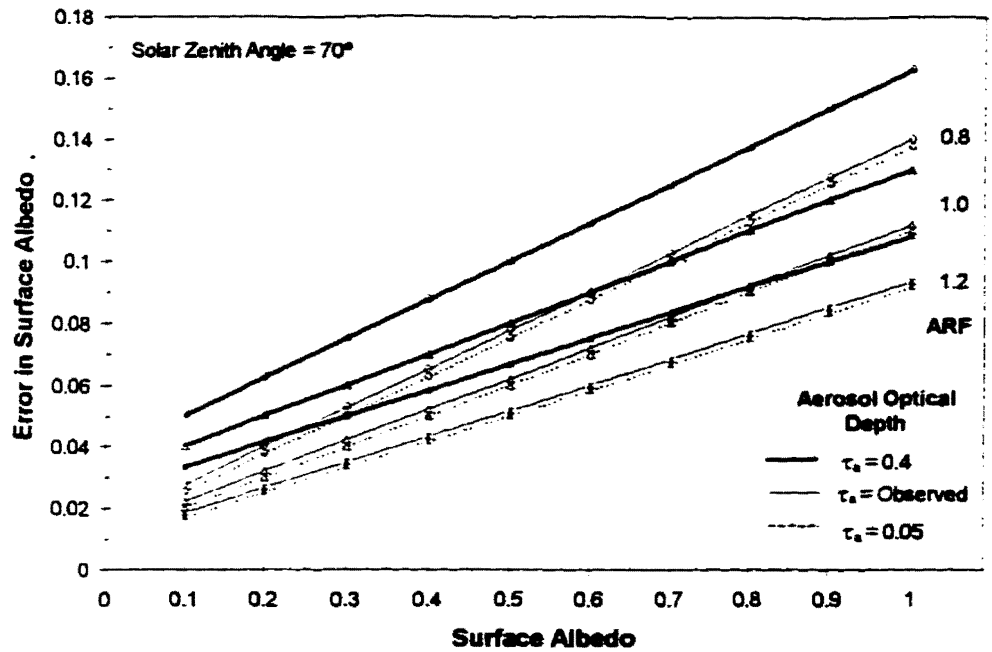
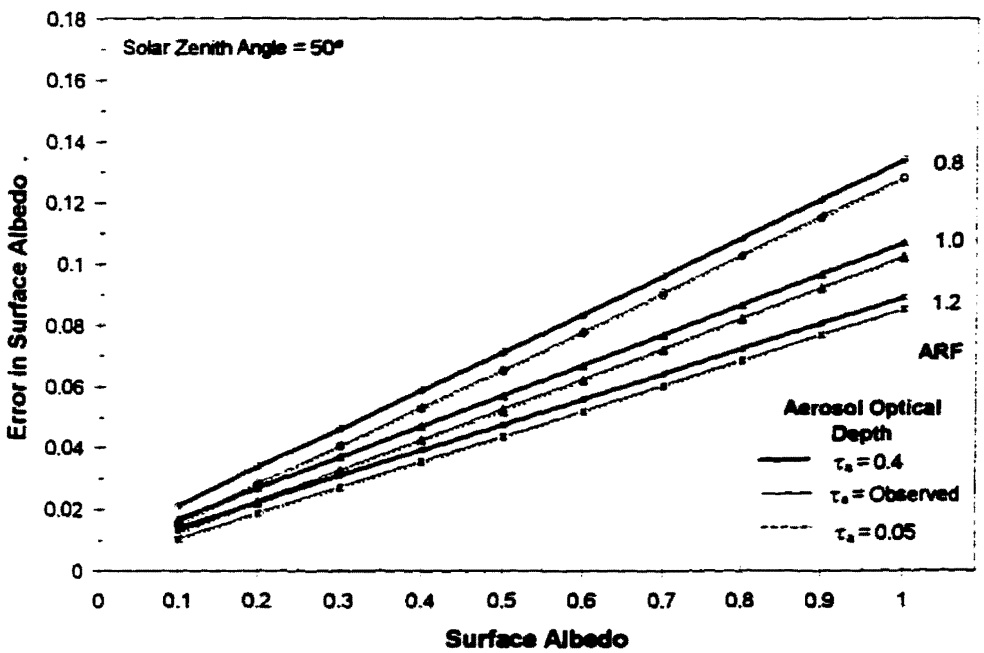
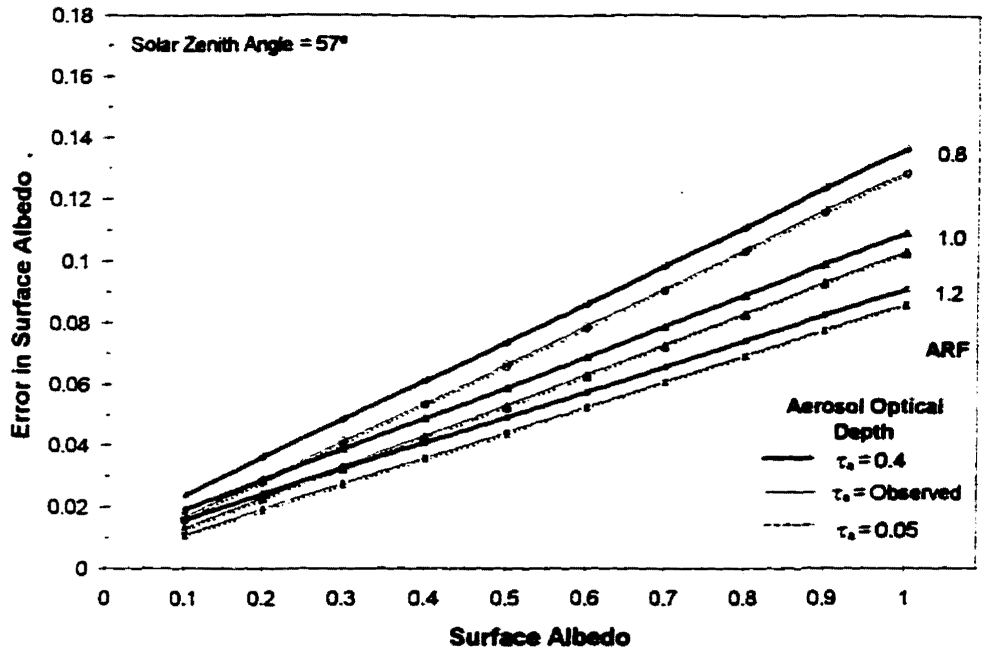


Figure 4.28 Error in calculated infrared albedo to due to 0.1 error in anisotropic reflectance factor based on true factors of 0.8, 1.0 and 1.2. Results are given for a range of aerosol optical depths: turbid (τ_a=0.4), mean observed (τ_a=0.1) and clear (τ_a=0.5) and solar zenith angles.

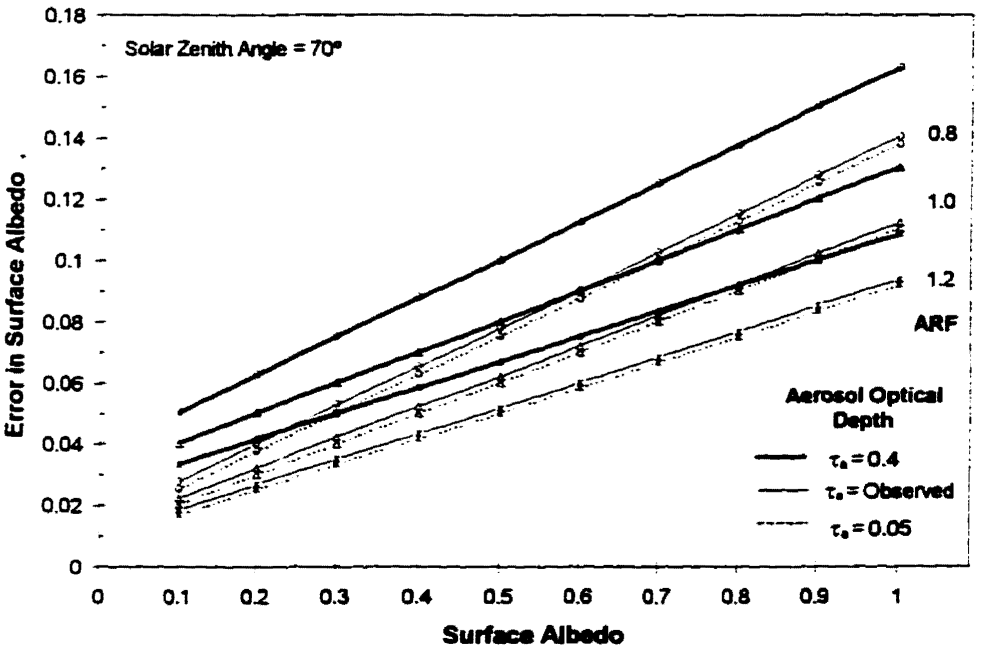
(a)



(b)


Solar Zenith Angle = 57°
Error in Surface Albedo
Surface Albedo
0.8
1.0
1.2
ARF
Aerosol Optical Depth
τa = 0.4
τa = Observed
τa = 0.05

(c)


Solar Zenith Angle = 70°
Error in Surface Albedo
Surface Albedo
0.8
1.0
1.2
ARF
Aerosol Optical Depth
τa = 0.4
τa = Observed
τa = 0.05

$$\Delta f = \frac{0.1\Delta\alpha_s'}{\Delta\alpha_s} \qquad [4\text{-}42]$$

Thus, in order to achieve an accuracy of 0.05 in visible surface albedo ($\Delta\alpha_s'$=0.05) for a surface with an albedo of 0.9 under a solar zenith angle of 70° (Figure 4.28), the anisotropic reflectance function (Δf) would need an accuracy of 0.1 x 0.05 / 0.13 or approximately 0.04. Over the range of ARFs examined here (0.8-1.2) the accuracy required would be 0.04-0.06. A surface with an albedo of 0.3 would only require an ARF accuracy in the range 0.11-0.16 to achieve an accuracy of 0.05 in visible surface albedo.

4.10.3 Atmospheric Correction

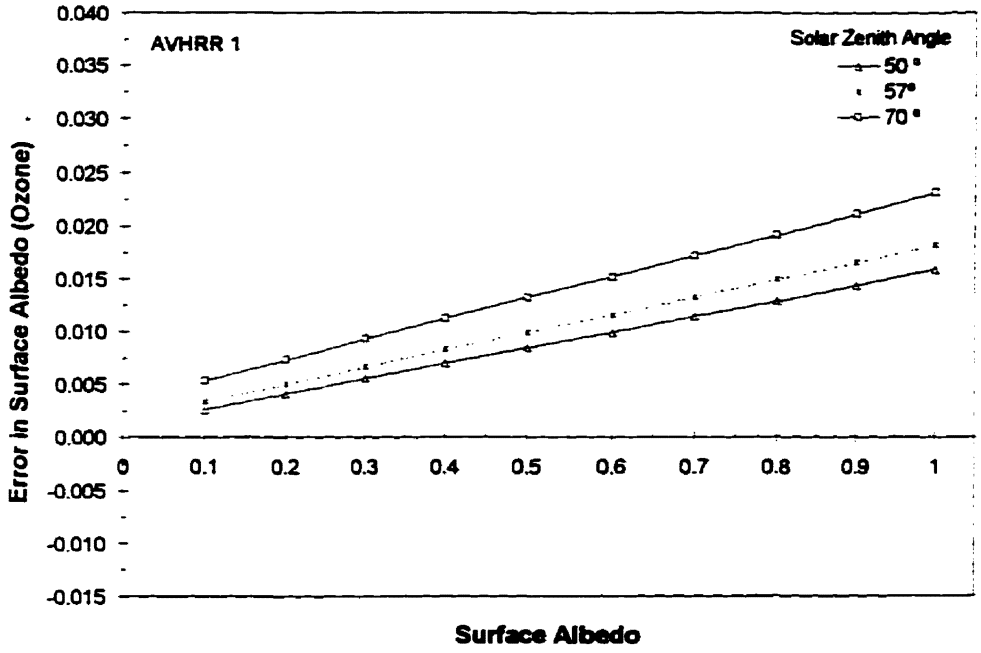
[4.41] is used to estimate the effect of uncertainty in the atmospheric correction procedure on the derived surface albedos. These estimates are made with the assumption that the error due to the derivation of TOA albedo and the anisotropic correction is zero. The major source of uncertainty in the atmospheric correction procedure arises from error in the description of the atmosphere, i.e. errors in the estimation of aerosol optical depth, ozone amount and water vapour amount. The resultant effect of error in each of these input variables on the surface albedo is examined in the following sections.

4.10.3.1 Ozone Amount

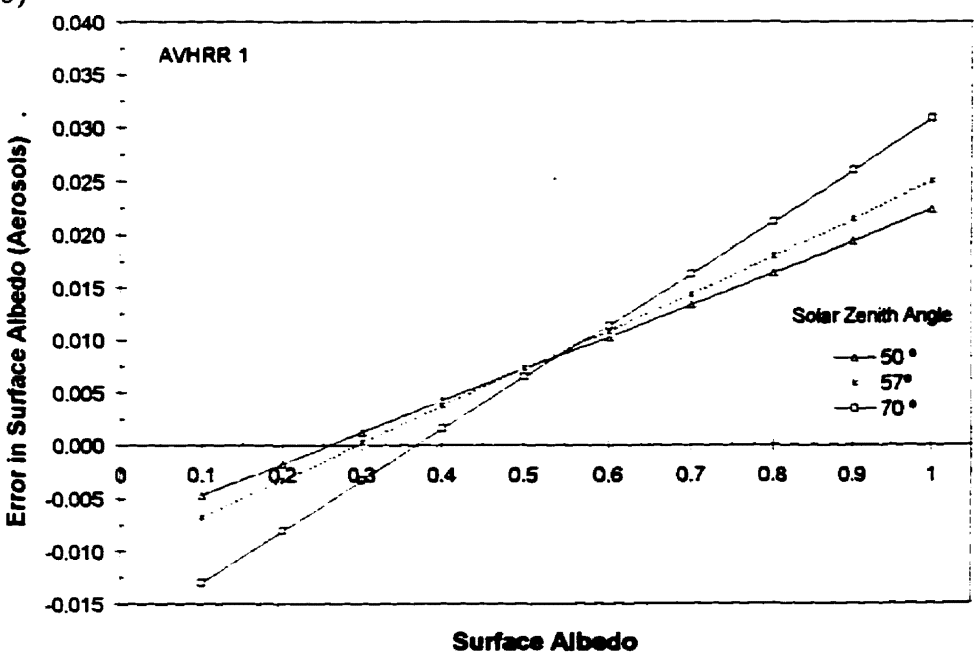
Figure 4.29(a) shows the sensitivity of the calculated visible albedo to the accuracy of the ozone amount input to the atmospheric correction model. The results are based on a mean observed aerosol optical depth of 0.1. For a 0.05 cm NTP error in ozone amount over a surface albedo of 0.9, the error of the calculated surface albedo would be 0.017 under the mean observed solar zenith angle of 57°. The magnitude of the albedo error increase linearly with the albedo of the surface and is greater over larger solar zenith angles. The ozone amounts measured in this study ranged from 0.28 to 0.41 cm NTP and

Figure 4.29 Error in calculated surface albedo due to (a) 0.05 cm NTP error in ozone amount, (b) 0.05 error in aerosol optical depth (visible albedo) , (c) 0.5 cm precipitable water error in water vapour amount and (d) 0.05 error in aerosol optical depth (infrared).

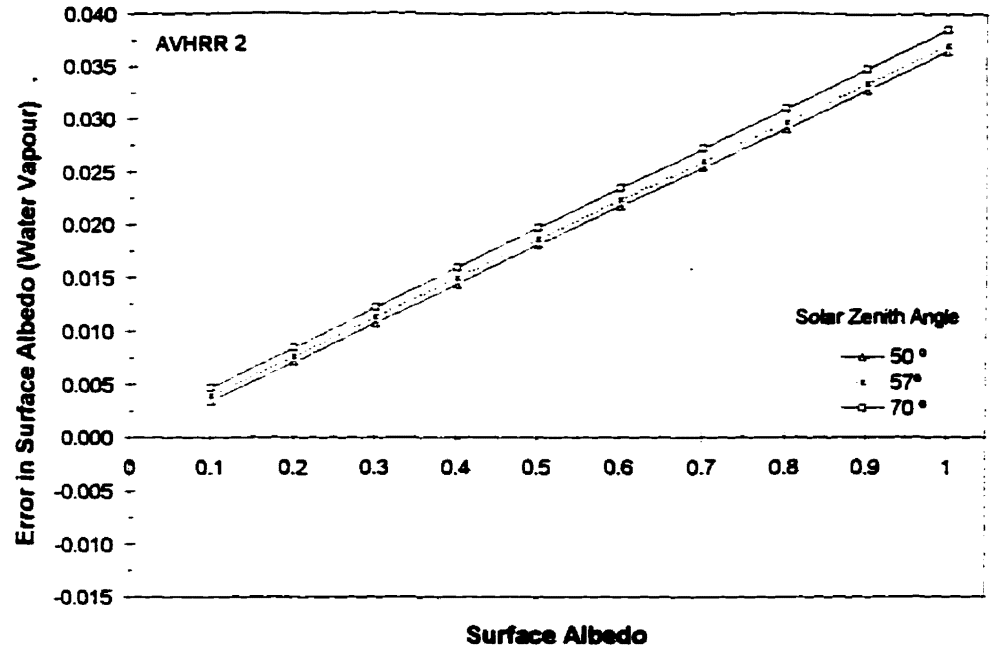
(a)



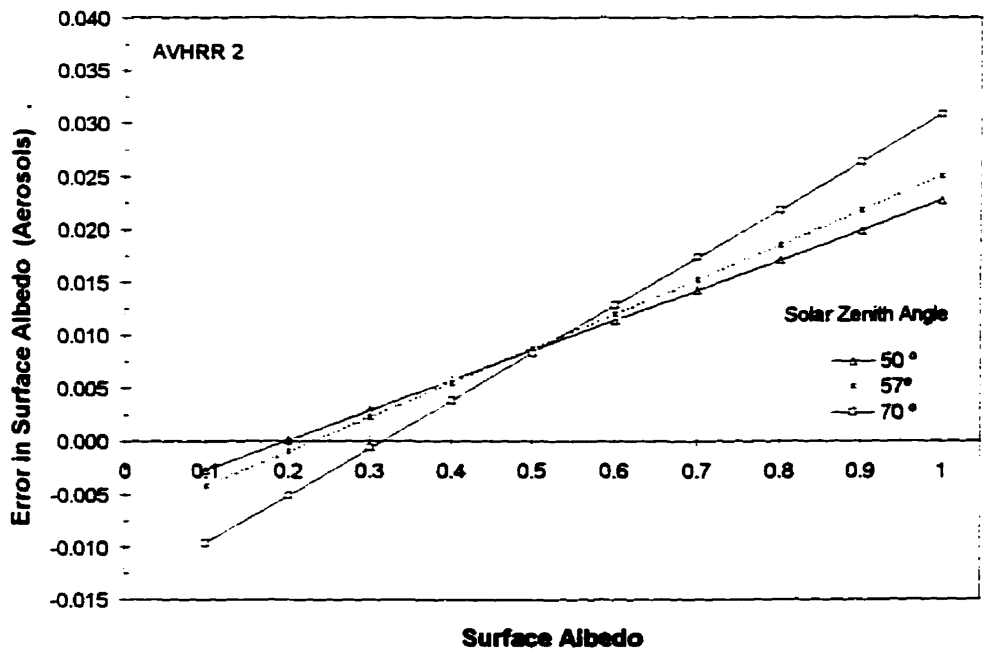
(b)



(c)


AVHRR 2
Error in Surface Albedo (Water Vapour)
0.040
0.035
0.030
0.025
0.020
0.015
0.010
0.005
0.000
-0.005
-0.010
-0.015
0
0.1
0.2
0.3
0.4
0.5
0.6
0.7
0.8
0.9
1
Solar Zenith Angle
50°
57°
70°
Surface Albedo

(d)


AVHRR 2
Error in Surface Albedo (Aerosols)
0.040
0.035
0.030
0.025
0.020
0.015
0.010
0.005
0.000
-0.005
-0.010
-0.015
0
0.1
0.2
0.3
0.4
0.5
0.6
0.7
0.8
0.9
1
Solar Zenith Angle
50°
57°
70°
Surface Albedo

represent daily averages. The largest standard deviation of the measured data is 0.005 cm NTP. This uncertainty results in an error in surface albedo of 0.002. The effects of using climatological ozone amounts instead of *in situ* measurements are examined next.

In most situations, *in situ* measurements of ozone amount are not available. In lieu of this, climatological observations are often used. They usually reside in the form of monthly averages from surface stations or satellite observations. The difference between the surface observed values (considered here to be the true ozone amount) and the climatological value is termed the error in ozone amount (Δoz). The Δoz can be used along with the results in Figure 4.29(a) to estimate the resultant error in surface albedo due to the use of climatological ozone observations. According to TOMS data presented in Keating *et al.* (1989), the zonal mean total column ozone amount for a latitude of 75° for the months of April, May, June and July are 0.462, 0.416, 0.370 and 0.332 respectively. The largest Δoz is -0.05 cm NTP which results in a surface albedo error due to ozone of -0.016 for mean atmospheric conditions. The negative sign of $\Delta\alpha_s$ signifies that the surface albedo would be too high by 0.016 if climatological ozone values were utilized. This error is relatively minor and thus, the use of climatological averages for ozone in the correction for ozone attenuation appears valid.

4.10.3.2 Water Vapour Amount

Figure 4.29(c) shows the effect that 0.5 cm error in the water vapour amount (precipitable water (w)) would have on the AVHRR 2 surface albedo under mean atmospheric conditions. For a surface with an albedo of 0.9, a 0.5 cm error in water vapour amount (Δw) would result in a surface AVHRR 2 albedo error ($\Delta\rho_s$) of 0.033. $\Delta\alpha_s$ increases linearly with surface albedo and is slightly dependent on solar zenith angle. In order to achieve an accuracy in AVHRR 2 surface albedo of ±0.05, the water vapour amount would require an accuracy of ±0.76 cm.

The precipitable water amounts used to estimate the atmospheric water vapour content were calculated by daily radiosonde data collected on overpass days. The accuracy of these data are dependent on the accuracy of the radiosonde data used to calculate the absolute humidities. The relative humidity sensor, pressure sensor and the temperature sensor are all subject to error. Elliott and Gaffen (1991) examine the accuracy and precision of radiosonde measurements used in long term climate studies. They point out the difficulty in obtaining accurate humidity measurements in cold, dry environments like the Arctic. However, since precipitable water is an integral, and the bulk of the integral in contained in the surface-500 mb level, these errors have only a small effect. Given this, the precipitable water amounts calculated here are estimated to be accurate only to ⇧5% (M. Serreze, personal communication). Based on the range of water vapour contents used in this study (0.33-3.1 cm) and the estimated accuracy of precipitable water estimates, Δw would range from 0.02 to 0.16 . Taking the largest error (Δw=0.16), the corresponding error in surface albedo for mean observed conditions would be 0.01.

4.10.3.3 Aerosol Optical Depth

The effects of error in the measured aerosol optical depth (Δaer) on the surface albedo measured by AVHRR 1 and AVHRR 2 are summarized in Figure 4.29(b) and 4.29(d) respectively. In terms of a surface with an albedo of 0.9 and assuming mean atmospheric conditions, the error in both AVHRR 1 and AVHRR 2 surface albedo for underestimating the aerosol optical depth by 0.05 is an underestimation of surface albedo by 0.02. Under the mean observed atmospheric conditions, both channels are showing the same sensitivity to Δaer. The error in surface albedo due to Δaer increases with solar zenith angle for surface albedos greater than 0.55 for AVHRR 1 and 0.5 for AVHRR 2 and vice versa for lower albedo surfaces. Under mean observed conditions, the $\Delta\alpha_s$ due to Δaer is zero over surfaces with an albedo of 0.3 for AVHRR 1 and zero over surfaces with an albedo of 0.23 for AVHRR 2. Over surfaces with albedos less than these values, an underestimate of aerosol optical depth results in an overestimate of surface albedo.

In order to estimate AVHRR 1 and 2 surface albedo with an accuracy of 0.05, the aerosol optical depth requires an accuracy of 0.13. Under a solar zenith angle of 70°, the required accuracy would increase to 0.1. These required accuracies would be lower for surfaces with albedos less than 0.9. Sun photometer measurements were used to estimate aerosol optical depths in this investigation. As previously stated, these measurements are considered accurate to 0.02, well within the required accuracy of 0.1 calculated above.

An aerosol parameter not examined here is the absorption fraction. The absorption fraction describes the proportion of incident radiation that is absorbed by an aerosol (1-SSA). Koepke and Kriebel (1987) found surface albedos estimated by the method used in this investigation are very sensitive to the aerosol's fractional absorption. The aerosol used to derive Koepke's correction coefficients is slightly absorbing with an absorption fraction of 0.11 at 0.55 μm, typical of a continental aerosol. In Koepke and Kriebel (1987), a 0.05 error in the aerosol fractional absorption was found to result in an error in the calculated surface albedo of 0.01 in clear conditions (τ_a=0.05) and 0.094 in turbid conditions (τ_a=0.4). These results refer to a surface with a broadband climatological albedo of 0.9 and a solar zenith angle of 58°. Thus when employing atmospheric correction models, care must be taken to choose the correct aerosol type. For example, the use of an oceanic aerosol model with an absorption fraction of 0.01 instead of the required continental type would result in an error in surface albedo of about 0.2 for turbid conditions. Clearly specification of the proper aerosol model is important to the correction of optical satellite imagery.

It is unfortunate that given the sensitivity of surface albedo to the prescribed aerosol optical depth, there is no wide-scale monitoring effort. Aerosol climatologies are few and information regarding the optical properties are rare and difficult to obtain. Given the transient nature of tropospheric aerosols and their wide variability in optical properties, the prescription of aerosol optical depth is the most difficult atmospheric parameter to characterize for the correction of remotely sensed data. In the case of AVHRR 1 and 2, it

has been shown that accurate prescription of aerosol type and amount is critical to the estimation of surface albedo from these channels.

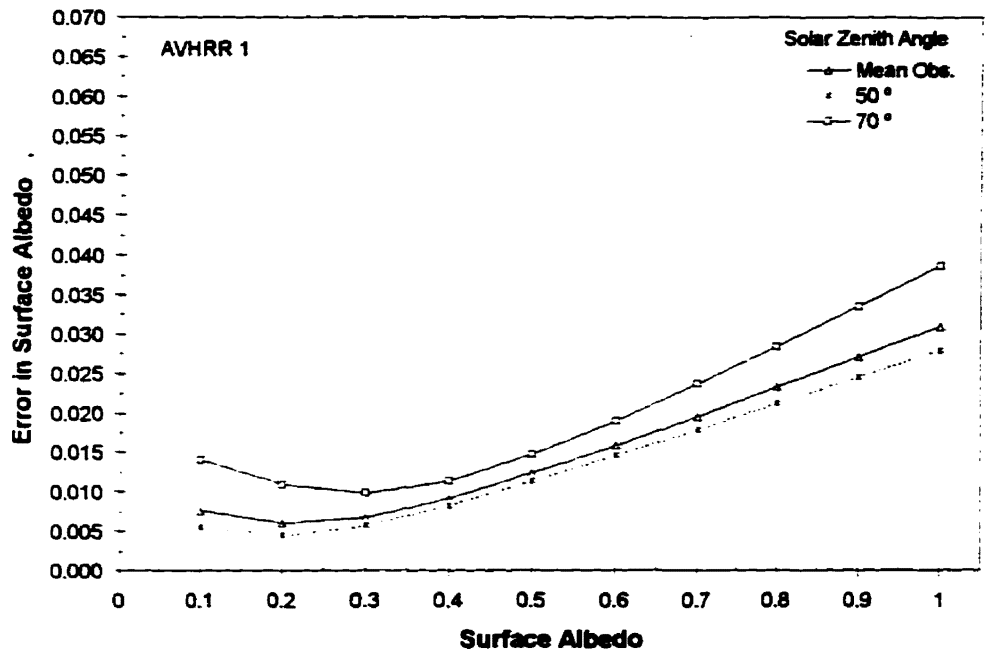
Based on the propagation of errors, the total uncertainty in surface albedo due to the atmospheric correction are summarized in figures 4.30 and 4.31 for clear and turbid conditions. Generally, the sensitivity of surface albedo to errors in the atmospheric correction increases with surface albedo, solar zenith angle and turbidity. Therefore, there is a greater need for accuracy in the atmospheric correction procedure during early spring period in the arctic when the surface is snow-covered, the atmosphere is somewhat hazy and solar zenith angles are large. This sensitivity decreases linearly with surface albedo. Also, AVHRR 2 albedo appears more sensitive to errors in the atmospheric correction. This is due to that channel's strong sensitivity to both aerosols and water vapour. The effect of using climatological data in the atmospheric correction on the precision of the method was examined. There was less than a 1% decrease in precision using climatological data input to the atmospheric correction. The lack of difference is likely due to the fact that the study site is located adjacent to a weather station. The climatological data was derived from data collected at the station. Thus, the climatological data characterizes atmospheric conditions well and does not differ greatly from the *in situ* sampled parameters. It is logical that this difference in precision will increase in other parts of the arctic not regularly monitored.

4.10.4 Narrow to Broadband Conversion

The error in the narrow to broadband conversion was expressed as the *rmse* of the converted AVHRR channels and the true broadband values over a collection of typical sea ice surfaces and under different atmospheric conditions. No correction was applied to AVHRR 1 since the surface narrowband albedo closely matched that of the visible broadband albedo for the much of the season. The exception was over a surface with 60% melt ponds, in which case AVHRR 1 underestimated visible albedo. Over all surfaces, the *rmse* ranged from 0.02 to 0.03. In terms of AVHRR 2, the error in using the narrowband

Figure 4.30 Error in calculated surface albedo due to total error in atmospheric correction for (a) visible albedo and (b) infrared albedo under clear conditions (aerosol optical depth = 0.05).

(a)



(b)

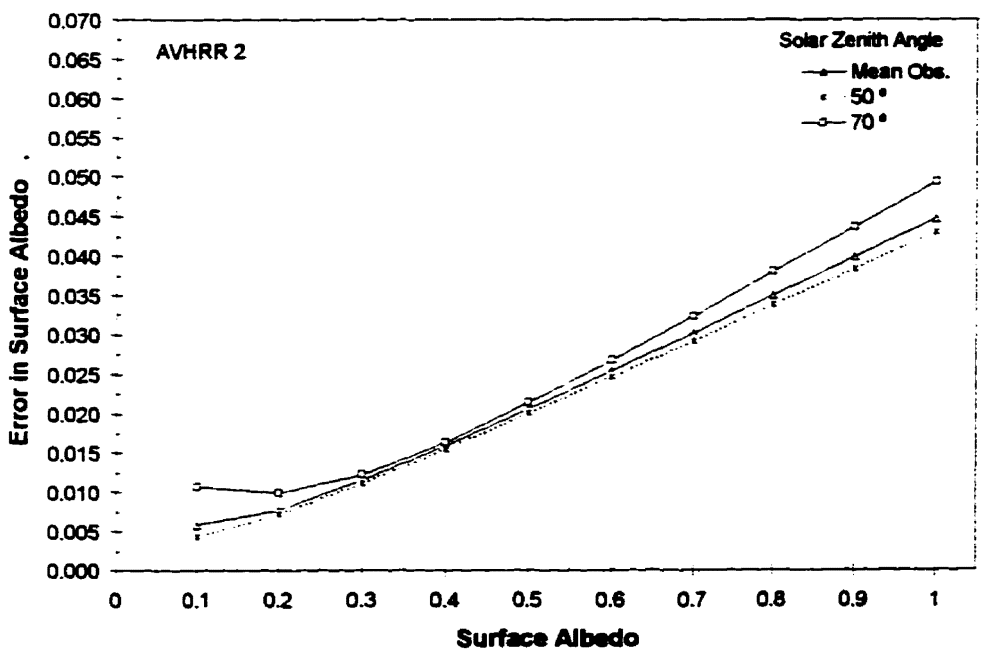
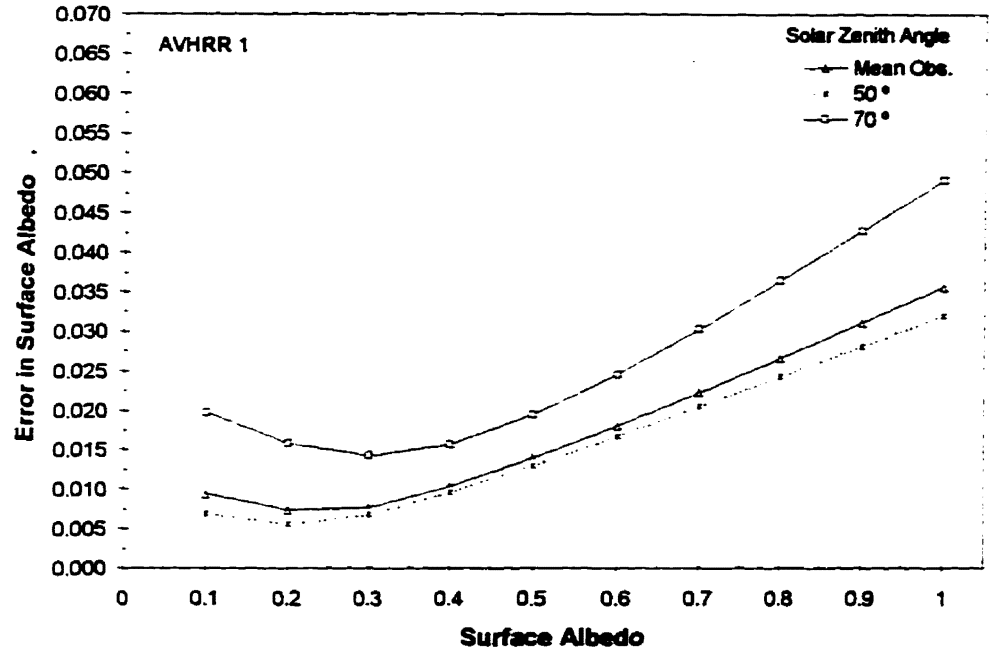
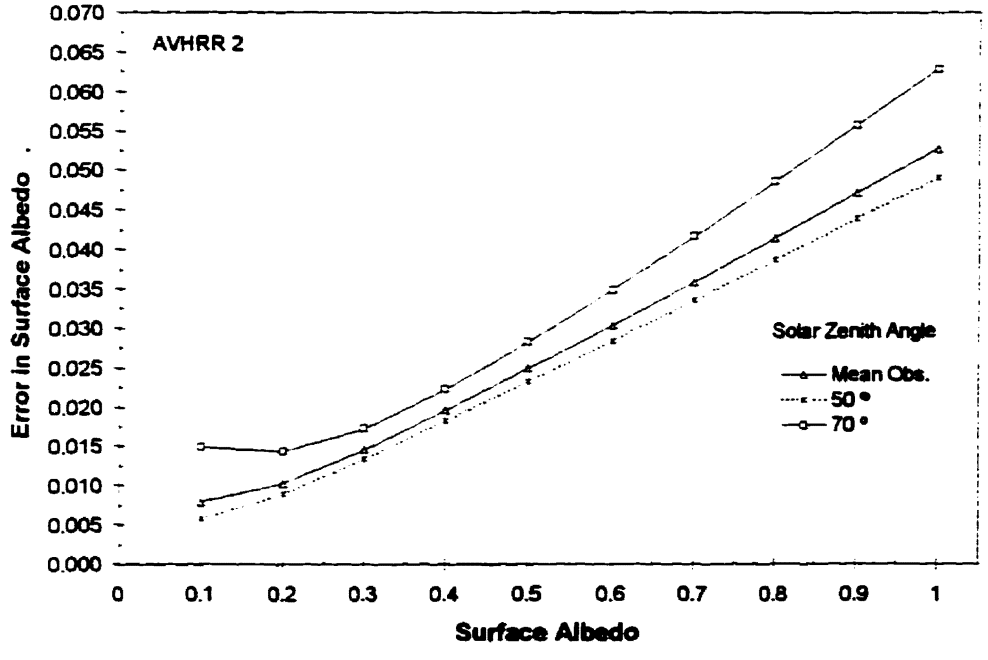


Figure 4.31 Error in calculated surface albedo due to total error in atmospheric correction for (a) visible albedo and (b) infrared albedo under turbid conditions (aerosol optical depth = 0.4).

(a)



(b)



surface albedo without adjustment to estimate broadband infrared albedo ranged from 0.19 to 0.21. These differences were largest over snow and ice surfaces and decreased significantly as the amount of surface water increased. This is logical given the position of the AVHRR 2 channel and the infrared spectra of these surfaces. A linear model was applied with good results (r^2=0.99). With a confidence level of 0.95, new predictions with this model based on the mean albedo of the simulated dataset are considered accurate to ±0.05.

4.11 Accuracy of Satellite Albedo Measurements

The previous section theoretically estimated the precision of the albedo inversion method and sources of uncertainty in the derived results. This section attempts to assess the accuracy of the derived surface albedos. Accuracy is defined here as the difference between the derived surface albedo and the true value. Although always desired, comparison of satellite-derived surface quantities to surface measurements is not always possible. This is especially true for polar experiments. Surface validation is critical to the development, evaluation and evolution of retrieval methodologies for remotely sensed data. However, its value to the process is directly related to one's ability to measure the pertinent variables over appropriate spatial, temporal and spectral resolutions with a high degree of accuracy. In order to validate satellite-derived surface albedo, surface measurements over an area sufficiently large enough to represent the pixel field-of-view is required. In the case of AVHRR, the area should be nominally 1.1x1.1 kms. Also, the surface instrument should be capable of reproducing the spectral characteristics of the sensor or the satellite-derived quantity. In the case of this investigation, coincidental surface measurements of visible and infrared broadband albedo would be required.

Attempts have been made to use surface transects collected over a typical pixel area for satellite validation purposes. In De Abreu (1993), transect measurements of broadband albedo were performed in SIMMS '92 coincident with AVHRR overpasses to assess the spatial

variability of surface albedo and thus allow for the later assessment of the accuracy of a satellite-retrieved albedo. However, much of the albedo variability over the sampling transects was attributed to changes in atmospheric conditions and instrument setup. This type of sampling required the radiometers to be set up several times over the transect increasing the opportunity for such error. Sources of this error are variations in instrument height, orientation to solar principal plane, shadowing and sensor leveling. More importantly, the grid transects required 1.5 - 2 hours to complete; a period over which irradiance conditions often changed.

The only realistic way to measure surface albedo over these scales is from an airborne platform such as an aircraft or balloon. In SIMMS '93, balloon photography was used to monitor the onset of melt conditions (Piwowar *et al.*, 1994). Unfortunately, no aerial measurements of albedo were collected[20]. The *in situ* spectral albedo measurements described in Chapter Three are representative of a small surface area (less than 0.25 km) and cannot be considered to be representative of the brightness of an AVHRR pixel. The surface based spectrometer is capable of emulating the response of AVHRR 1 and 2. However, its limited spectral range (0.4-1.0 μm) does not allow it to measure infrared albedo.

In spite of their obvious spatial and spectral limitations, the *in situ* spectral albedo measurements are compared to surface AVHRR 1 and AVHRR 2 channel albedos. While theoretically incapable of truly validating these measurements, the surface data provide some basis for comparison. Given the homogeneity of the sea ice surface in the early spring, it is assumed that, until the appearance of surface melt features, the point observations of spectral albedo are comparable to the albedo over the scale of a AVHRR pixel.

Surface spectral albedo data are transformed to emulate AVHRR 1 and 2 albedo by weighting the high resolution albedo measurements by the spectral response filter of

[20] Balloon-based measurements of broadband albedo were attempted in SIMMS '95.

AVHRR 1 and 2 and the incident irradiance. Satellite-derived AVHRR 1 and 2 surface albedo of the SIMMS '93 FYI site were extracted for each image date (2x2 pixels) and averaged. These are compared with the emulated AVHRR 1 and 2 surface albedos in Figure 4.32 and Table 4.23

Despite the poor precision of the method, Figure 4.32 and Table 4.23 indicate that the satellite-derived albedos compare very well with the surface albedo observations. Both sets of measurements capture the steady seasonal decrease in surface albedo early in the season. The discrepancy in the late June observations may be indicative of the inherent bias in point observations. At that time of the season, the surface was dotted with melt water and remnant snow/ice surfaces. The surface albedo observation was taken over a ponded surface and is thus biased toward that surface type. The AVHRR albedo measurement is representative of the ponded areas as well as the brighter snow/ice features, thus leading to the higher albedo value. This illustrates one of the inherent advantages of satellite derived measurements over point-based measurements.

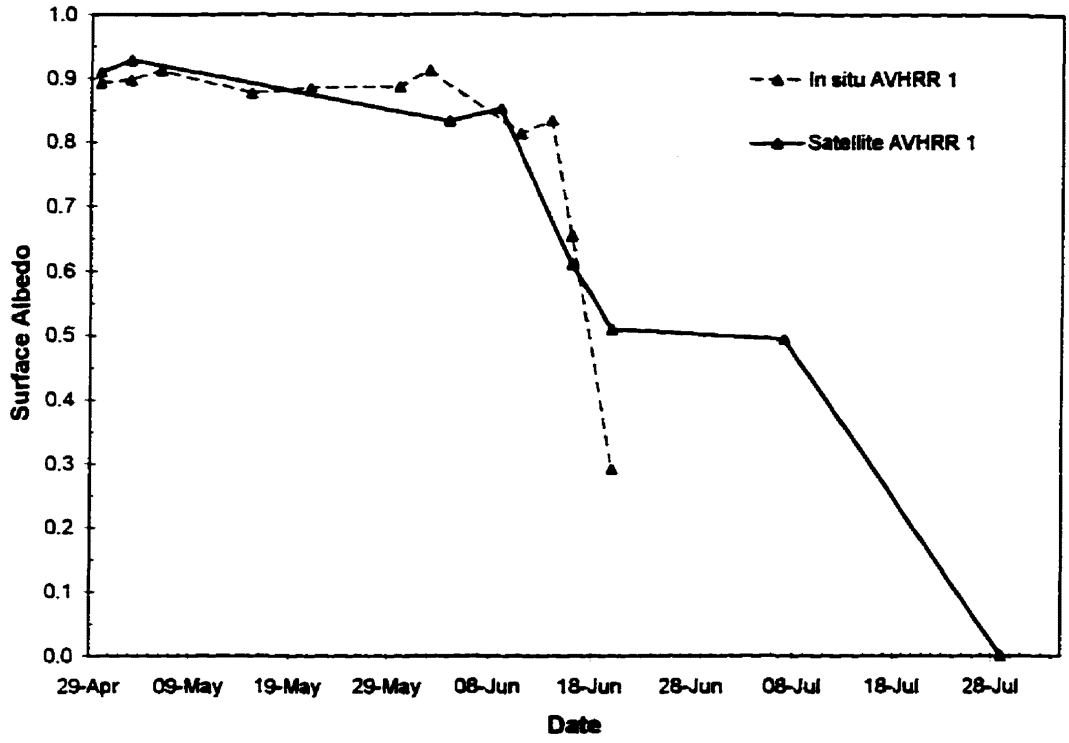
Although the estimated uncertainty in the derived values are large, comparison with surface measurements and results of previous investigations (De Abreu *et al.*, 1993) suggest that the derived albedos are at expected magnitudes. The results in Table 4.23 suggest that the rmse. of the satellite derived albedos is better than ±0.1 for both visible and infrared albedo.

4.12 Summary of Findings

This chapter examined the feasibility of using AVHRR data to estimate clear-sky broadband visible and infrared sea ice albedo. The methodology was described and a detailed sensitivity and error analysis were performed. The satellite-derived albedo were

Figure 4.32 Emulated surface measurements of AVHRR albedo data compared to (a) AVHRR 1 surface albedos and (b) AVHRR 2 surface albedos.

(a)



(b)

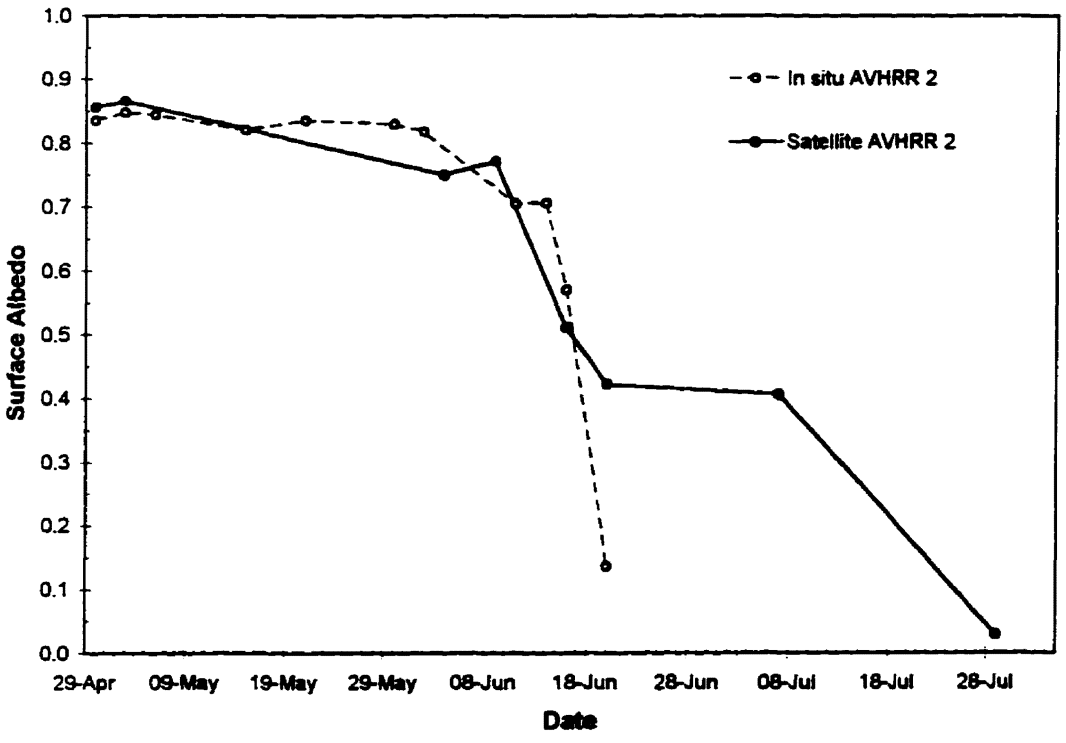


Table 4.23 Comparison between *in situ* and satellite measured visible and infrared albedo. June 20, July7 and July 20 data not included due to lack of representative *in situ* spectra.

Date	Visible Albedo			Infrared Albedo		
	In Situ	Satellite	Error	*In Situ*	Satellite	Error
April 30	0.89	0.91	-0.02	0.84	0.86	-0.02
May 3	0.90	0.93	-0.03	0.85	0.87	-0.02
June 2,4[+]	0.91	0.83	0.08	0.82	0.75	0.07
June 9	0.81	0.85	-0.04	0.70	0.77	-0.07
June 16	0.66	0.61	0.04	0.57	0.51	0.06
		r.m.s.e	*0.05*		*r.m.s.e.*	*0.07*

[+] *In situ* data collected on June 2, satellite data collected on June 4

compared to coincidental surface albedo measurements. This investigation revealed the following:

NOAA 12's AVHRR 1 and 2 has undergone significant calibration drift since launch

Past experience has shown that this sensor experiences significant decreases in sensitivity while in orbit. Ignoring this drift introduces large systematic errors into derived surface albedos. Thus, AVHRR 1 and 2 cannot be used to derive surface albedos without an update to its prelaunch calibration. Unlike other platforms, no update for NOAA 12's AVHRR had been performed prior to this study. Using coincidental surface and atmospheric measurements, an attempt was made to update the NOAA 12's AVHRR 1 and 2 prelaunch calibration. The results indicate an 8.6 % and a 25.1 % degradation in the sensitivity of AVHRR 1 and 2 respectively. It is not known whether the calibrations of the two channels have stabilized. Thus, the calibration update provided here should only be considered appropriate for the spring of 1993.

Recommendation: AVHRR sensors from all NOAA platforms should be included in ground-based calibration exercises. In the past, only calibrations from AVHRRs on odd-numbered NOAA platforms were updated due to their afternoon passes. Also, an onboard calibration source should be included in the next generation AVHRR. This is being considered (Rao, personal communication).

The extraction of surface albedo from AVHRR will remain imprecise while surface-independent sea ice ARFs are used.

The high solar zenith angles prevalent in the polar regions and wide scan angles of AVHRR demand accurate estimates of sea ice surface's anisotropy. Sensitivity analysis indicates that over snow-covered sea ice at an solar zenith angle of 70°, the ARF would need an accuracy of 0.04 to achieve a surface albedo with an accuracy of 0.05[21]. However, the required accuracy of the ARF decreases with surface albedo and atmospheric attenuation. While snow and ice are less anisotropic than other terrestrial surfaces, the variability of ARFs for snow and ice for a given sun-surface-sensor geometry is considerable and is seasonally-dependent. It is unknown whether the source of this variation is related primarily to inhomogeneities in the anisotropy of the surface or atmosphere. Regardless, the precision of inversion methodologies that utilize surface independent sea ice ARFs will be constrained by this high variance.

Recommendation: Defining the anisotropy of sea ice and its overlying atmosphere should be given highest priority. Since, in theory, radiative transfer modelling can explain the anisotropy of the atmosphere, the anisotropy of polar atmospheres should receive immediate attention. Of similar importance are the seasonal characteristics of sea ice BRDF. Field programs should continue to characterize sea ice anisotropy. Increased attention should be given to the anisotropy of large, mixed-surface areas. The MISR sensor on EOS-AM1 platform promises to address these issues and improve the extraction of TOA satellite albedos from past, present and future TOA satellite reflectance

[21] This estimate is based on the assumption that the atmospheric correction is correct.

measurements. The application of surface dependent ARFs will likely require apriori geotyping.

Over sea ice surfaces, the TOA albedo significantly underestimates the surface albedo, thus making atmospheric correction necessary.

Due to the long optical path lengths, atmospheric attenuation results in an underestimation of sea ice albedo in polar regions. This underestimation was found to be as large as 22% over a snow-covered sea ice in April. The masking effect of the atmosphere decreases with the seasonal decrease in the arctic atmosphere's aerosol optical depth. In fact, sensitivity analysis revealed that, in terms of atmospheric correction, the surface albedo is most sensitive to the accuracy of the input aerosol optical depth. Aerosol optical depth would have to be accurate to 0.1 for a surface with an albedo of 0.9 under a solar zenith angle of 70°.

Recommendation: Improved monitoring of optical characteristics of aerosols is required to facilitate proper atmospheric correction of optical data. Use of climatological values may be adequate in late season, but early spring applications are suspect due to episodic haze events. Once validated, methods to use AVHRR and other satellite imagery to estimate aerosol optical depth should improve corrections.

AVHRR 1 is a good estimate of visible albedo over most sea ice surfaces, while AVHRR overestimates infrared albedo over all sea ice surfaces.

Surface spectral albedo measurements indicate that AVHRR 1 provides a very good estimate of visible albedo over snow-covered sea ice, bare ice and open water surfaces. Over heavily ponded surfaces (60%), AVHRR 1 underestimates visible albedo by 0.07. AVHRR 2 consistently overestimates sea ice infrared albedo. A simple function relating the two variables was developed via simulation and surface measurements.

Recommendation: These theoretical findings would benefit from a companion empirical investigation. Presently, spaceborne investigation is not possible due to lack of

appropriate sensor combinations. However, *in situ* measurements with filtered pyranometers and spectral radiometer are possible.

Operational use of AVHRR to measure surface sea ice albedo requires improved cloud detection.

In this study, surface observations and rudimentary, manual cloud detection methods were used to detect clouds. In order to automate this procedure, an accurate operational cloud detection (masking) scheme is required. The similar reflectances of snow/ice and clouds in polar regions make this a formidable challenge. Fortunately, it is an active research area.

Recommendation: Utilize SIMMS experimental data to validate ISCCP cloud algorithm, as well as other automated cloud detection schemes.

4.13 Conclusions

This chapter assessed the ability of AVHRR 1 and AVHRR 2 satellite data to estimate sea ice visible and infrared surface albedo. The AVHRR polar dataset is attractive due to its accessibility, substantial archive and very frequent coverage of the polar regions. However, using visible and infrared satellite data from an operational meteorological satellite operating in polar regions presents formidable hurdles to the estimation of surface albedo. Most daunting is the need to account for the strong dependence of TOA sea ice reflectance to satellite view configuration. The need for improved information regarding the anisotropy of sea ice surfaces and polar atmospheres is paramount in the development of a precise inversion method. Also, the AVHRR's lack of onboard calibration is a serious obstacle to obtaining the absolute radiometric measurements necessary to estimate albedo. Regular calibration updates are thus required. The satellite's wide swath width and the large solar zenith angles in the arctic result in considerable atmospheric attenuation of the incident and reflected surface radiation. As a result, proper atmospheric correction is required before accurate surface albedos can be derived. Climatologists require daily surface albedo information with an accuracy of ± 0.05 (Henderson-Sellers and Wilson,

1983; Weaver and Troisi, 1996). Although the method examined here was calculated to be far less precise, in this study it produced surface albedos that appear to approach this level of accuracy.

5 LARGE-SCALE VARIABILITY IN SEA ICE ALBEDO

5.1 Introduction

In Chapter 3, *in situ* observations of spectral albedo were used to describe the seasonal evolution of sea ice visible and near-infrared albedo of snow-covered sea ice volumes on both first-year and multiyear ice. While clearly valuable for understanding the seasonal metamorphism of these specific surface types and the associated effect on albedo, these measurements lacked a spatial component seen as critical to climate studies of sea ice. Satellite remote sensing is the most efficient method of providing surface albedo information over the spatial and temporal scales important to climate studies. In the previous chapter, Chapter 4, the measurement of surface visible and infrared albedo from clear-sky AVHRR 1 and 2 data collected over the SIMMS 1993 experiment area during the spring transition months of April to July was described. The purpose of this chapter is to present the satellite-derived albedo data and interpret the spectral, seasonal and spatial variability of this multitemporal dataset with the assistance of the *in situ* observations made through most of the study period. The first analysis section, Section 5.4, examines each albedo image individually in the context of three seasonal periods and focuses mainly on the interscene variability in visible and infrared albedo. Some attention is given to intrascene variability on consecutive dates. When possible, the satellite-derived values are compared to equivalent parameterized sea ice albedo values from the CCC2 GCM [2.3-2.4] and Ebert and Curry's (1993) sea ice model (Table 2.2). In Section 5.5, multitemporal analysis is used to identify and interpret the major time-space characteristics

of sea ice albedo for the entire study season. In the final analysis section, Section 5.6, differences between visible and infrared albedo over the study period are examined.

5.2 Image Preparation

As described in the previous chapter, eight image dates were available for analysis: April 30, May 3, June 4, June 9, June 16, June 20, July 7 and July 29. These data span the entire melt cycle from the onset of melt conditions to the breakup of the ice cover. The following section describes the pre-analysis processing performed on the image data.

5.2.1 Registration of AVHRR Data

Although the AVHRR data were georegistered to a common map grid at AES, analysis showed that the images were slightly unaligned and that "nudging" was necessary. Thus, in order to examine change between image dates, an image to image registration was performed on the dataset. All images were registered to the June 4 dataset given its geometric fidelity caused by its near-nadir position in the AVHRR swath. Twelve ground control points were identified in each image, a second order polynomial function relating the input image to the June 4 image was determined and a nearest neighbour method was used to resample the original data. The registration error (RMSE) was less than one AVHRR pixel.

5.2.2 Sub-Area Extraction and Masking of Land/Ice

The original dimensions of the AVHRR scenes were 256 pixels by 256 lines. In order to focus on the SIMMS experiment region and to restrict analysis to those regions where surface conditions were known, 60 pixel by 60 line subareas were extracted for each date. This resulted in a 360 km^2 study site centered on Resolute Passage. Due to course spatial resolution of the sensor, the SIMMS intensive sampling areas are not individually resolved.

In order to restrict the digital analysis to ocean pixels of the study scene, these areas were interactively masked. The July 29 image was used to separate the land features from

ocean since the boundary between the two were most pronounced on this image date. Due to the coarse resolution of the sensor, pixels near the shoreline likely contain mixed responses (*mixels)* from both land and water. Attempts were made to exclude these shoreline mixels from the ocean mask. Any subsequent digital analysis of the dataset was restricted to pixels in the ocean mask. Application of the mask resulted in the dataset being reduced from 3600 pixels to 2564 pixels.

5.2.3 Generation of Difference Images

In order to assist in the analysis, difference images were generated for each pair of sequential dates for both the visible and infrared albedo. Difference images were generated for the following periods: April 30 to May3, May 3 to June 4, June 4 to June 9, June 9 to June 16, June 16 to June 20, June 20 to July 7 and July 7 to July 29[22]. These difference images ($\Psi\alpha$) were generated for band i at pixel j and line k by the following:

$$\Psi\alpha_{ijk} = \alpha_{ijk}(Q_2) - \alpha_{ijk}(Q_1) \qquad [5\text{-}1]$$

where $\alpha(Q_1)$ and $\alpha(Q_2)$ are the albedo values at time 1 and time 2. In this formulation, positive values indicate an increase in albedo between time 1 and time 2 and a negative change value indicates a decrease in albedo over this period. Assuming that the satellite derived albedos have an uncertainty of 0.05, $\Psi\alpha$ between images must be greater than ±0.1 to be considered real. To this end, $\Psi\alpha$ between -0.1 and +0.1 have been assigned a colour of white in the change images, indicating no discernible change. $\Psi\alpha > 0.1$ (an increase in albedo) was assigned a tone of blue, while $\Psi\alpha < -0.1$ (a decrease in albedo) was assigned a tone of yellow/red.

[22] Note that the period between T_1 and T_2 are different for each image set.

5.3 Scene Description

In Chapter 3, the ice conditions in the SIMMS '93 intensive sampling area were described and a brief description of the region's ice conditions was provided. The analysis in this chapter will show that the variability in surface albedo is dependent on the snow and ice characteristics over the AVHRR scene. Given this, it is useful to precede this analysis with a detailed review of the snow and ice conditions over the entire AVHRR study scene. Figure 5.1 illustrates the relative location of the AVHRR scene. ERS-1 SAR imagery of the SIMMS experiment region collected on April 21 is provided in Figure 5.2. This C-Band radar is sensitive to surface roughness conditions and is thus valuable for describing ice regimes and physiographic features in the AVHRR albedo scenes. Generally, when snowcovers are dry, the SAR signal from first-year ice is a strong function of surface roughness. Since rough ice conditions are more efficient backscatterers, these areas can be easily identified in Figure 5.2 by bright tones in radar imagery.

Figure 5.1 Relative location of AVHRR study scene (dashed lines)

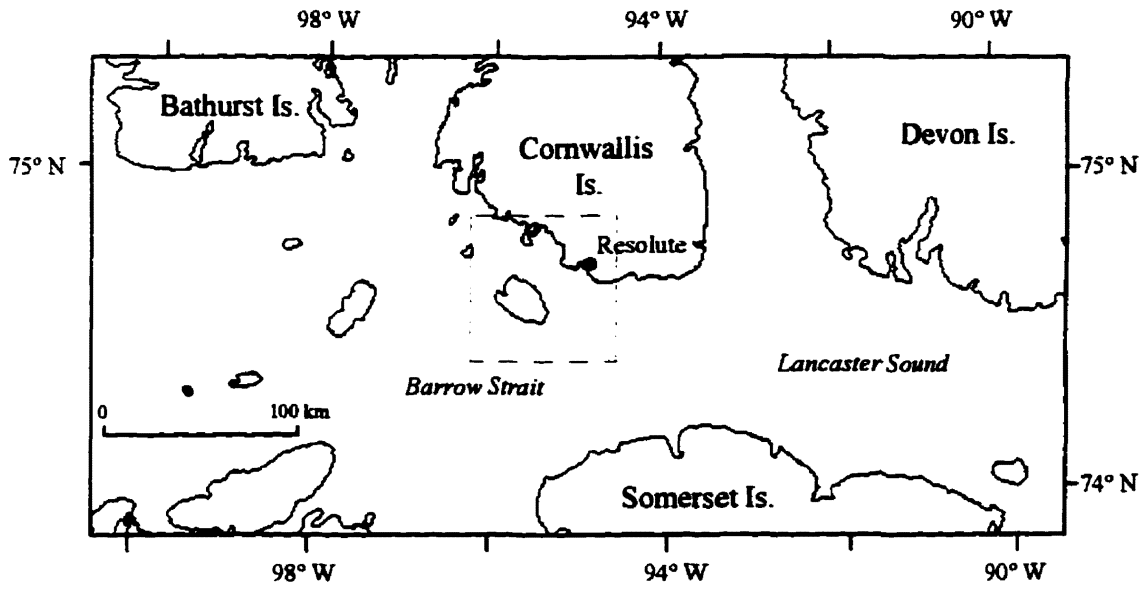
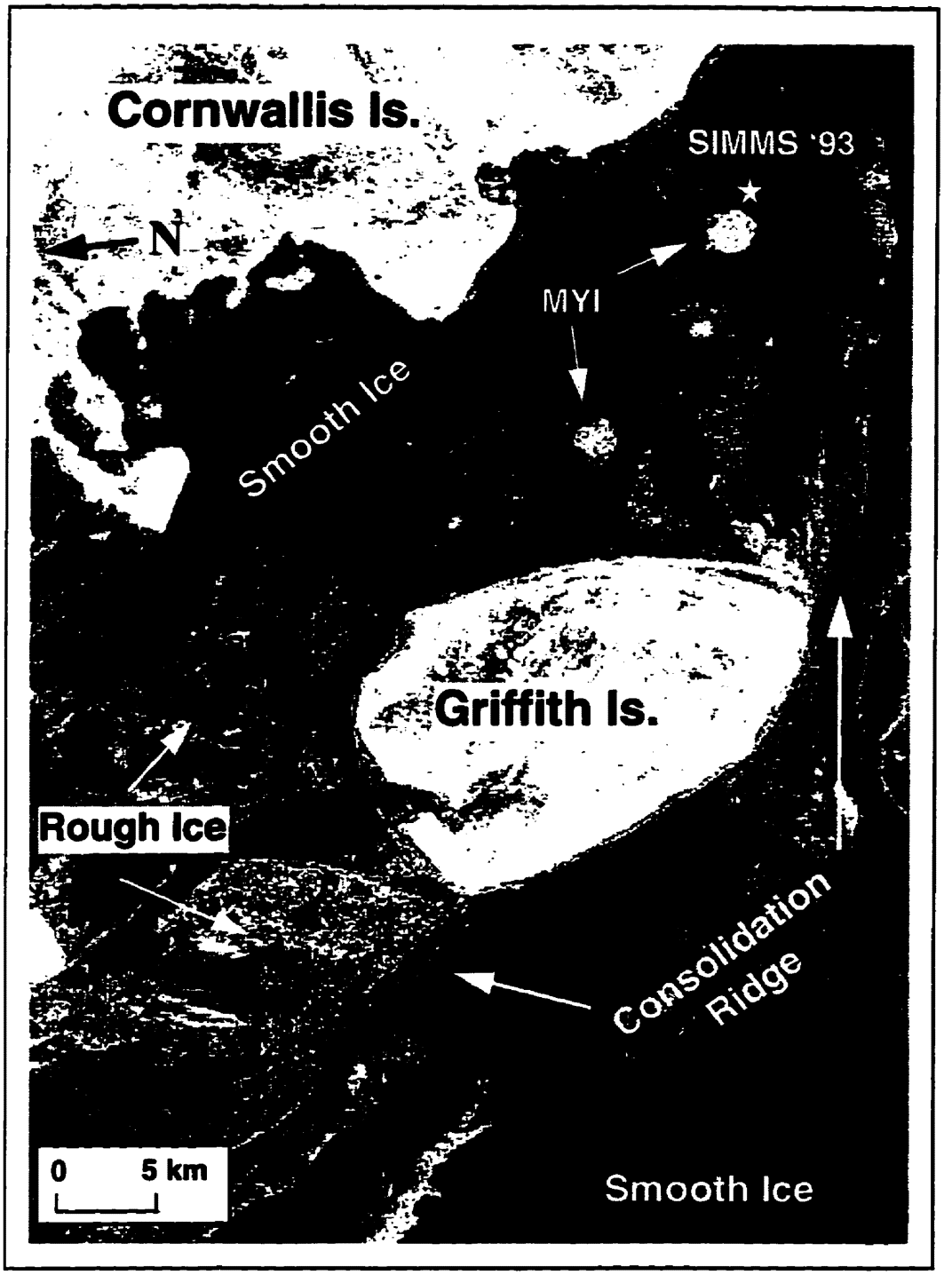


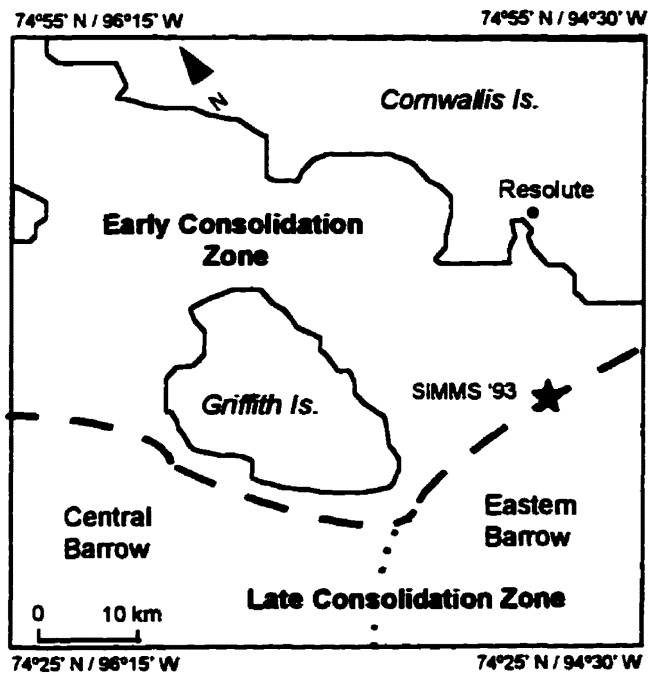
Figure 5.2 April 21, 1993 ERS-1 SAR image of SIMMS experiment region



5.3.1 Ice Conditions

As mentioned, the SIMMS experimental region is located amidst a wide variety of first-year ice types that differ mainly in their time and conditions of consolidation. Nominally, the AVHRR scene can be divided into two major consolidation regimes that are referred to here as *early* and *late* consolidation zones (Figure 5.3). The AVHRR scene is bisected by a consolidation ridge that demarks the transition between these two zones. The location of the ridge is shown in Figure 5.3 and is visible as a bright, sharp linear feature in Figure 5.2. This wide feature consisted of upturned angular ice blocks up to 2 metres in height which made the ridge virtually impassable. The SIMMS '93 sampling site was located on a pan of smooth first-year ice located in the middle of this consolidation ridge (Figures 5.2 and 5.3).

Figure 5.3 Ice regimes in AVHRR study scene. Dotted lines indicate ice regime boundaries.



5.3.1.1 Early Consolidation Zone

The early consolidation zone in this study is part of the McDougall ice sub-regime (Gorman, 1988). The regime is characterized by the fall consolidation of thick first-year ice with traces of multiyear ice. The consolidation of sea ice in the experiment region begins the previous fall in the bay areas. According to AES records, Resolute Bay consolidated in early October, 1992. Consolidation outside in Resolute Passage proceeds eastward through Barrow Strait and usually occurs in the passage area in December and January. Its maximum extent is delineated by the consolidation ridge across the southern mouth of Resolute Passage (Figure 5.2). At this time, an ice dam or ice bridge forms annually across Barrow Strait to the north-west of Griffith Island. This dam effectively halts the movement of heavier Arctic Ocean and archipelago ice from entering Lancaster Sound until approximately September of the next year. After the dam breaks, heavy, rough ice moves down Barrow St., some passing through Resolute Passage. In fact, SIMMS experiments were often located adjacent to a multiyear ice floe that was caught in the passage area during consolidation.

The formation of new ice in the passage, the transport of heavy ice through the passage and the occasional presence of second year ice in passage areas all result in a very complex icescape in the early consolidation area. The SAR image indicates that this zone is a mixture of smooth (dark, even tones) and rough first-year ice (brighter tones, more texture). Some well-defined multiyear ice floes were frozen within the first-year ice matrix in Resolute Passage. These are identified in Figure 5.2. A major rough ice area was also located north of Griffith Is. in the early consolidation zone. This thick, rough ice was likely freed when the Barrow St. ice dam broke and consolidated behind the new ice in Resolute Passage that same fall.

5.3.1.2 Late Consolidation Zone

In 1993, ice did not consolidate in the late consolidation zone until late March. ERS-1 data in late February confirmed that the ice was still moving in these areas. Unlike the early consolidation zone, new ice continues to form in the late zone over the winter and

move through these areas into Lancaster Sound and eventually into Baffin Bay. Movement of this new ice past the early consolidation zone is responsible for the massive shear zone ridge that formed at the boundary of these zones at the southern mouth of Resolute Passage. The late consolidation zone is divided by the Central Barrow and Eastern Barrow sub-regime (Figure 5.3). The shear zone ridge continued past Griffith Is. and served as a boundary between these two late consolidation sub-regimes. This feature marks the location of the Griffith Is. ice bridge which often forms and breaks up many times during consolidation of Barrow St.

The Central Regime is characterized by thin, smooth first-year ice. Essentially, this smooth, thin first-year ice moves eastward into the Eastern Barrow regime. The ice continues to grow and compresses as it reaches slower, heavier ice in Lancaster Sound. As a result, ice in the Eastern Barrow regime is often thicker and more heavily ridged. Surface sampling indicated that the ice in this zone was only 30 cm thick, much thinner than the thick (>1 m) ice found in the early consolidation zone. Like the early consolidation zone, the SAR indicates that smooth and rough first-year ice were the dominant ice surfaces in this regime. No multiyear ice was present in this zone.

5.3.2 Snow Conditions

While much is known about the ice characteristics of this region, relatively little is known regarding the distribution of snow on the sea ice. Unfortunately, the SAR data cannot provide information regarding snow deposition over the AVHRR scene. Snow depths were measured at designated areas outside of the SIMMS intensive site in support of airborne SAR calibration experiments. These observations indicate that, compared to the first-year ice at the SIMMS site, snow depths were significantly deeper in the early consolidation area of Resolute Passage. Transect sampling in the passage revealed snow depths averaging 20 cm (σ = 9 cm) on May 6. Similar transect measurements at the first-year ice site on the same day found an average snow depth of 8.5 cm (σ=3 cm). Further south, in the late consolidation area, average snow depth was still lower at 6 cm (σ=2 cm).

Although limited in number, the observations suggest that snow depths were much greater in the early consolidation zone.

Many interrelated factors contribute to explain the increased snow deposition in the early consolidation zone in 1993. Since much of annual snowfall occurs in the fall, those areas that have consolidated in these periods can support snow deposition. However, in the late consolidation zones, newly formed ice misses this major precipitation season. In the late consolidation zone, snow depth is largely dependent on the frequency of snow events in May and June, which are sparse. Naturally, any spring snowfall would likely contribute to snow volumes in the early consolidation zone as well.

Aside from precipitation, another important factor is the ice's ability to catch and retain deposited snow. This factor largely depends on surface roughness and exposure to wind. As mentioned in Chapter 2, rough ice features interrupt near-surface wind flow and encourage the deposition of airborne snow on the leeside of the feature due to the decrease in wind velocity. After the snow is deposited, the rougher ice surface is also capable of sheltering the snow from winds thus increasing its transience time. This roughness effect also extends to the topographic effects of the nearby islands. For the same reasons, they too encourage snow deposition in their *wind shadow*. In 1993, rough ice dominated the icescape of the early consolidation zone. This, along with its adjacency to the islands, served to encourage the deposition of snow. Conversely, the smoother, exposed icescape in the late consolidation zone encouraged the removal and transferal of any snow deposited. Moreover, much of this transient snow was likely trapped in the near shore, rough ice areas of the early consolidation zone.

5.4 Scene Variability of Visible and Infrared Sea Ice Albedo

Figures 5.4 and 5.5 respectively contain the final visible and infrared albedo maps for each AVHRR date. The dynamic ranges of these grey-scaled images have been restricted to ±2

σ to improved contrast. However, since this enhancement is scene-dependent, these images are not comparable across dates. In order to permit multi-date comparisons, the albedo images were density sliced to produce thematic albedo maps. The thematic maps in figures 5.6 and 5.7 allow a straightforward comparison of albedo between study dates. In order to afford this season-wide comparison, the thematic range of each image had to span the entire albedo range of 0-1. In order to avoid an inornate number of colour themes which would reduce clarity, the albedo values were separated into broad bins. While this resulted in a good representation large changes in albedo over the season, there was a loss of high frequency detail in some images.

In order to describe the distribution of albedo values, histograms of pixel values from the sea ice mask were generated for each image and placed adjacent to the albedo images in figures 5.4 and 5.5. Simple descriptive statistics were derived for each image and are presented within the histograms[23]. Specifically, the mean and standard deviation of the distribution is presented. The range of surface albedos is described by the first and third quartile (Q1 and Q3 respectively) of the distribution. The albedo distribution's similarity to a statistically normal distribution is described in a measure of kurtosis. Kurtosis is used to measure the concentration of albedo values around the mean. A normal distribution has a kurtosis of 0, while a positive value indicates the distribution has heavier tails than a normal distribution (platykurtic) and a negative value suggests that the distribution is low in the tail and more peaked than a normal distribution (leptokurtic). The symmetry of the albedo distribution is described by a measure of skewness. Positive skewness values indicate that distribution is biased towards larger albedo values. A negative skewness value indicates that the distribution is skewed toward lower albedo values. Again, a skewness value of zero indicates a normal distribution.

This section presents the AVHRR-derived albedo maps and examines the inter-scene variability for each visible and infrared image. The daily average air temperature during

[23] These statistical measures should be regarded with caution when the albedo distribution does not approach normality.

Figure 5.4(a) April 30 visible albedo

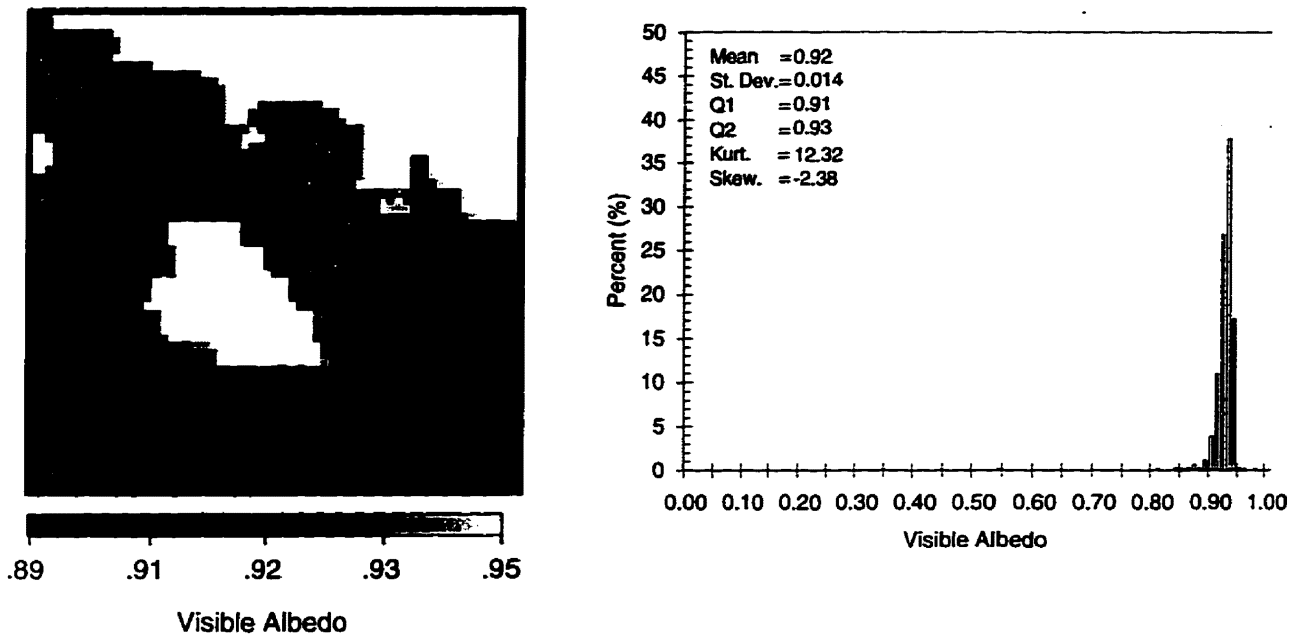


Figure 5.4(b) May 3 visible albedo

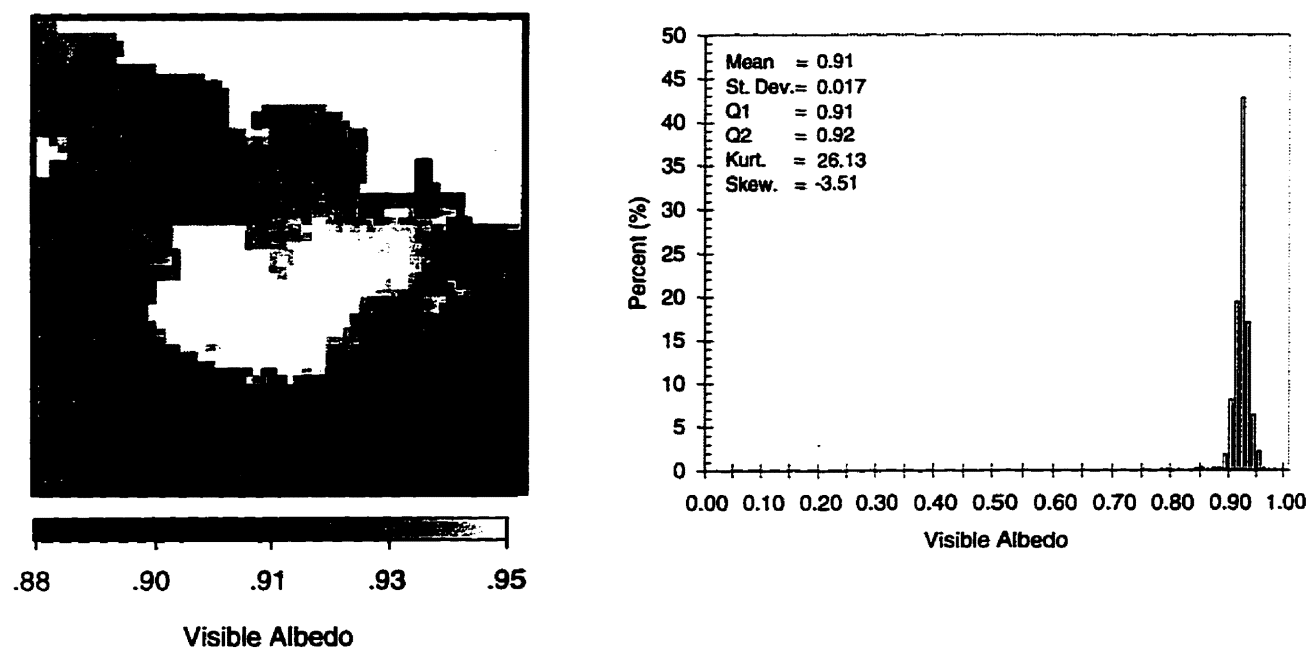
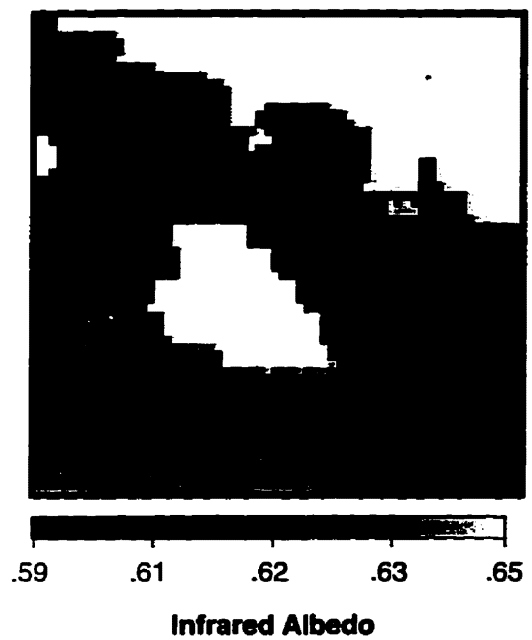


Figure 5.5(a) April 30 infrared albedo



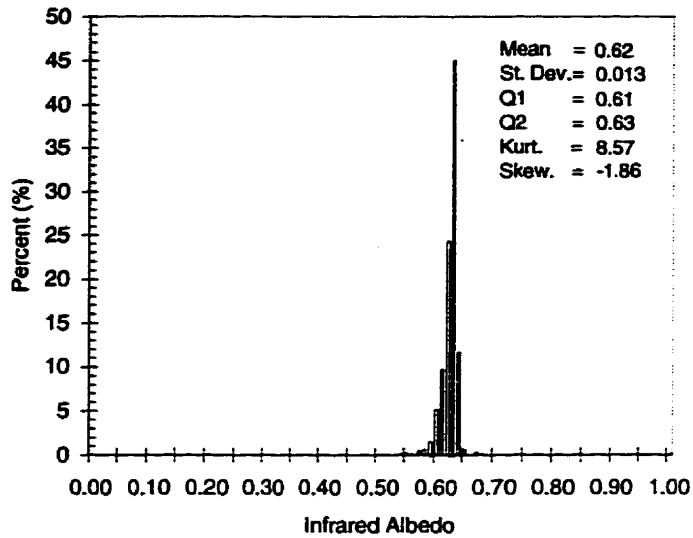
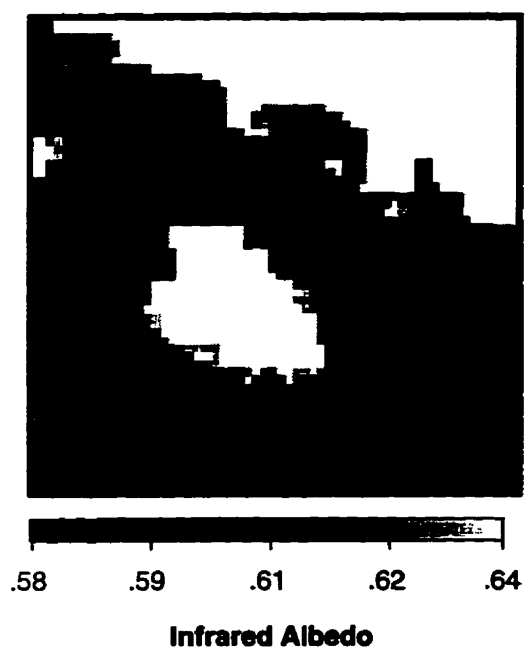


Figure 5.5(b) May 3 infrared albedo



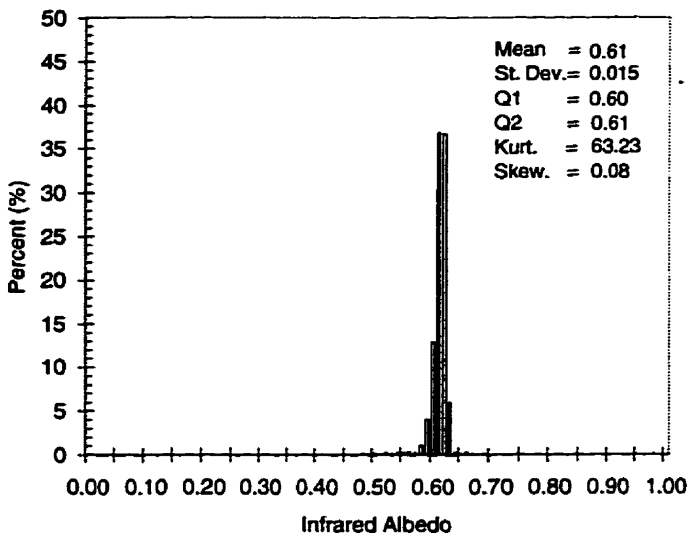
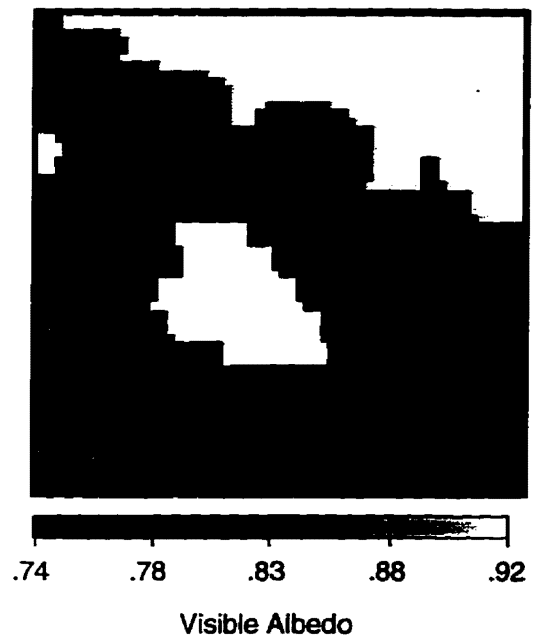


Figure 5.4(c) June 4 visible albedo



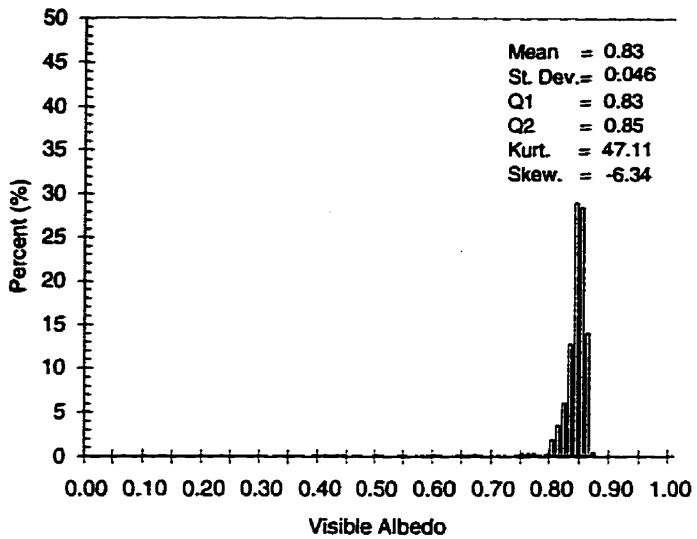
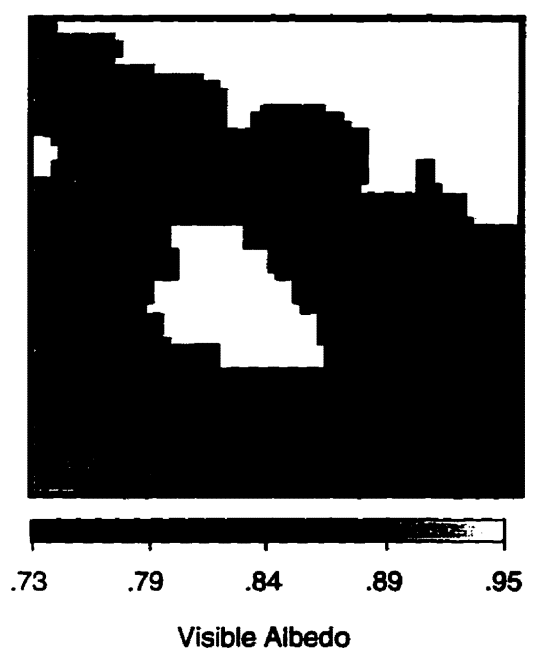


Figure 5.4(d) June 9 visible albedo



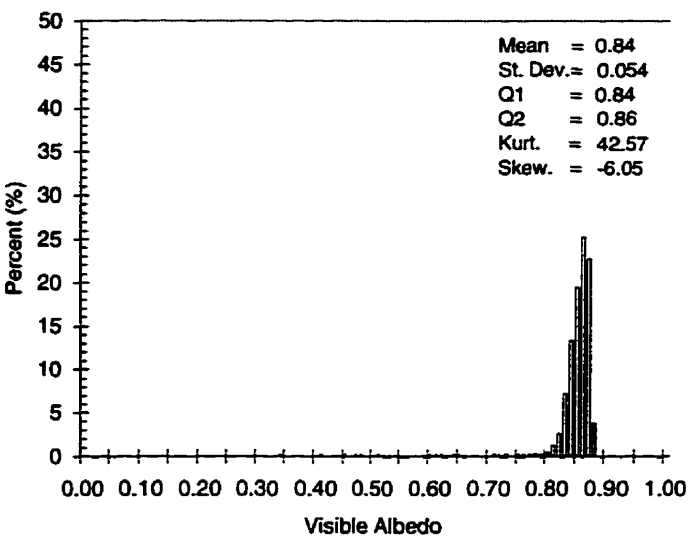
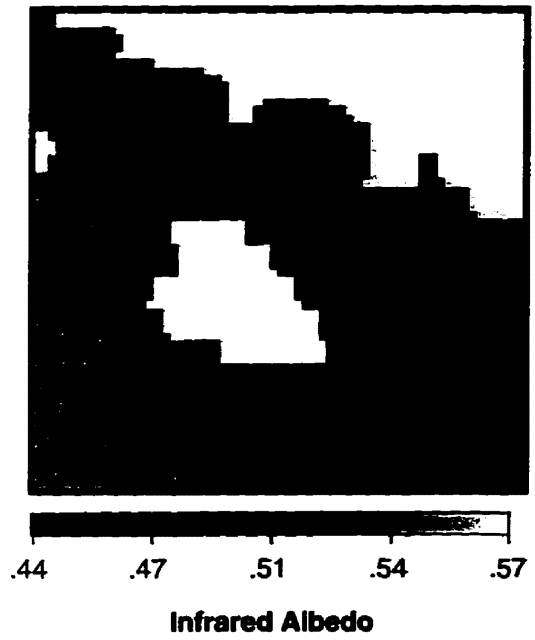


Figure 5.5(c) June 4 infrared albedo



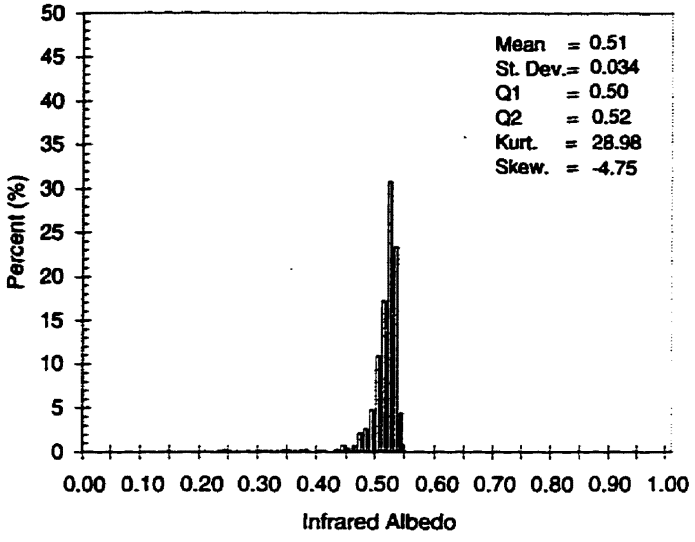
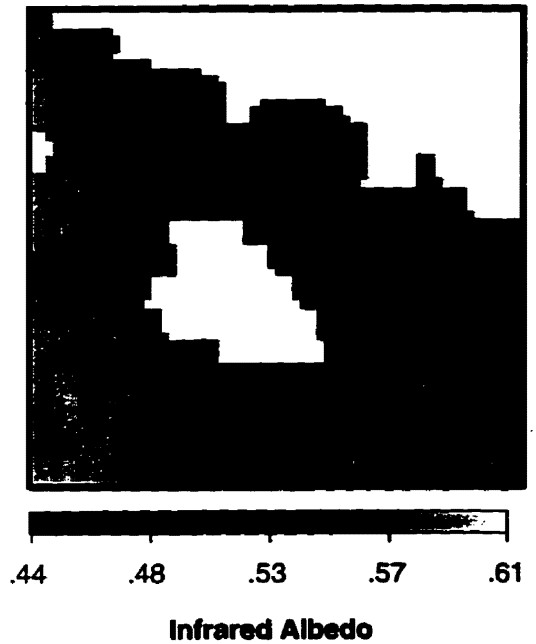


Figure 5.5(d) June 9 infrared albedo



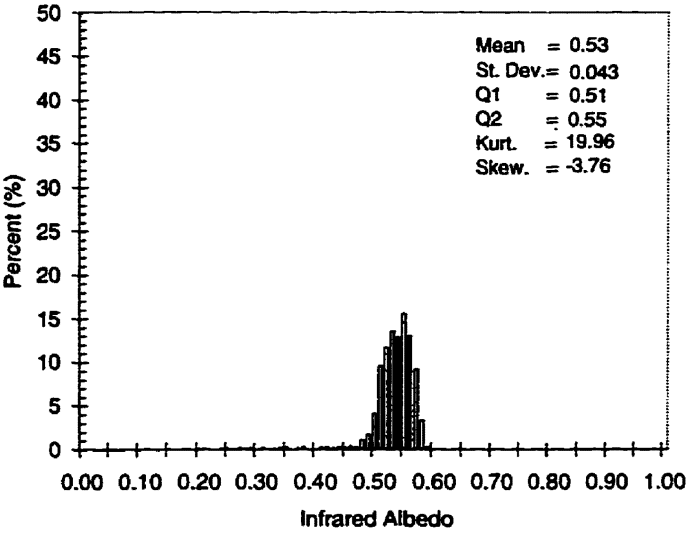


Figure 5.4(e) June 16 visible albedo

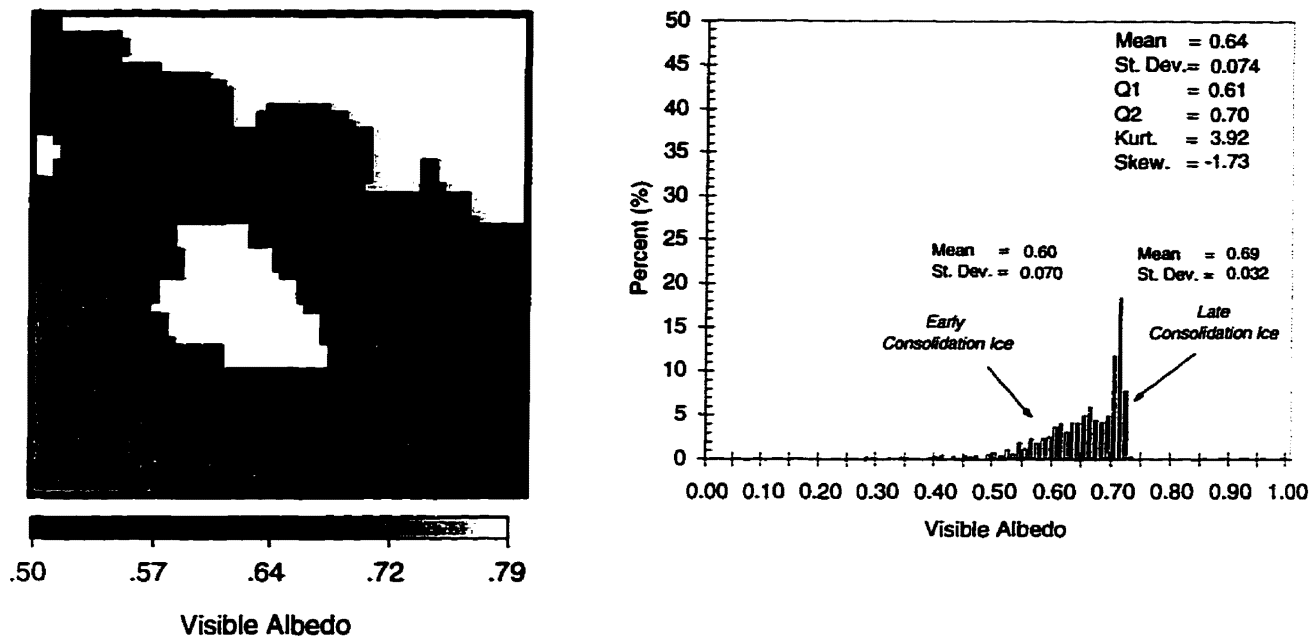


Figure 5.4(f) June 20 visible albedo

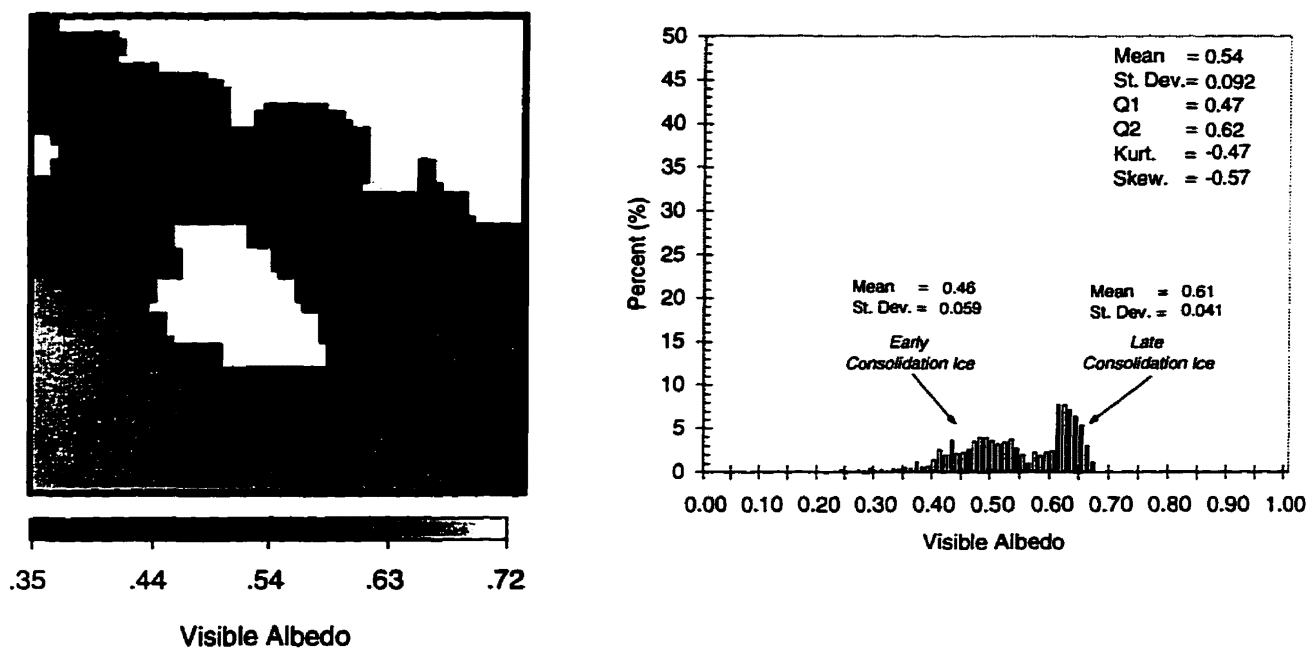


Figure 5.5(e) June 16 infrared albedo

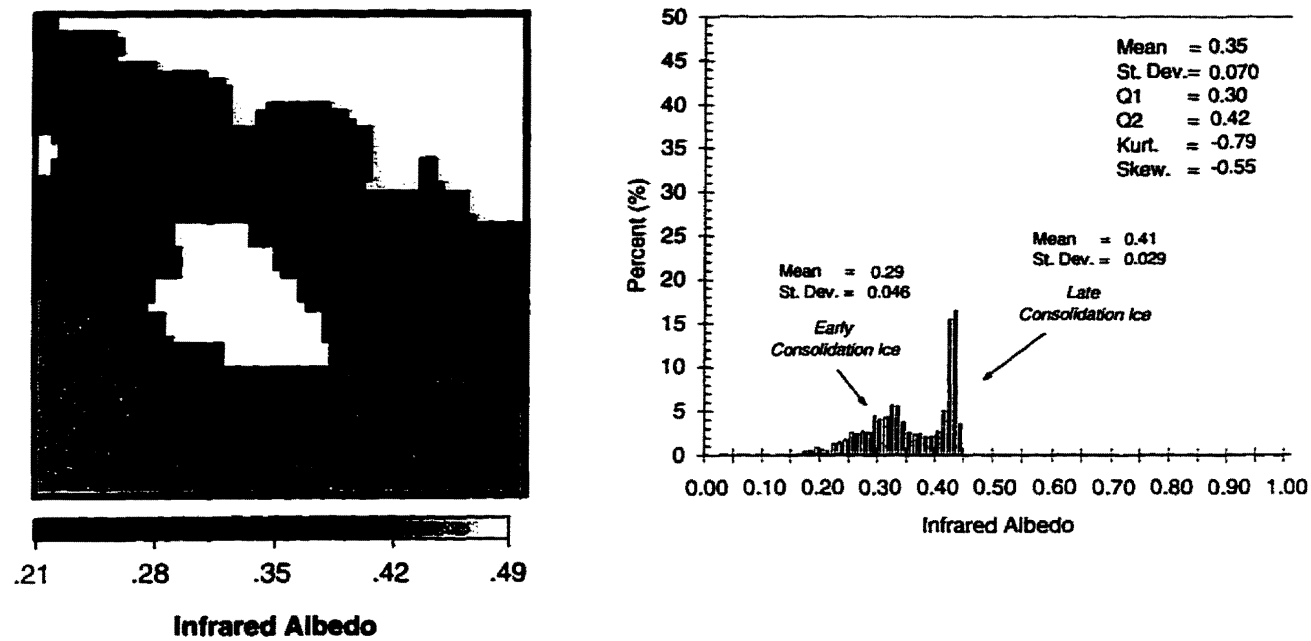


Figure 5.5(f) June 20 infrared albedo

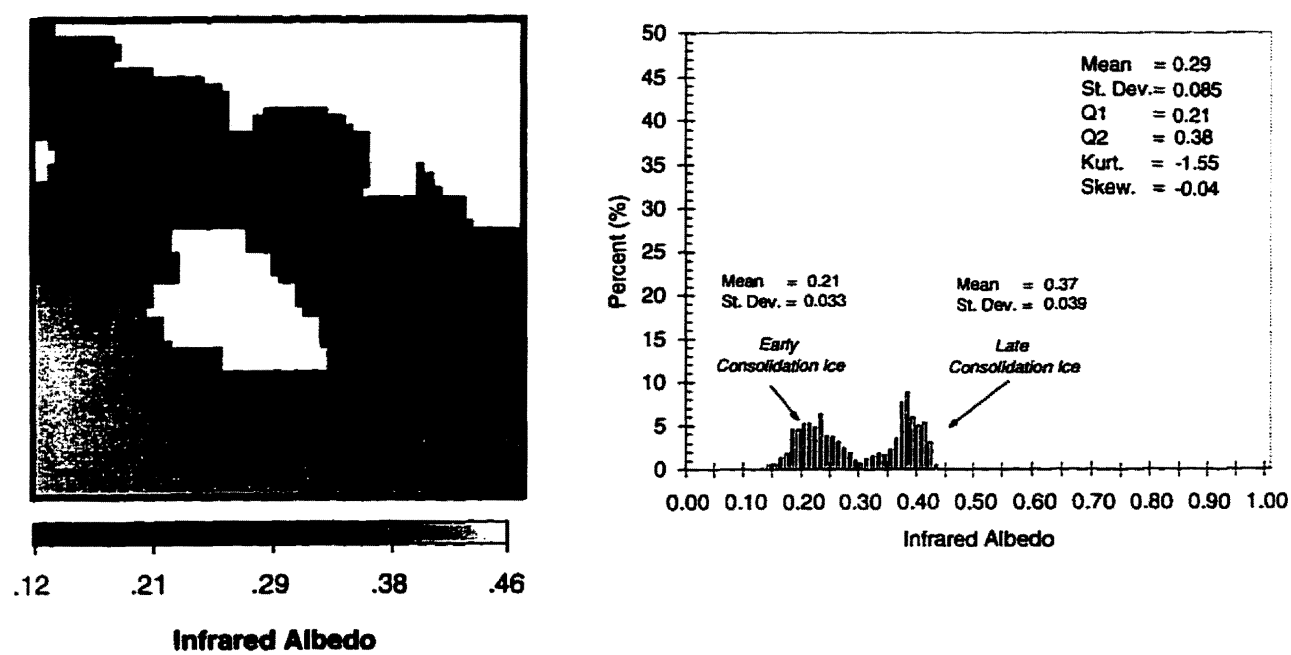


Figure 5.4(g) July 7 visible albedo

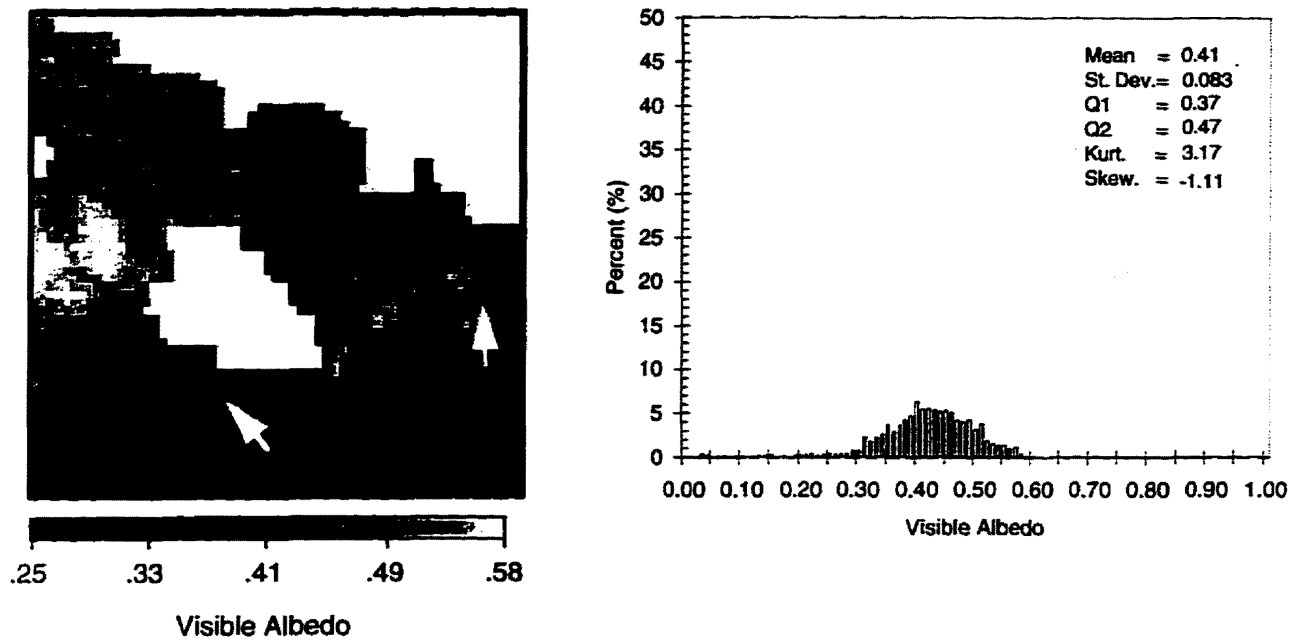


Figure 5.4(h) July 29 visible albedo

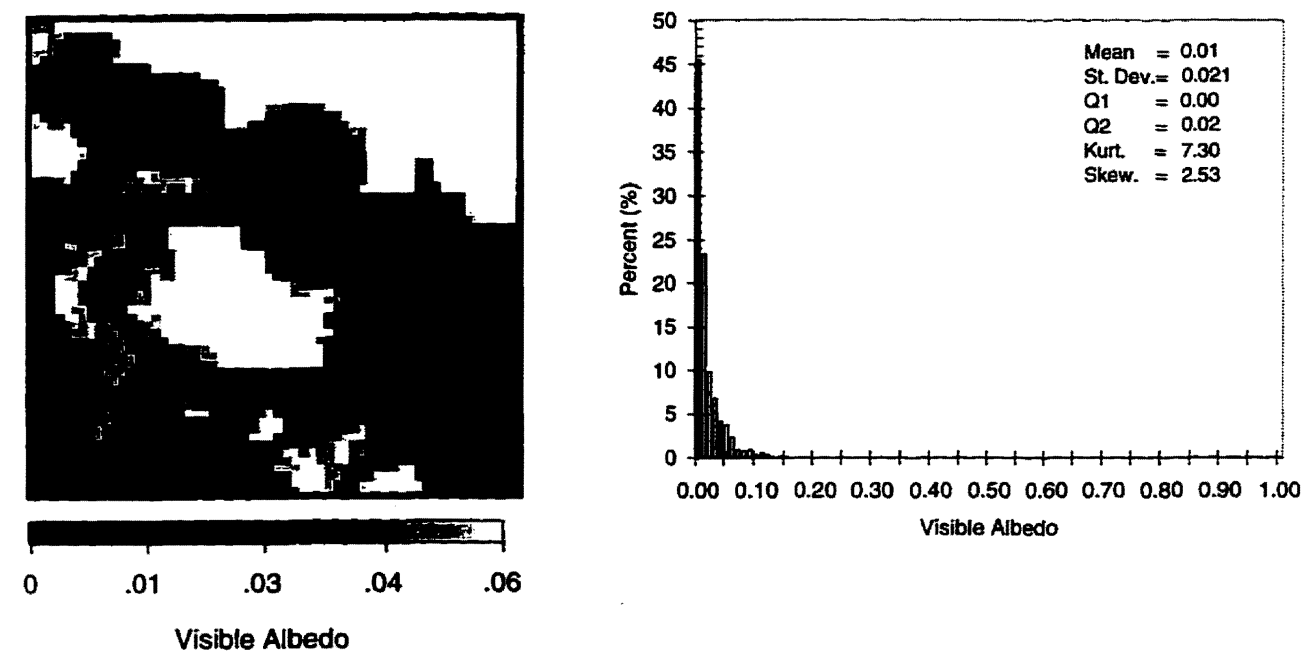
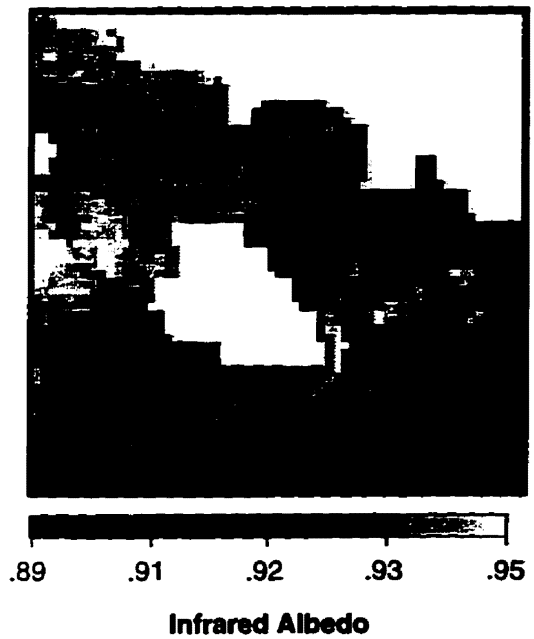


Figure 5.5(g) July 7 infrared albedo



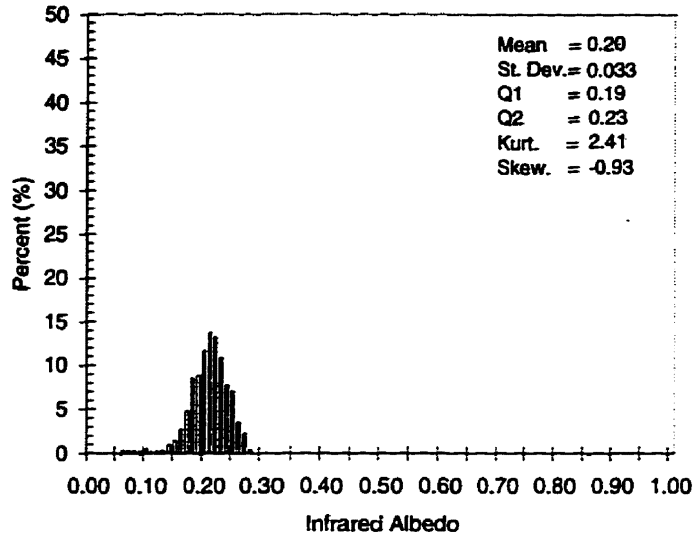
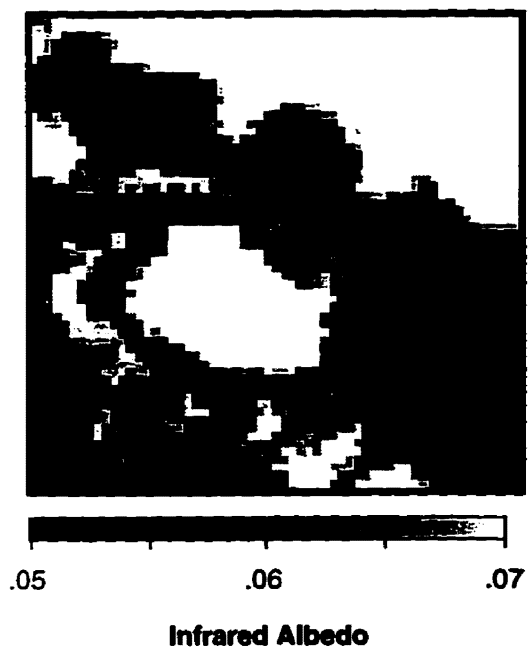
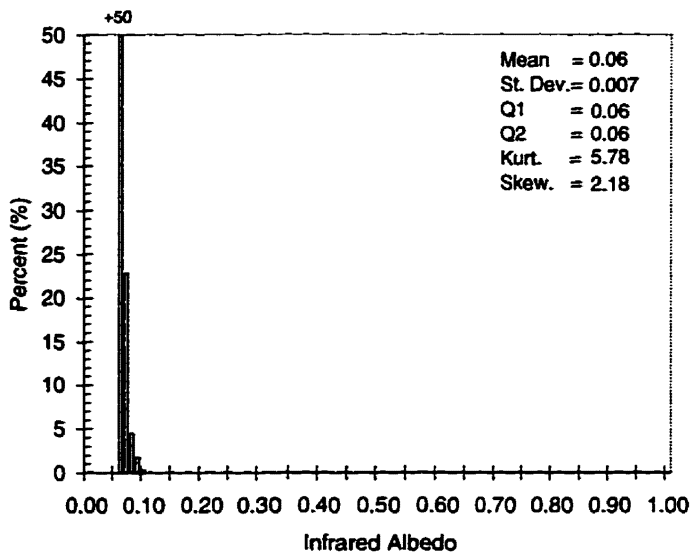


Figure 5.5(h) July 29 infrared albedo





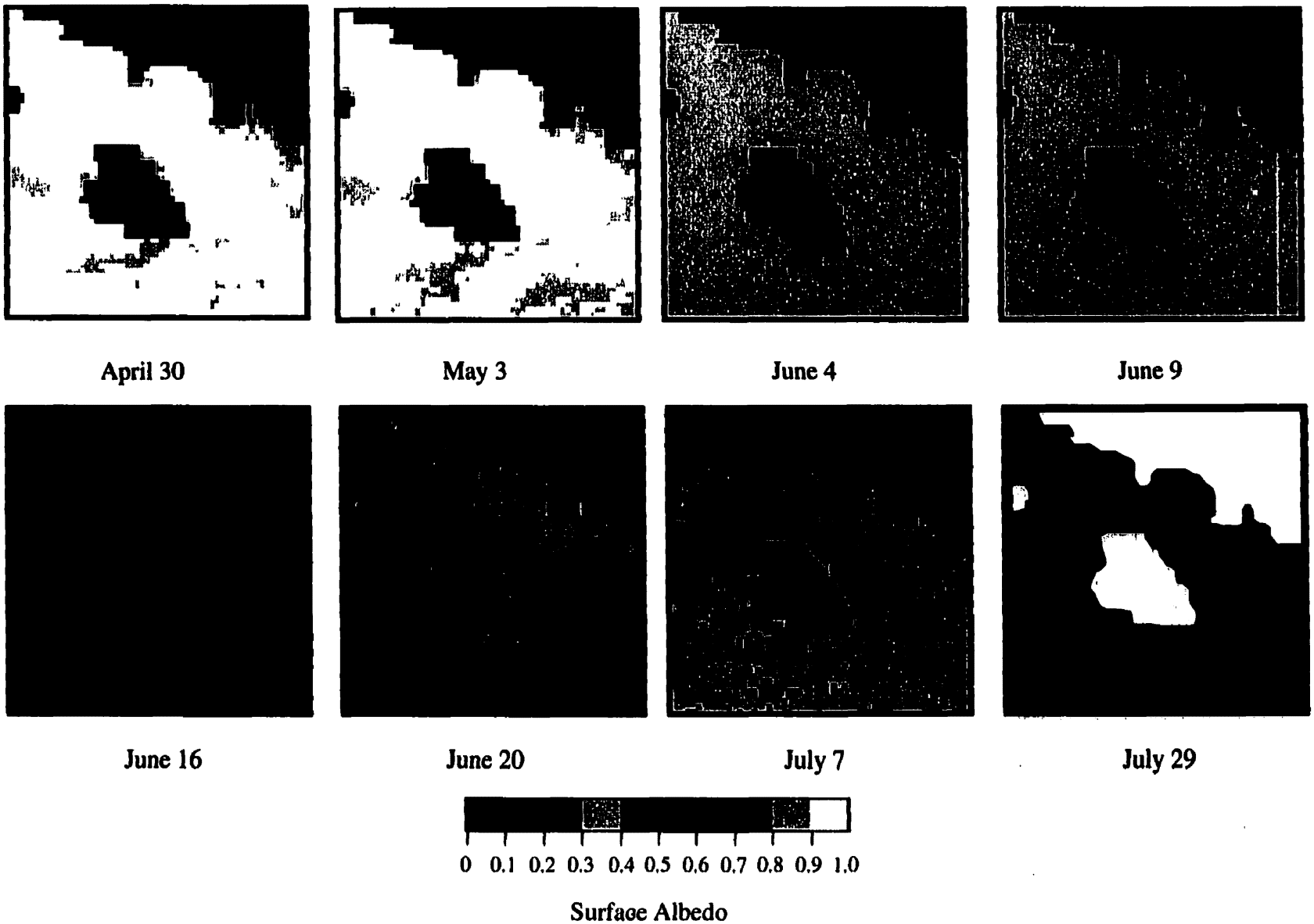


Figure 5.6 Thematic visible albedo maps

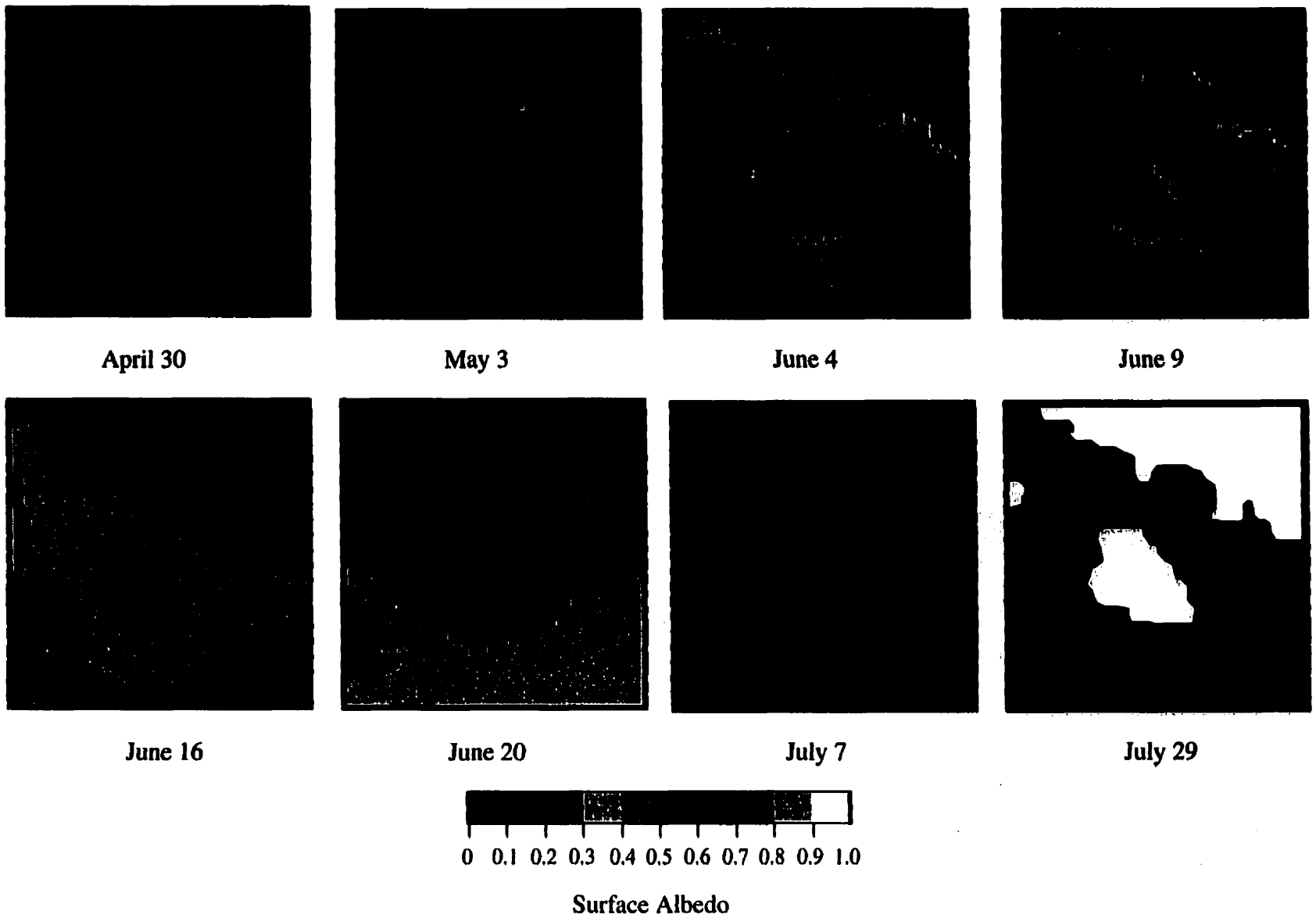
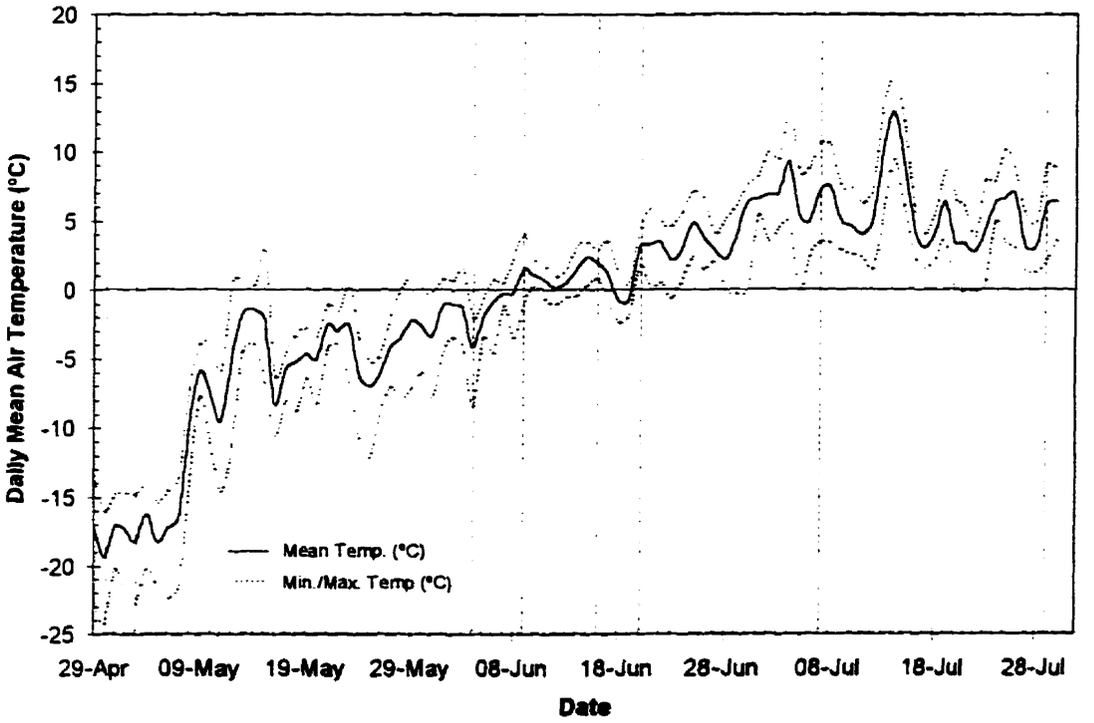


Figure 5.7 Thematic infrared albedo maps

these overpass dates are shown in Figure 5.8. Overpass dates are highlighted on the figure. The air temperatures measured at the first-year ice site will be used as a reference for temperatures across the AVHRR scene. However, the wide variety of surface conditions and the presence of land masses likely cause ambient temperatures to vary across the scene. For example, the seasonal temperature increase from near shore ice areas is expected to lead that of the first-year ice site. This type of variation can contribute to intra-scene surface albedo variability and should be considered when the site temperatures are incorporated in the ensuing discussion. Over the AVHRR study period, mean ambient air temperatures ranged from a low of -19 °C to a high of 12 °C. Mean daily average temperatures reach 0 °C on June 8. The change images described in Section 5.23 for both visible and infrared data can be found in Figure 5.9.

Figure 5.8 Daily mean air temperature during SIMMS '93. AVHRR albedo data available for marked dates. Note: After June 20, data measured at AES Resolute weather station.



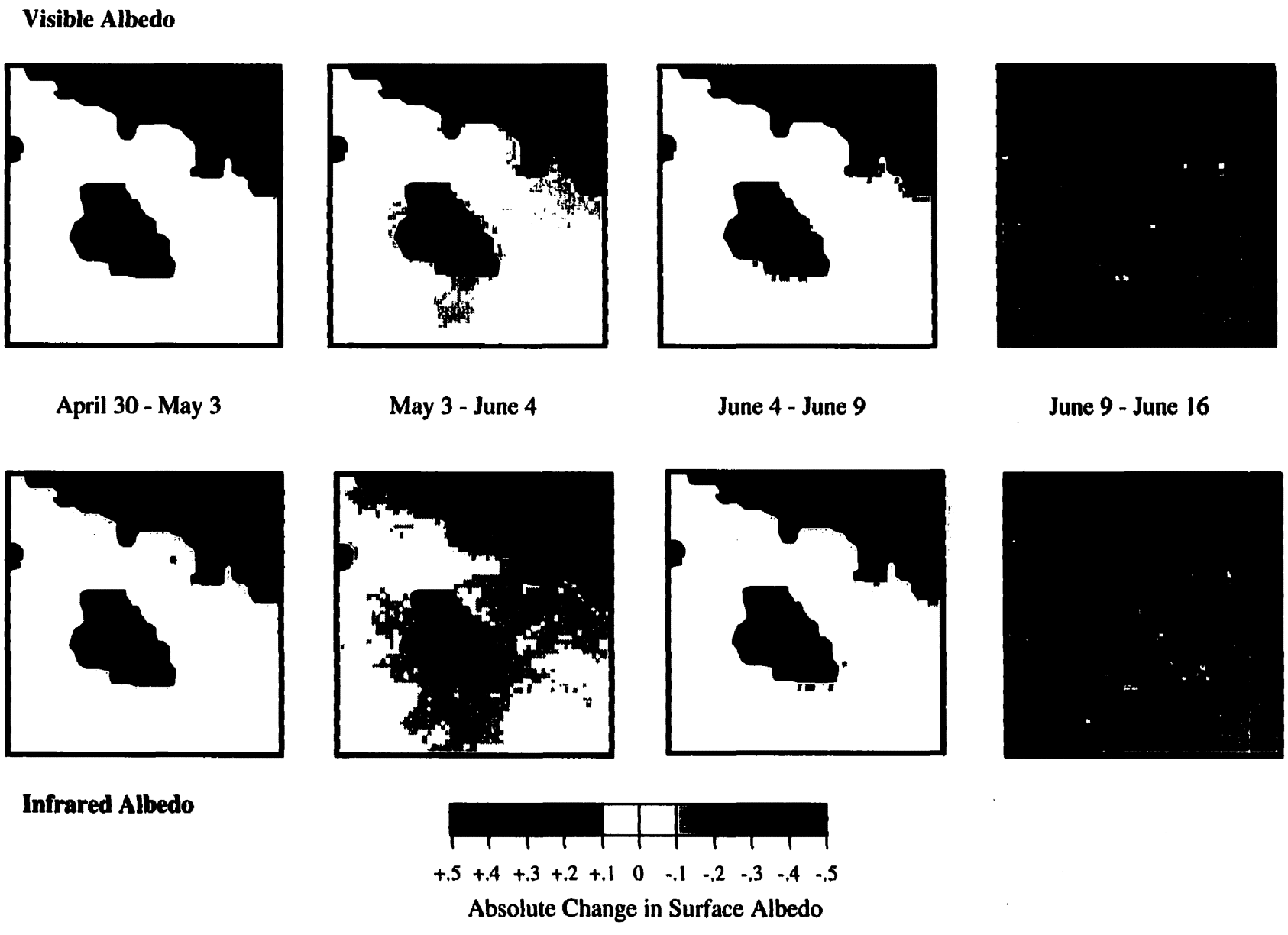


Figure 5.9 Absolute change in surface albedo between acquisition dates

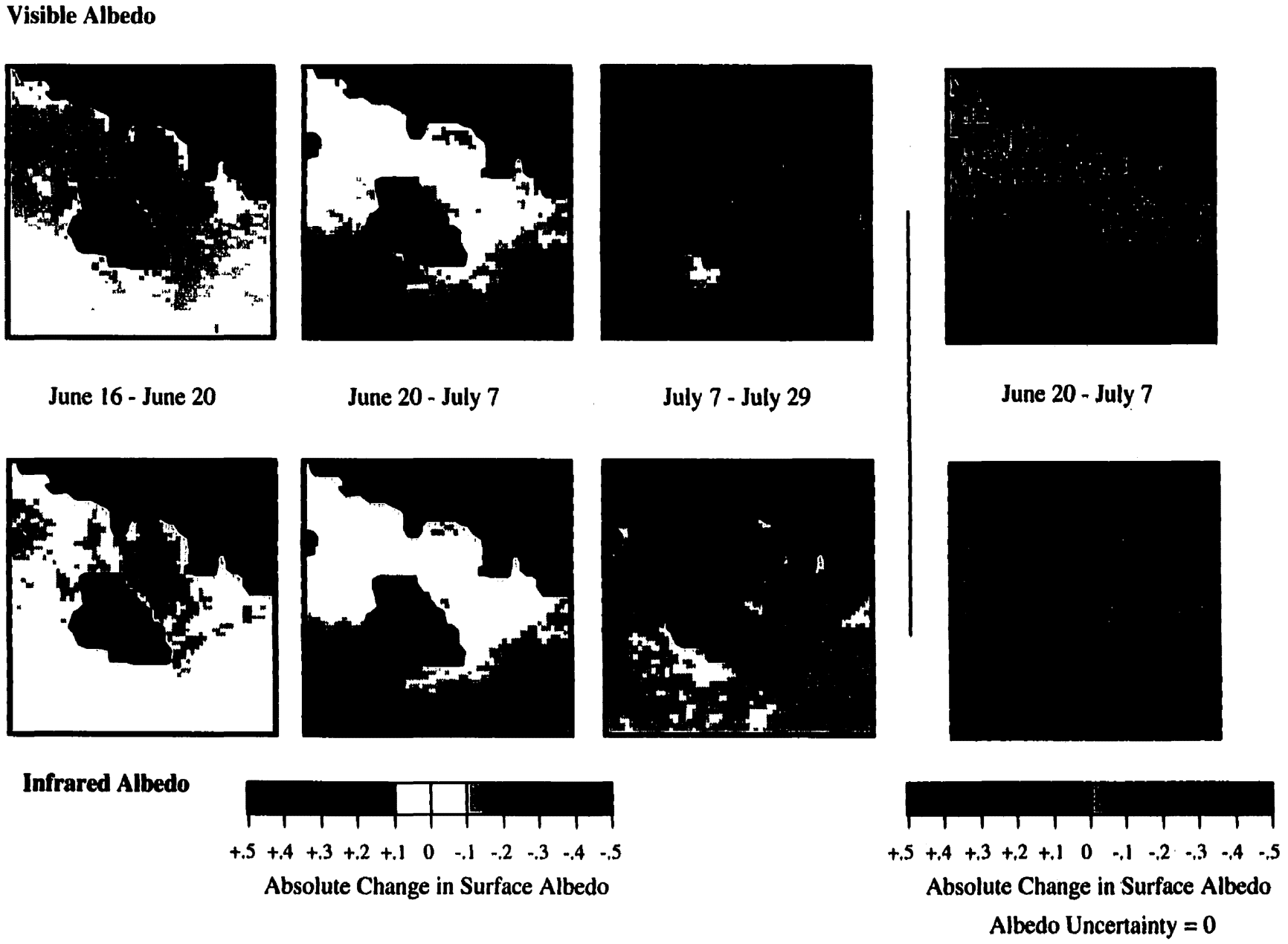


Figure 5.9 (Cont...) Absolute change in surface albedo between acquisition dates

5.4.1 April, May - Snow-Covered Sea Ice

The April and May albedo images, figures 5.4(a,b) and 5.5(a,b), indicate that, in early spring, the visible and infrared albedo range narrowly from 0.91-0.93 and 0.60-0.63 respectively. Surface observations indicate that this high albedo is due to the ubiquitous presence of relatively dry snow covering the sea ice at this time of year. Air temperatures ranging from -15 °C to -25 °C (Figure 5.8) signified that winter conditions dominated in this period. The change image for these two dates found no discernible change in albedo between these dates. At this time of year, surface albedo changes very slowly due to the predominantly cold ambient temperatures.

The AVHRR data indicates that the spatial variability of albedo over these early scenes was relatively low. However, the satellite data did reveal some variability over the scene. Areas of lower albedo (darker tones) can be found over both the visible and infrared albedo images for both dates. Examining the SAR image (Figure 5.2), these lower albedo images correspond to areas of rougher ice. These rough ice areas have a visible albedo 0.02-0.04 lower than the surrounding smoother ice areas. These lower albedo areas also lead to the negative skewness measures of the visible and infrared albedo distributions.

In early spring, there are three potential reasons for lower albedo in rougher ice areas and all are plausible here. First, upturned, ridged ice create shadows that may artificially lower satellite-measured albedo of rough areas. Secondly, upturned bare ice, often light blue in colour early in the spring, are left exposed since, due to gravity, deposited snow cannot settle on the inclined surfaces. Instead, deposited snow settles in the crevasses between these features. This was evident on the consolidation ridge adjacent to the SIMMS '93 experiment site. Thus the albedo of these areas will be dependent on the ratio of exposed ice areas to the surrounding snow-covered ice. This is likely a function of the degree of ice deformation. In other words, highly deformed features would likely have a larger proportion of upturned blocks of lower albedo, bare ice. The third reason relates to the effect of the rough ice on the microclimate of the ridged area. The complex topography

can encourage multiple reflections of the ice surfaces thus increasing the surface insolation. This can increase snow melt and decrease surface albedo.

This early season imagery suggests that sea ice albedo within Resolute Passage was slightly higher (0.02-0.03) than the scene average. The higher albedo in the area suggests increased snow coverage and/or a preponderance of newer snow. Due to the varied relief of the nearby islands, wind patterns, and relatedly, snow deposition patterns within Resolute Passage are very complex. This complicates the interpretation of small scale albedo patterns which may be a function of snow deposition in this part of the scene. Essentially, the high-albedo area under discussion is located in the Passage between Griffith Is. and Cornwallis Is.. Winds and airborne snow can be trapped and deposited between these two landforms. Within the passage, this loose new and old snow was continually being redistributed. An accumulation of new snow would result in a short term increase in albedo. Redistributed older snow can also cause a similar increase in albedo. Theoretically, larger particles will settle first in wind blown snow resulting in smaller, more reflective particles to be left in the near-surface layers of the volume (Grenfell *et. al.*, 1994).

In the case of the April 30 and May 3 images, a blizzard on April 28 and 29 with winds as high as 56 mph continued into the morning of April 30. Precipitation records show that snow fell periodically between April 23 to April 29. On April 28 and 29, approximately 5 cm of new snow fell. The average wind direction recorded at AES Resolute during the two days was 56°, or approximately originating northeast over Cornwallis Is.. This direction favors the transport and deposition of previously deposited and new snow from the large island onto ice in the passage area. A significant accumulation of this new snow within Resolute Passage was the likely source of the slightly higher albedo in this part of the scene.

Assuming at least 3 cm of new snow, the scene averaged visible albedo for April 30 and May 3 compares well with the CCC2 model prescription of 0.90 . However, the CCC2

infrared albedo for snowcover (α_{ir} =0.70) appears 0.08 too high. The CCC2 value is based on new snow. The lower AVHRR infrared albedo suggests that average snow grain size over the scene is larger than that of new snow (grain radii = 50-100 μm). Surface observations during SIMMS indicate that it is difficult to detect the presence of new snow on sea ice. New snow layers quickly metamorphose under twenty-four hours of insolation and are rapidly mixed with older snow layers due to wind action. This may explain the lower infrared satellite albedos despite the recently fallen snow. The discrepancy also highlights the possible need for different snow age factors for sea ice and terrestrial surfaces. The CCC2 model uses the same snow age factor for snow on land and on sea ice. This factor is based primarily on snow age in days. Due to continual daylight in the polar regions, one would expect that snow would age at a different, if not faster rate. As such, different snow age factors for sea ice and terrestrial surfaces may be justified. Similarly, the CCC2 model uses the same age factor for both the visible and infrared snow albedo. This implies that given the same residence time, both albedos will decrease identically. *In situ* and satellite observations made in this study reveal that infrared albedo is more sensitive to the aging of the snowcover and thus, separate age factors for the two albedos are warranted.

The early season AVHRR visible albedo data do not compare well with Ebert and Curry's parameterized dry snow values (α_{vis} =0.98) (assuming θ_z=65°). Their very high dry snow albedo values, modelled via Wiscombe and Warren's snow model (Chapter 3), are likely based on a pure, semi-infinite snowcover. These values, while appropriate for freshly fallen snow on sea ice, are unrealistic for snow-covered sea ice in the Archipelago and seems more appropriately labeled *new snow*. Its appropriateness in more remote Arctic locations is unknown given a lack of observational data. Due to the spectral distribution of incident radiation, infrared broadband snow albedo measured in this work should be 0.18-0.2 lower than Ebert and Curry's Band 2 (0.69-1.19 μm) albedo values. Given that, the satellite-derived infrared albedo is comparable to their parameterized dry snow value of 0.85, or equivalent to a 0.65 broadband infrared albedo. The agreement between infrared albedos and disagreement in the visible region suggests that the theoretical snow

volumes and the observed volumes differ in terms of impurity content and/or snow depth, but not grain size. The incorporation of impurities would reduce Ebert and Curry's dry snow value bringing it in closer agreement with the early season values observed in this work.

5.4.2 June - Surface Melt

In 1993, surface observations and the AVHRR image data indicate that June was a dynamic month in terms of sea ice albedo. In this month, increased insolation and positive ambient air temperatures cause substantial changes in the condition of the near-surface layers of the sea ice volume. This seasonal metamorphosis causes, and is caused by, dramatic reductions in surface albedo. The 1993 AVHRR data provide a unique and valuable record of sea ice visible and infrared albedo throughout this important transition month.

5.4.2.1 June 4, June 9

The June 4 visible and infrared albedo were 0.83 (σ=0.046) and 0.51 (σ=0.034) respectively (figures 5.4(c) and 5.5(c)). The June 9 visible and infrared albedo were 0.84 (σ=0.054) and 0.53 (σ=0.043) respectively (figures 5.4(d) and 5.5(d)). The high albedo and low variability indicates that the icescape was still covered predominantly by snow. In the early part of June, the region's visible and infrared albedo respectively decreased 9% and 15% from the winter values measured in late April and early May[24]. This change accompanied a temperature increase of approximately fifteen degrees Celsius. The appropriate change image in Figure 5.9 indicates the areas of discernible albedo decrease. The reason for the albedo decrease is twofold. First, surface observations on June 2 recorded that the ablation and redistribution of thin snow volumes allowed the underlying ice to show through in some areas. This resulted in a heterogeneous first-year ice surface consisting of dark grey and white patches. This would have the effect of decreasing the

[24] Since the albedo differences between June 4 and June 9 are within the accuracy of the satellite-derived albedos, they will be considered together.

visible and infrared albedo averaged over the area of an AVHRR pixel. This decrease was not captured by the spatially conservative crystal pit sampling.

A second reason for the decrease in albedo, more applicable to the infrared case, is the arrival of warmer ambient conditions as daily average air temperatures moved toward zero degrees in early June. This temperature increase resulted in dramatic changes to the snow volume which mark the arrival of previously described Wet Snow stage (*cf.* Chapter 3.4.4.2). Similar albedo decreases were detected in the crystal pit observations of June 11 and June 16[25] and were ascribed to the transformation of the snowcover from a pendular to a funicular regime. Warmer ambient temperatures encourage grain growth and increases the amount of liquid water in the pack. Both of these changes increase the absorption of infrared radiation and thus lowers the corresponding albedo. As expected, these types of changes would be most visible in areas where there was a significant snow volume and warmer ambient conditions. Areas of change in Figure 5.9 appear to be restricted to areas where there was a high deposition of snow and warmer ambient conditions, i.e. Resolute Passage and near shore areas. There was no discernible change in surface albedo between June 4 and June 9 although daily average temperatures at the FYI site increased from -4 °C to 2 °C. Curiously, allwave albedo measurements on these dates (Figure 3.18) show a slight increase in surface albedo.

The CCC2 parameterized visible and infrared snow albedos are allowed to range from 0.75 to 0.90 and 0.55 to 0.70 respectively. Based on the age factor employed, the minimum albedo values in these ranges are equivalent to snow 40 days old. The wet snow albedos observed on these two AVHRR dates fall within this parameterized range. The observed visible albedo is equivalent to modelled snow approximately 20 days old. However, the observed infrared albedo is equivalent to snow at least 40 days old. Again, this discrepancy may stem from the model's use of the same age factor for both visible and infrared albedos. Ebert and Curry's melting snow values (α_{vis} =0.871, α_{ir} =0.51) are comparable to the scene average albedos for June 4 and June 9. However, their

[25] No surface data were available for June 4 or June 9

assumption that the infrared albedo of snow linearly decreases to a bare ice value after a depth of 10 cm is questionable. This 10 cm depth is borrowed from Shine and Sellers (1985) thin snow parameterization for allwave albedo. At long wavelengths, only a few centimetres of snow is needed to make the volume semi-infinite, thus making the 10 cm level too high for their infrared bands.

5.4.2.2 June 16

The June 16 AVHRR albedo data reveal a sharp decrease in both visible and infrared data to 0.64 (σ=0.074) and 0.35 (σ=0.070) respectively (figures 5.4(e) and 5.5(e)). The change image in Figure 5.9 indicates that this decrease was scene-wide occurring more in the near shore areas and in the early consolidation zone. The daily mean air temperature at the first-year ice site was +2 °C, an increase of only 0.5 °C from June 9. Although there wasn't a large increase in temperature between the dates, the period between dates represented eight days above freezing. These average positive air temperatures accelerated surface melt and decreased albedo. Also, daily temperature minimums were just below 0 °C over this period. Without the refreezing brought about by night-time sub-zero temperatures, the upper layers of the sea ice volume began to decay rapidly . The June 16 image represents a transition from the Wet Snow stage to the Melt Pond stage described in Chapter 3.

The bimodal characteristics of the June 16 albedo data suggest the existence of two albedo classes in the AVHRR albedo data: a high-albedo surface with low variability in the zone of late consolidation and a lower albedo surface with higher variability in the early consolidation zone. An in-depth analysis of the environmental factors responsible for the evolution of these two classes is provided in a later section. In this section, discussion will be restricted to the description of the characteristics of these two albedo zones.

In the early consolidation zone, sea ice albedo decreased significantly from June 9. The visible and infrared albedo in this zone was 0.60 (σ=0.070) and 0.29 (σ=0.046)

respectively. Surface observations in Resolute Passage indicate that melt ponds formed earlier within this area than at the SIMMS experiment site. The lower, more variable albedo in the early consolidation zone suggests that surface ponding was more advanced in this part of the scene. It is difficult to estimate the percentage of the ice surface covered by melt water, but some indication is given by balloon photography collected on June 13. Via a 5 km transect from the SIMMS site to the shore of Cornwallis Island, balloon photos indicate that melt pond coverage ranged from 20% outside of the experiment site to 40% in near-shore areas (Piwowar *et al.*, 1995).

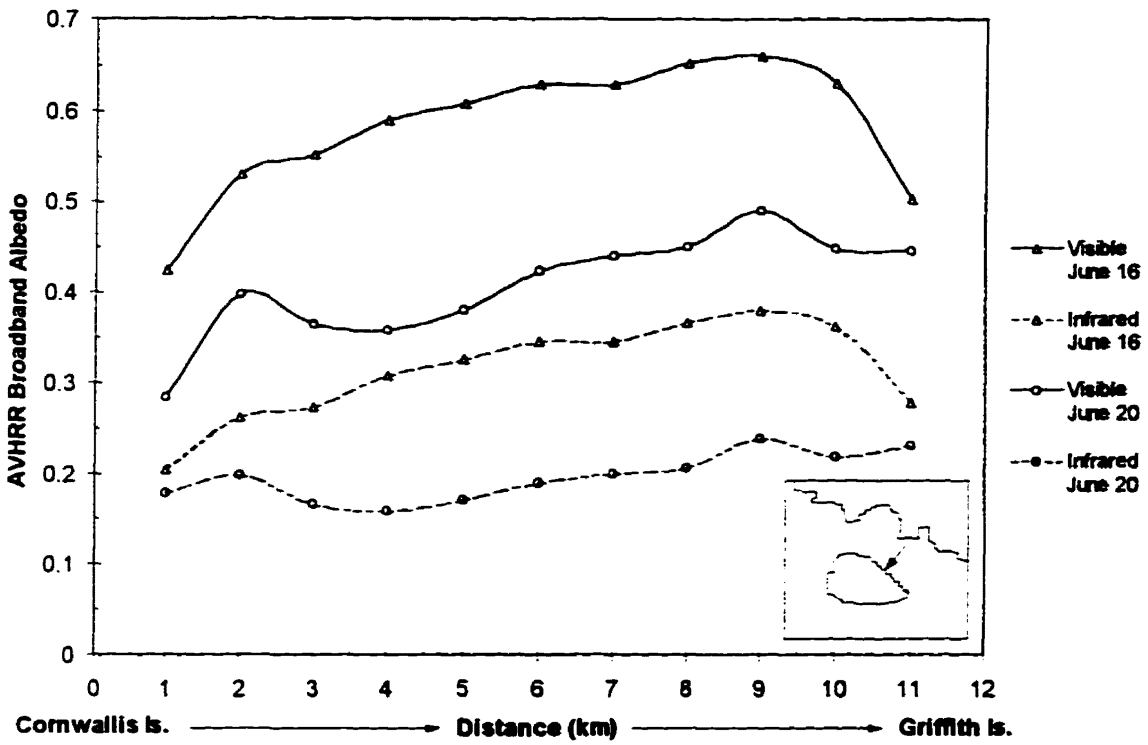
The dependence of sea ice albedo with distance from land is first evident in the AVHRR albedo data for June 16 and June 20[26]. In order to illustrate this effect, June 16 and June 20 AVHRR visible and infrared albedos were extracted from a transect that spanned Resolute Passage (see inset of Figure 5.10). These data are plotted against distance from Cornwallis Is. in Figure 5.10. Albedo from both dates increase rapidly within the first two kms from the island. This is consistent with Piwowar *et al.*'s (1995) findings that the size of melt ponds within the first two km of shore in 1993 averaged over 200 m^2, while those further out in the passage averaged only 50 m^2. After the first two kilometres, the albedo continues to increase, albeit at a much lower rate. Two kilometres out from Griffith Is., the albedo begins to decrease again as the land nears.

The decrease in albedo near land is primarily due to two factors. One, near shore areas are warmer due to the absorption and emittence of radiation by the often lower albedo land surface. This sensible heat is advected out over the colder ice surface. As a result, the near shore sea ice is warmed and melt is accelerated in these areas. As a result, surface albedo is lower in these areas. This effect is most dominant when the high-albedo snow has melted from the land, leaving behind the darker gravel surface. The other factor behind this pattern is the eolian transport and deposition of crustal material onto near shore sea ice. As discussed in Chapter 3, these particles usually settle in the upper layers

[26] Earlier AVHRR data indicating low albedo shore areas were ignored given the uncertainty in the land masking. These pixels may have included snow-free land.

of the ice volume and, due to their absorptive properties, reduces its albedo. This too leads to accelerated melting in these areas. Surface observations in 1993 confirm that the shore of Cornwallis Is. was bordered by dirty sea ice which appeared to extend 100 m out from shore.

Figure 5.10 Change in sea ice albedo with distance from shore



Unlike the early consolidation area, the magnitude of the albedo and the stability of its variance between June 9 and June 16 suggests that the late consolidated ice had not yet evolved into an extensively ponded surface. The albedo in this zone was consistent with the white ice visible albedo (α_{vis}=0.68) and near-infrared albedo[27] (α_{nir}=0.57) measured at the first-year ice site on the same day. This suggests that this zone was dominated by white bare ice surfaces and not significant amounts of surface water. The absence of surface water can be explained by the shallow snow volume. The ablation of the thin

[27] The difference between the infrared albedo and the near-infrared albedo is consistent with the spectral albedo of bare ice.

snow volume likely resulted in minimal surface water, which in turn discouraged the formation of large, lower albedo melt ponds.

The June 16 AVHRR data indicates that the spatial variability of infrared albedo is less than the variability of visible albedo during advanced melt conditions. This is consistent with the fact that visible albedo is sensitive to the volume conditions of the decaying snowcover and the underlying ice volume, both of which have characteristics and distributions that chance rapidly during this period. Thus, the AVHRR measured visible albedo would be sensitive to the distribution of snow/ice and ponded areas. Conversely, at infrared wavelengths, the albedo is sensitive to the very near-surface conditions of the ice volume. Since both a slush volume and the surface of a melt pond are both saturated, their infrared albedo are similar, and therefore, the satellite measured infrared albedo is less dependent on their distribution. This difference in sensitivity can also be extended to shallow and deep meltponds. While the visible albedo is sensitive to the evolution of a melt pond, the infrared albedo is not dependent on pond depth and thus less sensitive to the distribution of melt ponds of various depths.

5.4.2.3 June 20

By June 20, the scene's visible and infrared sea ice albedo decreased to 0.53 and 0.31 respectively (figures 5.4(f) and 5.5(f)). The June 16 to June 20 difference image in Figure 5.9 indicates that much of this decrease was restricted to the early consolidation zone. The largest decreases in albedo were found in Resolute Passage. On June 20, air temperatures at the first-year ice site ranged from 2°-5° C. The June 20 histograms indicate that the distribution of albedo over the scene is still bimodal and defined by the consolidation regimes. However, visible and infrared albedo in the late consolidation zone became more variable, while the albedo in the early consolidation zone became less dispersed. In the early consolidation zone, the low albedos (α_{vis}=0.46, α_{ir}=0.22) and the decrease in variability suggest that surface ponding was more extensive and as a result, the surface was becoming more homogeneous as the interstitial snow/ice areas decreased in area. Surface observations on June 20 estimated that melt ponds covered at least 60% of

Resolute Passage. Very low albedos in Allen Bay [28] indicate more extensive ponding in that area. In the late consolidation zones, the surface albedos are weighted more towards bare ice cover.

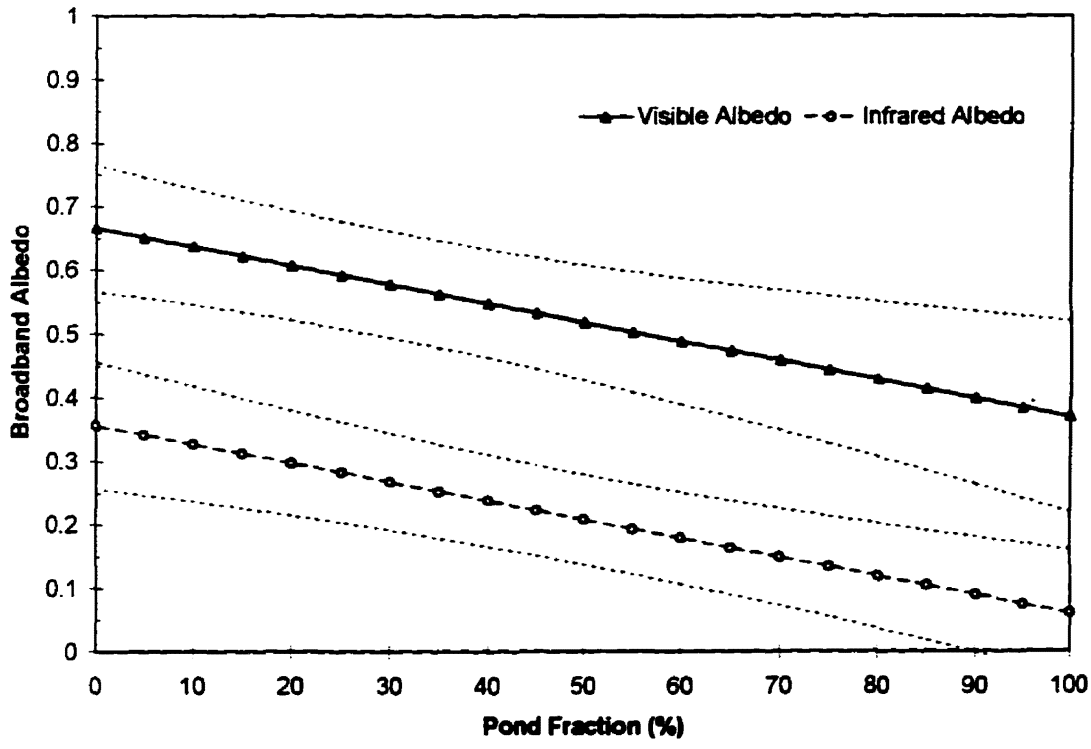
Again, satellite sensors record an areally averaged albedo. Thus the albedos presented here may not be comparable to surface measurements collected when the surface is undergoing advanced melt. Climatologists are not only interested in the regional albedo, they are also interested in the relative surface area covered by individual surfaces such as melt ponds. This information is necessary to determine heat storage and light transmission through the ice volume (Grenfell and Maykut, 1977). Thus, an examination of the ability of late season albedo images such as June 16 and June 20 to provide information regarding melt pond coverage was performed. Grenfell and Maykut (1977) related the regional allwave albedo of multiyear ice to the fraction of melt ponds using surface spectral albedos. This approach is used here. However, unlike Grenfell and Maykut (1977), the effects of the variability of the surface albedo on the estimated pond fractions are examined.

Assuming that the sea ice surface is composed of bare ice and melt ponds, the respective spectral albedos from figures 4.17 and 4.18 were used to calculate the visible and infrared albedo for a pixel containing differing proportions of these two surfaces. [4-25] was used to calculate the spectral albedo of the mixed surface. The final albedos were then calculated by integrating the mixed albedo over each broadband, weighted by the incident irradiance within each band. The resultant visible and infrared albedo are plotted against pond fraction in Figure 5.11. Based on the two input spectra used here, both albedos share a similar dependence on pond fraction. Included on the figure are error bars that represent the fraction results based on the observed variability of the visible and infrared albedo of bare ice and melt pond surfaces. In lieu of observational data regarding the variability of bare ice albedo, a conservative estimate of σ=0.1 was used here for both the visible and infrared case. Morrassutti's (1995) melt pond survey indicates the standard

[28] Allen Bay is the large bay located northeast of Resolute Bay

deviation of visible and infrared albedo over first-year ice melt ponds is σ =0.15 under overcast conditions. Since no data were available for clear-sky conditions, this value was used. The results in Figure 5.11 show that the large inherent variability in the albedo of both surface types makes it difficult to determine precise pond fractions using this approach. For example, a visible albedo of 0.60 represents a melt pond fraction that may range from 0 to 55%. Although less variable, the infrared albedo also can represent a wide range of pond coverage in some cases. These wide ranges have implications for those interested in using albedo measurements as proxy indicators for accurate measures of pond coverage. Similarly, others are investigating the use of microwave sensors to measure such proxy indicators of surface albedo as melt pond coverage. The precision of these proxy methods are questionable given the variability in the albedo of the constituent surface types examined here.

Figure 5.11 Clear sky broadband visible and infrared albedo vs. the proportion of melt ponds. Surface is considered as a mixture of bare ice and melt ponds. Dotted lines indicate error estimate based on ±one standard deviation.



5.4.3 July - Drainage and Breakup

Despite the twofold increase in average air temperature, the July 7 AVHRR data indicates that sea ice albedo (α_{vis}=0.41, α_{ir}=0.21) only decreased marginally since June 20 and in some areas (e.g. Allen Bay) increased in albedo (figures 5.4(g) and 5.5(g)). Although the changes are within the uncertainties of the derived albedos, they appear logical given conditions at that time. Importantly, the July 7 imagery reveals a reversal in the spatial pattern of surface albedo. On this date, the albedo of the late consolidation area (α_{vis}=0.38, α_{ir}=0.20) is slightly lower than the early consolidation zone. As a result of this decrease, the variability of sea ice albedo over the scene was reduced and the distribution of surface albedo appears again to be unimodal. The June 20 to July 7 difference image in Figure 5.9 indicates that albedo in the early consolidation remained stable, while albedo decreased significantly in the late consolidation zone. Also, this decrease was greater at visible wavelengths in this zone.

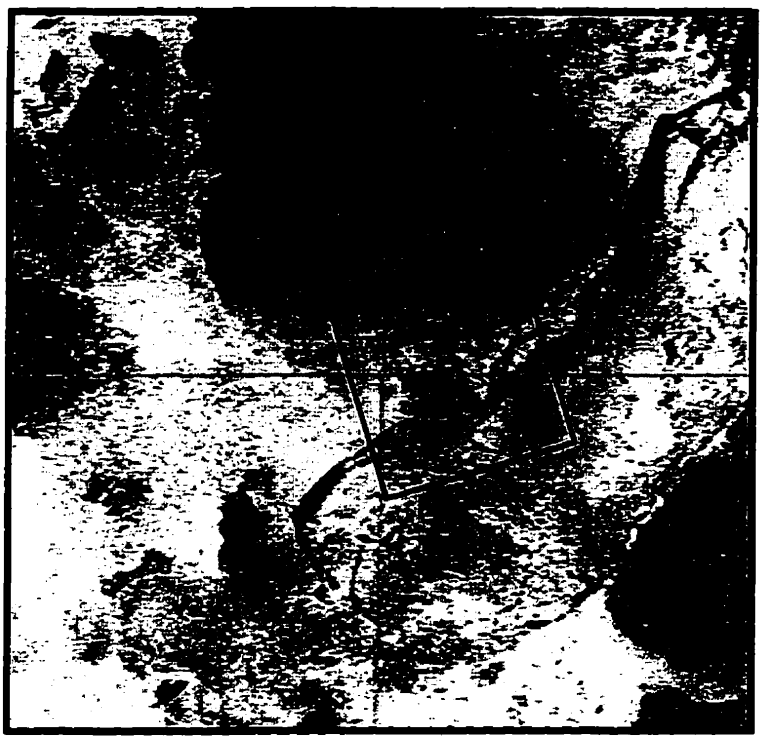
The relative stability of the albedo in the early consolidation zone suggests that ponding had reached its maximum extent. During SIMMS, this maximum was observed to be as high as 70-80% over first-year ice. Drainage of melt water through cracks, leads and sea holes regulates pond levels late in the melt period. In fact, on the final trip through Resolute Passage on June 20, melt water was found draining through several old seal holes. The beginning of breakup is often closely followed by a draining of surface water into newly opened cracks or leads. The remnant, well drained, porous white ice then eventually dominates the icescape resulting in an increase in surface albedo. This is a possible explanation for the apparent stability and, in some areas, an increase in surface albedo even though ambient temperatures have increased significantly. As mentioned earlier, this late season increase in surface albedo due to ice drainage is a phenomenon where observational data are sparse. The overall effect of this drainage on the regional albedo is unknown. The effect of the higher albedo drained ice may be offset by the decrease in albedo caused by the open water areas serving as the melt water sink. However, field observations in SIMMS '95 have shown that small open water areas can effectively drain much larger ice areas.

At first, the reduction in albedo and increase in its variability in the late consolidation zone appeared to suggest that surface ponding was extensive on this date. In fact, July 5 and July 7 quicklook TM imagery of the region (Figure 5.12(a) and (b)) indicates that the ice in the late consolidation area and the rest of Barrow St./Lancaster Sound was no longer consolidated, i.e. it had begun to breakup and move. .Northeasterly winds on July 5 moved weak ice away from Griffith Is. and created open water areas to the southwest of the island. Given the thinner ice and strong currents in Barrow St., the ice in this zone is first to break up. Its movement is dictated by ocean currents, winds and the remaining ice in the pack. On July 7, quicklook imagery shows that much of the open water areas had closed as the ice moved back into Griffith Is.. It is fair to conject that if AVHRR imagery were available for July 5, a larger decrease in albedo would have been found in the late consolidated ice area due to the presence of open water. The quicklook imagery reveal that the decrease in albedo and increase in this zone was due to the presence of open water cracks and leads.

The breakup in the late consolidation zone resulted in two areas of very low albedo in the July 7 imagery. The first is a large crack running perpendicular to the shore along the consolidation ridge. Its visible albedo and infrared albedo ranged from 0.1-0.2 and 0.08-0.10 respectively. The magnitude of both albedos suggest that the crack pixels are actually *mixels* of open water and adjacent snow/ice surfaces. The second much larger feature, located off the western shore of Griffith Is., is an open water polynya-like feature with visible and infrared albedos less than 0.05. As the sea ice volume decays, its strength decreases. Cracks and leads begin to form, usually along consolidation boundaries and along shorelines. The appearance of these breakup features expose the low-albedo, ocean water and lower the area albedo. During fall and winter, small areas of open water have a disproportionate effect on the energetics of polar regions. While, their importance lessens

Figure 5.12 Thematic Mapper Quicklook† imagery of 1993 ice breakup

(a) July 5



(b) July 7



† Quicklook imagery are reproduced here under the authority provided by the Canada Centre for Remote Sensing.

Figure 5.12 (Cont...)

(c) July 21



(d) July 31



† Quicklook imagery are reproduced here under the authority provided by the Canada Centre for Remote Sensing.

during the late spring and summer, open water areas are still significant in terms of their influence on ice ablation and kinematics. These areas act as radiation sinks and likely encourage melting and weakening of surrounding ice areas.

The July 5 TM imagery (Figure 5.12(a)) revealed that large areas of open water were present just outside the early consolidation zone along the shear zone ridge. A crack that large would efficiently drain much of the standing water in the early consolidation area. The light image tone in the early consolidation zone does suggest that ponding is now minimal in this ice area. The drainage of the early consolidation zone should result in noticeable change in the surface albedo. Specifically, the infrared albedo would increase due to the reduction in the proportion of surface water on the ice. The visible albedo is not expected to change immediately in response to a decrease in the areal fraction of surface water. However, the visible albedo may increase as drainage continues and the ice becomes more porous. The June 20 to July 7 difference image (Figure 5.9) does not indicate any large-scale change in surface albedo within the measurement uncertainty. Figure 5.9 includes a difference image for the same period based on the assumption that there is no measurement uncertainty and any change in albedo between dates is real. The new image indicates a widespread increase in infrared albedo in the early consolidation zone. In contrast, the visible difference image shows areas of both albedo increases and decreases. This difference pattern would support the theory of widescale drainage in the early consolidation zone suggested by the TM imagery of July 5 and 7.

The next available AVHRR image was July 29 (Figure 5.4(h) and 5.5(h)). Unfortunately, no interim albedo data of the pack's breakup was available. The July 29 imagery reveals that much of the ice has ablated and/or moved out of the passage. However, the contrast enhanced imagery indicates that some ice is still present in the passage. What is not evident is whether this ice is remnant of the passage's ice cover or whether it was passing through the area at time of image acquisition. Examining the full AVHRR scene reveals that there is still a significant amount of moving ice in the region and the open water in and surrounding Resolute Passage on this date is somewhat anomalous. Quicklook TM

imagery collected on July 21 and July 29 (Figure 5.12(c) and (d)) indicates that ice in the early consolidation zone was still fast on July 21, but much of the late consolidation zone was now open water. The July 29 quicklook imagery suggest that the ice has cleared out of Resolute Passage and small pieces of ice from the Barrow Strait ice dam were moving through the passage during the acquisition of the AVHRR imagery. According to the AVHRR data, this moving ice had a very low albedo.(α_{vis}=0.10, α_{ir}=0.08). The surrounding open water had a visible albedo of zero and a slightly higher infrared albedo. No surface observations are available to corroborate these breakup ice albedo values.

5.4.4 Summary

The AVHRR-derived albedo maps described the spatial and temporal variability of sea ice albedo over the 60 km by 60 km study region over the period April 30 to July 29. The seasonal evolution of visible and infrared albedo is summarized in figures 5.13 and 5.14. In cold winter conditions, the albedo of sea ice is high, relatively constant and spatially homogeneous. Variability in surface albedo at this time of year was associated with the lower albedo rough ice areas. Both visible and infrared albedo decrease in response to increased ambient temperatures brought on by increased solar insolation and advection of warmer air from southern latitudes. The greatest changes in albedo began when daily average air temperatures remained above -5 °C. In 1993, this period coincided with the first week of June. Most of the seasonal variability in surface albedo can be associated with the onset of ponding. During this period, the relatively high-albedo icescape was punctuated by low-albedo melt ponds and as a result, the spatial variability of visible and infrared albedo increased. The standard deviation of both visible and infrared albedo over the study scene reached as high as 0.09 during advanced melt conditions (Figure 5.4(f)). Ponds appeared first close to shore areas and then spread into Resolute Passage. The distribution of albedo indicated that there were two major ice states during this period: the lower albedo, heavily ponded early consolidation zone and the higher albedo bare ice late consolidation zone. Figures 5.13 and 5.14 show that the temporal albedo signal of

Figure 5.13 Seasonal change in satellite-derived visible and infrared albedo

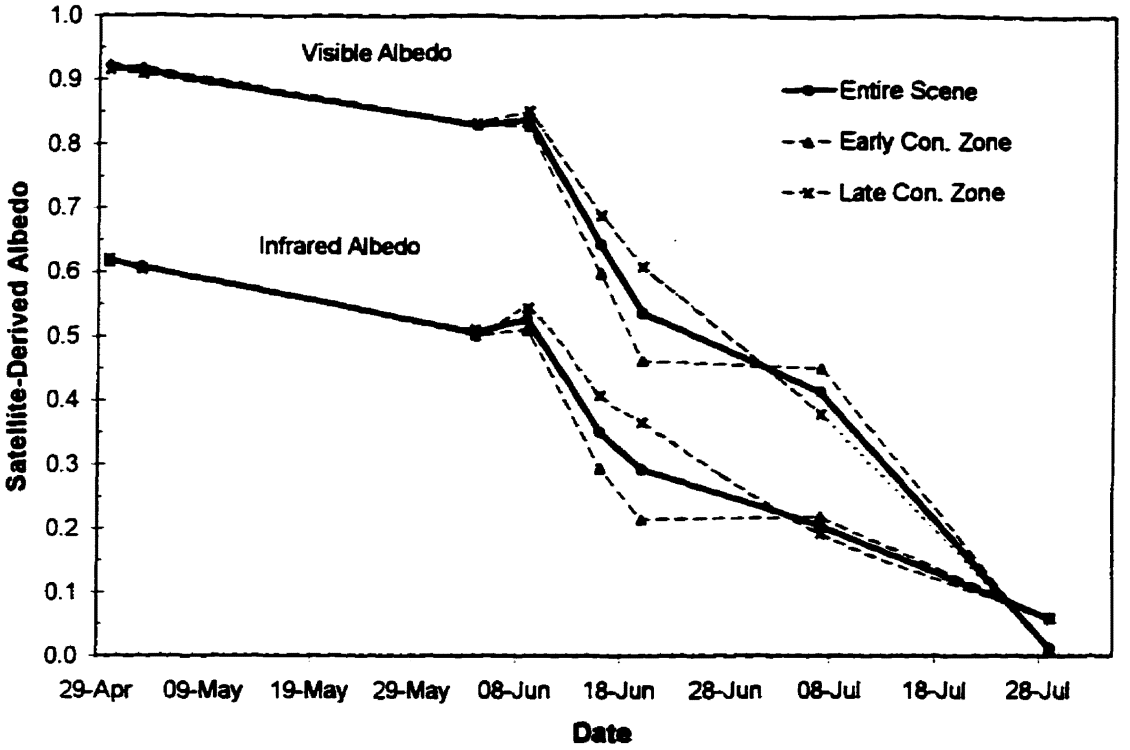
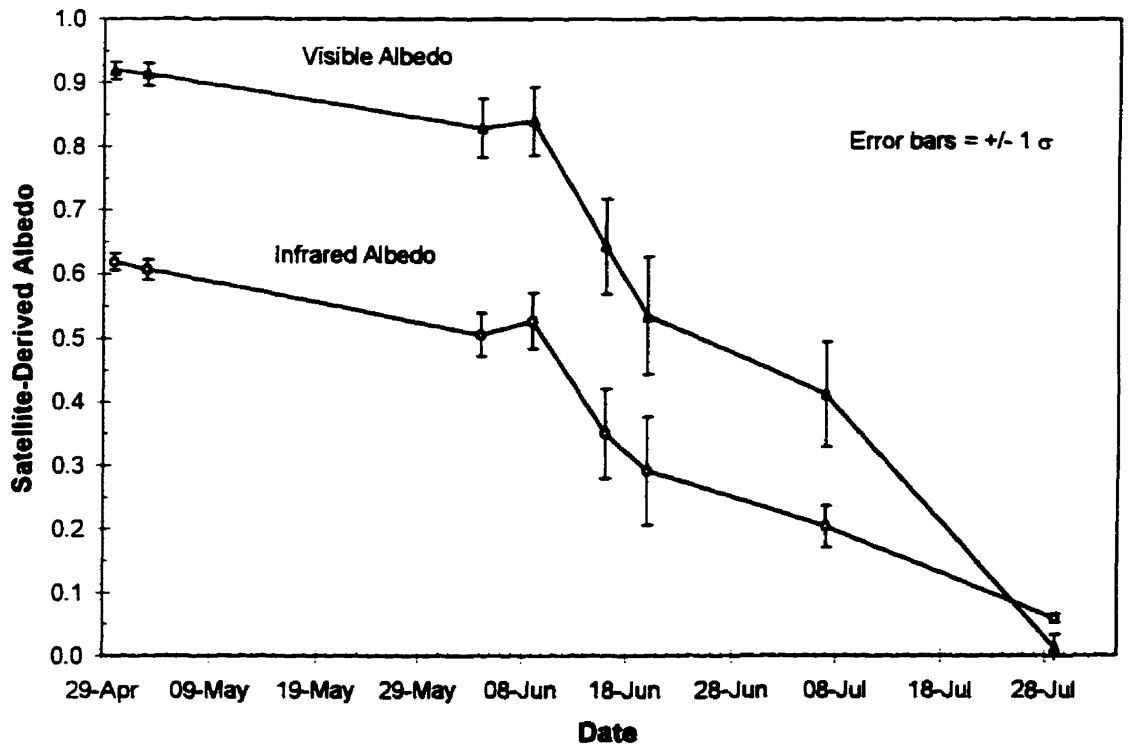


Figure 5.14 Seasonal variability in visible and infrared albedo over AVHRR scene



these two zones began to diverge on June 9 and reach maximum contrast on June 20. On July 7, the signal is reversed, i.e. the late consolidation zone has a lower albedo due to both the breakup of the thin ice in that zone and to the drainage of the early consolidation zone. The visible and infrared albedo eventually converge due to the replacement of the ice cover with open water.

5.5 Multitemporal Principal Component Analysis of AVHRR Albedo Data

In the previous section, the interscene variability of the study images was identified and interpreted. While highlighting important spatial patterns in sea ice albedo within each scene, this analysis did not consider the temporal or seasonal aspect of the dataset. In the context of remote sensing, multitemporal analysis examines change over a sequence of three-dimensional images: the first two dimensions represent the image pixel's x,y location in the image space, and the third dimension commonly represents the spectral attributes of the pixel. Registered together in a temporal sequence, the image set represents a four-dimensional dataset with time being the final dimension (Piwowar, 1994). Essentially, since images differ in time only, multitemporal analysis is based on the assumption that differences in imagery can be attributed mainly to time.

In light of the present day concern over environmental change, together with the proliferation of remote sensing data, multitemporal analysis over these types of image datasets is now particularly relevant. Unfortunately, unlike pairwise comparison techniques that operate on a pair of image dates (e.g. image differencing) (Singh, 1989; Howarth and Wickware, 1981), there are relatively few techniques available for the analysis of change in multiple date (greater than two) remote sensing images. The differences images contained in Figure 5.9 are useful for detecting albedo change over two dates, but are ineffective for describing change over multi-date data.

The goal of this analysis is to summarize the variability in satellite-derived sea ice albedo from April to July within the experiment region. The identification of these patterns is a

first step towards the identification of the physical variables in the AIO interface responsible for the seasonal variability in sea ice albedo on the regional scale. An analysis technique appropriate for such a *post hoc* analysis that has been accepted by both the climatology and remote sensing community is eigenvector analysis or as it is more commonly referred -- principal component analysis (PCA). PCA has been extensively used in the remote sensing community as a means of image enhancement (Walsh *et al.*, 1990), image compression (Haralick and Fu, 1983) and change detection in multitemporal image data (Fung and LeDrew, 1987). More specifically, in the polar remote sensing community, PCA has been utilized to examine the variability and interrelationships of sea ice and various atmospheric variables. Crane *et al.* (1982) used PCA to examine the spatial and temporal patterns of sea ice microwave signatures and atmospheric temperature/pressure data. PCA was used to reduce a Scanning Multichannel Microwave Radiometer (SMMR) sea ice dataset and the resultant components were then input to an ice classification algorithm (Rothrock *et al.*, 1988).

5.5.1 Overview of Technique

Principal component analysis is a multivariate procedure that transforms an n x m data matrix made up of n variables and m observations to another matrix where the new variables are weighted representations of each other and are orthogonal (uncorrelated) of each other (Johnston, 1984). In the context of remote sensing, the original data matrix commonly consists of the covariance or correlation of images of different spectral bands, multiple dates or both.

The original variables, transformed into a new set of uncorrelated variables $Y_1, Y_2, \ldots Y_t$, can be expressed as:

$$Y_j = a_{1j}X_1 + a_{2j}X_2 + \cdots + a_{Nj}X_N \qquad [5\text{-}2]$$
$$= a_j^T X$$

where a_{Nj} are eigenvectors determined from the covariance matrix C_X. The transformation can be described by the following three steps.

(1) Calculation of the covariance matrix

Consider a multidate image dataset recorded at a number of dates (n) at one spectral band X. The entire dataset could be represented by variables X_1, X_2, ... X_n. Interrelationships between the individual images can be represented by the covariance matrix CC_X of dimensions n x n. The covariance matrix can be estimated by

$$CC_X = \frac{1}{K-1}\sum_{j=1}^{K}(X_j - m)(X_j - m)^T \qquad [5\text{-}3]$$

where m is the mean vector of variable X. In multitemporal PCA analysis, it has been reported that PCA should be performed on the correlation matrix of X_n instead of the covariance matrix. By standardizing the input variables to zero mean and a variance of unity, any influence caused by variables measured with units that were not commensurable would be avoided. This is not expected to be a problem with this data since the input variables use identical units. However, if there are large differences in the variances of the input variables, certain variables may unduly influence the analysis. The results in figures 5.4 and 5.5 show that the level of variability varies widely between images. However, since we are interested in the variability of albedo, this variance structure should be preserved in the input dataset. As such, the covariance matrix is used to derive the eigenvectors and related principal components of the dataset.

(2) *Computation of eigenvectors*

The eigenvalues, E=[$\chi_{1,1}$, $\chi_{2,2}$, $\chi_{3,3}$, ... $\chi_{n,n}$], and eigenvectors, EV=[a_{kp} ... for k=1 to n images, and p=1 to n components] of the covariance matrix are computed such that:

$$EV * CC_Y * EV^T = \begin{bmatrix} \chi_{1,1} & 0 & 0 & 0 \\ 0 & \chi_{2,2} & 0 & 0 \\ 0 & 0 & \chi_{3,3} & 0 \\ 0 & 0 & 0 & \chi_{n,n} \end{bmatrix} \quad [5\text{-}4]$$

The matrix CC_Y is a covariance matrix whose diagonal elements, $\chi_{i,i}$, are called eigenvalues. These eigenvalues represent the variance of the pth principal component, where p=1 to n components. The first component extracted contains the most variance and the following components successively contain less variance. EV is the matrix of eigenvectors which diagonalize the matrix CC_Y. The computation of eigenvalues and eigenvectors are commonly available in most statistical analysis programs. Occasionally, rotation of the derived components results in less ambiguous variable loadings and thus simplifies subsequent interpretation (Gorsuch, 1983). Rotation was attempted in this study, but did not result in significant differences. As a result, the components presented here were not rotated.

(3) *Linear transformation of dataset*

The eigenvector matrix EV can be used to transform the original image dataset into the new uncorrelated system where a new image is created for each principal component. Specifically, each pixel in the original dataset ($DN_{i,j,p}$) is projected onto each principal component axis through the following linear transformation

$$DN'_{j,k,p} = \sum_{l=1}^{n} a_{kp} DN_{j,k,l} \quad [5\text{-}5]$$

where $DN_{j,k,l}$ is the original digital number or brightness value for image l for the pixel at column j row k, $DN'_{j,k,p}$ is the new value for principal component p for the pixel at column j row k and n is the number of images.

5.5.2 Results

PCA was performed on the following two datasets:

(1) Visible - April 30, May 3, June 4, June 9, June 16, June 20, July 7 and July 29
(2) Infrared - April 30, May 3, June 4, June 9, June 16, June 20, July 7 and July 29

For each principal component, the eigenvalues and the proportion of total variance that the component represents is presented in tables 5.1 and 5.2. Along with this information, the contribution of each image date to each component is expressed by the computed eigenvectors. Also, the principal component scores are mapped according to [5.5] and included with a graphical representation of the associated eigenvectors in Figure 5.15 Pixel values in the component images were normalized to have a mean of zero. The dynamic range of each image was restricted to $\pm 2\ \sigma$ to improve contrast.

Tables 5.1 and 5.2 show that the first three components represent over ninety percent of the variance in the multitemporal visible albedo dataset. Since the albedo images have been essentially normalized (i.e., atmospheric and view angle effects have been removed), albedo variance in the multitemporal dataset is expected to originate from

(a) changes to the physical conditions of the sea ice volume, and
(b) dataset noise.

By comparing the eigenvalues of the derived components to the level of uncertainty in the dataset, the contribution of each of these two sources of variability to the derived component can be estimated. Based on the eigenvalues in Table 5.1 and assuming an absolute error of 0.5 (σ^2=0.0025) in the visible albedo data, only the first three components in the visible PCA results can be assumed to physically significant, i.e. the variances of these components are all greater than 0.0025. As a result, only the first three components are examined here. In terms of the infrared albedo data, only the first component is less than the assumed level of noise in the data based on an albedo uncertainty of 0.08 (σ^2=0.0064). Since some of the remaining components contain a

Table 5.1 Eigenvalues and eigenvectors of covariance matrix for the visible albedo dataset.

	Principal Component							
	1	2	3	4	5	6	7	8
Eigenvalue	0.01440	0.00777	0.00282	0.00072	0.00044	0.00031	0.00021	0.00007
% Total Var.	53.8	29.0	10.5	2.7	1.6	1.2	0.8	0.3
Eigenvectors								
April 30	0.009	0.050	0.138	-0.035	-0.002	0.382	-0.314	0.856
May 3	0.005	0.059	0.152	-0.080	-0.027	0.627	-0.556	-0.514
June 4	0.213	0.264	0.515	-0.238	0.026	0.369	0.652	-0.035
June 9	0.317	0.240	0.532	-0.263	0.112	-0.557	-0.408	-0.015
June 16	0.589	0.061	0.072	0.799	-0.051	0.051	-0.010	-0.015
June 20	0.711	-0.213	-0.461	-0.474	-0.057	0.083	0.001	0.023
July 7	-0.018	0.903	-0.428	-0.017	0.002	-0.002	-0.027	0.007
July 29	0.030	-0.043	-0.091	0.048	0.990	0.079	0.013	-0.009

Table 5.2 Eigenvalues and eigenvectors of covariance matrix for the infrared albedo dataset.

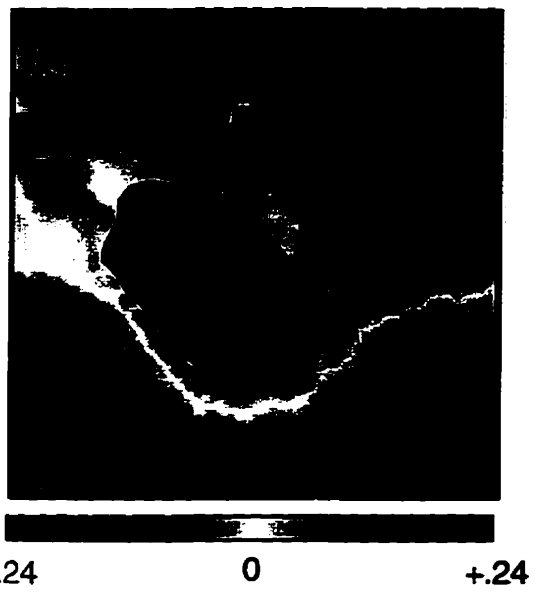
	Principal Component							
	1	2	3	4	5	6	7	8
Eigenvalue	0.01230	0.00241	0.00094	0.00057	0.00026	0.00013	0.00008	0.00004
% Total Var.	73.5	14.4	5.6	3.4	1.5	0.8	0.5	0.3
Eigenvectors								
April 30	0.032	0.104	-0.110	-0.025	0.489	-0.070	0.855	-0.016
May 3	-0.007	0.130	-0.101	-0.046	0.747	-0.414	-0.491	0.016
June 4	0.127	0.584	-0.120	-0.200	0.182	0.730	-0.141	0.050
June 9	0.260	0.607	-0.153	-0.314	-0.393	-0.531	0.068	-0.001
June 16	0.607	0.135	-0.028	0.783	0.005	-0.010	-0.024	-0.008
June 20	0.736	-0.403	0.193	-0.495	0.096	0.064	-0.018	-0.008
July 7	-0.071	0.284	0.950	0.040	0.077	-0.058	0.043	0.001
July 29	0.005	-0.031	0.006	0.012	-0.012	-0.031	0.028	0.998

significant amount of variance, the first three infrared components are included for examination in hope that the component images can aid in the distinction between patterns of useful albedo variability and that of random noise. Examination of the resultant principal components in Figure 5.15 reveal that the visible and infrared albedo datasets can be described by very similar components. The ordering of these components, however, differ between the two datasets.

5.5.2.1 Principal Component 1 - Visible and Infrared Albedo

The first principal components of the visible and infrared albedo ($PC1_{vis}$ and $PC1_{ir}$), shown in Figure 5.15(a) and (b), are quite similar. The components represent 54% and 74% of the variance in visible and infrared albedo respectively over the study period. The eigenvectors indicate that most of the variance in surface albedo over the study dates examined here occurred in the month of June. Specifically, the most variable conditions were found on July 16 and July 20 when surface ponding was present. Given the large variances in albedo on these dates, their strong influence on the first component was expected. In this month, the daily mean air temperature increased from -3 °C to 6 °C. During the month of June, the icescape transformed from a predominantly snow-covered surface into a heterogeneous mix of wet snow, melt ponds and bare ice. This transformation resulted in an increase in the variability of albedo.

The positive eigenvectors suggests that the resultant component images represent the distribution of albedo integrated over the month of June with most weight being placed on two late June dates. As a result, the component images strongly resemble albedo images of June 16 and June 20. In terms of PC1, the range of component scores represents relative albedo. High albedo is reflected in high positive scores and vice versa. The PC1 image describes the dominant patterns of visible albedo variability over the study period. By correlating these patterns with known characteristics of the sea ice surface, the



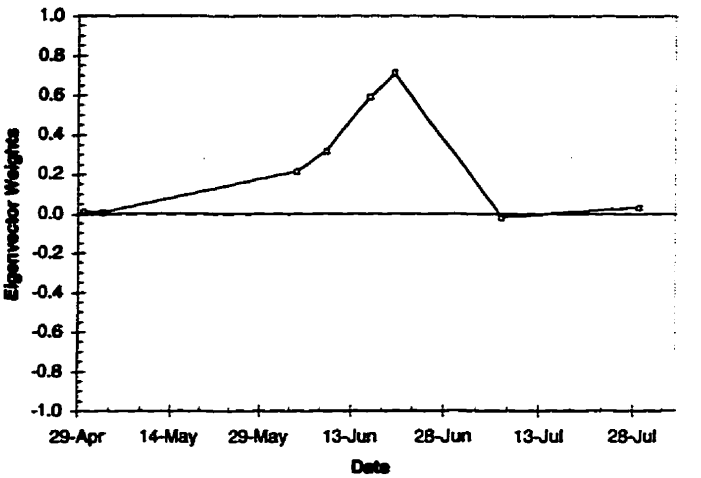
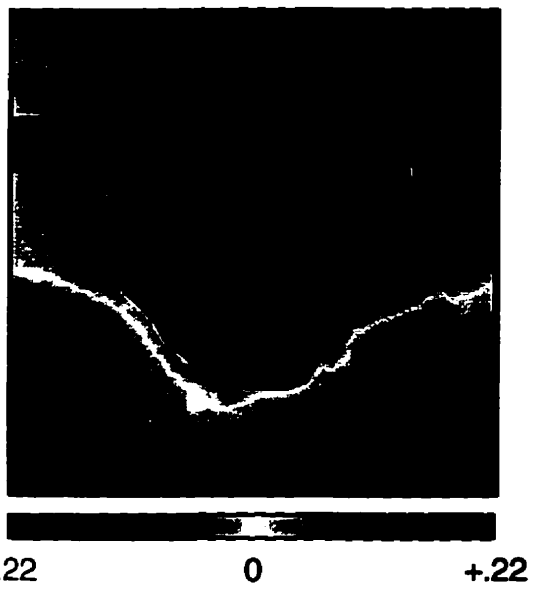


Fig. 5.15(a) Visible Albedo - Principal Component 1



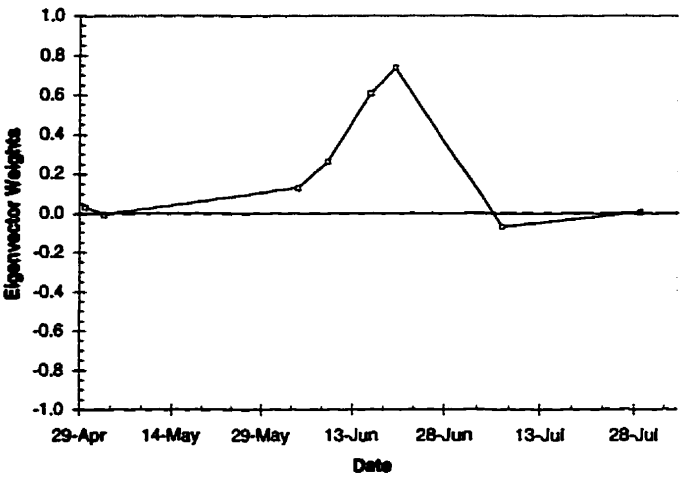


Fig. 5.15(b) Infrared Albedo - Principal Component 1

important factors controlling the spatial variability of sea ice can be identified. In $PC1_{vis}$ and $PC1_{ir}$, there appears to be two major albedo patterns over the AVHRR study scene. The most obvious pattern is the increase in albedo with distance from Cornwallis Is. As explained in Sec. 5.4.2.2 and by Figure 5.10, the advection of sensible heat and the eolian transport of crustal material onto the sea ice reduces the albedo near land.

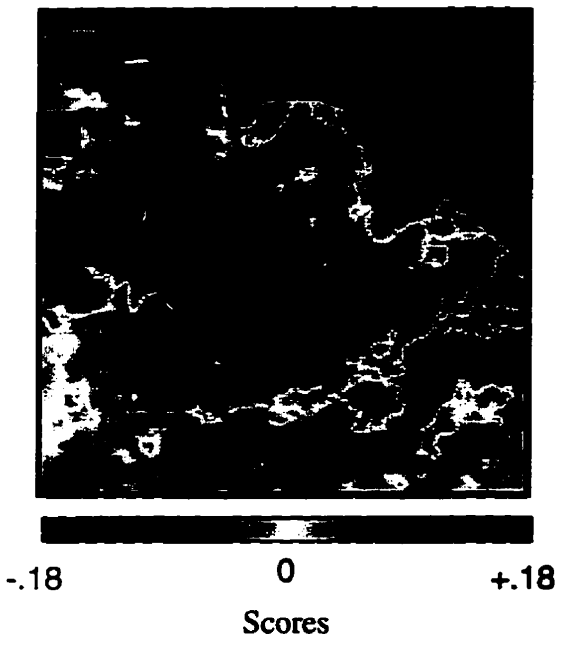
The second pattern is the apparent bisection of the image scene into distinctive albedo zones. Although appearing to be an extension of the land effect, this pattern appears independent of distance to land and thus believed to originate from a separate factor. The pattern is characterized by a boundary between the early and late consolidation ice areas that was described in Sec. 5.4.2.2.. Although detected in the April 30 imagery, this pattern is most visible during advanced melt conditions. It is hypothesized that the higher albedo in the late consolidation zone is reflective of the lower level of ponding in the area during this period. The pattern is more distinctive and the early consolidation zone is more homogeneous in $PC1_{ir}$ than $PC1_{vis}$. Initially, this albedo pattern was thought to be driven primarily by the proximity to land. However, this theory was inconsistent with the pattern of albedo off the southern tip of Cornwallis Is. and off the northwestern tip of Griffith Is. Instead, the albedo pattern closely follows the consolidation ridge shown in Figure 5.3. This has been confirmed by the coregistration of the albedo imagery with ERS-1 SAR data collected in the spring of 1993. This ridge separates the ice that consolidated in late 1992 with that ice consolidated in March, 1993.

In the early consolidation area, the lower albedo and higher variability suggest more extensive ponding in this zone. In the late consolidation area, the albedos are 0.1-0.2 higher and much less variable. Two factors are believed responsible for this distribution of albedo during advanced melt conditions in 1993. One -- since much of the ice's snowcover is deposited in the fall months, ice that consolidates in the fall have a tendency to have larger snow volumes. Two -- the opportunity for snow catchment is greater within these areas due to the proximity to land and increased surface roughness. Due to the smooth ice and distance from land, any snow that is deposited in the late zone likely

settles in areas with better catchment, like the nearby early consolidation zone. Both factors are responsible for deeper snowcovers in the early consolidation zone. Surface observations in both zones confirm that snowpacks were indeed deeper in the early zone (20-30 cm) than the late area (<10 cm). With the onset of melt conditions, this ultimately resulted in more melt water, which in turn, increased the degree of ponding on the ice surface. The albedo was thus lower and more variable in this zone. The results here indicate that in fast ice regimes like the archipelago, time of sea ice consolidation and the ensuing morphological surface characteristics are significant controls over the regional scale variability of surface albedo.

5.5.2.2 Principal Component 2 - Visible, Principal Component 3 - Infrared Albedo

Figure 5.15 (c) and (d) show that the second visible albedo component and the third infrared albedo component are similar. $PC2_{vis}$ accounts for a much larger portion of the seasonal variance in albedo-- 29%. In comparison, $PC3_{ir}$ only accounts for approximately 6%. The eigenvectors and the resultant component image indicate that this component represents the contribution of the breakup of the icescape to the albedo variability over the study scene. Again, breakup occurred in the late consolidation zone in the beginning of July and is captured here by the July 7 image. The late consolidated icescape was replaced by areas of open water and broken, moving ice. This resulted in a lowering of albedo in the area and an increase in its variability. The large areas of open water discussed in section 5.4.3 have very low scores in the component image. The early consolidated area was still fast on this day and as a result, had a higher albedo than the late zone. Again, consolidation zones appear to be controlling the large-scale distribution of surface albedo over the scene. Compared to the infrared albedo, there is a larger contrast between open water and bare ice albedo in the visible portion of the spectrum. Thus, breakup conditions are expected to contribute to a larger portion of variability in visible albedo than infrared albedo. This explains the larger portion of the seasonal variance explained by $PC2_{vis}$.



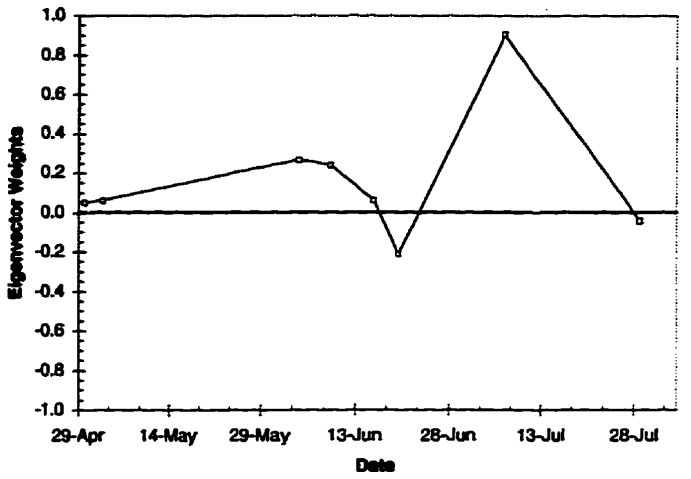
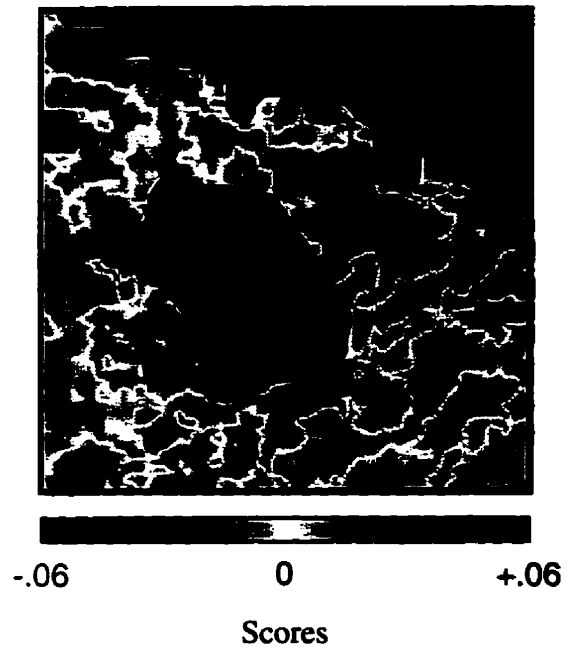


Fig. 5.15(c) Visible Albedo - Principal Component 2



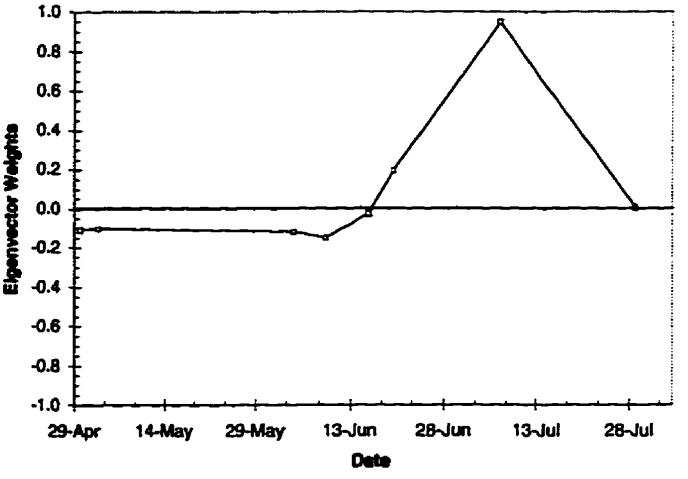
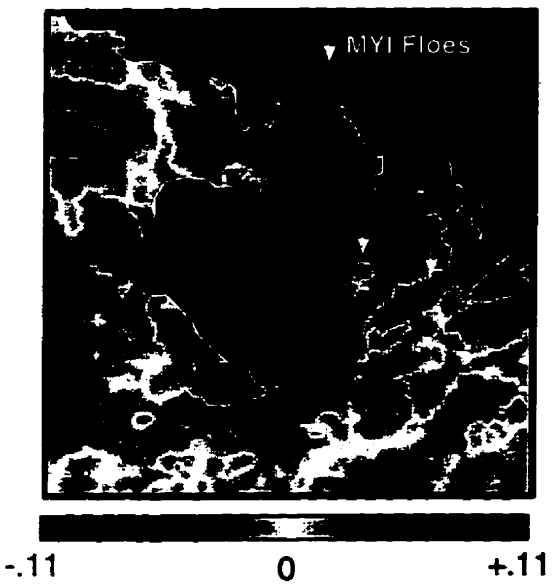


Fig. 5.15(d) Infrared Albedo - Principal Component 3

5.5.2.3 Principal Component 3 - Visible, Principal Component 2 - Infrared

$PC3_{vis}$ and $PC2_{ir}$ in Figure 5.15 (e) and (f) appear to describe similar distributions of surface albedo. $PC2_{ir}$ represents approximately 14% of the total seasonal variance in the infrared albedo dataset, while $PC3_{vis}$ represents approximately 11%. Both components load most heavily on June 4, June 9, June 20 and July 7. June 20 and July 7 dates load negatively on $PC3_{vis}$, while only the June 20 date loads negatively on $PC2_{ir}$. Based on the eigenvectors, areas of higher albedo on June 4, June 9 and lower relative albedo on June 20 will have the highest scores (darkest blue) on these components. The opposite is true in terms of the lowest component scores. This component describes the magnitude of change in albedo during the dynamic melt period. This was confirmed by tracking the change in visible and infrared albedo on these respective dates. The component image indicates that areas in the early consolidation zone experienced the greatest change in albedo relative to other areas in the scene. This is consistent with the metamorphosis of bright, deep snowcovers in these areas to dark, surface melt ponds. Areas which underwent less change in surface albedo are mapped as negative (red) values on the component image. These areas represent rough ridged areas, shore areas and much of the late consolidation zone. The lower the score, the less change in albedo over the loaded dates. In terms of very low scores, surface albedo was constant for much of the month. The lower scores in the near shore areas suggests that surface melt was underway in these areas at the beginning of June. The very high scores in $PC3_{vis}$ (dark blue tone) reveal large open water areas that were evident on July 7.

The slow change in the albedo of ridged areas is expected. Informal surface observations indicate that ridges often appear darker earlier in the season in comparison to the surrounding smooth, snow-covered icescape. This is often due to shadowing and the presence of bare, blue ice pieces. In advanced melt conditions, ridges appear brighter than the surrounded ponded icescape. Quite often, snow is still trapped in these rough ice



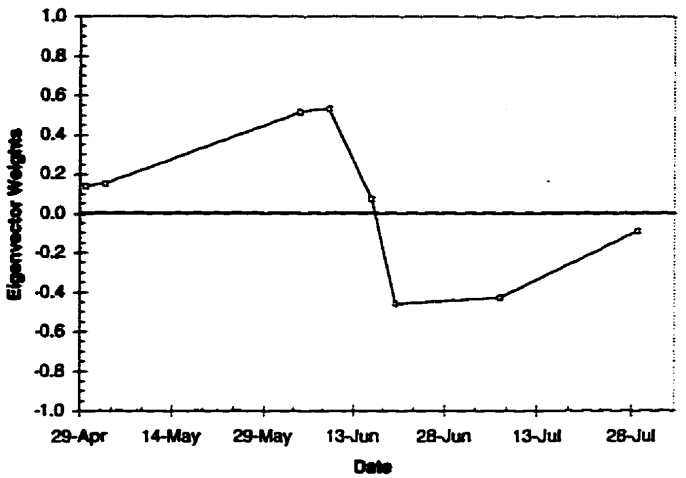
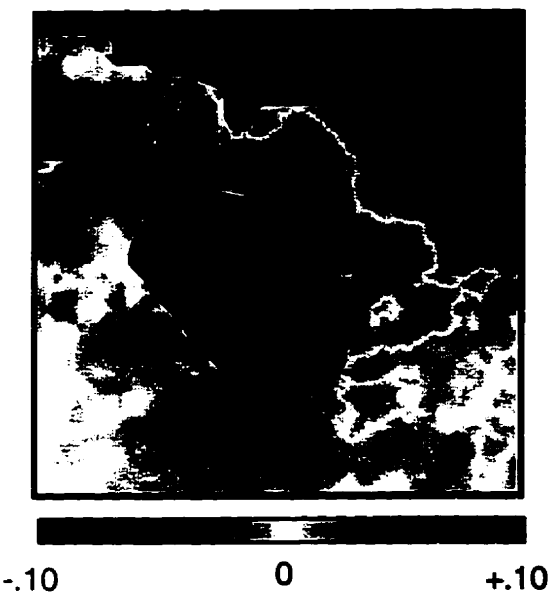


Fig. 5.15(e) Visible Albedo - Principal Component 3



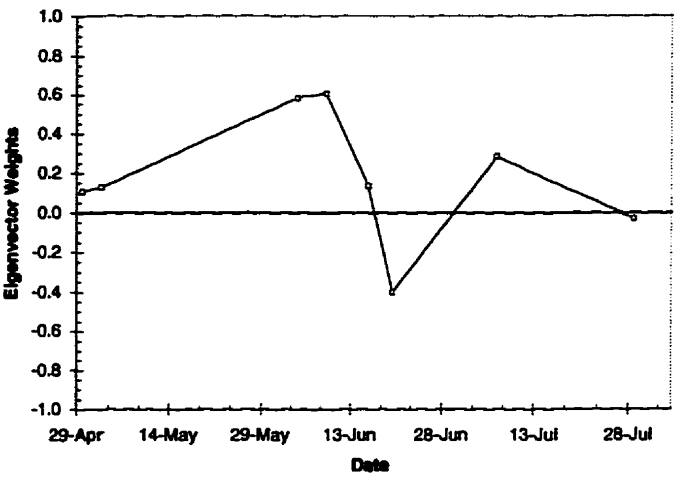


Fig. 5.15(f) Infrared Albedo - Principal Component 2

areas and the blue ice surface melt leaving behind a whiter frazil layer. The albedo of ridged areas can thus be out of phase with surrounding, smooth, snow-covered ice.

$PC3_{vis}$, and to a lessor degree, $PC2_{ir}$ reveal the location of two multiyear ice floes trapped within Resolute Passage. Arrows on Figure 5.15(e) denote their locations. The floe on the right is the sampled MYI floe described in Chapter 3. These old ice floes were approximately the size of an AVHRR pixel and thus could not be readily identified within the albedo imagery. However, it appears that the evolution of visible and infrared albedo of these floes were out of phase with that transition occurring in the surrounding first-year ice. Since these components describe the rate of albedo change during melt conditions, this floe was detected due to its slow change in albedo relative to that in the surrounding first-year ice matrix. Surface observations in 1993 and 1995 confirm this. During advanced pondings, helicopter observations indicated that the multiyear ice floe of the SIMMS 1993 site was indeed brighter than the surrounding first-year ice. Figure 3.32 shows a aerial balloon photo depicting late season first-year and multiyear ice in SIMMS '95. The difference in brightness between the two ice types is apparent. The reason for this difference is the presence of higher albedo hummock tops interspersed between the floe's melt ponds when ice/snow interstitial areas on the first-year ice were at a minimum during advanced melt conditions. Another potential reason for this phase difference is the rough ice area that typically surround multiyear ice floes trapped in first-year ice. Before consolidation, the collision of the thicker, old ice floe with the thinner surrounding first-year ice often causes the formation of a rough, ridged ice area surrounding the multiyear ice floe. Again, the albedo of rough ice areas was found to change slower than smooth, snow-covered first-year ice.

5.5.3 Summary

PCA proved to be a useful method for identifying and mapping the major variance structures in the seasonal albedo datasets. Although differently ordered in some cases, the principal components of the visible and infrared data were very similar. In terms of both

visible and infrared albedo, most of variability in albedo occurred during the month of June in 1993 -- more specifically, during the second half of the month when significant ponding was underway across the study scene. The PCA1 images suggest two environmental factors controlling the distribution of albedo on large spatial scales within the scene: proximity to land and snow depths related to time of consolidation. The influence of the first factor was observed *in situ*. However, the second factor was not identified until analysis of the AVHRR data. In terms of visible albedo, the next major source of albedo variation over the scene was the breakup of ice in the late consolidation zone. In terms of infrared albedo, this was the third component. The third major source of variability in visible albedo (and second in the case of infrared albedo) can be best described as the evolution of the icescape during the month of June. This component mapped areas that underwent relatively large changes in albedo and those that changed relatively little over the month of June. Smooth ice areas with significant snow volumes underwent the largest changes since they evolved into deep melt ponds. Rough ice and shallow snow late consolidation ice experienced the smallest relative change in albedo. Of interest is the ability of this component to map previously undetectable multiyear ice floes in Resolute Passage. It appears that due to the presence of hummocks and rough marginal ice, the evolution of the multiyear ice floe is out of phase with that of the surrounding smooth first-year ice.

5.6 Spectral Variability of Sea Ice Albedo

Chapter 3 discussed the spectral characteristics of sea ice albedo and how these characteristics change with the onset of melt conditions in the arctic. Through its visible and near-infrared channels, AVHRR is capable of providing multispectral information regarding the albedo of sea ice over large spatial areas. Given the seasonal dependence of the spectral albedo of sea ice, the relationship between the narrowband albedos of these two channels may be exploited to provide information regarding the conditions of the sea ice volume. Again, these data are required by those interested in the energetics of the

volume and in interpreting remotely sensed imagery. To this end, this section will examine how the relationship between the visible and infrared albedo of sea ice changed temporally and spatially over the region during the melt season.

5.6.1 Normalized Difference Snow-Ice Index (NDSII)

A simple way of assessing the spectral differences between the visible and infrared albedo of sea ice is to create difference images for each image date. These difference images demark sea ice areas where the visible and infrared albedo are similar and/or different. Considering the spectral albedo of sea ice, the difference between the albedos should be minimal over snow-covered and open water surfaces and at a maximum over ponded areas (Figures 4.17 and 4.18). The snow and ice retrieval algorithms for the new MODIS sensor plan to exploit similar relationships with snowcover through the incorporation of a *normalized-difference snow index* (NDSI) for the mapping of snow areas. The NDSI is identical to the normalized difference vegetation index (NDVI) and has been employed to map snow in mountainous areas using TM data (Dozier, 1989). Unfortunately, no similar products are scheduled to be produced from MODIS for sea ice in polar regions. This section will assess the utility of such an index in sea ice studies. The same index will be incorporated here, but examined in the context of sea ice data and thus consequently renamed the *normalized-difference sea ice index* or NDSII . The NDSII is defined as:

$$NDSII = \frac{\alpha_1 - \alpha_2}{\alpha_1 + \alpha_2} \qquad [5\text{-}6]$$

where α_1 and α_2 are the surface narrowband albedos for AVHRR 1 and 2 respectively. Such an index is used widely in remote sensing due to its simplicity in formulation, application and its effectiveness in vegetation studies. Quite often the imagery is applied to the TOA imagery in raw format, i.e. digital numbers are used to compute the index. Concerned over possible masking effects of the atmosphere, the surface narrowband albedos were used to calculate the NDSII here. NDSII images were created for each

image date and are presented in Figure 5.16. In this application, the NDSII ranges from 0 to 0.15. Pixels with similar visible and infrared albedos will have an NDSII close to 0. These pixels are representative of snow/ice and ocean surfaces. As snow volumes decay, the results of Chapter 3 suggest that their NDSII should increase as the contrast between the visible and infrared albedo increases. Pixels with high NDSII values (>0.10) are expected to consist of a high proportion of surface melt ponds. Before the individual images are examined, it is important to point out that the uncertainty in the index parameters, the narrowband visible and infrared albedo, results in an average uncertainty in the NDSII indices of approximately 0.1. This is error is large given the narrow range of the NDSII values presented here. Despite this uncertainty, the following NDSII images do illustrate the potential usefulness of the measure given more accurate input parameters.

5.6.1.1 NDSII- April 30 and May 3

In the April 30 albedo imagery (figures 5.4(a) and 5.5(a)), the study scene appears relatively homogeneous with the exception of darker rough ice areas. In Figure 5.16, the April 30 NDSII image reveals the existence of the two major consolidation regimes that only become apparent in the albedo imagery after the appearance of melt ponds. The early consolidation regime had slightly lower NDSII values than the surface in the late consolidation zone. Initially, the lower index values were thought to be due to an older snow volume covering the early consolidation zone. The snow in the early consolidation zone likely fell the previous fall, while the thin volume in the late zone fell likely within the last month. However, the blizzard described in section 5.4.1 would have likely deposited new snow over the entire scene. Also, it is thought that much of the fallen snow would have settled in the early consolidation zone. Examining the original albedo images, it appears that the difference in the NDSII values on this date was due to slightly higher visible albedo values in the early consolidation zone. Infrared albedo values are similar between zones.

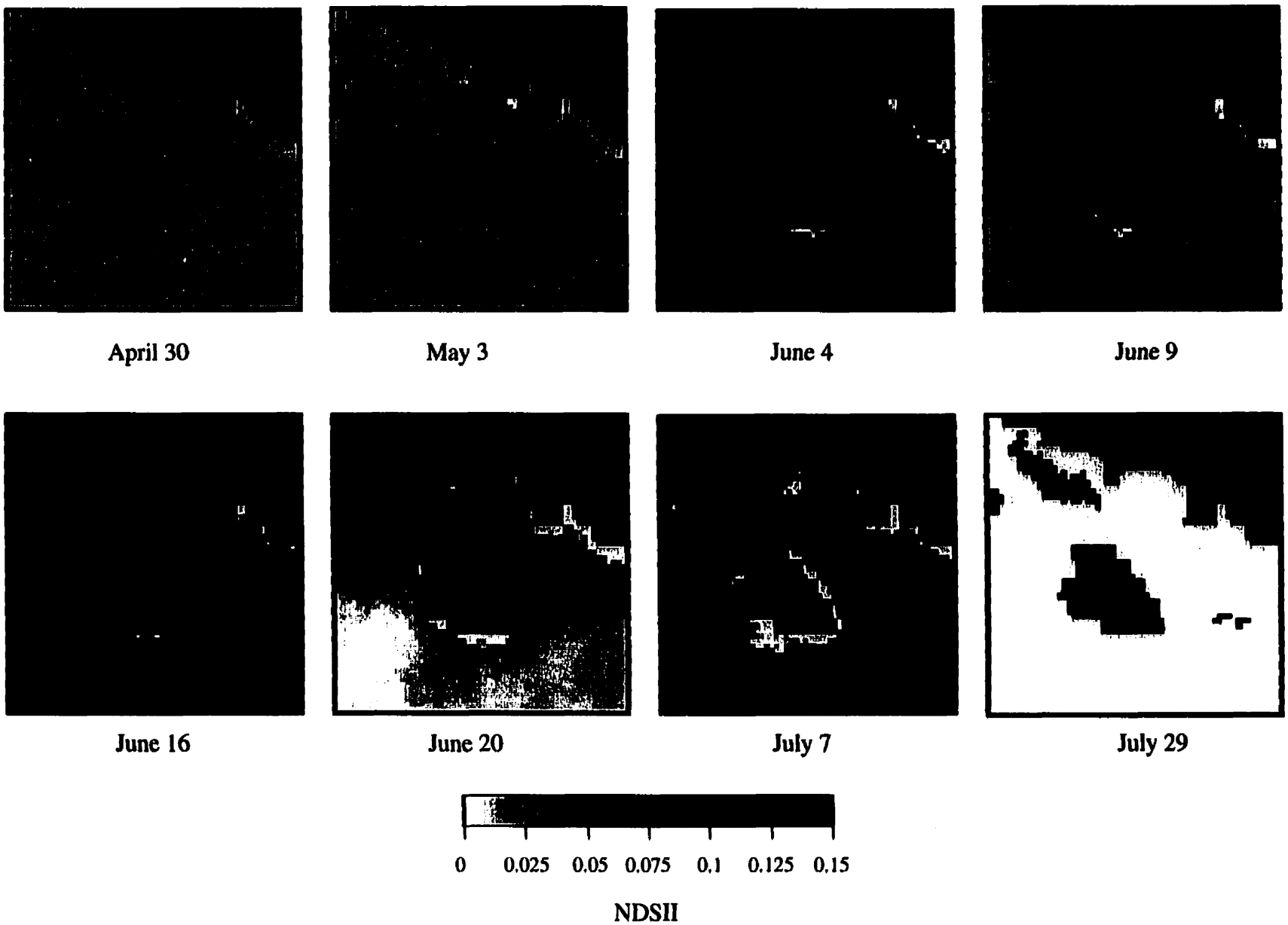


Figure 5.16 Seasonal change in Normalized Difference Sea ice Index (NDSII)

In Chapter 3, differences in the visible albedo of snow-covered sea ice were attributed to depth of the snowcover, i.e. finite or semi-infinite, and the presence of impurities. Both of these factors decrease visible albedo, but have little effect on the infrared albedo. Since the influence of impurities was unlikely to manifest itself consistently over such a large spatial area, the difference in the index values on April 30 is attributed to the finite snow volume in the late consolidation zone. Using the modelled spectral albedo data shown in Figure 3.2(b), the corresponding NDSII values were calculated based on irradiance conditions on April 30. The sensitivity of NDSII on snow depth is shown in Table 5.3. As the volume becomes more finite, i.e. snow depth decreases, the NDSII decreases due to the decrease in visible albedo. In the early consolidation zone, the snow volumes were expected to be semi-infinite. In the late consolidation zone, the snow volume was finite, allowing the underlying ice surface to reduce the volume albedo. As demonstrated in Table 5.3, this difference would manifest itself in a slightly higher NDSII values in the early zone. The differences found between the indices of the two consolidation zones on April 30 was likely caused by snow depth. Although present, this pattern is not as apparent in the May 3 NDSII image.

Table 5.3 Dependence of NDSII on snow depth. NDSII data emulated from modelled data in figure 3.2(b).

Snow Depth	Semi-infinite	40 cm	20 cm	10 cm	5 cm
Visible Albedo	0.93	0.93	0.92	0.89	0.85
Infrared Albedo	0.80	0.80	0.80	0.79	0.77
NDSII	0.072	0.071	0.066	0.056	0.047

5.6.1.2 NDSII - June 4,9,16,20

The NSDII images in Figure 5.16 capture the evolution of the sea ice volume from the Wet Snow stage to the Melt Pond stage. Since wet, decaying snow volumes have greater contrast between visible and infrared albedos, the higher values in the June 4 and June 9 imagery likely map areas of wet snow. These areas are found predominantly in the passage. The rapid increase in NDSII value on June 16 and June 20 signals the arrival and intensifying of ponding in the passage. Of all of the sea ice surfaces, melt ponds are expected to display the highest NDSII due to the sharp wavelength dependence of the spectral albedo. As expected, the areas of ponding appears to be restricted to the early consolidation zone. The reason behind the increase in NDSII in the late consolidation area on June 20 is not apparent. The NDSII suggests cloud contamination. However, it is not clear why the distribution of the cloud follows the morphology of the ice surface so closely. Also, coincidental surface observations and examination of the AVHRR thermal channels do not indicate the presence of clouds. It is possible that the noise (error) in one or both of the derived albedos could be responsible for the questionable values. Although further validation is warranted, NDSII appears capable of mapping the progression of melt over sea ice.

5.6.1.3 NDSII - July 7,29

The July 7 NDSII image shows a decrease in NDSII in Resolute Passage. This decrease in the contrast between visible and infrared albedo also suggests that surface water in the early consolidation zone decreased due to drainage. The breakup of the late consolidation zone resulted in only slight changes in the index from June 16. The variability of the index, however, suggests a change in the ice volume. Open water areas appear as white on the image. Finally, the disappearance of the ice cover results in an NDSII of near zero since there is very contrast between the visible and infrared albedo of water. This may prove useful for mapping large areas of open water.

5.6.2 Summary

The seasonal changes in the spectral dependency of sea ice albedo allow for the mapping of the state of the sea ice volume using visible and infrared albedo data. The NDSII proved to be an easily implemented measure capable of exploiting some of these differences. With scene identification, the index can be used to monitor the evolution of the ice surface. However, since different ice states can have the same NDSII, the index is not optimal. At a cost to implementation, a more complex index employing a thresholding scheme would likely result in improved results and less reliance on scene identification. Also more recent techniques like spectral mixture analysis (Shimabukuro and Smith, 1991) may be useful to those interested in mapping the state of the ice volume using multispectral data.

5.7 Summary of Findings

The AVHRR-derived albedo data revealed important time-space characteristics of visible and infrared albedo that were not detected through traditional *in situ* sampling. The following will summarize these findings in the context of the following seasonal categories: *Winter/Onset of Melt*, *Advanced Melt* and *Breakup/Dispersal*. Also, recommendations are provided when appropriate.

5.7.1 Winter/Onset of Melt

The Winter/Onset of Melt period coincides with the Dry and Wet Snow period described in Chapter 3. It was characterized by sub-zero air temperatures and the presence of an overlying snow volume on much of the ice surface. The following was observed:

Visible and infrared albedo was high and invariable across the icescape

The AVHRR observations confirmed what was casually observed at the surface site. In the winter and onset of melt conditions, the albedo of sea ice is high and compared to later

periods, relatively invariable in time and in space. PCA indicated that these early dates contributed minimally to the overall seasonal variance. The lack of variation in this part of the season make it least sensitive to the simple prescription of surface albedos.

Sea ice snow volumes are impure in study region

The visible albedo of sea ice in the winter season suggest that the snowcovers were impure. Pure snowcovers have visible albedos approaching 0.98. The source of impurities range from crustal material from nearby land masses and advected graphitic carbon (soot) particles scavenged out of the atmosphere. This soot may be from haze events or from nearby air traffic. The prescribed visible albedo value of Ebert and Curry's parameterization appears too high for winter archipelago snow-covered sea ice due to its assumption of a snowcover free of impurities. The increased absorption in an impure snowpack is estimated to be 5-10% higher than a pure snowpack (Clarke and Noone, 1985). Thus impurities represent a perturbation to the ice volume energy's balance and have the potential to increase ablation. Also, unlike snow grains, impurities do not melt and run off. Thus as the snow volume ablates, the influence of the impurities may increase (Barrie, 1986). Sensitivity studies have shown that small changes in sea ice albedo may have considerable effects on the evolution of the ice volume. Shine and Sellers (1985) showed that decreasing the allwave albedo of dry snow from 0.8 to 0.75 decreased the modelled ice thickness by over a metre and moved up the date of snow melt and the appearance of bare ice by one week.

Recommendation: Snow on sea ice in the Canadian Archipelago is not pure and any attempt to parameterize visible sea ice albedo should account for the consequent decreased reflectance. Increased observations of snow pack impurities (radiative characteristics, mixing ratios) in arctic snow volumes are required.

Infrared albedo decreased more than visible albedo with the onset of melt conditions

As conditions changed from winter (end of April) to the onset of melt (end of May), the metamorphism of the icescape's snowcover resulted in larger decreases in infrared albedo

(18%) than visible albedo (9%). Since infrared albedo is more sensitive to the changing structure of the snow volume, this difference is logical and agrees with surface spectral albedo observations made in this study. This finding has implications for the CCC2 parameterization of snow which assumes that the visible and infrared albedo of snow decrease identically with snow age.

Recommendation: Ideally, climate models should employ a physically-based snow albedo model capable of reflecting the evolution of visible and infrared snow albedo. Realistically, today's GCMs cannot accommodate such models. However, the simpler parameterizations that they do use should consider the different rates of seasonal decrease for these two broadband albedos.

Spatial variability in visible sea ice albedo is caused by snow depth variability

On April 30, visible albedo in the early consolidation zone was slightly higher (0.02) than that measured in the late consolidation zone. Since there was no difference in infrared albedo between the zones, this distribution of albedo was dependent on the thickness of the snowcover. In the late consolidation zone, the significantly thinner snowcover resulted in the underlying darker ice to slightly lower the visible albedo. This microphysical difference resulted in a larger scale albedo pattern that essentially bisected the image along the consolidation boundary.

Recommendations: In order to accurately simulate and predict the spatial variability of albedo, models will have to incorporate realistic distributions of snow on sea ice. Towards this, models will have to properly model ice freeze-up, solid precipitation, eolian transport of snow and ice kinematics that control surface roughness. To aid in this, observational studies must focus on large-scale distributions of snowcover. Of specific interest should be the distribution of grain sizes and snow depths, and those factors responsible for snow distribution over sea ice.

Spatial variability in sea ice albedo is caused by distribution of rough ice areas

Due to their complex structures, a myriad of factors interact to control the evolution of surface albedo in rough ice and ridged areas. This complexity belies any simple parameterization regarding the seasonal evolution of albedo in ridged areas. Although ridged and rubble ice accounts for a large proportion of the ice surface in the arctic, there is little, if any, information regarding the evolution of surface albedo in these structures. This dearth of information may be a product of the logistical difficulties involved in making radiometric measurements over ridged ice. The satellite data examined here did reveal small differences in surface albedo occurring over large spatial scales. Most obvious was the lower visible and infrared albedo found in areas of ridged and rubble ice. These rough ice areas had albedos typically 0.03-0.04 lower than smooth ice areas. The source of this difference is thought to be due both to the presence of bare ice and the effects of shadowing in the ridge structures. If shadowing was the primary source of the lower albedo, the albedo difference is a function of viewing geometry and thus is not physically meaningful. Due to the high solar zenith angles in polar regions, shadowing is a significant factor for albedo monitoring near land masses and in very rough ice areas. Since the low-albedo structures were found in various orientations across the scene, bidirectional characteristics of these rough surfaces were not thought to be responsible for the contrast with the surrounding smooth ice areas.

Recommendations: The seasonal albedo of very rough and ridged ice area requires more observation. Of specific interest is the identification of those factors that control the seasonal evolution of albedo in these rough ice areas. Studies should incorporate active radar data (SAR) which appear to be sensitive to ice structure before the onset of melt conditions.

5.7.2 Advanced Melt

Daily mean air temperatures at the FYI site reached 0° C on June 8. After that date, the average daily temperature stayed above zero causing rapid ablation of snow volumes and exposed bare ice surfaces. Over sea ice, the arrival of the Advanced Melt period is usually characterized by the appearance of surface melt features. In 1993, the appearance of surface melt ponds increased both the small and large-scale spatial variability of sea ice albedo. The satellite data revealed the following:

The development of melt ponds dramatically increases the spatial variability of sea ice albedo

PCA indicated that the largest source of seasonal variation in visible and infrared albedo was the distribution of melt ponds over the AVHRR scene. From June 9 to June 20, the variability of visible albedo nearly doubled increasing from σ=0.05 to σ=0.09. At the height of melt, melt ponds can cover 60-80% of the surface of first-year ice. The high variability in the albedo of the early consolidation zone on June 16 and June 20 indicates a variety of concentrations of surface states within an AVHRR pixel. The moment of largest albedo variability coincides with the onset of ponding when the surface is a mixture of bare ice, wet snow and melt ponds (June 16). As the melt ponds begin to dominate the icescape and the proportion of bare ice and snow diminishes, the spatial variability in the ponded area begins to decrease (June 20). These low-albedo melt features control the ablation of the sea ice cover and thus can be a significant factor in the areal extent and thickness distribution of sea ice in the arctic.

In near shore areas, surface albedo was inversely proportional to distance from land.

The AVHRR data revealed a distinct lowering of albedo in near shore sea ice areas. The effect was most apparent off the south-facing shore of Cornwallis Is. and after the snow disappeared on the land. PCA identified this shore effect as a major component in the seasonal variability of sea ice albedo distribution over the study scene. Surface and

satellite observations indicate that melt ponds formed first in near-shore areas. The reason for the reduced albedo (and increased melting) in these zones was the warming and contaminating effects of the snow-free land. Onset of melt conditions is expected earlier in these areas. This process suggests that, after the onset of melt, the distribution of sea ice albedo in the Archipelago is somewhat determined by the influence of nearby land masses. Langleben's (1966) measurements in the arctic indicate that the warming effect of land in coastal regions can account for as much as 25% of the net energy gain at the surface.

Recommendation: Observational studies should take into consideration this near-shore bias in albedo during the collection and interpretation of data. The influence of near-shore topography on this effect should be assessed, i.e. is the warming effect more prominent opposite south-facing high elevation shore areas ?

Large-scale distribution of albedo over the scene closely resembled the pattern of consolidation regimes.

The correlation between the distribution of albedo over the scene with the location of the early and late consolidation regime was the most surprising finding of the satellite study. With the onset of ponding, these two regimes began to contrast in terms of surface albedo. During advanced ponding, the visible and infrared albedo was 0.15-0.16 lower in the early consolidation zone than in the late zone. PCA identified this pattern as a major contributor the seasonal spatial variance in sea ice albedo over this scene. The difference was attributed to the lack of ponding in the late consolidation zone. Since ablation of the overlying snow volume is the major cause of surface ponding on sea ice, the reason for the low ponding in this ice regime was attributed to significantly lower snow volumes. Shallow snow volumes may be a characteristic of this late consolidation ice regime. Limited surface observations and the age, structure of the ice in this zone support this hypothesis. This finding further highlights the importance of snow distribution in determining sea ice albedo patterns.

Recommendations: The applicability of these findings to other ice areas in the Archipelago and other seasonal ice zones (Baffin Bay) should be assessed. The relationship between snow depth and ponding characteristics must be clarified.

The seasonal decrease in multiyear ice albedo is not in phase with first-year sea ice during advanced melt conditions

While the albedo of multiyear ice undergoes a seasonal decrease similar to that of first-year ice, the AVHRR data revealed that the physical differences between the two ice types become significant in terms of their late season albedo signals. PCA indicated that these signals begin to diverge with advanced melt conditions. Specifically, in this period, the albedo of multiyear ice decreased at a slower rate than that of the surrounding first-year ice. In the Winter/Onset of Melt period, the albedo of multiyear ice is similar to that of first-year ice. Albedo differences between the two ice types at this time of year can be attributed to the condition of the surface layers of the hummocks -- which can range from snow-covered ice to bare, blue ice. The spring ablation of the snow volumes on both ice types results in surface melt ponds. As the season progresses, melt ponds on first-year ice expand laterally across the icescape unchecked by physical boundaries. Conversely, on multiyear ice, melt pond widening is limited by the surrounding hummocks. Instead, multiyear ice melt ponds deepen with time. This effectively preserves the melt pond to hummock ratio which essentially defines the areal albedo of the floe. As a result, during advanced melt conditions, a multiyear floe often has a higher albedo than that of the surrounding first-year ice matrix. The increased ponding on first-year ice is a major factor in the annual ablation of the seasonal ice cover.

Recommendations: Surface albedo parameterizations should incorporate the difference in ponding fraction maximums between first-year and multiyear ice types. Also, since the ponding on multiyear ice is somewhat dependent on the hummock to melt pond ratio, and since this ratio is dependent on ice age, the possibility that ponding fraction maximums

may vary between multiyear ice of different ages should be explored. Overall, a more hydrologic approach to understanding melt pond evolution over major ice types is needed.

5.7.3 Breakup / Dispersal

The July 7 and 29 AVHRR data described the distribution of surface albedo during the breakup and dispersal of ice in the study region. As the icescape began to break up, the number of surface ice types increased to include open water and brash ice. The two image dates revealed the following:

The distribution of surface albedo follows the *deconsolidation* pattern

One of the largest changes in surface albedo occurs when the ice surface is replaced by open water. The July 7 image indicates that the appearance of open water and subsequent lowering of surface albedo was restricted to the late consolidation area. This is logical since the breakup of the icescape almost mirrors the consolidation pattern in this ice regime (Gorman, 1988). The general pattern of sea ice albedo was again dictated by the consolidation zones. However, unlike the earlier period, the late consolidation zone had a lower albedo. Of interest is the fact that although the early consolidation area had a significantly lower albedo over the melt season and subsequently absorbed more incident radiation, breakup occurred first in the higher albedo, late consolidation area. In this case, the thinness of the ice in this zone and the strong sub-ice current was the critical factor in determining the breakup of the icescape.

Recommendations: In order to properly simulate the decay of the spring/summer sea ice cover, sea ice models will require not only treatment of volume thermodynamics, but also some treatment of ice kinematics and ocean dynamics.

The divergence and convergence of ice can cause significant fluctuations in surface albedo over very short temporal periods.

The movement of unconsolidated ice in the late consolidation zone resulted in fluctuations in surface albedo as the fraction of open water varies. This variability is dependent on wind, current action and the consolidation characteristics of surrounding ice. Important is the fact that advected ice can cause surface albedo to actually increase in this late stage. Since they cannot properly incorporate these dynamics, one dimensional sea ice models may not be able to simulate the effects of ice convergence and divergence on surface albedo. However, increases in the areal fraction of open water may overwhelm changes due to the thermodynamics of the ice volume.

Recommendations: See above.

The visible albedo of sea ice is more variable than infrared albedo during ice breakup

The visible albedo of sea ice varies widely during the breakup of the icescape. This is in response to the wide variety of ice surfaces during this period. Albedo values ranged from 0, denoting open water, to 0.6, indicating the presence of wet snow and/or bare ice. PCA identified breakup conditions as a major source of seasonal variance in visible albedo. In contrast, infrared albedo was found to be less sensitive to the distribution of breakup ice types. Since all of these ice surfaces essentially have wet surfaces, the penetration depth of incident infrared radiation is quite shallow. Thus, the infrared albedo is less sensitive to the distribution of these ice surfaces.

Melt water drainage results in increases in surface albedo

TM and AVHRR data indicated that widespread drainage took place in the early consolidation zone before July 7. This rarely sampled event was triggered by the appearance of large open water cracks in the adjacent late consolidation zone and within the large consolidation ridge. The seasonal decrease of sea ice albedo can be temporarily stalled or reversed with the drainage of first-year ice volumes. This has implications for

simple temperature-dependent sea ice albedo parameterizations. Infrared sea ice albedo appears to be more sensitive to ice drainage due to its sensitivity to the proportion of surface water. Drainage events may also increase the amount of freshwater under the ice, thus decreasing the upward transport of heat into the ice (Maykut and Perovich, 1987) and thus slow ablation.

Recommendation: Sea ice albedo parameterizations should include effects of drainage on surface albedo. An accurate treatment would likely require the incorporation of a snow hydrologic model. However, these changes will require more observations of this late season process over both first-year and multiyear sea ice.

Finally, a point unrelated to a specific period:

SAR imagery greatly assisted in the interpretation of spatial variability of sea ice albedo.

Given the reliance of surface albedo on the physical characteristics of the sea ice surface, the ability of winter/early spring SAR imagery to delineate consolidation boundaries and smooth/rough ice areas was a great aid in the interpretation of albedo patterns. Work is currently underway to link SAR backscatter to surface albedo through proxy indicators and direct electromagnetic modelling (Barber, 1991).

Recommendation: The strong resemblance between albedo and SAR backscatter patterns observed in this study encourages this direction of inquiry. Statistical analysis between backscatter level and surface albedo within this study area should and will be performed. Of specific interest is the seasonal limitations of any significant relationship.

5.8 Conclusions

The main purpose behind the incorporation of AVHRR data was to expand both spatially and temporally on the albedo observations performed at the surface study sites. It is impossible to capture the full temporal and spatial dimensions of surface albedo through surface sampling. The satellite-derived albedo dataset allowed for the identification and interpretation of the large-scale temporal and spatial variability in sea ice visible and infrared albedo. As expected, the multitemporal AVHRR albedo dataset revealed relationships between the ice volume and albedo that were not discovered through *in situ* observation. PCA consolidated the seasonal albedo variance into interpretable components that allowed the identification of the major time-space relationships of sea ice albedo during the spring/summer melt season. The component images assisted in the interpretation of the environmental factors controlling the large and small scale seasonal variability in sea ice visible and infrared albedo.

Analysis of the AVHRR albedo data indicate that, during spring melt, the spatial and temporal variability of sea ice albedo is considerable over the small regional area examined here. The seasonal evolution of sea ice albedo, contrary to common parameterizations in GCMs, is not a simple function of surface temperature and defies prescription. Instead, it is evident that regional scale variability in sea ice albedo is also controlled by the state of the sea ice volume and its overlying snow volume, ice kinematics, atmospheric dynamics and local physiography. These complex interactions belie the use of simple prescriptions of sea ice albedos in large-scale climate models. Results of the AVHRR analysis illuminate the need for realistic, physically-based sea ice albedo parameterizations in order to properly simulate the decay of the sea ice volume.

6 CONCLUSIONS

Given the rudimentary representation of sea ice albedo in today's climate models, it is questionable whether these simulations properly capture the evolution of albedo over seasonal and regional scales. In view of sea ice albedo's leverage in controlling the amount of energy entering the volume, this possible deficiency has significant implications for the proper simulation of the growth and decay of the icescape. As such, there exist two immediate needs:

(1) assess whether current parameterizations can properly simulate the spatial and temporal characteristics of sea ice albedo, and if required,
(2) develop more realistic (physically-based) parameterizations of sea ice albedo.

Critical to both tasks is the ability to systematically observe the seasonal evolution of sea ice albedo, especially during the dynamic spring melt period. Traditionally, surface observation programs have been the medium for sea ice albedo information. Clearly, given the expanse of the polar basins and the wide variability in sea ice albedo shown in this study, the albedo data derived from surface programs are limited due to the inherently conservative spatial and temporal constructs of the sampling. As a result, many have espoused the potential of satellites to provide surface information at scales suitable for climate studies. Unfortunately, few studies have demonstrated the use of these platforms for monitoring climate variables in polar regions.

This thesis has demonstrated the utility of AVHRR satellite data in mapping the variability of clear sky visible and infrared albedo. The value of this expanding image archive has been recognized and efforts are underway to maximize its usefulness to the polar climate community. The AVHRR albedo data collected for this investigation provided a unique opportunity to map the spring evolution of albedo in a seasonal sea ice zone over a large area. While the insights provided by the satellite data highlighted the advantages of orbital observation over *in situ* sampling, the relationship between the satellite data and surface observations were shown here to be clearly symbiotic. For the first time, coincidental surface observations were available to aid in the derivation and interpretation of the satellite-derived albedo patterns. Furthermore, *in situ* albedo measurements were utilized to assess the accuracy of the derived albedos in polar regions. Understandably, this type of validation, although critical in satellite climate studies, is rare in the polar scientific community.

While the uncertainty in the inversion methodology utilized in this study has been shown to be large, the advent of future sensors will improve the utilization of archived and operational AVHRR data for mapping surface albedo. Until then, incorporation of surface albedo values derived via this approach (e.g. Polar Pathfinder Program) should be performed with the conclusions of Chapter 4 in mind. Two major caveats stand out in terms of their influence on an estimated albedo product.

This study, as well as others, has shown that the pre-launch calibration of AVHRR 1 and 2 severely deteriorates with time and, consequently, its application will result in a large underestimation in visible and especially infrared albedo. In light of this, the Polar Pathfinder program will only utilize those satellites where calibration updates are available (i.e. NOAA 9, 11). Efforts to update NOAA 10 and 12 AVHRR 1 and 2 calibrations should be made. This would significantly increase the amount of data available and greatly improve the opportunity for clear sky imagery. The updated calibration coefficients derived in this study are a first step towards achieving this.

The other major caveat is the incorporation of Taylor and Stowe's anisotropic reflectance factors for the correction of the viewing effects of the sensor. The published variances of these factors imply that they have limited precision for climate studies. It is unknown whether the variation in the factors are an inherent function of the seasonal icescape, the overlying atmosphere, a function of error (e.g. cloud contamination, scene misidentification), or more likely, some combination of these factors. Further investigation into the anisotropy of sea ice surfaces and overlying atmospheres is thus required to accurately correct for this viewing effect. Also, the dependence of scene anisotropy on sensor resolution and frequency should be examined. In the meantime, possible steps to reduce this effect (e.g. data averaging) should be considered .

Due to the wide possible range of ice surface ARFs, it is anticipated that some type of geotyping will be required before the anisotropy of the surface is properly corrected for. This is especially true for imagery collected during spring melt conditions. Scene identification can be assisted by AVHRR data thresholding and/or complementary information provided by coincidental microwave imagery. In this study, surface observations allowed for the discrimination of surface types and application of the appropriate scene model. Research priority should be given to developing mixed ARFs characteristic of heterogeneous advanced melt surfaces.

In situ and satellite observations examined in this thesis assisted in the identification of those environmental factors responsible for the regional and seasonal scale variability in sea ice albedo. During spring melt, the spatial and temporal variability of sea ice albedo is considerable over the small regional area examined here. The seasonal evolution of sea ice albedo, contrary to some parameterizations in GCMs, does not appear to be a simple function of surface temperature. Instead, this study revealed that the variability in sea ice albedo is also controlled by the physical state of the sea ice volume and its overlying snow volume, ice kinematics, and local physiography. As such, sea ice albedo is sensitive to the variability of these other AIO components. This suggests that a simple, non-physical, representation of sea ice albedo cannot capture this spatial and temporal variability.

The findings of this study as they pertain to the variability of clear-sky sea ice albedo are summarized here with the aid of feedback diagrams[29]. By assuming a closed system, these diagrams assist in illustrating and describing the apparent relationships between those components that together control the variability of sea ice albedo within the seasonal ice regime examined in this study. In order to improve clarity, a separate diagram is presented for the Winter/Onset of Melt and Advanced Melt/Breakup periods. The former period is defined by the absence of melt ponds. The latter period begins with the appearance of melt ponds. Diagrams such as these should not be considered inclusive. Further study should attempt to clarify the components of these diagrams and most importantly, provide means whereby their interactions (links) can be accurately quantified. Here they are utilized as a medium to identify those variables and environmental processes found to interact with surface albedo and subsequently control the variability observed within this study. Since this study concentrated on a seasonal ice regime, these findings, while applicable in some cases to multiyear ice volumes, are most pertinent to first-year sea ice.

6.1 Winter/Onset of Melt

6.1.1 Visible Albedo

Figures 6.1 and 6.2 contain the feedback diagrams for the visible and infrared early melt visible and infrared albedo respectively. In this early period, variability in visible albedo was low (σ=0.01-0.02) and dependent on the visible fraction of lower albedo bare sea ice. The central loop in figure 6.1 indicates that the distribution of snow essentially controls the visible albedo during the Winter/Onset of Melt period. This suggests that the ability to simulate snow distribution or *patchiness* is required to properly estimate a region's or model grid's surface albedo and consequently, its surface energy balance. In the winter, the distribution of snow is primarily controlled by three factors.

[29] The concept of a feedback diagram was explained in Section 2.2.2.2.

Figure 6.1 Winter/Onset of Melt visible albedo feedback.

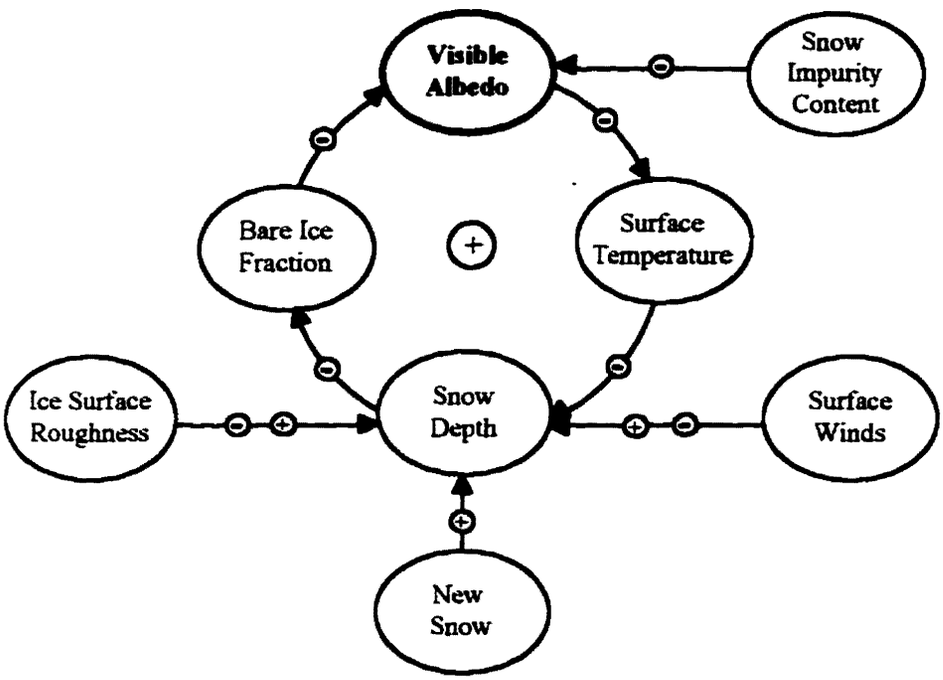
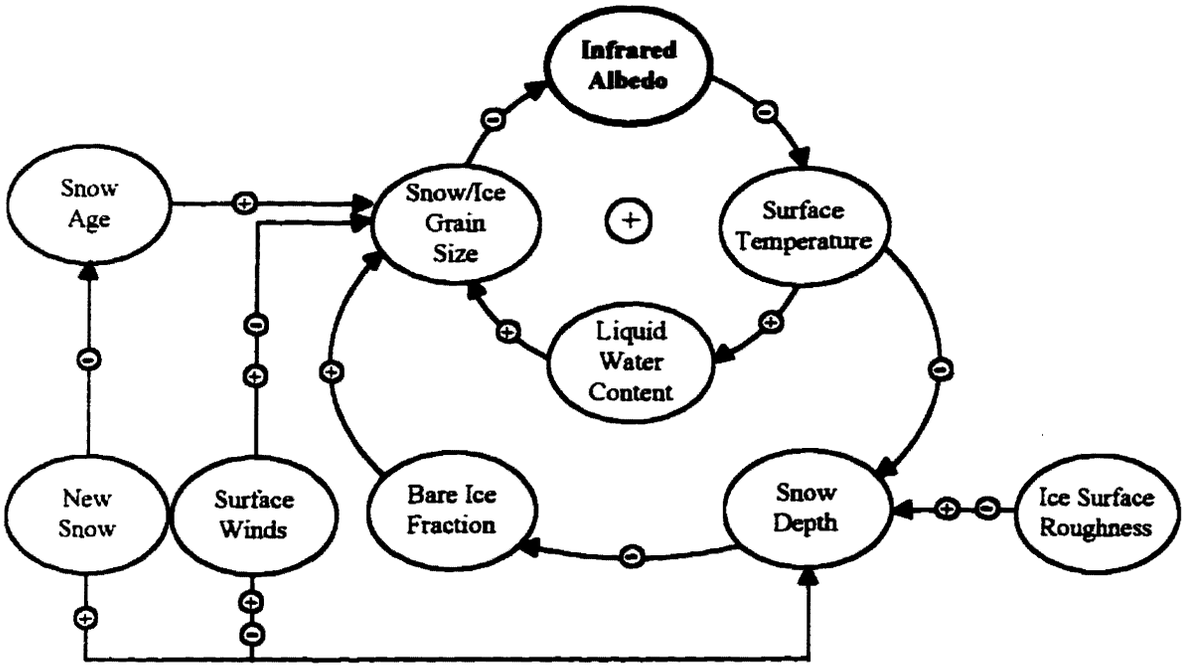


Figure 6.2 Winter/Onset of Melt infrared albedo feedback



First, ice surface roughness can encourage or discourage the accumulation of snow. During the early melt stages, satellite data in this study indicated that ridged ice areas have lower albedos relative to surrounding flat ice areas. This was speculated to be a result of an increased presence of lower albedo bare ice pieces. However, surface observations have shown that these same rough ice areas can also encourage the accumulation of snow, thus leading to a higher albedo. The albedo of rough ice areas is clearly complex and requires further study.

Second, new snow increases snow depth and reduces the influence of the covered ice surface on surface albedo. Fresh snow thus increases visible albedo. When in abundance, new snow can slow and/or delay spring melt. Above average spring snowfall in SIMMS '92 is believed partly responsible for the delay in ice melt and breakup in that year. The third factor influencing snow depth is surface winds. Seasonal snow volumes are continually being redistributed by wind. This is especially true for new spring snow. Depending on catchment conditions, some areas increase in snow depth, while others decrease. This variability in snow depths can manifest in visible albedo variability as shallower snow volumes alternate between finite and semi-infinite states. The climatic implications of such variability, though likely insignificant, are unknown. However, this variability does influence the surface energy balance over short time scales.

Surface observations indicate that the visible albedo remained relatively high (α_{vis}=0.89) until the first week of June. Both surface and satellite observations indicate that as spring temperatures approached zero degrees, snow depth decreased through melt. If the ablation was significant, the underlying lower albedo ice surface would decrease the volume's overall albedo. This in turn would encourage increased surface temperatures and further volume ablation. As indicated by the central loop in Figure 6.1, this albedo-temperature feedback is positive, i.e. self-enforcing.

Finally, the effects of snow impurities on sea ice visible albedo have been observed and modelled. The two primary sources of impurities in arctic snow volumes are airborne

carbon-based pollutants (soot) and crustal material advected from nearby terrestrial surfaces. These pollutants increase absorption in the volume at short wavelengths resulting in a decrease in visible albedo. In winter conditions, snow on nearby land features in the archipelago for the most part prevented the advection of crustal material onto the nearby sea ice. However, surface observations indicated that, with the removal of the snow from the land, coastal sea ice areas were quickly contaminated by eolian material. As a result, sea ice areas close to land were found to have lower visible albedos which contributed to the regional variability in visible albedo. While thought to be important to the ablation of the underlying ice volume, the effect of biological contamination was not examined in this study.

6.1.2 Infrared Albedo

In the early melt season, the variability in infrared albedo (σ=0.01-0.02) is controlled primarily through the physical characteristics of the surface layer of the sea ice volume. Specifically, the size of the snow and/or ice grain in this layer controls the amount of infrared absorption. Larger grains increase the opportunity for absorption and thus decrease the overall surface albedo. In cold winter temperatures, as with visible albedo, variability in infrared albedo over large areas is controlled by the bare ice fraction. As a result, April and May visible and infrared albedo maps revealed similar patterns of albedo. As Figure 6.2 indicates, the distribution of snow controls the fraction of bare ice during cold conditions. The amount of snow is controlled by new snow deposition, surface winds and ice surface roughness. These factors were discussed previously in section 6.1.1.

In terms of snow-covered ice volumes, the infrared albedo is sensitive to the average grain size of the surface layer. A change in snow grain size in this layer will result in a change in infrared albedo. After deposition, snow grains change shape and tend to increase in size through metamorphism. In Figure 6.2, this process is accounted by a snow age factor. Since this critical layer is most exposed to the environmental elements, infrared albedo exhibited more short term variability than visible albedo over semi-infinite snow volumes.

As a result, infrared albedo may serve as an indicator of the onset of melt over sea ice. This has the potential to be used to assess interannual changes in the timing of this event and relatedly, provide information for assessing potential climate change in polar regions.

New snow has the potential to increase the infrared albedo in two ways. As discussed in the previous section, it can reduce the fraction of bare ice by increasing snow depth. Secondly, new snow can reduce the snow age factor and thus reduce the grain size of the volume's surface layer substantially. Also, surface winds continually redistribute this loose, transient surface layer. Assuming larger grains settle first within a volume, surface winds can cause smaller snow grains to displace larger surface grains at the surface resulting in an increase in surface albedo. Albeit, these increases are minor in light of the much larger seasonal decrease in infrared albedo.

The interior of the feedback loop in Figure 6.2 suggests that a positive feedback exists between infrared albedo and surface temperature during the onset of melt conditions. With the onset of melt conditions, surface observations indicated that warmer temperatures doubled the amount of liquid water in the snow volume. An increase in liquid water effectively increased the snow grain size resulting in a decrease in infrared albedo. This contributed to the rise in surface temperature and likely to further ablation of the volume. Until the total ablation of the snowcover, this feedback appears to be the primary mechanism behind the seasonal decrease in infrared albedo.

6.2 Advanced Melt/Breakup

PCA analysis indicated that most of the seasonal albedo variability occurred during the advanced melt period when the high-albedo icescape was punctuated with low-albedo melt ponds. This period was characterized by the rapid ablation of both the snowcover and underlying ice volume caused by the dramatic increase in the amount of solar radiation

absorbed within the ice volume. The subsequent breakup of the icescape and the appearance of leads and cracks further increased the regional variability in surface albedo.

With the appearance of melt ponds, both the visible and infrared albedo over the study scene decreased dramatically in the advanced melt period (α_{vis}=0.83→ 0.64, α_{ir} =0.51→0.35). During this period, positive ambient temperatures rapidly ablated the snow volume. The resultant melt water pooled on the sea ice forming a network of lower-albedo melt ponds. The fraction of the icescape occupied by melt ponds, or pond fraction, was a major control on the regional albedo. In Figure 6.3, pond depth is included with pond fraction for the visible albedo case. Observations of first year ice melt ponds made during SIMMS '94 indicated that clear sky visible albedo decreases steadily with pond depths up to 0.5 metres (Morassutti and LeDrew, 1995). After this critical depth, visible albedo was found to level out, no longer responsive to pond depth. The critical depth for near-infrared (0.4-0.7 μm) albedo appears to be 0.2 metres.

As shown in Figure 6.3 and 6.4, the positive feedback between surface temperature, pond fraction and albedo signifies a continual decrease in visible and infrared albedo during this period. Surface and satellite observations indicated that nearby land exercises some control over the evolution of sea ice albedo. In coastal areas, the land exerts a warming effect on the adjacent icescape. As a result, pond formation was more intense in near shore areas. Also, eolian material from nearby islands can be deposited in near shore melt ponds. These particles settle on the pond bottom or if fine enough, are suspended in the pond's water column. This contamination directly decreases the visible albedo through increased absorption.

The feedback diagrams for this period indicate that snow depth has both a positive and negative link to pond depth and fraction. The negative link is obvious. As the snow volume ablates, the melt water increases the pond fraction. However differences in ponding fractions between the early and late consolidation regimes suggested that ponding is most extensive in areas where large snow volumes existed. This explains the positive

Figure 6.3 Advanced Melt/Breakup visible albedo feedback

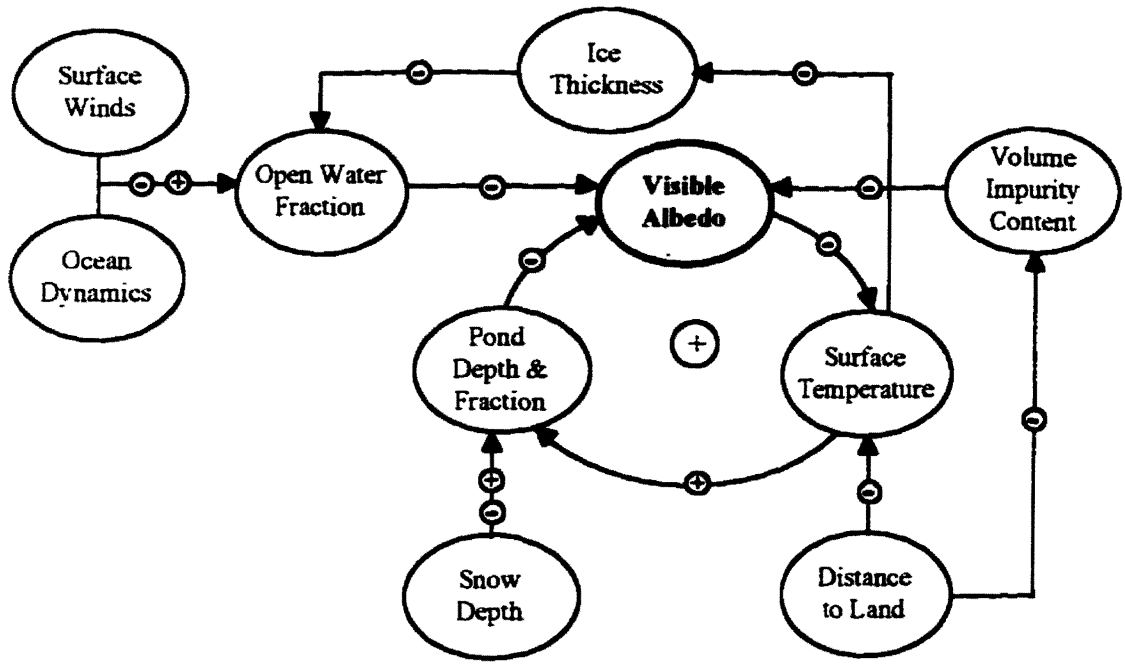
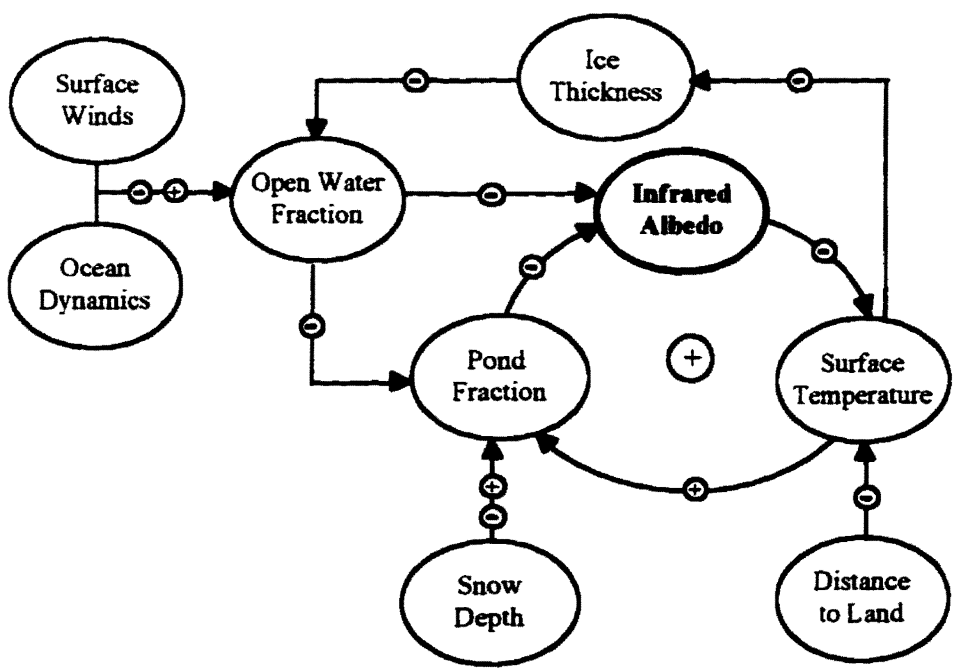


Figure 6.4 Advanced Melt/Breakup infrared albedo feedback



link between snow depth and pond fraction in Figure 6.3 and 6.4. This study showed that differences in snow depth was a likely factor in the difference in pond development found in the early and late consolidation ice regimes. Closer examination of the development of melt ponds within different ice regimes is warranted. The role of large roughness features, such as ridges, on the evolution of melt ponds is also not clear. While rough ice assists in the catchment of snow and thus may affect pond formation indirectly, its direct role in the hydrology of the icescape is uncertain. Surface observations seem to indicate that the first melt ponds are often found *hidden* amidst rough ice features.

During breakup, the divergence of the icescape resulted in an increase in low-albedo open water areas such as leads and cracks. The resultant decrease in albedo is directly proportional to the *open water fraction*. With the breakup of the late consolidation area, visible albedo decreased 0.1-0.3 albedo units. The breakup of the icescape is due to the weakening of the ice matrix instigated by ablation of the ice volume. Figure 6.3 indicates that warmer spring temperatures result in a decrease in ice thickness. Depending on the ice regime, this thinning may be enough to weaken the matrix and allow ice floes to separate along consolidation lines. The unconsolidated ice is then free to follow ocean currents and/or surface winds. Analysis of the TM imagery indicated that the ice cover also converges, likely in response to surface winds and/or ocean currents and tides. As shown in Figures 6.3 and 6.4, this ice movement can increase or decrease an area's albedo through increases and decreases in open water fraction. These results suggest that it is unlikely that a straight thermodynamic simulation of sea ice can accurately estimate sea ice albedo over a GCM grid element over short time periods. Thus, in order to capture these rapid seasonal fluctuations in sea ice albedo, a coupled ice-ocean model with ice and ocean dynamics is required.

An increase in open water fraction was shown to indirectly result in a short-term increase (+0.1) in the infrared albedo of adjacent ice areas (Figure 6.4). This appears to be due to a decrease in pond fraction by increased melt water drainage into nearby open water areas. In this case, an increase in lead fraction can lead to an increase in infrared albedo. Since

the visible albedo of melt ponds is more sensitive to the condition of the pond bottom and much less sensitive to the overlying water volume, the image data showed that drainage had a less clear effect on visible albedo. Important is the fact that the effect of the lead on regional albedo may be out of proportion with its area since only a small lead or crack has the potential to drain a large expanse of ice. This has implications for large scale climate models whereby small leads and cracks are at sub-resolution scale, but have potentially significant climatic impacts over larger regional scales.

Although the SIMMS experiment has concluded, sea ice albedo remains a principal focus within future polar projects such as the Collaborative Integrated Cryosphere Experiment (C-ICE) and Surface Heat Budget of the Arctic Ocean (SHEBA) experiment planned for autumn 1997. C-ICE plans to continue the themes of the original SIMMS experiments, focusing on sea ice in the Canadian Archipelago. Unlike SIMMS, SHEBA will attempt to sample throughout the entire year and will be located within the Arctic Basin. Polar scientists recognize the value in long-term, multicomponent observation programs such as SIMMS, C-ICE and SHEBA. In terms of future observations of sea ice albedo, pertinent recommendations have been made throughout this work. However, the following points deserve reiteration:

(1) The large scale regional variability in sea ice albedo identified in this investigation highlights the need for surface programs to take a more regional approach toward site selection and sampling. This is especially true in the Archipelago where several different consolidation regimes appear to invoke considerable influence in the seasonal evolution of albedo. This type of approach would complement the intensive volume observations and place them in proper spatial context. Experience in SIMMS has shown that simple albedo transects have difficulty in capturing the true spatial variability due to measurement error stemming from changing irradiance conditions and instrument setup inconsistencies. The SIMMS experiment proved the feasibility of using a tethered balloon as a platform for *instantaneous* ice observations over larger scales. The incorporation of an radiometric instrument payload on such a platform would permit a valuable "scaling up" of surface

albedo measurements. These data are invaluable for validating and interpreting coincidental satellite data.

(2) This study highlighted the importance of melt pond evolution in controlling both visible and infrared sea ice albedo in the study area. Surface observations suggest that the development and decay of these features is a complicated function of the local ice conditions and the partitionment of energy within the pond itself. These features should continue to be a major focus of surface programs. It is suggested here that more attention be given to the examination of the *hydrology* of the icescape, i.e., the sources of melt water (e.g. snow volumes), the spatial and temporal variations in the storage of melt water on the icescape, and the physical aspects of the icescape that regulate the transfer of water between reservoirs (ponds, ocean). A better understanding of these processes will assist in explaining the apparent difference in the late season evolution of albedo between first-year and multiyear ice surfaces observed on the surface and detected by the PCA in this investigation.

(3) In field studies, melt pond features are often the primary focus of late season sampling. Unfortunately, as was the case in this study, this results in little or no attention given to the albedo of snow/ice interstitial areas. Since these features cover at least 20% of the icescape, they deserve some consideration in albedo studies. The assumption that these areas possess an albedo identical to the snow covered ice surface that preceded ponding is incorrect. Like melt ponds, these interstitial areas also evolve through the late season. The seasonal albedo of interstitial ice areas, especially multiyear ice hummocks, require more attention in field studies.

(4) This study has expanded on the relatively short-term observations of sea ice albedo in the past by examining its evolution over the entire spring decay period. However, the evolution of sea ice albedo in the fall freeze-up period is not well known, and, given the fact that it encompasses much of the other half of the sunlit portion of the year, it deserves more attention. According to its ambitious temporal scope, the SHEBA experiment

promises to be an important step towards defining the freeze-up characteristics of sea ice albedo and those factors responsible for its variability. Of specific interest is the identification of the ranges of visible and infrared albedo of new ice types, e.g. grease, nilas, grey-white.

(5) In this study, some of the greatest changes in regional albedo was due to the convergence and divergence of ice during the breakup period. Albeit these are high frequency events, ice movement has the potential to increase or decrease an area's albedo dramatically. Relatedly, ice dynamics are responsible for the development of large scale roughness features on sea ice (e.g. ridges) that appear to possess complicated seasonal histories of sea ice albedo. These findings are a further impetus for improved incorporation of sea ice dynamics in large scale climate models. Also, future surface observations should attempt to examine the evolution of sea ice albedo in ridged ice areas and contrast this seasonal signal with that of smoother icescapes.

Even *in lieu* of new data, the SIMMS dataset still has considerable potential for further albedo study. For the most part, the dataset examined in this study represented only one year of observation in one small part of the Canadian Archipelago. The next logical step in this investigation is the expansion of both its spatial and temporal focus. Of specific interest is the further validation and/or improvement of the ice-albedo feedback diagrams presented previously. Given its regional and temporal scope, the SIMMS dataset can accommodate the following inquiries: Do the relationships suggested by the feedback diagrams produced here hold for other parts of the archipelago ? How applicable are these results, which essentially describe a seasonal first-year ice regime, to the Arctic Basin where multiyear ice dominates ? What is the interannual variability in surface albedo patterns in this region ? Can the incorporation of SAR imagery with AVHRR improve the identification and understanding of regional albedo ?

Over the last ten to fifteen years, the parameterization of sea ice albedo in large scale climate models has markedly improved. This betterment was ushered in by increased

observation and more realistic incorporations of sea ice growth and decay within these models. However, the inability of current simulations to reproduce important sea ice variability in polar regions suggests that the sea ice component of these models requires further improvement. By the close of this century, the Mission to Planet Earth Program promises more frequent remote sensing data at various resolutions and at various frequencies. The anticipated synergism between these new sensors and planned concurrent surface programs promises to further our understanding of important climatic variables such as sea ice albedo. These future developments can only lead to more realistic simulations of sea ice albedo, and in turn, more accurate predictions of future sea ice and climate conditions in the polar regions.

Appendix 1. Wiscombe and Warren Snow Model

The snow model of Wiscombe and Warren (1980) is used derive snow spectral albedo over the solar spectrum for a variety of snow grains sizes. The model considers a snowpack to consist of ice spheres who's scattering and absorption properties are dictated by Mie theory. The delta-Eddington approximation (Joseph *et al.*, 1976) , a scattering approximation considered appropriate for strongly forward scattering media (Warren, 1982), is used to simulate scattering within the snowpack.

The snow albedo model requires the following single scattering quantities: the snow volume's optical depth (τ_S), the snow grain's asymmetry factor (g) and single scattering albedo (w). The snow volume's optical depth is approximated by

$$\tau_S = \frac{3LEWQ_{ext}}{4r\eta_{ice}} \qquad [\text{A1-1}]$$

where L is the equivalent depth of liquid water in the snowpack (g cm^{-2}), r is the mean snow grain radius, η_{ice} is the density of ice (0.917 g cm^{-3}) and Q_{ext} is the dimensionless extinction efficiency. Here, a wavelength-independent value of 2 is taken for Q_{ext}. Although spectral values of Q_{ext} computed by Mie theory would provide slightly more realistic albedos (Grenfell and Warren, 1994), the value of 2 is acceptable for the large grain sizes examined here.

The asymmetry factor ranges from -1 to 1, where g=0 for isotropic scattering and g=1 for total forward scattering. The asymmetry factor of ice grains typically range from 0.88-1.0 over the solar spectrum. The following parameterization taken from Choudhury and Chang (1981) for semi-transparent ice spheres (refractive index=1.33) was used to calculate the spectral asymmetry factor (g_λ):

$$g_\lambda = 0.87\exp(-2k_\lambda r) + 0.97\left[1-\exp(-2k_\lambda r)\right] \qquad [\text{A1-2}]$$

where k_l is the spectral absorption coefficient of pure ice. The spectral absorption coefficient is equivalent to

$$k_\lambda = \frac{4\pi m_{im}}{\lambda} \qquad \text{[A1-3]}$$

where m_{im} is the imaginary part of the refractive index of pure ice. The m_{im} values used here are based on laboratory measurements by Grenfell and Perovich (1981) which are summarized in Warren (1984).

The single scattering albedo is also a dimensionless quantity describing the probability that a photon intercepted by an ice grain will be scattered rather than absorbed. A simple parameterization for single scattering albedo which accurately reproduces Mie results for large spheres is (Sagan and Pollack, 1967):

$$\omega = 0.5 + 0.5\exp(-1.67kr) \qquad \text{[A1-4]}$$

The delta-Eddington approximation requires the following transformations of the Mie variables:

$$g^* = \frac{g}{1+g} \qquad \text{[A1-5]}$$

$$\omega^* = \frac{(1-g^2)\omega}{1-g^2\omega} \qquad \text{[A1-6]}$$

$$\tau_S^* = (1-\omega g^2)\tau_S \qquad \text{[A1-7]}$$

Four models are considered here: finite and semi-infinite snowpacks under two illumination conditions -- direct and diffuse irradiation. The following models were taken directly from Wiscombe and Warren (1980).

Assuming a direct incident beam at zenith angle $q_z = \cos^{-1}u_0$ and a finite snowpack overlying a diffusively-reflecting surface of albedo A, the snowpack albedo (α_f) for the finite case is calculated as:

$$Q\alpha_f(\mu_0) = 2\left[P\left(1-\gamma+\omega^*b^*\right)+\omega^*\left(1+b^*\right)\frac{\gamma\xi\mu_0 - P}{1-\xi^2\mu_0^2}\right]$$
$$\times\exp\left(\frac{-\tau_S^*}{\mu_0}\right) - \omega^*b^*\left(Q^- - Q^-\right)+\omega^*\left(1+b^*\right) \qquad \text{[A1-8]}$$
$$\times\left(\frac{Q^-}{1+\xi\mu_0} - \frac{Q^-}{1-\xi\mu_0}\right)$$

where

$$a^* = 1-\omega^*g^*$$
$$b^* = g^*/a^*$$
$$\xi = \left[3a^*(1-\varpi^*)\right]^{1/2}$$
$$P = 2\xi/(3a^*)$$
$$\gamma = (1-A)/(1+A)$$
$$Q^{\pm} = (\gamma \pm P)\exp(\pm\xi\tau_S^*)$$
$$Q = (1+P)Q^- - (1-P)Q$$

Under direct beam irradiation, the spectral albedo of a semi-infinite snowpack (i.e. $\tau_S \rightarrow 0$) reduces to:

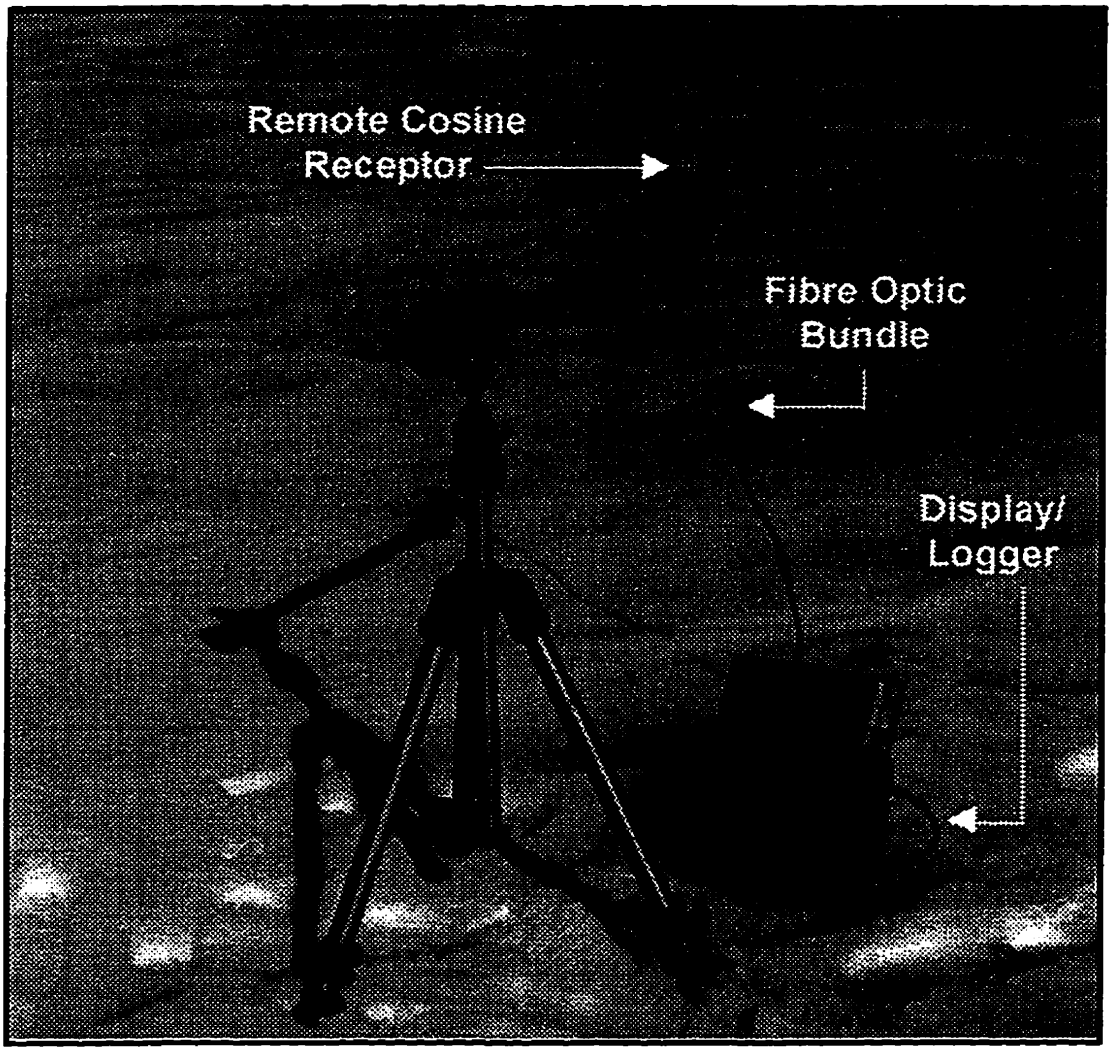
$$\alpha_\infty(u_0) = \frac{\omega^*}{1+P}\frac{1-b^*\xi\mu_0}{1+\xi\mu_0} \qquad \text{[A1-9]}$$

In the semi-infinite limit, the diffuse spectral albedo of a snowpack was calculated by

$$\alpha_\infty^d = \frac{2\omega^*}{1+P}\left\{\frac{1+b^*}{\xi^2}\left[\xi - \ln(1+\xi)\right] - \frac{b^*}{2}\right\} \qquad \text{[A1-10]}$$

In the finite case, the calculation of diffuse spectral albedo (a_f^d) can be time consuming due to the evaluation of exponential integrals. Wiscombe and Warren point out that the diffuse finite albedo is equivalent to the direct finite case under solar zenith angles of 46-53°. When required, the diffuse finite albedo was taken from the equivalent direct finite case.

Appendix 2. ASD Spectometer Setup



Note: Instrument position is typical of incident irradiance measurement

Appendix 3. Correcting Clear-Sky Spectral Albedo for Cosine Error

The accuracy of the cosine receptor was determined at the ISTS Optics Laboratory after returning from the field. The cosine receptor was set up identically to field use and was illuminated by a standard tungsten lamp source. The voltage of the lamp was monitored to ensure a constant supply of illumination. Care was taken to prevent stray light from contributing to the incident illumination. The RCR was mounted on a rotary stage and positioned normal to light source. The stage was then stepped in 5° increments to simulate changes in the illumination incident angles from 0-90°. Spectral irradiance (E_λ) measurements were collected at each step. Seckmeyer and Bernhard (1993) and Grenfell and Warren (1994) present virtually identical techniques for the correction of irradiance data collected by cosine receptors. The second method is used here. Deviation from a cosine response (ε_λ) was determined by comparing the measured response of the instrument at a particular incident angle ($S_\lambda(\theta)$) with the cosine response expected at that angle, $\cos(\theta)S_\lambda(0°)$. A fractional deviation of the measured response was determined as follows:

$$\Delta_\lambda^{rcr} = \frac{S_\lambda(\theta) - \cos\theta(S_\lambda(0°))}{\cos\theta(S_\lambda(0°))} \qquad [\text{A3-1}]$$

The variation of Δ_λ^{rcr} with illumination angle is shown in Figure 3.14. The error in cosine response increases with wavelength and with the incident angle of illumination. In order to account for Δ_λ^{rcr} and derive correct surface spectral albedos (α_λ), both incident and reflected irradiance fields must be adjusted for error in cosine response. Assuming the incident irradiation field (E_λ) is made up of a direct (D) and diffuse (d) component and that the reflected irradiance field (M_λ) is diffuse, the true spectral albedo is given by

$$\alpha_\lambda = \frac{M(true)}{E_\lambda^D(true) + E_\lambda^d(true)} \qquad [\text{A3-2}]$$

Thus, in order to correct for incorrect RCR response, the spectral irradiance of incoming diffuse irradiance at time of measurement is needed. Unfortunately this was not measured in the1993 experiment. Upon the discovery of the RCR problem, it was added to the

experiment program in 1995. Clear-sky measurements of E_λ^d were collected by shading the diffuser with an opaque disk mounted to the RCR on a rotating arm. The disk was adjusted until the diffuser was completely covered. These measurements were taken during the same season and at the same time of day as the 1993 measurements and are considered applicable to the problem here. The diffuse/total ratio (v) for 1995 is shown in figure A3.1. Similar data measured at the South Pole (Grenfell *et al.*, 1994) is added for comparison. Air molecules and suspended ice crystals in the atmosphere diffuse atmospheric light at a level inversely proportional to the wavelength of incident radiation. Using the measured global irradiance (E_λ), the diffuse/total ratio is used to determine E_λ^D and E_λ^d

$$E_\lambda^d = v \cdot E_\lambda \qquad [\text{A3-3}]$$

$$E_\lambda^D = E_\lambda - E_\lambda^d \qquad [\text{A3-4}]$$

The true direct component of the incident irradiance is calculated by:

$$E_\lambda^D(true) = \frac{E_\lambda^D}{1 + \Delta_\lambda^{rr}(\theta)} \qquad [\text{A3-5}]$$

where θ refers to the solar zenith angle at the time of observation.

Assuming that the observed diffuse incident and reflected radiation fields were isotropic, we can utilize the following correction factor, CF, to correct the observed diffuse radiation:

$$CF_\lambda = \frac{0.5}{\int_0^1 [1 + \Delta_\lambda^{rr}(u)] \cdot u \cdot du} \qquad [\text{A3-6}]$$

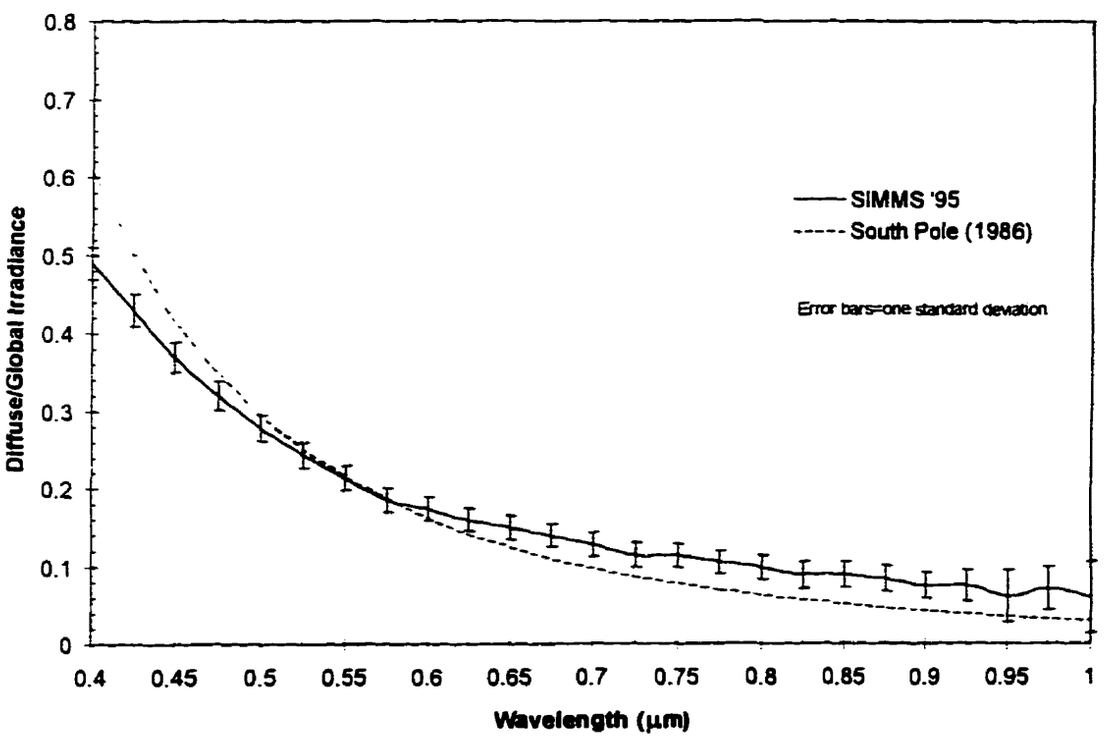
where u is $\cos\theta$. Thus, the true observed albedo on is then found by

$$\alpha_\lambda = \frac{CF_\lambda M_\lambda}{CF_\lambda E_\lambda^d + E_\lambda^D / [1 + \Delta_\lambda^{rr}(\theta)]} \qquad [\text{A3-7}]$$

On cloudy days, the incident and reflected radiation is assumed to consist entirely of isotropic diffuse radiation. The correction in A3-7 thus cancels out for cloudy day data and is not necessary.

Using the lab data, direct and diffuse correction factors were determined for the full range of incident angles for the wavelength range of the radiometer. Since all field measurements were collected under solar zenith angles in the range 50-60°, average correction factors derived from the 50°, 55° and 60° data were determined. Correction factors varied slightly over this range justifying the use of an averaged value. This resulted in an added uncertainty to the corrected albedo of 1-1.5%.

Figure A3.1 Ratio of diffuse/total irradiance on clear days. South Pole data based on empirical fit to data collected by Grenfell et al., (1994).



Appendix 4. Determining Clear-sky Surface Global Irradiance

The global spectral irradiance ($E_{s\lambda}$) at the surface consists of two components -- a direct ($E^D{}_\lambda$) and diffuse ($E^d{}_\lambda$) component. The following expresses the global spectral irradiance on a horizontal surface:

$$E_{s\lambda} = E^D_\lambda \cos\theta + E^d_\lambda \qquad [\text{A4-1}]$$

The global spectral irradiance is expressed in W m^{-2} μm^{-1}. The direct component of surface irradiance on a horizontal surface is a function of the exoatmospheric irradiance adjusted for mean sun-Earth distance ($E_{TOA\lambda}$) and the atmosphere's total transmissivity (T_λ) adjusted for atmospheric path (air mass):

$$E^D_\lambda = E_{TOA\lambda} T_\lambda \cos\theta \qquad [\text{A4-2}]$$

The direct component of irradiance was determined by Lowtran 7 using transmission functions determined for the prescribed atmospheric conditions.

Diffuse radiation is caused by scattering of incident and reflected radiation by air molecules and aerosols (Dave, 1978; Iqbal, 1981). The diffuse component of irradiance can form a significant portion of the global irradiance at high latitudes over high-albedo surfaces. This is mainly due to multiple reflections between the surface and the atmosphere. Here the diffuse component is separated into the following components after Brine and Iqbal (1983):

$$E^d_\lambda = E^d_{r\lambda} + E^d_{a\lambda} + E^d_{m\lambda} \qquad [\text{A4-3}]$$

where $E^d_{r\lambda}$ is the diffuse spectral irradiance produced by Rayleigh scattering at the ground after one pass through the atmosphere, $E^d_{a\lambda}$ is the diffuse spectral irradiance produced by aerosols at the ground after one pass through the atmosphere, and $E^d_{m\lambda}$ is the diffuse spectral irradiance produced by multiple reflections. This approach *(two-stream approximation)* assumes that the scattering of molecules and by aerosols can be separated. The following expressions are all empirical and approximate in nature.

The diffuse irradiance due to Rayleigh scattering at the ground generated by an exoatmospheric irradiance on a horizontal surface at the TOA is calculated as follows:

$$E^d_{r\lambda} = E_{TOA\lambda} \cos(\theta) T_{ma\lambda} \left[0.5(1 - T_{r\lambda}) T_{a\lambda}\right] \qquad [\text{A4-4}]$$

where $T_{ma\lambda}$ is the transmittance due to molecular absorption (ozone, mixed gases (CO_2, O_2), water vapour), $T_{r\lambda}$ is the transmittance due to Rayleigh scattering and $T_{a\lambda}$ is the transmittance due to aerosol attenuation. The above equation assumes that half of the diffuse radiation is scattered towards the surfaces.

The diffuse irradiance due to aerosol scattering is the most difficult component of the diffuse irradiance to estimate. The major reason is the difficulty in accurately describing the characteristics of the scattering aerosols. Here, the optical characteristics of the aerosols are based on empirical and theoretical observations. The following expression was used to calculate $E^d_{a\lambda}$ after the first pass through the atmosphere:

$$E^d_{a\lambda} = E_{TOA\lambda} \cos(\theta) T_{ma\lambda} \left[g_\lambda \omega_\lambda (1 - T_{a\lambda}) T_{r\lambda}\right] \qquad [\text{A4-5}]$$

where g_λ and ω_λ are the aerosol's asymmetry factor and single scattering albedo respectively. These optical parameters for [A3-5] are taken from Blanchet and List (1982) and are based on a relative humidity of 70%.

The amount of diffuse irradiance reaching the ground due to multiple reflections between the ground and atmosphere was calculated as follows

$$E_{m\lambda}^{d} = Q_{\lambda}\left(\frac{\alpha_{s\lambda}\alpha_{atm\lambda}}{1-\alpha_{s\lambda}\alpha_{atm\lambda}}\right) \qquad [\text{A4-6}]$$

where $\alpha_{s\lambda}$ and $\alpha_{atm\lambda}$ are the surface spectral albedo and atmospheric albedo. The atmospheric albedo is estimated by

$$\alpha_{atm\lambda} = T_{ma\lambda}\left[0.5(1-T_{r\lambda})T_{u\lambda} + (1-g_{\lambda})\omega_{\lambda}(1-T_{a\lambda})T_{r\lambda}\right] \qquad [\text{A4-7}]$$

Q_{λ} in [A3-6] refers to the direct and diffuse irradiance reaching the ground on a horizontal surface after the first path through the atmosphere. It is calculated by

$$Q_{\lambda} = \left(E_{r\lambda}^{d} + E_{a\lambda}^{d}\right) + E_{\lambda}^{D}\cos(\theta) \qquad [\text{A4-8}]$$

This assumes that the reflected radiation is isotropic.

The above calculations were made at a spectral resolution of 35 cm^{-1} (0.0003 μm at 0.4 μm and 0.055 μm at 4.0 μm). The direct irradiance and transmission functions were determined by the Lowtran 7 radiative transfer code. The calculations of diffuse irradiance were taken from an approach presented in Iqbal (1983). The global, direct and diffuse spectral irradiance for a clear-sky day for a solar zenith angle of 60° is shown in Figure 4.16.

LITERATURE CITED

Allison, I., R.E. Brandt and S.G. Warren (1993). East Antarctic sea ice: Albedo, thickness distribution, and snowcover. *J. of Geophysical Research.* 98(C7):12417-12429.

Arrigo, K.R., C.W. Sullivan and J.N. Kremer (1991). A bio-optical model of Antarctic sea ice. *Journal of Geophysical Research.* Vol. 96(C6):10 581-10 592.

Barber, D.G, D. Johnson and E.F. LeDrew (1991). Measuring climatic state variables from SAR images of sea ice: The SIMS SAR validation site in Lancaster Sound. *Arctic,* 44(1):108-121,

Barrie, L.A., R.M. Hoff and S.M. Daggupaty (1981). The influence of mid-latitudinal pollution sources on haze in the Canadian Arctic. *Atmospheric Environment,* 15(8):1407-1419.

Barrie, L.A. (1986). Arctic air pollution: An overview of current knowledge. *Atmospheric Environment,* Vol. 20(4):643-663.

Barry, R.G. (1996). The parameterization of surface albedo for sea ice and its snowcover. *Progress in Physical Geography,* Vol. 20(1):63-79.

Barry, R.G., A. Henderson-Sellers, K.P. Shine (1984). Climate sensitivity and the marginal cryosphere In Climate Processes and Climate Sensitivity, Geophysical Monograph 29 (5), Ed. J.E. Hansen and T. Takahashi, AGU, Washington, D.C., 368 p.

Blanchet, J. and R. List (1984). *On the optical properties of arctic haze* In Aerosols and Their Climatic Effects. Ed. H.E. Gerber and A. Deepak. A. Deepak Publishing, Hampton, Virginia, 300 p.

Blanchet, J.P. (1982). Application of the Chandrasekhar mean to aerosol optical paramaters. *Atmosphere-Ocean,* Vol. 20:189-206.

Blanchet, J.P. (1989). Toward estimation of climatic effects due to arctic aerosols. *Atmospheric Environment,* Vol. 23(11):2609-2625.

Bohren, C.F. and B.R. Barkstrom (1974). Theory of the optical properties of snow. *Journal of Geophysical Research.* Vol. 79:4527-4535.

Bohren, *CF.* and D.R. Huffman (1983) Absorption and scattering of light by small particles. John Wiley, New York, 530 p.

Borowski, E.J. and J.M. Borwein (1991). *The Harper Collins Dictionary of Mathematics,* HarperPerennial, NewYork, 660 p.

Brest, C.L. and W.B. Rossow (1992). Radiometric calibration and monitoring of NOAA AVHRR data for ISCCP. *International Journal of Remote Sensing,* Vol. 13(2):235-273.

Bryazgin, N.N. and A.P. Koptev (1969). O spektral'nom al'bedo snezhno-ledyanogo pokrova [Spectral albedo of snow-ice cover]. *Problemy Arktiki i Antarktiki*, Vyp. 31:79-83.

Buckley R.G. and H.J. Trodahl (1987). Thermally driven changes in the optical properties of sea ice. *Cold Regions Science and Technology*, Vol. 14:201-204.

Budyko, M.I. (1969). The effect of solar radiation variations on the climate of the Earth, *Tellus*, 21:611-619.

Carrol J.J and B.W. Fitch (1981). Effects of solar elevation and cloudiness on snow albedo at the South Pole, *J. of Geophysical Research*, 86(C6):5271-5276.

Carsey, F.D. Prospects for describing and monitoring from space the elements of the seasonal cycle of sea ice, *Annals of Glaciology*, 5:37-42, 1984.

Carsey, F.D., Arctic sea ice distribution at end of summer 1973-1976 from satellite microwave data, *J. of Geophysical Research*, 87:5809-5835, 1982.

Carsey, F.D., R.G. Barry and W.F. Weeks (1992). Introduction In *Microwave Remote Sensing of Sea Ice*. Ed. F.D. Carsey. Geophysical Monograph 68, American Geophysical Union, 462 p.

Che, N. and J.C. Price (1992). Survey of the radiometric calibration results and methods for visible and near infrared channels of NOAA 7, 9 and 11 AVHRRs. *Remote Sensing of the Environment*, Vol. 41:19-27.

Chen, T.S and G. Ohring (1984). On the relationship between clear-sky planetary and surface albedos. *Journal of Atmospheric Science*, Vol. 41:156-158.

Chernigovsky, N.T. (1963). Radiatsionnnyye svoystva ledyanogo pokrova tsentral'noy Arktiki [Radiational properties of the central Arctic ice cover]. *Trudy Arkticheskogo I Antarkticheskogo Nauchno-Issledovatel'skogo Institua*, Tom 253:249-260.

Choudhury B.J. and A.T.C. Chang (1981). On the angular variation of solar reflectance of snow, *J. of Geophysical Research*, 86(C1):465-472.

Chylek, P., V. Ramaswamy and V. Srivastava (1983) Albedo of soot-contaminated snow, *J. of Geophysical Research*. Vol. 88(C15):10 837-10 843.

Chylek, P., V. Ramaswamy and V. Srivastava (1983). Albedo of soot-contaminated snow. *Journal of Geophysical Research*, Vol. 88(C15):10837-10843.

Cihlar, J., D. Manak, and M.D. D'Iorio (1994). Evaluation of compositing algorithms for AVHRR data over land. *IEEE Transactions on Geoscience and Remote Sensing*, Vol. 32(2):427-437.

Clarke, A.D. and K.J. Noone (1985). Soot in the arctic snowpack: A cause for perturbations in radiative transfer. *Atmospheric Environment*, Vol. 19(12):2045-2053.

Clarke A.D., R.J. Charlson and L.F. Radke (1984). Airborne observations of Arctic aerosol-IV. Optical properties of Arctic haze. *Geophysical Research Letters*. Vol. 11:405-408.

Cogley, J.G. and A. Henderson-Sellers (1984). Effects of cloudiness on the high-latitude surface radiation budget. *Monthly Weather Review*, Vol. 112(5):1017-1032.

Colbeck S.C. (1979). Grain clusters in wet snow. *J. of Colloid and Interface Science*. 72(3):371-384.

Crane, R.G. and M. R. Anderson (1989). Spring melt patterns in the Kara/Barents Sea: 1984. *GeoJournal*, Vol. 18(1):25-33.

Crane, R.G., R.G. Barry and H.J. Zwally (1982). Analysis of atmosphere-sea ice interactions in the Arctic Basin using ESMR microwave data. *International Journal of Remote Sensing*, Vol. 3(3):259-276.

Curry, J.A., F.G. Meyer, L.F. Radke, C.A. Brock and E.E. Ebert (1990). Occurrence and characteristics of lower tropospheric ice crystals in the Arctic. *International Journal of Climatology*, Vol. 10:749-764.

Curry, J.A., J.L. Schramm, E.E. Ebert (1995). Sea ice-Albedo climate feedback mechanism. *Journal of Climate*, Vol. 8(2):240-247.

Dalzell, W.H. and A.F. Sarofim (1969). Optical constants of soot and their application to heat-flux calculations. *Journal of Heat Transfer*. Vol. 91:100-104.

De Abreu, R.A. (1995) *Spectral Measurements* In SIMMS 1995 Data Report. Ed. K. Misurak, C.P. Derksen, E.F. LeDrew and D.G. Barber. ISTS Report ISTS-EOL-SIMS-TR95-003, Dept. of Geograpy, U. of Waterloo, Waterloo, Ont.

De Abreu, R.A., D.G. Barber, K. Misurak and E.F. LeDrew (1995). Spectral albedo of snow-covered first-year and multiyear sea ice during spring melt. *Annals of Glaciology*. Vol. 21:337-342.

De Abreu, R.A., J. Key, J.A. Maslanik, M.C. Serreze and E.F. LeDrew (1994) Comparison of *in situ* and AVHRR-derived broadband albedo over Arctic sea ice. *Arctic*. Vol. 47(3):288-297.

Denoth, A. (1980). The penular-funicular liquid transition in snow. *Journal of Glaciology*. Vol. 25(91):93-97.

Dey B. (1981). Monitoring winter sea ice dynamics in the Canadian arctic with NOAA-TIR images. *Journal of Geophysical Research*. Vol. 86(C4):3223-3235.

Dozier J., S.R. Schneider and D.F. McGinnis Jr. (1981). Effects of grain size and snowpack water equivalence on visible and near-infrared satellite observations of snow. *Water Resources Research*. 17(4):1213-1221.

Dozier, J. (1989). Estimation of properties of alpine snow from Landsat Thematic Mapper, *Advanced Space Research*. Vol.9(1):207-215

Duggin, M.J. (1981). Simultaneous measurement of irradiance and reflected radiance in field determination of spectral reflectance, *Applied Optics*, 20:3816-3818.

Ebert, E.E. (1992). Pattern recognition analysis of polar clouds during summer and winter. *International Journal of Remote Sensing*, Vol. 13(1):97-109.

Ebert, E.E. and J.A. Curry (1993). An intermediate one-dimensional thermodynamic sea ice model for investigating ice-atmosphere interactions. *Journal of Geophysical Research*, Vol. 98(C6):10085-10109.

Elliott, W.P. and D.J. Gaffen (1991). On the utility of radiosonde humidity archives for climate studies. *Bulletin American Meteorological Society*, Vol. 72(10):1507-1520.

Everitt, B. (1980). *Cluster Analysis*. Halsted Press, New York, 136 p.

Flato, G.M. and W.D. Hibler III (1992). On modelling pack ice as a cavitating fluid. *Journal of Physical Oceanography*, Vol. 22:626-651.

Fletcher, J.O. *The heat budget of the Arctic Basin and its relation to climate*, Rep. R-444-PR, Rand Corporation, Santa Monica CA, 1965.

Fung, T. and E.F. LeDrew (1987). Application of principal component analysis to change detection, *Photogrammetric Engineering and Remote Sensing*, Vol. 53(12):1649-1658.

Fung, T. and E.F. LeDrew (1987). Application of principal components analysis. *Photogrammetric Engineering and Remote Sensing*, Vol. 53(12):1649-1658.

Garrity, C. and B. Burns (1988). *Electrical and physical properties of snow in support of BEPERS-88*. Report MWG 88-11. York University, North York, Ontario, 65 p.

Gorman, R.W. (1988). *Sea Ice Characteristics of the Parry Channel*. M.A. Thesis, Carleton University, Ottawa, Ont. 197 p.

Gorsuch, Richard L. (1983). *Factor Analysis*. Lawrence Erlbaum Associates, Hillsdale, N.J., 425 p.

Gray, D.M. and D.H. Male (1981). *The Handbook of Snow*. Pergamon Press, Willowdale-Ontario, 776 p.

Grenfell, T. (1979). The effects of ice thickness on the exchange of solar radiation over the polar oceans. *Journal of Glaciology*. Vol. 22(87):305-320.

Grenfell, T.C. (1983). A theoretical model of the optical properties of sea ice in the visible and near infrared, *J. of Geophysical Research*. Vol. 88(C14):9723-9735.

Grenfell, T.C. (1991). A radiative transfer model for sea ice with vertical structure variations. *Journal of Geophysical Research*. Vol. 96(C9):16 991-17 001.

Grenfell, T.C. and G.A. Maykut (1977). The optical properties of ice and snow in the Arctic Basin, *J. of Glaciology*, 18(80):45-463.

Grenfell T.C. and D.K. Perovich (1981). Radiation absorption coefficients of polycrystalline ice from 400-1400 nm. *J. of Geophysical Research*, Vol. 86(C8):7447-7450.

Grenfell T.C. and D.K. Perovich (1984). Spectral albedos of sea ice and incident solar irradiance in the Southern Beaufort Sea. *J. of Geophysical Research*, Vol. 89:3573-3580.

Grenfell, T. and D.K. Perovich (1986). Optical properties of ice and snow in the polar oceans. II: Theoretical calculations. *SPIE*. Vol. 637 Ocean Optics:242-251.

Grenfell, T.C., D.J. Cavalieri, J.C. Comiso, M. Drinkwater, R.G. Onstott, I. Rubenstein, K. Steffen, D.P. Winebrenner (1992). Considerations for microwave remote sensing of thin sea ice In *Microwave Remote Sensing of Sea Ice*. Ed. F.D. Carsey. Geophysical Monograph 68, American Geophysical Union, 462 pp.

Grenfell, T.C., S.G. Warren and P. C. Mullen (1994). Reflection of solar radiation by the Antarctic snow surface at ultraviolet, visible, and near-infrared wavelengths. *J. of Geophysical Research*. Vol. 99(D9):18 669-18 684.

Gutman, G., D. Tarpley, A. Ignatov and S. Olsen (1995). The enhanced NOAA global land dataset from the Advanced Very High Resolution Radiometer. *Bulletin of American Meteorological Society*. Vol. 76(7), pp. 1141-1156.

Hall, D.K. (1988). Assessment of polar climate change using satellite technology. *Reviews of Geophysics*. Vol. 26(1):26-39.

Hall, D.K. and J. Martinec (1985). *Remote Sensing of Ice and Snow*, Chapman and Hall, New York, 189 p.

Haralick, R.M. and K. Fu (1983). Pattern Rcognition and Cassification In *The Manual of Remote Sensing*, R.N. Coldwell, Ed. Falls Church, Va: ASPRS, Vol. 1:793-805.

Henderson-Sellers, A. and N.A. Hughes (1982). Albedo and its importance in climate theory, *Progress in Physical Geography*, 6(1):1-44.

Henderson-Sellers, A. and Wilson, M.F. (1983). Surface albedo data for climatic modelling, *Reviews of Geophysics and Space Physics*, 21:1743-1778.

Hibler, W.D. (1980). Sea ice growth, drift, and decay, In Dynamics of Snow and Ice Masses, Ed. S.C. Colbeck, Academic Press, Toronto, 468 p.

Holben, B.N., Y.J. Kaufman, and J.D. Kendall (1990) NOAA-11 AVHRR visible and near-IR inflight calibration. International Journal of Remote Sensing 11(8):1511-1519.

Howarth, P.J. and G. Wickware (1981). Procedures for change detection using Landsat digital data. *International Journal of Remote Sensing*, Vol. 2:277-291.

Iqbal, M. (1983). *An Introduction to Solar Radiation*. Academic Press, Toronto, 390 p.

Jaenicke, R. (1984). Physical aspects of the atmospheric aerosol In *Aerosols and their climatic effects*. Ed. H.E. Gerber and A. Deepak. A. Deepak Publishing. Virginia, USA, 297 pp.

Johnston, R.J. (1984). *Multivariate Statistical Analysis in Geography*. Longman, New York, 280 p.

Justice, C.O., T. Eck, D. Tanre and B. Holben (1991). The effect of water vapour on the NDVI derived for the Sahelian Region from NOAA/AVHRR data. *International Journal of Remote Sensing*, Vol. 12:1165-1188.

Keating, G.M., M.C. Pitts and D.F. Young (1989). Ozone reference models for the middle atmosphere (New CIRA), in *Handbook for MAP*, G.M. Keating (Ed.). SCOSTEP, Vol. 31:1-36.

Kellog, W.W. (1983). Feedback mechanisms in the climate system affecting future levels of carbon dioxide, *J. of Geophysical Research*, Vol. 88:1263-1269.

Key, J. and R.G. Barry (1989). Cloud cover analysis with Arctic AVHRR data, 1. Cloud Detection. *J. of Geophysical Research*, Vol. 94:18 521-18 535.

Kidwell, K.B. (1991). *NOAA Polar Orbiter Data Users Guide*. US Dept. of Commerce, NOAA NESDIS, Washington, D.C. 250 p.

Kimes, D.S., J.A. Kirchner and W.W. Newcomb (1983). Spectral radiance errors in remote sensing ground studies due to nearby objects. *Applied Optics*. Vol. 22:8-10.

Kind, R.J. (1980). Snow drifting In *Dynamics of Snow and Ice Masses*, Ed. S.C. Colbeck, Academic Press, Toronto, 468 p.

Kneizys, F., E. Shettle, L. Abreu, J. Chetwynd, G. Anderson, W. Gallery, J. Selby, and S. clough (1988). *User's Guide to LOWTRAN 7*. Air Force Geophysics Laboratory, AFGL-TR-88-0177, Environmental Research Papers, No. 1010, Bedford, MA. 137 pp.

Koepke, P. (1982). Vicarious satellite calibration in the solar spectral range by means of calculated radiances and its application to METEOSAT. *Applied Optics*, Vol. 21(5):2845-2854.

Koepke, P., (1989). Removal of atmospheric effects from AVHRR albedos. *Journal of Applied Meteorology* 28(12):1341-1348.

Koepke, P., T. Kriebel, (1987). Improvements in the shortwave cloud-free radiation budget accuracy. Part I: Numerical Study Including Surface Anisotropy. *Journal of Climate and Applied Meteorology*, Vol. 26:374-395.

Kondratyev, K.Y., V.V. Kozoderov, O.I. Smokty (1992). *Remote Sensing of the Earth from Space: Atmospheric Correction*. Springer-Verlag, New York, 478 p.

Langham, E. (1981). Physics and properties of snowcover In *Handbook of Snow, Principles, Processes, Management and Use*,, Permagon Press, Toronto, 776 p.

Langleben, M.P. (1966). On the factors affecting the rate of ablation of sea ice. *Canadian Journal of Earth Sciences*, Vol.3(4):431-439.

Langleben, M.P. (1968). Albedo measurements of an arctic ice cover from high towers, *Journal of Glaciology*. Vol. 7(50):289-297.

Langleben, M.P. (1971). Albedo of melting sea ice in the southern Beaufort Sea. *Journal of Glaciology*, 10(58):101-104.

Langleben, M.P. (1972). The decay of an annual cover of sea ice, *J. of Glaciology*, 11(63), pp. 337-344.

LeDrew, E.F. (1986). Sensitivity of the Arctic climate: A factor in developing planning strategies for our Arctic heritage, *Environmental Conservation*, Vol. 13(3):215-228.

LeDrew, E.F. (1992). Remote sensing of atmosphere-cryosphere interactions in the polar basin. *The Canadian Geographer, Vol.* 36(4):336-350.

LeDrew, E.F., M. Strome and F. Hegyi (1995). *The Canadian Remote Sensing Contribution to Understanding Global Change.* Dept. of Geography Publication Series, No. 38, University of Waterloo, 434 p.

LeDrew, E.F. and D.G. Barber (1994). The SIMMS program: A study of change and variability within the Marine Cryosphere. *Arctic*, Vol. 47(3):7787-7802.

Lenoble, J. (1993). *Atmospheric Radiative Transfer.* A. Deepak Publishing, Hampton, Virginia, 532 p.

Liljequist, G.H. (1956). Energy exchange of an Antarctic snow field: Short-wave radiation In *Norweigian-British-Swedish Antarctic Expedition, 1949-52 Scientific Results.* Vol.2(1A), Norsk Polarinstitutt, Oslo.

Lillesand, T.M. and R.W. Kieffer (1987). *Remote Sensing and Image Interpretation.* John Wiley & Sons, Toronto, 723 p.

Lindsay R.W. and D.A. Rothrock (1993). The calculation of surface temperature and albedo of Arctic sea ice from AVHRR. *Annals of Glaciology*, Vol. 17:391-397.

Lindsay R.W. and D.A. Rothrock (1994) Arctic sea ice albedo from AVHRR. *Journal of Climate.* 7(11):1737-1749.

Lyon, A.J. (1970). *Dealing With Data.* Pergamon Press, Toronto, 392 p.

Male, D.H. (1980). The Seasonal Snowcover. In *Dynamics of Snow and Ice Masses*, Ed. S.C. Colbeck, Academic Press, Toronto, 468 p.

Marshunova, M.S. (1961). Osnovnyye zakonomernosti radiatsionnogo balansa podstilayushchey poverkhnosti I atmosfery v Arctike [Principal characteristics of the radiation balance of the underlying surface and of the atmosphere in the Arctic]. *Trudy Arkticheskogo I Antarkticheskogo Nauchno-Issledovatel'skogo Institua*, Tom 229:5-23.

Maxwell, J.B. (1980). *The Climate of the Canadian Arctic Islands and Adjacent Waters - Vol. 1.* Environment Canada, 531 p.

Maykut, G.A. Large-scale heat exchange and ice production in the central arctic, *J. of Geophysical Research*, 87(C10):7971-7984, 1982.

Maykut, G. and D.K. Perovich (1987). The role of shortwave radiation in the summer decay of a sea ice cover. *J. of Geophysical Research*, Vol. 92:7032-7044.

Maykut G. and N. Untersteiner (1971). Some results from a time-dependent thermodynamic model of sea ice. *J. of Geophysical Research.* Vol. 76(6):1550-1575.

McCormack, M.P., P. Wang and L.R. Poole (1994). Stratospheric Aerosols in Cloud In *Aerosol-Cloud-Climate Interactions.* Ed. Peter V. Hobbs, Academic Press, 237 p.

McGuffie, K., J.G. Cogley and A. Henderson-Sellers (1985). Climatological analysis of arctic aerosol quantity and optical properties at Resolute, N.W.T. *Atmospheric Environment*, Vol. 19(5):707-714.

McLain, D.H. (1974). Drawing contours from arbitrary data points. *The Computer Journal.* Vol. 17:318-324.

Meehl, G.A. and W.M. Washington (1990). CO_2 sensitivity and snow-sea-ice albedo parameterization in an atmospheric GCM coupled to a mixed-layer ocean model. *Climatic Change*, Vol. 16:283-306.

Milton, E.J. (1982). Field measurement of reflectance factors: A further note, *Photogrammetric Engineering and Remote Sensing*, 48(9):1474-1476.

Misurak, K.M., D.G. Barber, E.F. LeDrew (1993). *SIMMS'93 Data Report*. Report ISTS-EOL-SIMS-TR93-007, Earth Observations Laboratory, U. of Waterloo, Waterloo, Canada.

Misurak, K.M. (1993). *Snow Geophysical Properties* In SIMMS'93 Data Report. Edited by K.M Misurak, D.G. Barber, E.F. LeDrew. Report ISTS-EOL-SIMS-TR93-007, Earth Observations Laboratory, U. of Waterloo, Waterloo, Canada.

Morassutti, M. Surface albedo parameterization in sea-ice models (1989). *Progress in Physical Geography*, Vol. 9:348-366.

Morassutti, M. (1992). Component reflectance scheme for DMSP-derived sea ice reflectances in the Arctic Basin. *International Journal of Remote Sensing*, 13(4):647-662.

Morassutti, M.P. and E.F. LeDrew (1995). *Melt Pond Dataset for Use in Sea Ice and Climate-Related Studies*. Report ISTS-EOL-TR95-001, Earth Observations Lab, U. of Waterloo, Waterloo, Ont. 53 p.

Mullen, P.C. and S.G. Warren, (1988). Theory of the optical properties of lake ice. *Journal of Geophysical Research*, 93:8403-8414.

Neckel, H. and D. Labs (1984). The solar radiation between 3300 and 12500 Å. *Solar Physics*, Vol. 90:205-258.

Neter, J., W. Wasserman and M.H. Kutner (1985). *Applied Linear Statistical Models*. Irwin Press., Homewood, Ill., 1127 p.

O'Brien , H. and R.H. Munis (1975). *Red and Near-infrared Spectral Reflectance of Snow*, CRREL Rep. 332, Hanover, N.H., 18 p.

Overland, J.E. and P.S. Guest (1991). The arctic snow and air temperature budget over sea ice during winter. *J. of Geophysical Research*, Vol. 96:4651-4662.

Paltridge, G.W. and C.M.R. Platt (1976). *Radiative Processes in Meteorology and Climatology*, Elseviar Co., 318 p.

Perovich, D.K. (1990). Theoretical estimates of light reflection and transmission by spatially complex and temporally varying sea ice covers. *J. of Geophysical Research*. Vol. 95(C6):9557-9567.

Perovich, D.K. (1994). Light reflection from sea ice during the onset of melt. *Journal of Geophysical Research*, Vol. 99(C2):3351-3359.

Perovich, D.K. and T.C. Grenfell. (1981). Laboratory studies of the optical properties of young sea ice. *J. of Glaciology*. Vol. 27:331-346.

Pinker, R.T. and L.L. Stowe (1990). Modelling planetary bidirectional reflectance over land, *International Journal of Remote Sensing*, Vol. 11:113-123.

Pinty B., G. Szejwach and J. Stum (1985). Surface albedo over the Sahel from METEOSAT radiances. *Journal of Climate and Applied Meteorology*, Vol. 24(2):108-113.

Piwowar, J.M, K.A. McIntyre and E.F. LeDrew (1995). Characteristics of pond formation on a melting sea ice surface. *Proceedings, 17th Canadian Symposium on Remote Sensing*, June 13-15,Saskatoon, Canada, pp. 141-146.

Piwowar, J.M. (1993). Arctic sea ice: climate change: multitemporal image analyis: Summary and prospects. ISTS Report ISTS-EOL-TR93-006, Earth Observations Laboratory, U. of Waterloo, Wateloo, Ont. CA, 72 p.

Prabhakara, C., H.D. Chang, and A.T.C Chang (1982). Remote sensing of precipitable water over the oceans from Nimbus 7 microwave instruments. *Journal of Applied Meteorology.*, Vol. 21:59-68.

Preuss, H. and J.F. Geleyn (1980) Surface albedos derived from satellite data and their impact on forecast models. *Archives of Meterology, Geophysics and Bioclimatology B*, Vol. 29:345-356.

Price, J.C. (1987) Radiometic calibration of satellite sensors in the visible and near IR: History and outlook. *Remote Sensing of Environment*, Vol. 22:3-9.

Rao, C.R.N. and J. Chen (1995). Inter-satellite calibration linkages for the visible and near-infrared channels of the Advanced Very High Resolution Radiometer on the NOAA-7, -9 and -11 spacecraft. *International Journal of Remote Sensing.* Vol. 16(11):1931-1942.

Raschke, E., T.H. Vonder Haar, R.W. Bandeen and M. Pasternak (1973). The annual radiation balance of the Earth atmosphere system during 1969-1970 from Nimbus 3 measurements. *Journal of the Atmospheric Sciences*, 30:341-364.

Robinson, D.A., G. Scharfen, M.C. Serraze, G. Kukla, and R. Barry (1986). Snow melt and surface albedo in the Arctic Basin, *Geophysical Research Letters*, 13(9):945-948.

Robinson, D.A., G. Scharfen, M.C. Serraze, R. Barry, G. Scharfen and G. Kukla (1992). Large-scale patterns and variability of snow melt and parameterized surface albedo in the Arctic Basin. *Journal of Climate*, 5(10):1109-1119.

Ross, B. and J. Walsh, A comparison of simulated and observed fluctuations in summertime surface albedo in the Arctic Basin, *J. of Geophysical Research*, Vol. 92(C12):13115-13125, 1987.

Rothrock, D.A., D.R. Thomas and A.S. Thorndike (1988). Principal component analysis of satellite passive microwave data over sea ice. *J. of Geophysical Research*, Vol. 93(C3):2321-2332.

Rothrock, D.A., D.R. Thomas and A.S. Thorndike (1988). Principal component analysis of satellite passive microwave data over sea ice. *J. of Geophysical Research*, Vol. 93(C3):2321-2332.

Roujean, J.L, M. Leroy, A. Podaire and P.Y. Deschamps (1992). Evidence of surface reflectance bidirectional effects from a NOAA/AVHRR multi-temporal data set. *International Journal of Remote Sensing*, Vol. 13(4):685-698.

Saunders, R.W. (1990). The determination of broad band surface albedo from AVHRR visible and near-infrared radiances. *International Journal of Remote Sensing* 11(1):49-67.

Schlosser, E. (1988). Optical studies of Antarctic sea ice. *Cold Regions Science and Technology*, Vol. 15:289-293.

Seckmeyer G. and G. Bernhard (1993). Cosine error corrections of spectral UV-irradiances. *SPIE Proceedings*, 2049:140-151.

See, Linda M. (1990). *Surface and Atmospheric Effects on Remotely-Sensed Reflectances.* Master of Science Thesis, McMaster University, Ontario, 196 p.

Sellers, W.D. (1969). A global climatic model based on the energy balance of the Earth-Atmosphere system, *J. of Applied Met.*, Vol. 8:392-400.

Semtner, A.J. (1984) On modelling the seasonal thermodynamic cycle of sea ice in studies of climatic change. *Climatic Change*, Vol. 6, pp. 27-37.

Serreze M., J. Maslanik and J. Key (1993). Cloud data, albedo transects and multiyear ice floe analysis In *SIMMS'93 Data report*. Ed. K. Misurak, D.G. Barber and E.F. LeDrew. ISTS-EOL-SIMMS-TR92-003. Waterloo: Earth Observations Laboratory, ISTS and the Department of Geography, University of Waterloo, Waterloo.

Shaw, G.E. (1982). Atmospheric turbidity in the polar regions. *Journal of Applied Meteorology*, Vol. 21:1080-1088.

Shimabukuro, Y.S. and J.A. Smith (1991). The least-squares mixing models to generate fraction images derived from remote sensing multispectral data. *IEEE Transactions of Geoscience and Remote Sensing*, GE-29(1):16-20.

Shine, K. (1984). Parameterization of the shortwave flux over high-albedo surfaces as a function of cloud thickness and surface albedo. *Quarterly Journal of the Royal Meteorological Society*, Vol. 110:747-764.

Shine, K.P. and A. Henderson-Sellers (1985). The sensitivity of a thermodynamic sea ice model to changes in surface albedo parameterization. *J. of Geophysical Research*, Vol. 90(D1):2243-2250.

Singh, A. (1989). Digital change detection techniques using remotely-sensed data. *Int. J. of Remote Sensing*, 6(6):989-1003.

Slater, P. (1980) *Remote Sensing: Optics and Optical Systems.* Addison-Wesley Publishing Company, Don Mills-Ontario, 575 pp.

Smirnov, A. A.Royer, N.T. O'Neill and A. Tarussov (1994). A study of the link between synoptic air mass type and atmospheric optical parameters. *Journal of Geophysical Research*, Vol. 99(D10):20967-20982.

Steffen, K., R. Bindschadler, Casassa, G., J. Comiso, D. Eppler, F. Fetterer, J. Hawkins, J. Key, D. Rothrock, R. Thomas, R. Weaver, R. Welch (1993) Snow and ice applications of

AVHRR in polar regions: report of a workshop held in Boulder, Colorado, 20 May 1992. *Annals of Glaciology*, Vol. 17:1-16.

Stone, R.S and J.R. Key (1993). The detectibility of arctic leads using thermal imagery under varying atmospheric conditions. *Journal of Geophysical Research*, Vol. 98, No. C7:12 469-12 482.

Stone, R.S., J.R. Key and E.G. Dutton, (*in press*). Properties and decay of stratospheric aerosols in the Arctic following the 1991 eruptions of Mount Pinatubo.

Tanre, D., B.N. Holben, and Y.J. Kaufmann, Y.J. (1992). Atmospheric correction algorithm for NOAA-AVHRR products: Theory and application. *IEEE Transactions on Geoscience and Remote Sensing*, Vol. 30(2):231-248.

Taylor, V.R.and L.L. Stowe (1984). *Atlas of reflectance patterns for uniform Earth and cloud surfaces (NIMBUS-7 ERB -- 61 days)*. NOAA Technical Report NESDIS 10, 66 p.

Teillet P.M. and B.N. Holben (1994) Towards operational radiometric calibration of NOAA AVHRR imagery in the visible and near-infrared channels. *Canadian Journal of Remote Sensing*. Vol. 20(1):1-10.

Teillet, P.M. (1992). AVHRR radiometric-atmospheric correction. *Remote Sensing of the Environment*, Vol. 41:185-195.

Thomas, C.W. (1963). On the transfer of visible radiation through sea ice and snow. *Journal of Glaciology*, Vol. 4:481-484.

Toll, D.L. (1993). Estimation of a regional land surface albedo using narrow band satellite radiance data. *Proceedings for 1989 IGARRS Symposium*, pp. 1286-1288.

Tukey, J.W. (1977). *Exploratory Data Analysis*. Addison-Wesley, Reading, MA. 600 p.

Vermote E., D. Tanre, J.L. Deuze, M. Herman, J.J. Morcrette (1994) *Second simulation of the satellite signal in the solar spectrum (6S)*. Goddard Space Flight Center, Code 923, Greenbelt MD. 134 pp.

Vermote, E. and Y.J. Kaufman (1995). Absolute calibration of AVHRR visible and near-infrared channels using ocean and cloud views. *International Journal of Remote Sensing*. Vol. 16(13):2317-2340.

Vermote, E., L.A. Remer, C.O. Justice, Y.J. Kaufman, D. Tanre (1995). *MODIS Algorithm Technical Background Document. Atmospheric Correction Algorithm: Spectral Reflectances (MOD09)*. Modis Science Team and Associates, EOS ID# 2015, 41 p.

Wadhams, Peter (1994). Remote sensing of snow and ice and its relevance to climate change processes In *Remote Sensing and Global Climate Change*. Ed. R.A. Vaughan and A.P. Cracknell. Springer-Verlag, New York, 495 pp.

Walsh, S.J, J.W. Cooper and I.E. Von Essen (1990). Image enhancement of Landsat Thematic Mapper data and GIS data integration for evaluation of resource characteristics, *Photogrammetric Engineering and Remote Sensing*, vol. 56(8):1135-1141.

Walsh, Stephen J., J.W. Cooper and I.E. Von Essen (1990). Image enhancement of Landsat Thematic Mapper data and GIS data integration for evaluation of resource characteristics. *Photogrammetric Engineering and Remote Sensing*, Vol. 56(8):1135-1141.

Warren, S.G. (1982). Optical properties of snow. *Reviews of Geophysics and Space Physics*. Vol. 20(1):67-89.

Warren, S.G. and W.J. Wiscombe (1980). A model for the spectral albedo of snow, II: Snow containing atmospheric aerosols, *J. of Atmospheric Sciences*, 37:2734-2745.

Weaver, R.L. and V.J. Troisi (1996). Remote sensing data availability from the Earth Observation System (EOS) via the Distributed Active Archive Center (DAAC) at NSIDC, *Vol. 1 - Proceedings from IGARSS '96*. Lincoln, Nebraska, 27-31 May. pp. 651-655.

Weeks, W.F. (1976). Sea ice conditions in the arctic, *AIDJEX Bulletin*, No. 34:173-205.

Weeks, W.F. (1981). Sea ice: The potential of remote sensing, *Oceanus*, 24:39-48.

Welch, R.M., S.K. Sengupta, A.K. Goroch, P. Rabindra, N. Rangaraj and M.S. Navar (1992). Polar cloud and surface classification using AVHRR imagery: An intercomparison of methods. *Journal of Applied Meteorology*, 31(5):405-420.

Wilson, L.D., J. A. Curry, T.P. Ackerman (1993). Satellite retrieval of lower-tropospheric ice crystal clouds in the polar regions. *Journal of Climate*, Vol. 6(7):1467-1472.

Wiscombe W.J. and S.G. Warren (1980). A model for the spectral albedo of snow, I: Pure snow, *J. of Atmospheric Sciences*, 37:2712-2733.

Yamanouchi, T. and S. Kawaguchi (1992). Cloud distribution in the Antarctic from AVHRR data and radiation measurements at the surface. *International Journal of Remote Sensing*, Vol. 13(1):111-127.